Doctoral Dissertation
Doctoral Program in Electrical, Electronics and Communications Engineering (33rd cycle)

Microcavity photonic crystal lasers and quantum dot lasers epitaxially grown on silicon: theory and numerical modelling

Marco Saldutti

* * * * *

Supervisor
Prof. Mariangela Gioannini

Politecnico di Torino

. . . .

Marco Saldutti
Turin,

Summary

In this thesis, we deal with theoretical and numerical modelling of semiconductor lasers targeted at on-chip optical communications. Specifically, we focus on photonic crystal lasers, where the optical cavity is carved out of a semiconductor slab by strong, periodic modulation of the slab refractive index. These lasers are promising sources for optical interconnects, as they are microscopic and have low threshold current, as well as reduced energy cost. We also cover quantum dot (QD) lasers epitaxially grown on silicon. In addition to other well-known advantages, QDs offer enhanced tolerance against threading dislocations (TDs) in the crystalline structure. These dislocations are caused by the mismatch in the lattice constant and thermal expansion coefficients between the silicon substrate and III-V semiconductor materials grown above. Therefore, QDs are a highly attractive active material for on-chip applications. In Chapter 1, we briefly draw up this overarching research context.

In Chapter 2, we investigate the modal properties of passive photonic crystal cavities. We model a photonic crystal cavity as an effective Fabry-Perot resonator. The travelling modes are the Bloch modes of the waveguide on which the cavity is based. By this approach, we derive compact and transparent expressions for the resonance condition and field distribution, which agree with previous predictions based on fitting of finite-difference time-domain (FDTD) simulations. By our approach, we also analyze the scaling of radiation loss with the size of the cavity and offer new insights.

In Chapter 3, we analyze the optical propagation in active photonic crystal waveguides, with a special interest in slow-light effects associated with material gain. In fact, photonic crystal waveguides may support significant slow-light, meaning that the group velocity may be much smaller than the vacuum light speed. In this propagation regime, the modal gain per unit length is enhanced as compared to conventional waveguides under the same pumping conditions, with possible applications to compact optical amplifiers and lasers. We view the presence of material gain as a weak perturbation to a reference photonic crystal waveguide with purely real refractive index. Thus, we expand the field in the basis of the counter-propagating Bloch modes of this reference waveguide. Owing to the presence of gain, a distributed feedback sets is between these Bloch modes, which would be otherwise uncoupled. By this coupled-Bloch-mode approach, we derive a scattering matrix formulation which efficiently describes the optical propagation in active photonic crystal waveguides in the presence of slow-light.

Our model confirms previous results that a fundamental limitation to the slow-light gain enhancement is posed by the gain itself. Furthermore, we offer new insights on the impact of a generally complex refractive index perturbation. In particular, we show that slow-light semiconductor optical amplifiers may benefit from a smaller linewidth enhancement factor.

In Chapter 4, we leverage the scattering matrix formulation of the previous chapter to investigate the impact of slow-light on the oscillation condition of various types of photonic crystal lasers. These include lasers with photonic bandgap mirrors, photonic heterostructure mirrors and a new kind of photonic crystal laser, known as the Fano laser. Our approach goes beyond the conventional picture of slow-light simply reducing the mirror loss and offers new insights. Furthermore, it is flexible and adaptable to the laser configuration of interest. In fact, the laser cavity may generally consist of various sections, either passive or active, with each section modelled by a scattering matrix.

By expanding the oscillation condition around the lasing point, in Chapter 5 we derive a rate equation model which self-consistently accounts for slow-light, including the gain-induced distributed feedback. This approach is potentially applicable to various kinds of lasers, including the Fano laser. We focus on lasers with photonic bandgap mirrors and presents preliminary results on the stationary and small-signal characteristics.

Finally, in Chapter 6 we deal with the continuous wave operation of Fabry-Perot, QD lasers epitaxially grown on silicon. As compared to previous approaches, we employ a drift-diffusion transport model, augmented with conventional rate equations for photons and carriers in the dot-in-a-well (DWELL) layers. Our analysis reveals that TDs in the DWELL layers are those responsible for the degradation of the laser performance. We demonstrate that the asymmetric transport of electrons and holes explains the quenching of the power emitted on the ground state above the excited state lasing threshold under dual state emission. Furthermore, we show that electrostatic effects lead to an optimum p-type modulation doping minimizing the ground state threshold current, an effect evidenced by recent experiments.

Acknowledgements

A number of people have made possible the development and conclusion of this project and must therefore be acknowledged.

First and foremost, I must express sincere gratitude to my family, for their tireless support and love. Albeit far away in space, we have been deeply close in spirit. Without my family, I would have never made it to the end of this journey.

A special mention obviously goes to my supervisor, Mariangela, for her constant guidance, time and patience throughout these years. Her emphasis on necessary context and motivations has been an invaluable source of inspiration and encouragement to broaden my view and improve myself. I would also like to acknowledge all members of my group at Politecnico di Torino. In particular, I am indebted to Paolo Bardella and Lorenzo Columbo, for both the numerous technical discussions and (equally important!) social activities. I am grateful to Federica Cappelluti and Alberto Tibaldi, for the stimulating research collaborations on quantum dot lasers on silicon. I wish to express my gratitude to Prof. Ivo Montrosset, for his sincere interest in my work and his precious feedback. Furthermore, I cannot fail to mention Prof. Renato Orta. His clarity of presentation, attention to details and insights have truly served as a model to me.

Two people from DTU Fotonik have also greatly contributed to this project. Prof. Jesper Mørk, to whom I am indebted for all his invaluable insights, suggestions and, importantly, for his confidence in me. Thorsten S. Rasmussen, whom I sincerely thank for his support during (and not only) my external stay at DTU Fotonik. Technical and less technical discussions with Thorsten have always been helpful.

Last but not least, I must acknowledge all my friends, who have accompanied me in this journey. Thanks for listening and for being there when I needed.

Marco Saldutti

Dissemination of research

Peer-reviewed journal publications

M. Saldutti, T. S. Rasmussen, M. Gioannini and J. Mørk, *"Theory of slow-light semiconductor optical amplifiers"*, Optics Letters **45**, 21, pp. 6022-6025 (2020).

M. Saldutti, A. Tibaldi, F. Cappelluti and M. Gioannini, *"Impact of carrier transport on the performance of QD lasers on silicon: a drift-diffusion approach"*, Photonics Research **8**, 8, pp. 1388-1397 (2020).

M. Saldutti, J. Mørk and M. Gioannini, *"Resonance condition and field distribution in line-defect photonic crystal cavities"*, Proceedings of SPIE **11301**, 113010W (2020).

M. Saldutti, P. Bardella, J. Mørk and M. Gioannini, *"A Simple Coupled-Bloch-Mode Approach to Study Active Photonic Crystal Waveguides and Lasers"*, IEEE Journal of Selected Topics in Quantum Electronics, **45**, 6 (2019).

Conference contributions

M. Gioannini, **M. Saldutti**, A. Tibaldi and F. Cappelluti, *"Carrier Transport in Quantum Dot Laser on Silicon: impact of traps and p-type modulation doping on laser performance"*, accepted for oral presentation, Semiconductor and Integrated Opto-Electronics (SIOE) Conference 2021.

M. Saldutti and M. Gioannini, *"Rate equation analysis of slow-light photonic crystal lasers"*, accepted for oral presentation, Conference on Lasers and Electro-Optics/Europe (CLEO/Europe) 2021.

M. Saldutti, J. Mørk and M. Gioannini, *"Resonance condition and field distribution in line-defect photonic crystal cavities"*, oral presentation, SPIE Photonics West 2020.

M. Saldutti, A. Tibaldi, F. Cappelluti, F. Bertazzi and M. Gioannini, *"Study of CW performance of QD lasers on Silicon including carrier transport in the SCH barrier"*, oral presentation, SPIE Photonics West 2020.

M. Saldutti, J. Mørk and M. Gioannini, *"A simple approach, based on coupled mode theory, to study PhC lasers"*, poster presentation, Conference on Lasers and Electro-Optics/Europe (CLEO/Europe) 2019.

M. Saldutti, J. Mørk, P. Bardella, I. Montrosset and M. Gioannini, *"Coupled Bloch-Wave Analysis of Active PhC Waveguides and Cavities"*, oral presentation, International Conference on Numerical Simulation of Optoelectronic Devices (NUSOD) 2018.

M. Saldutti, J. Mørk, P. Bardella, I. Montrosset and M. Gioannini, *"Coupled Bloch-Wave Analysis of PhC Lasers"*, poster presentation, European Semiconductor Laser Workshop (ESLW) 2018.

Contents

Chapter 1

Research context

1.1 Introduction

The internet traffic has experienced a gigantic increase in the past two decades [22], as dramatically illustrated by Fig. 1.1. Such tremendous growth generates continuing demands for data links with higher bandwidth and lower power consumption. With this regard, optical links may offer advantanges as compared to their electrical counterpart. As a matter of fact, transition from electrical to optical communication has been observed when the product of bandwidth and transmission distance exceeds 100 Gb/s × m [67, 86]. For instance, distributed feedback (DFB) lasers [61, 104] are used in long-haul optical communications. These lasers have an energy cost around 1 pJ/bit. Over shorter distances, inside data centres and supercomputers, vertical-cavity surface-emitting lasers (VCSELs) [42, 156] are widely employed, because they have a lower energy cost around 100 fJ/bit. Optical links are also expected to be advantageous in the so-called *computercom* networks, i.e. on-chip communications [95]. In fact, power consumption and heat generation currently represent a significant limitation to the performance of processor chips. A major contribution to this power consumption is not

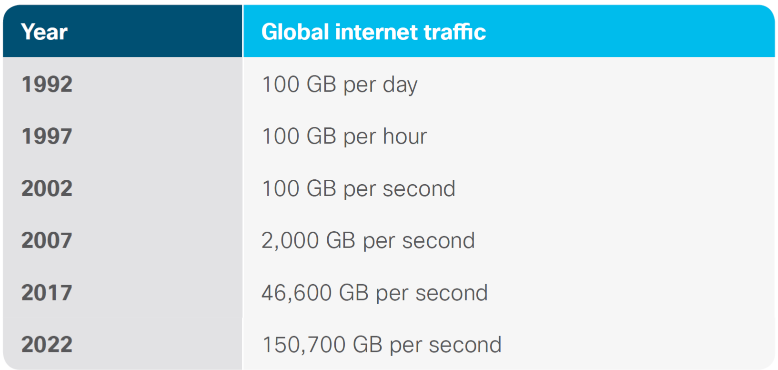

Year	Global internet traffic
1992	100 GB per day
1997	100 GB per hour
2002	100 GB per second
2007	2,000 GB per second
2017	46,600 GB per second
2022	150,700 GB per second

Figure 1.1: Global internet traffic in the last two decades. Reproduced from [22].

due to logic operations within transistors, but rather to transfer of data through electrical wires [67]. This also constitutes an environmental issue, as the global usage of electricity ascribed to communication technologies is constantly increasing [5].

The solution is enabling on-chip optical communication, with an architecture consisting of electrical processing and optical data transfer [106]. For this integration of optics and electronics, a new generation of semiconductor lasers is required, featuring:

- reduced energy cost,
- small footprint,
- and silicon-compatibility.

Specifically, the energy cost should be lower than 10 fJ/bit [95], a target which remains elusive to VCSELs. On the contrary, photonic crystal lasers [54, 24, 89] are promising candidates. In these lasers, the optical cavity is formed by introducing a defect within an otherwise (ideally) perfect photonic crystal structure. This structure is carved out of a semiconductor material via strong, periodic refractive index modulation. The region surrounding the defect collectively acts as a distributed Bragg reflector, thereby tightly confining light to the defect. Various implementations exist, which essentially differ

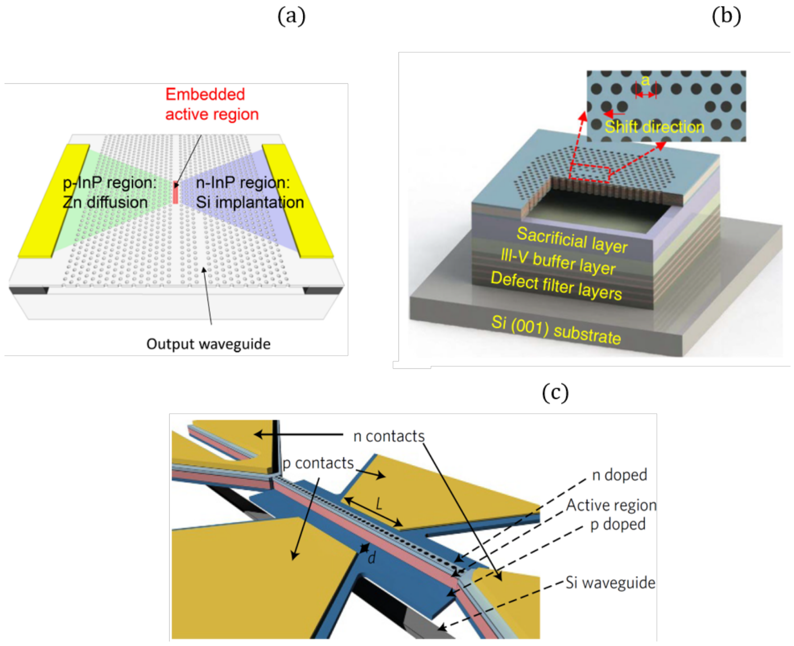

Figure 1.2: Examples of microcavity-based photonic crystal lasers. (a) Lambda-scale-embedded active region photonic crystal (LEAP) laser [89]. (b) Photonic crystal laser epitaxially grown on silicon [187]. (c) Hybrid indium-phosphide on silicon nanolaser diode [24]. (a), (b) and (c) are reproduced from [142], [187] and [24] respectively.

in the nature of the defect and type of pumping. These defect-based photonic crystal lasers can be collectively denoted by *microcavity-based photonic crystal lasers* [126]. As an example, Fig. 1.2 illustrates specific implementations. Other types of photonic crystal lasers exist, which are not defect-based. In these devices, lasing is achieved thanks to a strong distributed feedback throughout a perfectly periodic lattice [92]. These photonic crystal lasers are outside the scope of this thesis. Therefore, unless otherwise specified, when talking about photonic crystal cavities and lasers throughout this thesis, we will implicitly refer to defect-based photonic crystal structures.

Photonic crystal lasers allow to scale down the active region, while keeping a high quality factor. As a result, they exhibit low threshold current and small energy cost, with a wavelength-scale active region. As an example, Fig. 1.3 illustrates the energy cost as a function of the active region for DFB lasers, VCSELs and lambda-scale-embedded active region photonic crystal lasers (LEAP lasers) [89], which are a particular type of photonic crystal lasers. A schematic illustration of a LEAP laser is reported in Fig. 1.2(a). Regarding silicon-compatibility, heterogeneous [24, 159] and, more recently, epitaxial [187] integration of photonic crystal lasers on silicon have been also demonstrated. Fig. 1.2(b) and (c) shows examples of, respectively, epitaxially and heterogeneously integrated photonic crystal lasers.

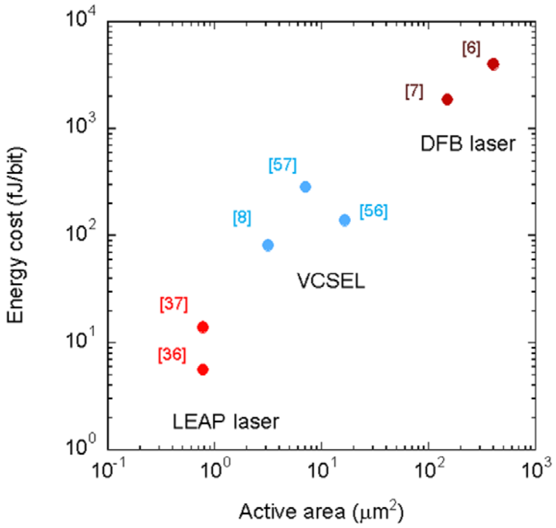

Figure 1.3: Energy cost as a function of the active region area for various semiconductor lasers. The LEAP laser is the so-called lambda-scale-embedded active region photonic crystal laser. References in this figure are numbered as in [89], from which the figure is reproduced.

Essentially, heterogeneous integration [62, 86] consists in pre-patterning the waveguide for the laser output power on a silicon-on-insulator (SOI) substrate. Films of III-V semiconductor material are grown separately on a III-V substrate. Then, the III-V films are bonded to the previously patterned SOI substrate and, after bonding, the laser is processed by standard lithographic techniques. On the other hand, epitaxial integration [78, 76] is viewed as the ultimate solution to minimize the complexity and cost of the fabrication process and improve the integration density of silicon photonic integrated circuits. Within this approach, lasers are directly grown on silicon via epitaxy, without need of bonding. For a thorough review of various approaches to integrate lasers on silicon, we refer to [175].

A major challenge for epitaxial integration is represented by the mismatch in the lattice constant and thermal expansion coefficients between silicon and III-V semiconductor materials. This mismatch leads to threading dislocations [164], which act as non-radiative recombination centres and degrade the laser performance. This issue can be tackled by employing quantum dots (QDs) as the laser active material. In fact, QDs have been proved to be much more tolerant than quantum wells (QWs) to threading dislocations [78]. Carriers are highly localized within QDs, thereby reducing the probability of interaction with defects [74]. This feature adds to other well-known advantages of QDs, such as low threshold current, large differential gain, enhanced tolerance to temperature growth and increased stability against optical feedback [152]. These advantages make QDs highly attractive for on-chip applications [107, 111].

This thesis fits in this overarching research context of semiconductor lasers for on-chip optical communications. It builds up on two projects. A first project is devoted to photonic crystal structures, with a special focus on slow-light effects in active waveguides and lasers. In this respect, Prof. Jesper Mørk of DTU Fotonik has been, on several occasions, an invaluable source of suggestions and ideas. Photonic crystal structures fabricated and characterized in his group have often inspired the investigations of this thesis. These also include Fano lasers, on which I focused during my external research stay at DTU Fotonik from January, 2020 to July, 2020. A second project covers instead quantum dot lasers on silicon, as part of an ongoing collaboration with the group of Prof. Matteo Meneghini at University of Padova. A detailed outline of the chapters of this thesis is provided in Sec. 1.3.

1.2 Rate equations analysis of microcavity lasers

Photonic crystal lasers are compact, microscopic lasers where one longitudinal mode usually dominates by far over the others. For this reason, coupling of modes in space and time can be usually neglected and conventional rate equation models well capture the main characteristics of the laser [85, 126]. In this section, we employ a conventional rate equation model [23] to roughly quantify figures of merit such as threshold current, output power and energy cost, which should be considered when designing microcavity lasers for computercom applications [87]. Therefore, this section serves as an introduction to the main advantages of the small active (and mode) volume of microcavity lasers, such as photonic crystal lasers. This simple picture, though, is challenged in the slow-light region of photonic crystal lasers, where the presence of gain may induce a strong distributed coupling between the counter-propagating modes of the laser cavity. This is one of the main motivations of this thesis, as further outlined in Sec. 1.3.

The rate equations for the carrier density N and photon density N_p read [23]

$$\frac{dN}{dt} = \frac{\eta_i I}{qV_N} - R - v_g g N_p \tag{1.1a}$$

$$\frac{dN_p}{dt} = \Gamma v_g g N_p + \Gamma R_{\mathrm{sp}} - \frac{N_p}{\tau_p} \tag{1.1b}$$

Here, η_i is the injection efficiency, I the injected current, q the electron charge and V_N the volume of the active region. R is the total carrier recombination rate and g the gain per unit length. $v_g = c/n_g$ is the group velocity, with c being the vacuum light speed and n_g the group index. Γ is the total confinement factor (i.e. accounting for all the active layers), which defines the mode volume $V_p = V_N/\Gamma$. R_{sp} is the spontaneous emission rate coupled to the lasing mode, while τ_p is the photon lifetime. This is related to the cavity quality factor (Q-factor) Q and threshold gain g_{th} by

$$\frac{1}{\tau_p} = \frac{\omega}{Q} = \Gamma v_g g_{\mathrm{th}} \tag{1.2}$$

with ω being the mode angular frequency. In photonic crystal lasers, the group velocity may be significantly reduced due to the strong, longitudinal refractive index modulation (an effect thoroughly discussed in Sec. 3.1). It should be emphasized, though, that the group velocity entering laser rate equations for cavity quantities (such as Eqs. (1.1a) and (1.1a)) should only reflect *material* dispersion [101]. The carrier recombination rate can be expressed as [23]

$$R(N) = AN + BN^2 + CN^3 \tag{1.3}$$

Here, A and B are the non-radiative and radiative recombination coefficient respectively, while C is the Auger coefficient. The gain per unit length is given by

$$g = \frac{g_0}{1 + \epsilon N_p} \ln\left(\frac{N + N_{s_0}}{N_{\mathrm{tr}} + N_{s_0}}\right) \tag{1.4}$$

with g_0 being the empirical gain coefficient, N_{s_0} the gain coefficient fitting parameter and N_{tr} the transparency carrier density. The gain saturation with increasing photon density is described by the gain compression factor ϵ.

For an excellent discussion on the application of the rate equation model to photonic crystal lasers, we refer to [126]. In the following, we follow the approach of [87], thereby neglecting for simplicity the spontaneous emission coupled to the lasing mode in Eq. (1.1b). This means that spontaneous emission enhancement due to Purcell effect [169, 108] is not taken into account. As shown in [126], the enhanced spontaneous

Symbol	Parameters	Values
A	Non-radiative recombination coefficient [s^{-1}]	5.0×10^{8}
B	Radiative recombination coefficient [$\mathrm{cm}^3\,\mathrm{s}^{-1}$]	1.7×10^{-10}
C	Auger coefficient [$\mathrm{cm}^6\,\mathrm{s}^{-1}$]	1.0×10^{-28}
d	Active layer thickness [nm]	6
α_i	Intrinsic loss [cm^{-1}]	15
w	Active region width [nm]	300
η_i	Injection efficiency	0.4
n_g	Group index	3.8
λ	Operating wavelength [μm]	1.55
T	Temperature [K]	300
g_0	Empirical gain coefficient [cm^{-1}]	1742
N_{s_0}	Gain coefficient fitting parameter [cm^{-3}]	-1.05×10^{18}
N_{tr}	Transparency carrier density [cm^{-3}]	1.405×10^{18}
ϵ	Gain compression factor [cm^3]	3×10^{-17}
V_{b_0}	Built-in bias voltage [V]	0.6

Table 1.1: Parameters for rate equation analysis [87]

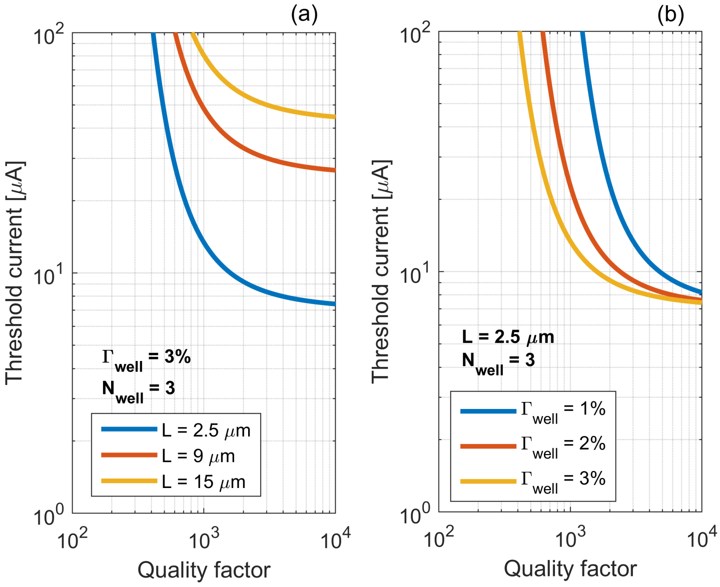

Figure 1.4: Threshold current versus Q-factor for different values of (a) the cavity length L and (b) confinement factor Γ_{well} of a single active layer. In (a), Γ_{well} is 3%, while in (b) L is 2.5 μm. In both cases, the active region consists of 3 active layers.

emission would lower the lasing threshold, smooth the transition from below to above threshold and increase the modulation bandwidth. The parameters are summarized in

Tab. 1.1. They reflect typical LEAP lasers with electrical injection [87].

An essential requirement for lasers targeted at computercom applications is a low threshold current I_{th}. From Eq. (1.1a), one finds

$$I_{\mathrm{th}} = \frac{qV_N}{\eta_i} R(N_{\mathrm{th}}) \tag{1.5}$$

with N_{th} being the threshold carrier density. Therefore, one should reduce the active region volume to lower the threshold current. However, a high Q-factor should be also maintained. In fact, from Eqs. (1.2) and (1.4) the threshold carrier density reads

$$N_{\mathrm{th}} = \left(N_{\mathrm{tr}} + N_{s_0}\right) \exp\left(\frac{\omega}{v_g Q \Gamma_{\mathrm{well}} N_{\mathrm{well}} g_0}\right) - N_{s_0} \tag{1.6}$$

Here, Γ_{well} is the confinement factor of a single active layer and N_{well} the number of active layers, with $\Gamma = \Gamma_{\mathrm{well}} N_{\mathrm{well}}$. Fig. 1.4 shows the threshold current as a function of the Q-factor for different values of (a) the cavity length L and (b) confinement factor Γ_{well}. At a given value of the Q-factor, the threshold current decreases as the cavity length is reduced, owing to the smaller active region volume. Furthermore, a larger confinement factor Γ_{well} also lowers the threshold current, due to the smaller threshold carrier density. The number of active layers N_{well} should be optimized in dependence of the Q-factor. This is highlighted by Fig. 1.5, showing the threshold current versus

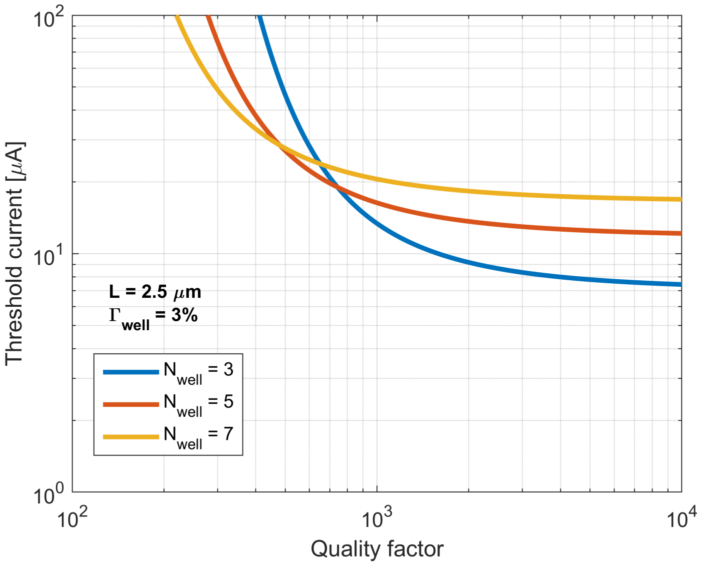

Figure 1.5: Threshold current versus Q-factor for different values of the number N_{well} of active layers. The cavity length is 2.5 μm. The confinement factor Γ_{well} of a single active layer is 3%.

the Q-factor for different values of N_well. The number of active layers minimizing the threshold current stems from the trade-off between two effects. On the one hand, the threshold carrier density diminishes with increasing N_well if the Q-factor is sufficiently low. On the other hand, the active region volume builds up as N_well grows, thereby increasing the threshold current. This effect prevails at high values of the Q-factor.

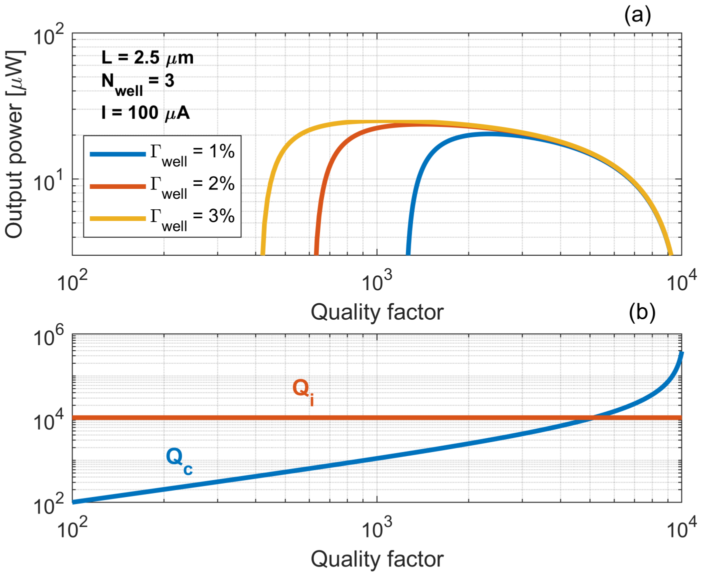

Figure 1.6: (a) Output power versus Q-factor for different values of the confinement factor Γ_well of a single active layer. The cavity length is $L = 2.5\,\mu$m, the number of active layers $N_\text{well} = 3$ and the bias current $I = 100\,\mu$A. (b) Q_c contribution to the Q-factor for a given Q_i versus the Q-factor itself.

A second requirement to be taken into account in the laser design is the output power. Above threshold, from Eq. (1.1a) one finds

$$N_p = \frac{\eta_i}{q\omega} \frac{Q}{\left(V_N/\Gamma\right)} \left(I - I_\text{th}\right) \tag{1.7}$$

From this equation, it is clear that a larger ratio between the Q-factor Q and mode volume V_N/Γ enhances the photon density for a given threshold current. To compute the output power, we may express the Q-factor in terms of two contributions [87]

$$\omega/Q = \underbrace{\omega/Q_i}_{v_g\alpha_i} + \underbrace{\omega/Q_c}_{v_g\alpha_m} \tag{1.8}$$

Here, Q_i accounts for photons lost due to the cavity intrinsic loss α_i and Q_c for those leaving the cavity via output coupling, i.e. because of the mirror loss α_m. The output power is

$$P_\text{out} = \frac{\hbar\omega N_p \left(V_N/\Gamma\right)}{1/\left(v_g\alpha_m\right)} = \frac{\hbar\omega}{q}\eta_i \frac{Q_i}{Q_i + Q_c}(I - I_\text{th}) \tag{1.9}$$

As a consequence, the Q-factor controls the slope efficiency, which tends to unity in the limit $Q_c \ll Q_i$, that is $\alpha_m \gg \alpha_i$. As Q_c increases, the slope efficiency degrades and the output power is reduced. This effect is evident in Fig. 1.6(a), showing the output power versus the Q-factor Q for different values of Γ_{well} and a given bias current. Q_i is fixed and defined by the group index and intrinsic loss in Tab. 1.1. Q_c is instead computed from Q_i and Q by means of Eq. (1.8) and reported in Fig. 1.6(b). For a given Γ_{well}, the output power initially builds up as the Q-factor grows, owing to the increasingly smaller threshold current. However, as the Q-factor is further increased, the output power saturates and then steeply diminishes, because of the reduction of the slope efficiency. Consequently, while a larger Q-factor always improves the threshold current, an optimum Q-factor exists which maximizes the output power. The larger the confinement factor Γ_{well} is and the smaller this Q-factor becomes, since the threshold current is reduced.

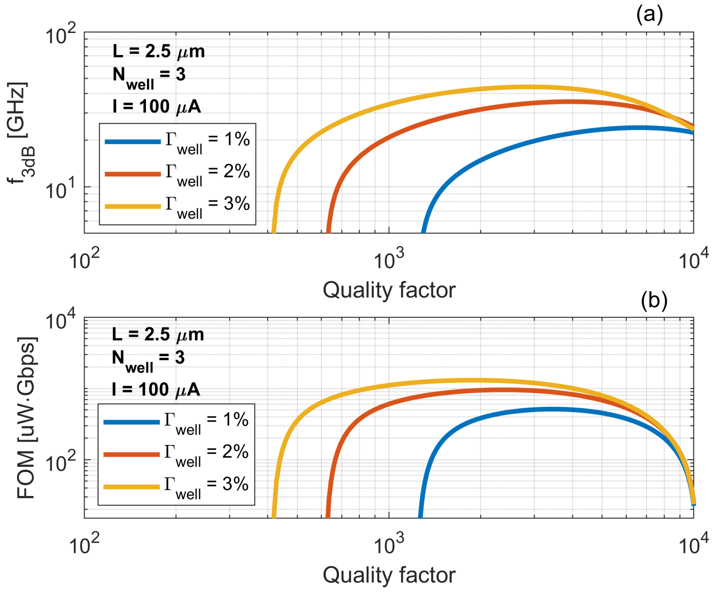

Figure 1.7: (a) 3-dB direct modulation bandwidth and (b) FOM versus Q-factor for different values of the confinement factor Γ_{well} of a single active layer. The cavity length is $L = 2.5\ \mu$m, the number of active layers $N_{\text{well}} = 3$ and the bias current $I = 100\ \mu$A.

In addition to threshold current and output power, the 3-dB direct modulation bandwidth $f_{3\text{dB}}$ is another important figure of merit orienting the laser design. The angular frequency $\omega_{3\text{dB}} = 2\pi f_{3\text{dB}}$ can be generally expressed as [23]

$$\omega_{3\text{dB}} = \sqrt{\omega_R^2 - \frac{1}{2}\gamma^2 + \frac{1}{2}\sqrt{\gamma^4 - 4\gamma^2\omega_R^2 + 8\omega_R^4}} \tag{1.10}$$

with ω_R being the relaxation resonance (angular) frequency and γ the damping factor.

Above threshold, ω_R and γ read [23]

$$\omega_R = \sqrt{\frac{\eta_i \Gamma_{\text{well}} N_{\text{well}}}{q V_N} v_g \frac{a_0}{1+\epsilon N_p} (I - I_{\text{th}})} \tag{1.11a}$$

$$\gamma = K \frac{\omega_R^2}{4\pi^2} + \frac{1}{\tau_{\Delta N}} \tag{1.11b}$$

Here, K is the so-called $K-$factor

$$K = 4\pi^2 \left(\frac{Q}{\omega} + \frac{\epsilon}{v_g a_0} \right) \tag{1.12}$$

The differential gain $a_0 = (\partial g/\partial N)|_{\epsilon=0}$ and differential carrier lifetime $\tau_{\Delta N} = (\partial R/\partial N)^{-1}$ are evaluated at the lasing threshold. In the limit of low damping (i.e. $\gamma \ll \omega_R$), the 3-dB modulation bandwidth $f_{3\text{dB}}$ is proportional to ω_R. Therefore, reducing the threshold current, scaling down the active region volume and increasing the confinement factor are effective strategies to increase the modulation bandwidth. In this respect, photonic crystal lasers offer clear advantages. As an example, Fig. 1.7(a) shows $f_{3\text{dB}}$ as a function of the Q-factor for different values of Γ_{well} and a given bias current. Initially, as the Q-factor grows, the modulation bandwidth steeply increases, due to the strong reduction of the threshold current. However, at high values of Q, the damping factor is strong enough to make $f_{3\text{dB}}$ saturate and then even decrease. The figure also emphasizes that the bandwidth significantly improves with a larger confinement factor if Q is not too high. A convenient figure of merit encompassing both the static and dynamic characteristics may be [87]

$$\text{FOM} = B \cdot P_{\text{out}} \tag{1.13}$$

Here, $B = 1.3 f_{3\text{dB}}$ is the data rate which is assumed to be achievable under direct non-return-to-zero modulation [168]. The FOM is reported in Fig. 1.7(b) as a function of the Q-factor under the same conditions of Fig. 1.6(a) and Fig. 1.7(a). As a result of the constraints simultaneously imposed by the Q-factor on ouput power and modulation bandwidth, the optimum Q-factor is usually within the range 1000-3000.

As an alternative, the energy cost EC is often employed [106] to describe the laser energy efficiency in terms of static and dynamic characteristics. It is defined as [87]

$$\text{EC} = \frac{P_{\text{in}}}{B} = \frac{I V_{b_0} + R_s I^2}{B} \tag{1.14}$$

Here, $P_{\text{in}} = I V_{b_0} + R_s I^2$ is the electrical power absorbed by the laser, with V_{b_0} being the built-in bias voltage and R_s the series electrical resistance. This is related to the electrical resistivity ρ_s by $R_s = \rho_s / L$. Fig. 1.8 illustrates the energy cost as a function of $f_{3\text{dB}}$ for a given value of the Q-factor. Each color denotes a different value of the cavity length, with the solid (dotted) line corresponding to $\rho_s = 10^4\ \Omega \cdot \mu\text{m}$ [87] ($\rho_s = 0$). The

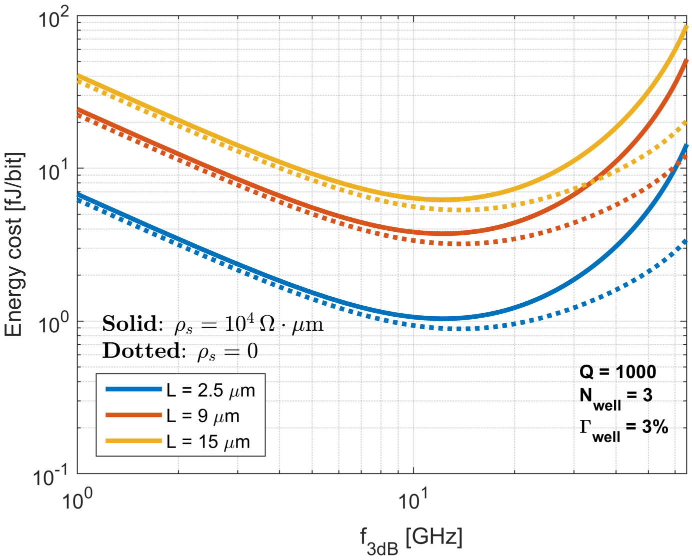

Figure 1.8: Energy cost versus 3-dB direct modulation bandwidth, with each color corresponding to a different value of the cavity length. The electrical resistivity ρ_s is $10^4\,\Omega\cdot\mu\text{m}$ (solid) and 0 (dotted). The Q-factor is $Q = 1000$, the number of active layers $N_{\text{well}} = 3$ and the confinement factor of a single active layer $\Gamma_{\text{well}} = 3\%$.

figure highlights that an optimum modulation bandwidth exists which minimizes the energy cost, as also noted in [106]. An optimum occurs irrespective of R_s, although a smaller electrical resistance obviously reduces the energy cost. Furthermore, we have verified that neglecting the gain compression factor improves the energy cost at high values of bandwidth (as expected), but it does not alter the trend in Fig. 1.8 from a qualitative point of view. This trend can be easily understood by assuming $\gamma \ll \omega_R$ (i.e. low damping), leading to $f_{3\text{dB}} \approx \frac{\omega_R}{2\pi}\sqrt{1+\sqrt{2}}$ [23]. In this case, by using Eq. (1.11a) and neglecting the gain compression factor, we may express the data rate B as

$$B = 1.3 f_{3\text{dB}} \approx \frac{1.3}{2\pi}\sqrt{\left(1+\sqrt{2}\right)\frac{\eta_i \Gamma_{\text{well}} N_{\text{well}}}{qV_N} v_g a_0 (I - I_{\text{th}})} \tag{1.15}$$

From Eq. (1.15), the bias current reads $I = I_{\text{th}} + B^2/\zeta$, with ζ being a proportionality factor independent of the bias current

$$\zeta = \frac{1.69}{4\pi^2}\left(1+\sqrt{2}\right)\frac{\eta_i \Gamma_{\text{well}} N_{\text{well}}}{qV_N} v_g a_0 \tag{1.16}$$

By inserting the expression of the bias current into Eq. (1.14) and neglecting for simplicity the electrical resistance, one finally finds

$$\text{EC} \approx \left(\frac{I_{\text{th}}}{B} + \frac{B}{\zeta}\right) V_{b_0} \tag{1.17}$$

This equation reveals that at low data rates the power consumption is dominated by the threshold current, with the energy cost being inversely proportional to the data rate. However, as one demands larger and larger data rates, the required excess current $I - I_{\text{th}}$ increases and gradually dominates the power consumption. Therefore, the energy cost deteriorates as the data rate grows. Overall, Fig. 1.8 emphasizes that a close relationship exists among size, speed and energy efficiency [106]. Compact lasers are necessary to minimize the energy cost. In fact, the energy cost benefits twofold from a shorter cavity length, i.e. a smaller active volume. Firstly, via reduction of the threshold current. Secondly, via the enhanced modulation bandwidth at a given current in excess to threshold (i.e. a larger ζ). The small values of energy cost around 1-10 fJ/bit outline that photonic crystal lasers are good candidates for computercom applications. It is instructive to estimate from Eq. (1.17) the optimum data rate which minimizes the energy cost. For this purpose, we may express I_{th} as $\frac{qV_N}{\eta_i}\frac{N_{\text{th}}}{\tau_s}$, with τ_s being an effective carrier lifetime. By setting to zero $\partial\,(\text{EC})\,/\partial B$, one finds the optimum date rate

$$B_{\text{opt}} = \sqrt{\frac{1.69}{4\pi^2}\left(1+\sqrt{2}\right)\Gamma_{\text{well}} N_{\text{well}} v_g a_0 \frac{N_{\text{th}}}{\tau_s}} \tag{1.18}$$

This equation explains why the optimum bandwidth in Fig. 1.8 is independent of the cavity length. In fact, since the Q-factor is fixed, the threshold carrier density does not vary with the cavity length. As a result, the optimum bandwidth stays the same.

1.3 Outline

In the following, we provide a detailed outline of the following chapters.

In Chapter 2, we deal with passive photonic crystal cavities. These cavities are usually analyzed by rigorous approaches, such as finite-difference time-domain or various frequency domain methods [71]. However, these approaches are computationally demanding and based on a global analysis of the cavity, which often obscures the underlying physics. On the contrary, in Chapter 2 we develop a transparent and efficient modelling framework [136] for the analysis of passive photonic crystal cavities. Within this framework, the cavity is modelled as an effective Fabry-Perot resonator for the Bloch modes of the waveguide on which the cavity is based. By this approach, as compared to previous investigations [118, 178], we provide new insights on the resonance condition and field distribution in passive photonic crystal cavities.

In Chapter 3, we focus on active photonic crystal waveguides. It is well known that photonic crystal waveguides may support significant slow-light [65, 9]. This means that the group velocity may be much smaller than the vacuum light speed. In this propagation regime, the modal gain per unit length which can be achieved in a photonic crystal waveguide with active material may be significantly enhanced as compared to a conventional active waveguide under the same pumping conditions [29]. This slow-light gain enhancement may enable the realization of shorter optical amplifiers [97, 18] and more compact lasers [178], suited to computercom applications. However, this strategy cannot be pursued uncritically, since a fundamental limitation to the slow-light gain enhancement is posed by the gain itself [41, 19]. In Chapter 3, we elaborate on the model presented in [19], from which we derive a convenient scattering matrix formulation [137, 139]. By this approach, the presence of material gain is viewed as a weak perturbation to a reference photonic crystal waveguide with purely real refractive index. Therefore, the optical propagation in the active waveguide is described by a scattering matrix for the amplitudes of the forward- and backward-propagating Bloch modes of the reference waveguide. Owing to the presence of gain, a distributed feedback sets is between these Bloch modes, which would be otherwise uncoupled. The model is applied to investigate the impact of slow-light in compact semiconductor optical amplifiers [139]. In particular, we show that, for a given material gain, devices with smaller linewidth enhancement factor may offer better performance.

In Chapter 4, we investigate the impact of slow-light on the oscillation condition of various photonic crystal lasers. After a quick review of the currently most promising types of photonic crystal lasers, we focus on some specific implementations based on line-defect waveguides. We go beyond the conventional picture [105, 178] according to which slow-light simply enhnaces the modal gain or, equivalently, reduces the mirror loss. On the contrary, we employ the scattering matrix formulation developed in Chapter 3 to offer new insights. In particular, the model is applied to lasers with photonic bandgap mirrors [178] and photonic heterostructure mirrors [148], the latter being similar to LEAP lasers. Furthermore, we explore the impact of slow-light on the tuning characteristics of a new, recently proposed photonic crystal laser, the so-called Fano laser [102].

In Chapter 5, we derive a rate equation model which self-consistently accounts for slow-light in photonic crystal lasers. In fact, the conventional picture would predict an increase of the photon lifetime due to the slow-light reduction of the mirror loss. Thus, the laser modulation speed could be compromised by slow-light [105, 106]. However, as discussed in Chapter 4, slow-light does not simply reduce the mirror loss. Owing to the gain-induced distributed feedback between the forward- and backward-propagating Bloch modes, the computation of a photon lifetime is not straightforward. We note that the photon lifetime is an essential parameter for the laser dynamic characteristics. With these motivations in mind, in Chapter 5 we present the preliminary stages of our investigations.

Finally, in Chapter 6 we set aside photonic crystals to deal with quantum dots on silicon as an active material. We focus on Fabry-Perot, quantum lasers epitaxially grown on silicon [17, 57]. Currently, these devices are considerably longer (measuring hundreds of μm) than photonic crystal lasers. Therefore, they are not directly suited to computercom applications. However, they represent an instrumental platform for studying the properties of the active material epitaxially grown on silicon. In particular, we investigate three relevant issues regarding the continuous wave operation of these lasers.

Namely, the impact of threading dislocations [59]; the quenching of the power emitted on the ground state above the excited state lasing threshold, in the presence of double state lasing [49]; and the existence of an optimum p-type modulation doping which minimizes the ground state threshold current [186]. As compared to previous approaches [38, 80], we employ a drift-diffusion transport model [39, 165], augmented with conventional rate equations for photons and carriers in the quantum dot layers. This analysis sheds light on the role of carrier transport and offers new [138] insights.

Chapter 2

Passive Photonic Crystal Cavities

In this chapter, we deal with passive photonic crystal cavities based on line-defect waveguides. In Sec. 2.1, we provide an overview on photonic crystal cavities and explain the main concepts behind their working principle. Furthermore, we provide motivations for this chapter. In the following sections, we present our investigations on the resonant modes of line-defect cavities. Specifically, in Sec. 2.2 we deal with the dispersion relation and Bloch modes of the waveguide on which the cavity is based. In Sec. 2.3, we obtain the resonance condition. In Sec. 2.4, we derive simple analytical expressions for the longitudinal resonant modes of the cavity. In Sec. 2.5, we focus on the fundamental resonant mode, which is thoroughly analyzed both in the real and reciprocal space. In particular, we investigate the scaling of the radiation loss with the size of the cavity. Finally, in Sec. 2.6 we draw the conclusions.

2.1 Introduction and motivation

It is well known that defects in the crystalline structure of semiconductor materials (such as impurity doping atoms) introduce additional states within the *electronic* bandgap [158]. Similarly, defects in the periodic pattern of refractive index making up a photonic crystal lead to additional states within the *photonic* bandgap [179]. By introducing a line-defect or a point-defect, one can create a waveguide or a resonant cavity, which can guide light efficiently or confine it tightly. As an example, Fig. 2.1(a) shows a photonic crystal slab based on an hexagonal lattice of holes. Fig. 2.1(b) and (c) depict, respectively, a waveguide and a cavity carved out of the crystal. This type of lattice ensures a large photonic bandgap for TE polarization (i.e. with the electric field lying within the plane of periodicity) [55] and is often employed in the realization of photonic crystal lasers. In this case, the slab also includes the active medium, made of strained quantum wells [119, 121] or quantum dots [30, 187] which provide high gain for TE-polarized light. The holes are drilled in a slab of semiconductor material with large refractive index (for instance, GaAs, InP or Si). The slab is surrounded by a cladding with low

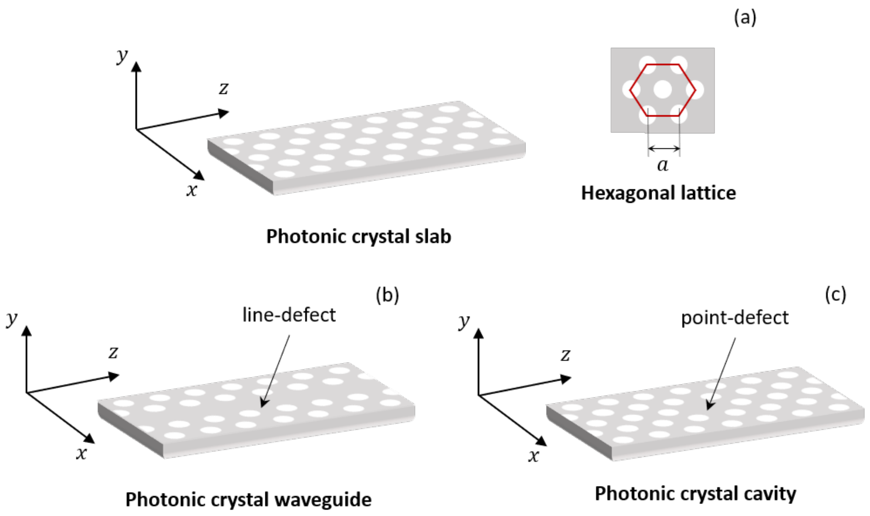

Figure 2.1: (a) Two-dimensional photonic crystal based on an hexagonal lattice of holes. Associated (b) photonic crystal waveguide and (c) photonic crystal cavity. The holes are drilled in a slab made of semiconductor material, with high refractive index contrast between holes and slab.

refractive index (usually, air). The lattice constant *a* and slab thickness are on the order of the guided wavelength and half the guided wavelength respectively. The cavity in Fig. 2.1(c) is often denoted as *LN cavity*, with N corresponding to the number of missing holes [118].

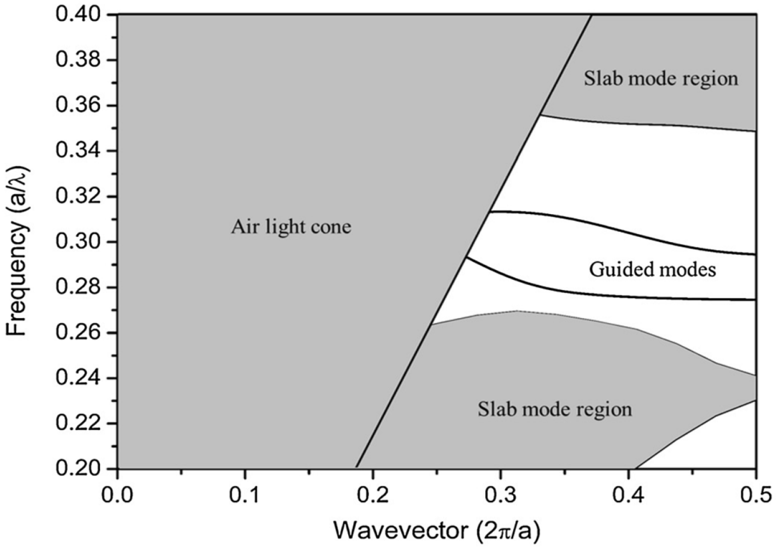

Figure 2.2: Band structure of a line-defect waveguide with air cladding. Reproduced from [27].

Fig. 2.2 shows the band structure of a line-defect waveguide such as that in Fig. 2.1(a), with the cladding made of air. The figure is reproduced from [27] and highlights the main features of the band structure. The x-axis reports the wavevector along the propagation direction (i.e. z, in our case) restricted to the *positive* half of the first Brillouin zone. Indeed, the band structure in the first Brillouin zone is symmetric with respect to the origin [150]. The two bands denoted by *guided modes* correspond to the modes which are fully guided along the line-defect. These modes are confined in the vertical direction (i.e. y-direction) by total internal reflection, while confinement in the lateral direction (i.e. x-direction) is ensured by the photonic bandgap. *Theoretically*, these modes are truly lossless. Out-of-plane radiation losses only occur, in practice, due to fabrication imperfections, which are generally indicated as *disorder*. Later, we will return to this point, to outline the difference as compared to the radiation loss occurring in a cavity. For further details on losses in photonic crystal waveguides induced by disorder, we refer to Sec. 3.1.2. The point where the wavevector is equal to π/a is the upper limit of the first Brillouin zone and is often denoted as *photonic band edge* or simply *band edge*. It corresponds to the cutoff frequency of the guided mode. At this frequency, the group velocity is ideally equal to zero. The regions of the band structure indicated as *slab mode region* include the continuum of modes which are confined along the vertical direction by total internal reflection, but are delocalized in the lateral direction. Finally, the *air light cone* is the so-called *leaky region* (often simply indicated as *light cone*), where the wavevector is too small to fulfil the condition of total internal reflection. Consequently, these modes are not only delocalized in the lateral direction, but also in the vertical one.

2.1.1 Photonic crystal cavities

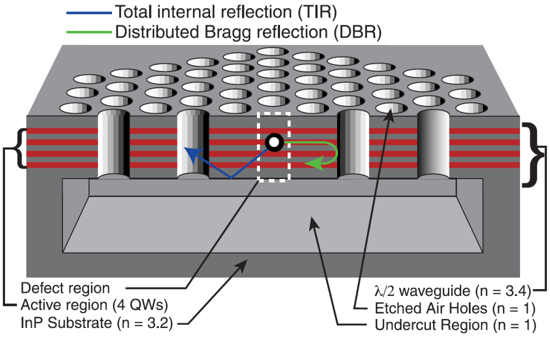

Figure 2.3: Photonic crystal laser based on an LN cavity. Reproduced from [119].

We now turn our attention to photonic crystal cavities, by focusing on specific implementations. The light confinement in LN cavities is illustrated by Fig. 2.3. The figure is reproduced from [119], which was the first demonstration of a photonic crystal laser based on this type of cavity. As in the case of waveguides, light is confined in the vertical (lateral) direction by total internal reflection (by the photonic bandgap). However, due to the finite size of the cavity, there is always a fraction of wavevector components of the cavity resonant mode lying in the leaky region. Therefore, even in the ideal case of a structure with no fabrication imperfections, the resonant cavity suffers from radiation loss [3]. If the cavity is not properly designed, this loss can severely limit the quality factor (Q-factor). In fact, due to the small size of the cavity, the resonant mode may broadly extend in the reciprocal space, with a large amount of wavevector components which cannot fulfill the condition of total internal reflection. By displacing the holes at the edges of the cavity, the fraction of wavevector components in the leaky region can be significantly reduced and the Q-factor consequently increased. The procedure is summarized by Fig. 2.4, which is reproduced from [2]. The arrows indicate the hole displacement, with each each letter corresponding to a pair of holes being displaced. By this technique, the Q-factor computed by finite-difference time-domain (FDTD) simulations is increased from few thousands up to around 10^5. Importantly, the mode volume is almost unchanged and remains on the order of the cubic guided wavelength. The experimental values of the Q-factor are lower (owing to fabrication imperfections and impurities [7]), but well confirm the optimization trend. We refer to Sec. 2.1.2 for further details on the physical principle behind this optimization strategy.

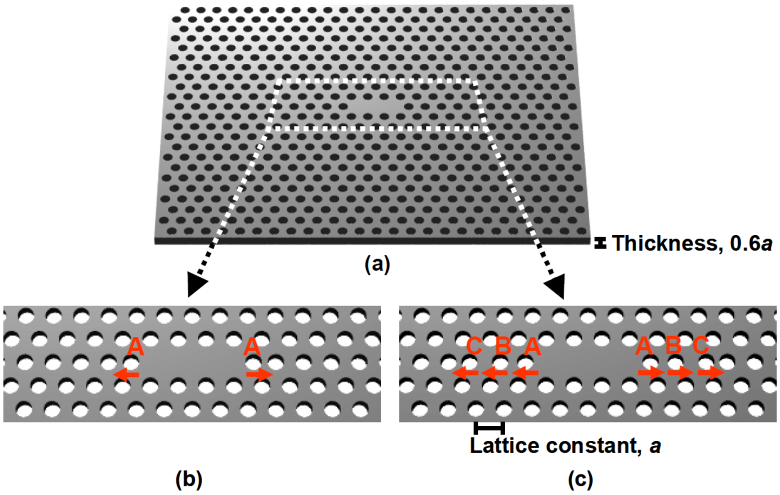

Figure 2.4: Optimization of a point-defect photonic crystal cavity by displacing the holes at the edges. The arrows indicate the hole displacement, with each each letter corresponding to a pair of holes being displaced. Reproduced from [2].

A type of photonic crystal cavity which is even more promising in terms of Q-factor is the so-called *photonic* heterostructure cavity [155]. The working principle is summarized by Fig. 2.5, which is reproduced from [7]. The cavity is formed by connecting line-defect waveguides with different lattice constants. Essentially, the larger lattice

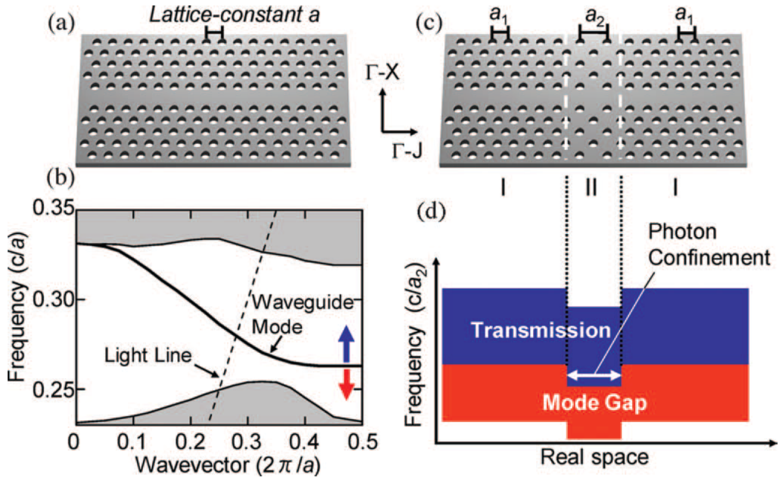

Figure 2.5: (a) Line-defect waveguide and (b) corresponding band structure. The blue (red) arrow in (b) denotes the pass-band (stop-band), where propagation of photons through the waveguide is allowed (inhibited). (c) Photonic heterostructure cavity. (d) Schematic representation of the band diagram of the photonic heterostructure cavity along the waveguide direction. Reproduced from [7].

constant in region II as compared to regions denoted by I (see Fig. 2.5(c)) induces a relative shift of the band edge of the line-defect waveguides corresponding to the various regions. Specifically, an increase (decrease) in the lattice constant results in a shift of the band edge to lower (higher) frequencies (see Fig. 2.5(b) and (d)). This ensures an effective confinement of photons along the waveguide direction. In fact, photons which are allowed to propagate in region II find themselves within the bandgap of regions I. The experimental Q-factor of this cavity was found to be around $6 \cdot 10^5$, with a mode volume on the order of the cubic guided wavelength [7]. The superior Q-factor of the heterostructure cavity stems from the gentler field confinement, which suppresses the field spectral content within the leaky region.

Various modifications and improvements of the heterostructure cavity have been demonstrated. For instance, the lattice constant can be varied more gradually by increasing the number of regions which make up the heterostructure. This approach has led to a theoretical Q-factor with a record value of 10^9, while keeping a mode volume of one cubic guided wavelength [163]. However, tuning the lattice constant is not the only technique to engineer the photonic bandgap. This can be also performed by varying the waveguide width [162].

The modification of the lattice constant and waveguide width are *structural* changes. However, another intriguing and possibly *reconfigurable* modification is the refractive index modulation. One can of course change the refractive index of adjacent waveguide sections in a structural manner. This approach has indeed culminated in the demonstration of high-speed electrically pumped photonic crystal lasers [160], which are reviewed

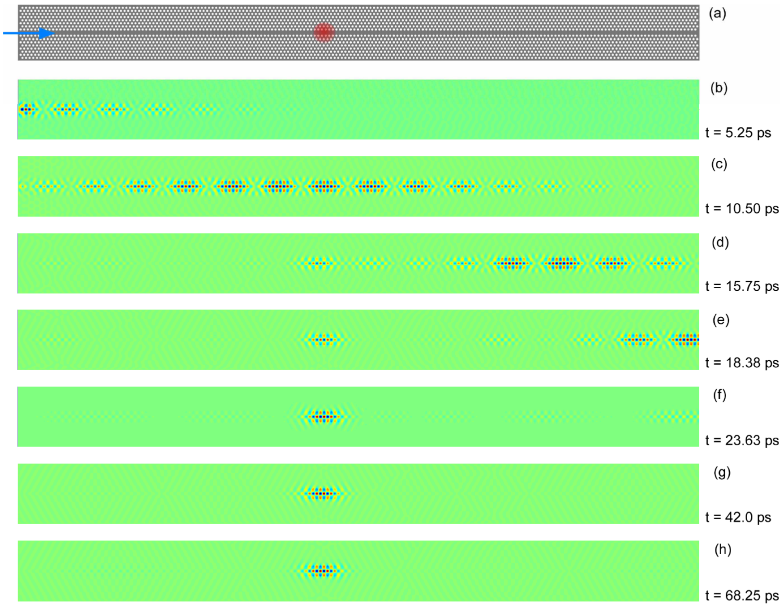

Figure 2.6: FDTD simulation of photon pinning by dynamic refractive index modulation. (a) Line-defect waveguide. The blue arrow indicates the light pulse injected into the waveguide. The red spot indicates the pulse focused on the waveguide at $t = 11.025$ ps to locally tune the refractive index. The waveguide is 80 μm long. (b)-(h) Snapshot of the optical field distribution at various time instants. Reproduced from [115].

in Sec. 4.1. However, the refractive index can be also tuned *dynamically*, thus inducing, on demand, a photonic heterostructure cavity. This can be done, for instance, by shining an optical pulse at a given location along a line-defect waveguide. Through optical nonlinearities, the refractive index is locally changed and a high-Q heterostructure cavity is formed, which effectively traps photons injected from the waveguide input [115]. Fig. 2.6 summarizes the FDTD simulations carried out in [115]. The relative refractive index modulation $\Delta n/n$ is around 10^{-3}. Interestingly, the theoretical Q-factor for this type of cavity is extremely high (larger than 10^9).

2.1.2 Radiation loss and light cone

After this overview, we can now have a closer look at the electric field inside an LN cavity in the reciprocal space. These concepts are preliminary for the analysis which we carry out in the following sections.

At a given frequency, the time-averaged power radiated out of the cavity is proportional to the integral within the light cone of the *spatial* Fourier transform of the electric field intensity [171]. Therefore, as anticipated in Sec. 2.1.1, suppressing the wavevector components of the field within the light cone is an effective strategy to maximize the Q-factor. This can be better understood by considering that the Fourier transform of the electric field spatial profile consists of a set of plane waves, each with a given wavevector **k**. The light cone is determined by the component of **k** which is *tangential* to the interface between slab and cladding [3]. We denote the magnitude of this component by $|k_{\parallel}|$, with $|k_{\parallel}|^2 = k_x^2 + k_z^2$ (see Fig. 2.1 for the reference system). If $|k_{\parallel}|$ cannot be conserved at the interface, there is total internal reflection. Otherwise, the plane wave with that wavevector can leak out of the slab. As a consequence, the light cone corresponds to the region in the reciprocal space defined by

$$|k_{\parallel}| < \frac{\bar{\omega}}{c} n_{\text{clad}} \tag{2.1}$$

with $\bar{\omega}$ being the angular frequency of the resonant mode and n_{clad} the cladding refractive index. Therefore, one should in principle take into account the two-dimensional spatial distribution of the field in the xz-plane of the LN cavity (see Fig. 2.1(c)). Furthermore, it should be emphasized that TE-like modes in these cavities have *two* electric field components (E_x and E_z in our reference system), both possibly coupling to radiation modes.

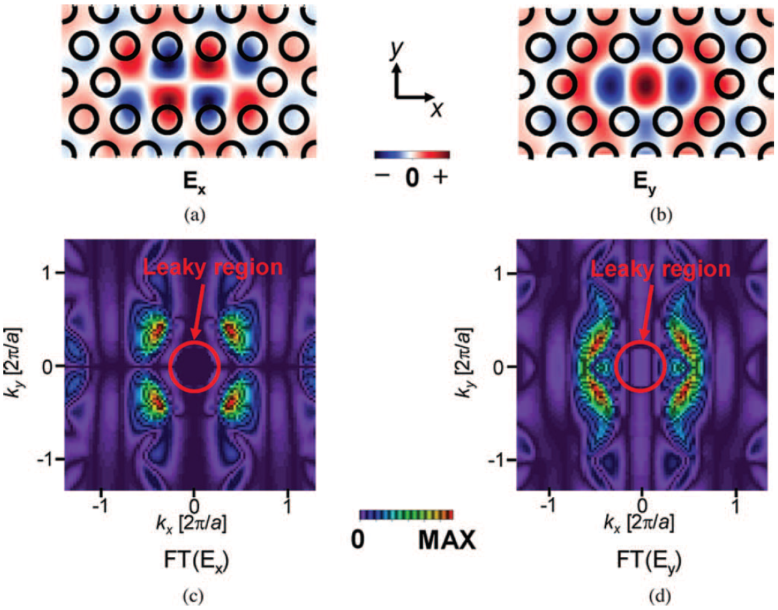

Figure 2.7: Spatial distribution of the (a) longitudinal and (b) lateral electric field component in an LN cavity. Spatial Fourier transform of the (c) longitudinal and (d) lateral component. Reproduced from [7].

In practice, the analysis can be considerably simplified. Firstly, it turns out that the *longitudinal* field component (E_z in our reference system) has a much smaller spectral content within the light cone as compared to the *lateral* one (E_x in our reference system). This is outlined by Fig. 2.7, which is reproduced from [7] (notice the difference in the reference system adopted therein). Therefore, we may only consider the lateral component. In the following sections, when computing the resonance condition and analyzing the resonant modes in the real and reciprocal space, we make indeed this approximation.

Secondly, one can actually go further and reduce the analysis to one dimension by only considering the field spatial distribution along the *longitudinal* direction, as suggested by various authors [2, 118]. In fact, the fraction of wavevector components within the light cone is mainly caused by the broadening along the x-axis in Fig. 2.7(d), with this broadening due to the field variation along the longitudinal direction in the real space. In the following sections, we make use of this approximation as well.

In light of these considerations, one can easily understand the strategy which has guided researchers in the optimization of the Q-factor of LN cavities. The rule of thumb is that the spatial envelope of the field should vary as gradually as possible at the edges of the cavity. Intuitively, this can be understood by assuming the cavity to be one-dimensional. In this case, the field of the resonant mode in the real space may be expressed as the product of an envelope and a sinusoidal wave with spatial period given by the guided resonant wavelength. Therefore, abrupt changes in the envelope lead to high frequency components in its spatial Fourier transform. These components are then transferred to the light cone upon convolution of the envelope Fourier transform with the Fourier transform of the sinusoidal wave, thus degrading the Q-factor. As a consequence, these abrupt changes should be avoided [7]. This is exactly the raison d'être of the displacement of holes at the edges of the cavity in Fig. 2.4. Indeed, by displacing the holes, the periodicity of the crystal on either side of the cavity is perturbed and its reflection somehow weakened. Therefore, the field penetrates deeper within the crystal and is more gently confined within the cavity.

2.1.3 Motivation of this chapter

The general advantage of photonic crystal cavities is that they are small and have a high quality factor. Broadly speaking, the strength of the light-matter interaction scales with Q/V, with Q being the quality factor and V the mode volume. Indeed, a larger Q/V essentially means that photons are confined for a *longer* time in a *smaller* volume.

A laser would obviously benefit of a large Q/V in terms of its threshold current. In fact, the threshold carrier density exponentially decreases with increasing Q-factor and optical confinement factor (see Eq. (1.6) in Sec. 1.2). In addition, a larger Q/V enhances the relative fraction of spontaneous emission coupled to the lasing mode as compared to the undesired spontaneous emission into other modes (Purcell effect) [108]. These benefits allow for compact and energy efficient lasers, which are strongly required for photonic integrated circuits and optical interconnects [87]. However, the advantages are not limited to lasers. A larger Q/V implies a higher intracavity light intensity per unit input power [113]. This means that devices relying on optical nonlinearities (for instance, optical switches) would also be more energy efficient [153]. In sensors, a larger

Q/V results in a better detection sensitivity [20]. A high Q-factor also enables adiabatic frequency conversion [162], with possible applications to photonic memories. This is a general and completely classical wave phenomenon, whose experimental observation in the optical domain has been allowed by the long photon lifetime of photonic crystal cavities. Essentially, the cavity resonance frequency is dynamically tuned by changing the cavity refractive index within the photon lifetime, while the cavity is holding a light pulse. As a result, the frequency of the resonant mode is adiabatically shifted in proportion to the shift in the cavity resonance frequency. The refractive index is changed such that the light trapped within the cavity, at the new frequency, is more strongly coupled with the output. Therefore, a light pulse much shorter than the photon lifetime is emitted. This phenomenon suggests a way to store and release photons on demand, with arbitrary timing.

Overall, these are only a few examples illustrating why high-Q photonic crystal cavities have attracted large interest. For an excellent review of the many possible applications of these cavities, we refer to [113].

Photonic crystal cavities can be analyzed by rigorous approaches, such as finite-difference time-domain (FDTD) or various frequency domain methods, which directly solve Maxwell's equations over the entire structure. From the analysis of the simulation results, the Q-factor is obtained. Essentially, the FDTD method computes the Q-factor from the decay rate in time of the electromagnetic energy stored within the cavity (i.e. the photon lifetime). In the frequency domain, the Q-factor is instead obtained from the ratio between the real and imaginary part of the complex eigenfrequency of the resonant mode [70]. Various techniques are discussed and compared in [71].

However, these approaches are computationally demanding. Furthermore, they rely on a global analysis of the cavity, from which gaining physical insights is not always straightforward. On the other hand, it has been shown that the photon confinement in passive photonic crystal cavities based on line-defect waveguides can be largely understood in terms of a Fabry-Perot picture [70]. Essentially, these cavities behave as effective Fabry-Perot resonators for the *Bloch* modes of the waveguide.

Inspired by this idea, in this chapter we develop a transparent and efficient modelling framework for the analysis of passive photonic crystal cavities. This framework is then extended in Chapter 3 and Chapter 4 to structures with optical gain. Specifically, in this chapter we derive analytical expressions for the resonant modes of passive photonic crystal cavities solely based on the knowledge of the Bloch modes of the associated line-defect waveguide. By this approach, we study the scaling of the radiation loss with the cavity length, which has recently received attention in the context of passive cavities [118] and lasers [178]. Our analysis offers new insights on the results presented in those studies, which rely on different approaches.

In [118], a systematic investigation of LN cavities is carried out by FDTD simulations. Specifically, the field distribution and Q-factor of these cavities are analyzed. Being based on direct solution of Maxwell's equations, the FDTD method is rigorous, but time-consuming. In addition, it often obscures the underlying physics. As compared to [118], we provide analytical expressions derived in a transparent manner, without need of fitting. In [178], the approach of [145] is applied to LN cavities. Essentially, the photonic crystal cavity is described by a stepwise variation of the average permittivity along the propagation direction. The modes of a given cavity, possibly affected by disorder, are expanded on the basis of the Bloch modes of the ideal cavity (i.e. without disorder) truncated to a given order. By inserting this expansion into Maxwell's equations, a finite generalized eigenvalue equation is obtained. By solving this equation, one finds the modes of the disordered cavity with the corresponding eigenfrequencies. This approach is applied in [178] to investigate the scaling of the Q-factor versus cavity length with and without disorder. Our analysis clarifies specific aspects of the results of [178] in the absence of disorder and suggests a possible, simple interpretation of the impact of disorder.

2.2 Dispersion relation and Bloch modes

To compute the resonant modes of an LN cavity, we need three ingredients: 1) the dispersion relation and 2) Bloch modes of the line-defect waveguide on which the cavity is based; 3) the resonance condition of the cavity. In this section, we focus on the first two ingredients.

2.2.1 Dispersion relation

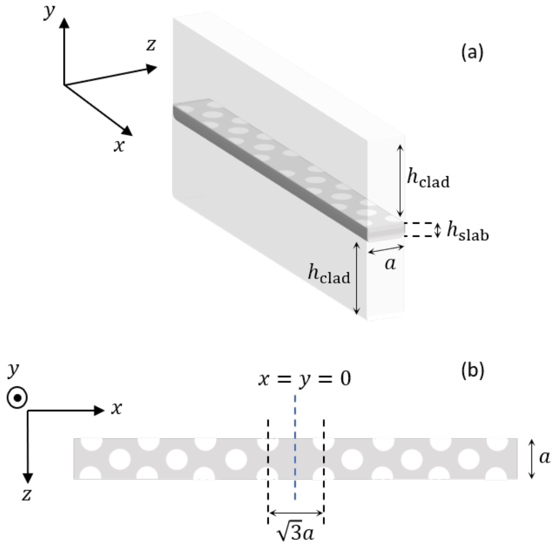

Figure 2.8: (a) Three-dimensional and (b) top view of a supercell to compute dispersion relation and Bloch modes of a line-defect waveguide.

The photonic band structure of a perfect crystal may be computed by the plane wave expansion method [47, 56]. Essentially, by making use of Bloch's theorem [8], Maxwell's equations in the frequency domain are recast as a linear eigenproblem, with the frequency being the eigenvalue. The eigenstate is then expanded in a plane wave basis (i.e. a Fourier series) truncated to a given order. The problem is thus turned into a finite generalized eigenproblem, with the eigenvector given by the basis coefficients. This matrix eigenproblem can be finally solved by standard linear algebra techniques [47] or more efficient algorithms [56].

Strictly speaking, Bloch's theorem applies to perfectly periodic lattices. For two -dimensional lattices, this implies that one should assume the crystal to be translationally invariant along the third direction. However, this limitation may be circumvented by the so-called *supercell* method [150]. This method allows to compute the band structure of photonic crystal slabs and waveguides. Fig. 2.8 shows the supercell which may be used for the photonic crystal waveguide in Fig. 2.1(b). Within the supercell approximation, the supercell is periodically replicated in all the three dimensions and the band structure of this artificial three-dimensional lattice is computed. The supercell consists of a single lattice constant a along the z-direction, along which the waveguide is indeed periodic. The dimensions along the x- and y-direction should instead be chosen so as to ensure a significant decay of the guided modes towards the boundaries. This condition can be easily met, since the guided modes are strongly localized to the line-defect. With these choices, the eigenmodes of the artificial three-dimensional lattice well approximate those of the line-defect waveguide.

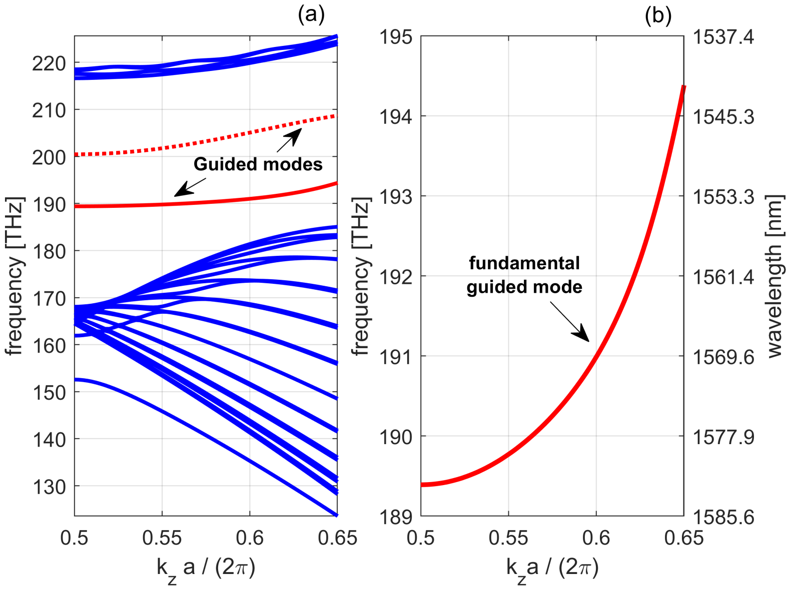

Figure 2.9: (a) Band structure of the line-defect waveguide TE-like modes. The blue lines represent a subset of the continuum of slab modes. (b) Band corresponding to the fundamental guided mode.

Parameters	**Values**
Lattice constant a [nm]	438
Slab refractive index n_{slab}	3.17
Hole radius r	0.25a
Slab thickness h_{slab} [nm]	250
Cladding refractive index n_{clad}	1

Table 2.1: Line-defect waveguide simulation parameters

Throughout this thesis, we employ the MIT-Photonic-Bands (MPB) implementation of the plane wave expansion method to compute the dispersion relation and Bloch modes of a line-defect waveguide within the supercell approximation [56]. The simulation parameters reflect the photonic crystal lasers of [178] and are summarized in Tab. 2.1. Fig. 2.9(a) shows the band structure of the TE-like modes. The guided modes are in red, with the fundamental mode denoted by the solid line. The blue lines represent a subset of the continuum of slab modes. Fig. 2.9(b) is a zoom on the band corresponding to the fundamental guided mode, which is the dispersion relation we need for our analysis. As explained in Sec. 2.4, our formulation requires the forward- and backward-propagating Bloch modes. For this reason, we compute the band structure in the left-hand side of the *second* Brillouin zone (i.e. $k_z \in [\pi/a,\ 2\pi/a]$), where the group velocity is positive and the corresponding Bloch mode is thus forward-propagating. The backward-propagating mode is then obtained as the complex conjugate, as we will also see in Sec. 2.3.

2.2.2 Bloch modes

MPB provides the Bloch modes in a fully vectorial form (that is, x, y and z component) and with three-dimensional spatial dependence, namely

$$\mathbf{E}_{\pm}(\mathbf{r}) = \mathbf{e}_{\pm}(\mathbf{r})e^{\pm ik_z z} \tag{2.2}$$

Here, $\mathbf{E}_+$ ($\mathbf{E}_-$) is the electric field of the forward-propagating (backward-propagating) guided mode and $\mathbf{r}$ is the position vector. The envelopes $\mathbf{e}_{\pm}$ are z periodic, with the period given by the lattice constant a. k_z is the wavenumber along the z-direction. The Bloch modes are normalized, at each frequency, such that

$$\int_V \epsilon_0 n_b^2(\mathbf{r})|\mathbf{e}_+(\mathbf{r})|^2 dV = 1 \tag{2.3}$$

Here, V is the volume of the supercell and n_b the background refractive index, with $n_b = n_{\text{slab}}$ ($n_b = n_{\text{clad}}$) in the slab (cladding). As explained in Sec. 2.1.2, for a qualitative understanding of the radiation loss in LN cavities, it suffices to consider the lateral field component along the longitudinal direction. Therefore, in the following we drop the vectorial notation and implicitly refer to the lateral field component along the *centerline* of the waveguide. This line is denoted by $x = y = 0$ in Fig. 2.8(b), with $y = 0$ corresponding to the middle of the slab along the vertical direction.

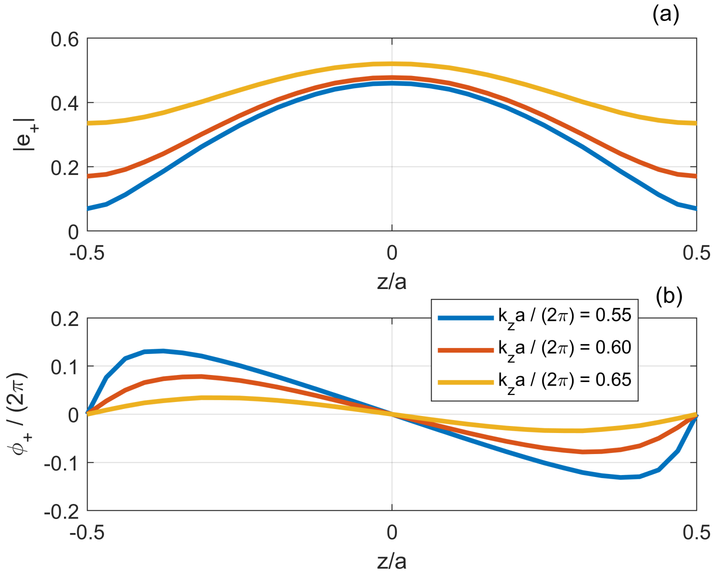

Figure 2.10: Bloch modes of line-defect waveguides. (a) Magnitude and (b) phase of the lateral electric field component of the forward-propagating Bloch mode in a unit cell. Each color corresponds to a different value of the wavenumber. The mode is evaluated along the centerline of the waveguide, indicated as $x = y = 0$ in Fig. 2.8(b).

Fig. 2.10 shows (a) the magnitude and (b) phase of the forward-propagating Bloch mode in a unit cell at different values of the wavenumber. Fig. 2.10 highlights that, as the wavenumber approaches the band edge at π/a, 1) the peak-to-peak amplitude increases and 2) the phase linearly varies with z over a larger and larger portion of the unit cell. These features are common to Bloch modes of one-dimensional Bragg gratings [183]. Moreover, whichever the frequency, the phase is zero at the input and output of the unit cell. Being periodic, the Bloch modes can be expanded in a Fourier series

$$e_+(z) = \sum_q b_q e^{+iq\frac{2\pi}{a}z} \tag{2.4}$$

The spatial harmonics b_q are reported in Fig. 2.11(a) for the modes in Fig. 2.10, with the colours being the same as therein. The harmonics with q other than -1 and 0 are negligible. Therefore, we may express e_+ as

$$e_+(z) = b_0 + b_{-1} e^{-i\frac{2\pi}{a}z} \tag{2.5}$$

Furthermore, as a result of the variation in the peak-to-peak amplitude (see Fig. 2.10(a)) and the linear $z-$dependence of the phase (see Fig. 2.10(b)), the magnitude of b_{-1} approaches the spatial average b_0 as the wavenumber moves towards the band edge. This

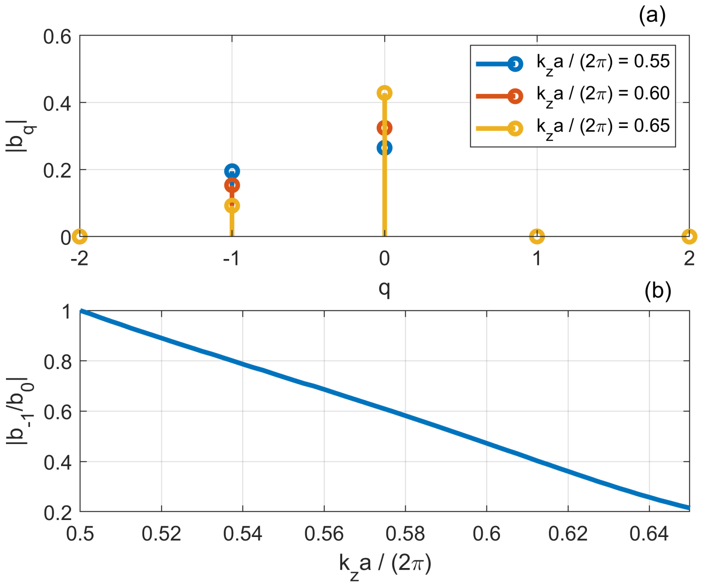

Figure 2.11: (a) Magnitude of the spatial Fourier harmonics of the modes in Fig. 2.10, with the colours being the same as therein. The $x-$axis reports the order q of the harmonics. (b) Magnitude of the ratio between the spatial harmonic of order -1 and the average.

is emphasized by Fig. 2.11(b), showing the magnitude of the ratio $|b_{-1}/b_0|$ versus the wavenumber.

The physical interpretation of this behaviour is straightforward. Upon insertion of Eq. (2.5) into Eq. (2.2), the forward-propagating Bloch mode reads

$$E_+(z) = \underbrace{b_0 e^{+ik_z z}}_{\text{FW}} + \underbrace{b_{-1} e^{-i\left(\frac{2\pi}{a}-k_z\right)z}}_{\text{BW}} \tag{2.6}$$

In other terms, a Bloch mode results (as expected [140, 65]) from the interference of a forward (FW) and backward (BW) component, whose *relative strength* corresponds to the ratio b_{-1}/b_0. If the mode as a whole is forward-propagating, then the forward component is stronger, i.e. $|b_{-1}/b_0| < 1$. In the limit $|b_{-1}/b_0| = 1$, the backward and forward component balance out. Thus, the *net* velocity at which the mode as a whole propagates, which is the group velocity, is zero and the mode is a standing wave. This is the reason why $|b_{-1}/b_0|$ tends to unity as k_z approaches the band edge.

The ratio b_{-1}/b_0 encodes the composition of the Bloch mode, which depends on the waveguide geometry and detuning from the band edge. For instance, in the case of one-dimensional Bragg gratings, the ratio is directly related to 1) the grating coupling coefficient and 2) detuning of the operation frequency from the Bragg frequency (see Eq. (6.41) in [23]).

2.3 Resonance condition

In this chapter, we model and analyze passive LN cavities as effective Fabry-Perot resonators [70]. In this section, we derive the resonance condition. Fig. 2.12 illustrates this type of cavity, with conventional photonic bandgap mirrors. These mirrors are broadband and generally have high reflectivity [70]. The left (right) mirror reflection coefficient is r_L (r_R) and L is the cavity length. The figure also indicates the choice of the unit cell reference planes which we adopt throughout this thesis, with a being the lattice constant. In light of the considerations in Sec. 2.1.2, we only consider the *lateral* electric field component along the *centerline* of the cavity [118]. This line is indicated by $x = y = 0$ in Fig. 2.12, with $y = 0$ corresponding to the middle of the slab along the vertical direction. We expand the field in the basis of the two *guided* counter-propagating *Bloch* modes

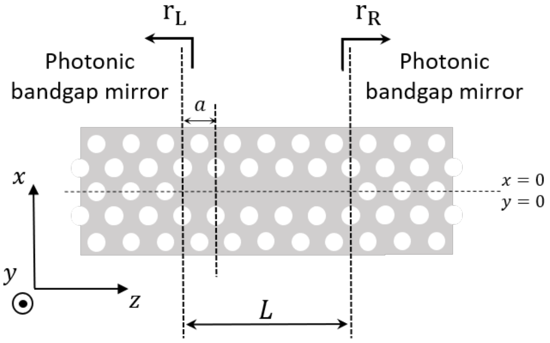

Figure 2.12: LN cavity, with N denoting the number of missing holes.

$$E(z) = c_+(z)e_+(z) + c_-(z)e_-(z) \tag{2.7}$$

with $e_\pm$ being the forward- (+) and backward-propagating (−) Bloch modes and $c_\pm$ the corresponding expansion coefficients. In the absence of optical gain and disorder, the Bloch modes are only coupled at the mirrors. In this case, one finds

$$E(z) = \tilde{F}e^{+ik_z z}e_+(z) + \tilde{B}e^{-ik_z z}e_-(z) \tag{2.8}$$

where while $\tilde{F}$ ($\tilde{B}$) is the amplitude of the forward (backward) Bloch mode. We set the point $z = 0$ at the centre of the cavity. Therefore, the left (right) mirror is located at $z = -L/2$ ($z = L/2$) and the boundary conditions read

$$\tilde{F}e^{+ik_z\frac{L}{2}}e_+\left(\frac{L}{2}\right)r_R = \tilde{B}e^{-ik_z\frac{L}{2}}e_-\left(\frac{L}{2}\right) \tag{2.9a}$$

$$\tilde{B}e^{-ik_z\left(-\frac{L}{2}\right)}e_-\left(-\frac{L}{2}\right)r_L = \tilde{F}e^{+ik_z\left(-\frac{L}{2}\right)}e_+\left(-\frac{L}{2}\right) \tag{2.9b}$$

The backward mode e_- is the complex conjugate of e_+ [120, 141]. By using this property, the boundary conditions can be recast as

$$\tilde{F}\left[e^{+ik_z\frac{L}{2}}e^{+i\phi_+\left(\frac{L}{2}\right)}r_R\right] - \tilde{B}\left[e^{-ik_z\frac{L}{2}}e^{-i\phi_+\left(\frac{L}{2}\right)}\right] = 0 \tag{2.10a}$$

$$\tilde{F}\left[e^{-ik_z\frac{L}{2}}e^{i\phi_+\left(-\frac{L}{2}\right)}\right] - \tilde{B}\left[e^{+ik_z\frac{L}{2}}e^{-i\phi_+\left(-\frac{L}{2}\right)}r_L\right] = 0 \tag{2.10b}$$

where ϕ_+ is the phase of e_+. The resonance condition is that Eqs. (2.10a) and (2.10b) have a solution other than the trivial solution $\tilde{F} = \tilde{B} = 0$. By enforcing the determinant of the coefficient matrix to be zero, we obtain

$$r_L r_R e^{+2i\left[\phi_+\left(\frac{L}{2}\right)-\phi_+\left(-\frac{L}{2}\right)\right]}e^{+2ik_zL} = 1 \tag{2.11}$$

With our choice of a unit cell (see Fig. 2.8(b)), ϕ_+ is zero at the unit cell input and output, as shown in Fig. 2.10(b). This implies that, with our choice of the reference planes for the cavity length L (see Fig. 2.12), one finds

$$\phi_+(\pm L/2) = 0 \tag{2.12}$$

if L consists of an integer number of unit cells. In this case, if the phase of the left and right mirror is equal to either zero or π, from Eq. (2.11) one obtains

$$k_z - \frac{\pi}{a} = m\frac{\pi}{L} \tag{2.13}$$

with m being an integer. Eq. (2.13) governs the detuning of the wavenumber k_z from the band edge for the longitudinal resonant mode of order m.

Importantly, FDTD simulations of passive LN cavities have revealed that the resonant modes do obey Eq. (2.13) to good approximation [118]. Therefore, we take this agreement as a strong indication of the fact that the phase of a photonic bandgap mirror at the reference plane in Fig. 2.12 may be approximated with either zero or π. In Sec. 2.4, we suggest that zero is the right approximation.

2.4 Resonant modes

Equipped with the understandings of the previous sections, we now examine the spatial dependence of the electric field of a resonant mode. This dependence is shown to agree with the FDTD simulations of [118].

First of all, we assume that an integer number of periods of the Bloch modes $e_\pm$ fits into the cavity length L as denoted in Fig. 2.12. Secondly, we assume the mirrors to have 1) frequency-independent reflection coefficients and 2) zero penetration length. In practice, the field is evanescent within the mirrors, with a frequency-dependent decay constant [143]. However, here we are only interested in the field spatial dependence within the cavity length L, which is enough to reproduce the main findings of [118]. We briefly comment in Sec. 2.5.2 on the impact of a non-zero penetration length. Under these simplifying assumptions and by usage of Eq. (2.7), the electric field within the cavity may be expressed as

$$E(z) = w(z, L)\left[\tilde{F} e^{+ik_z z} e_+(z) + \tilde{B} e^{-ik_z z} e_-(z)\right] \tag{2.14}$$

Here, the window function $w(z, L)$ accounts for the field confinement and is defined as

$$w(z, L) = \begin{cases} 1, & |z| \leq L/2 \\ 0, & |z| > L/2 \end{cases} \tag{2.15}$$

By using Eq. (2.12), the boundary condition at the right mirror from Eq. (2.10a) can be recast as

$$\tilde{B} = \tilde{F} e^{+ik_z L} r_R \tag{2.16}$$

We denote the wavenumber k_z of a resonant mode as k_2 and insert the expansion of Eq. (2.5) into Eq. (2.14), leading to

$$\begin{aligned} E(z) = w(z, L)\Big[\tilde{F}\left(b_0 e^{+ik_2 z} + b_{-1} e^{-i\frac{2\pi}{a}z} e^{+ik_2 z}\right) \\ + \tilde{B}\left(b_0^* e^{-ik_2 z} + b_{-1}^* e^{+i\frac{2\pi}{a}z} e^{-ik_2 z}\right)\Big] \end{aligned} \tag{2.17}$$

where $*$ denotes the complex conjugate. By defining the wavenumber

$$k_1 = \frac{2\pi}{a} - k_2 \tag{2.18}$$

and by usage of Eqs. (2.17) and (2.16), the electric field of a resonant mode can be recast as

$$E(z) = \tilde{F} w(z, L)\left[\left(b_0 e^{+ik_2 z} + b_{-1} e^{-ik_1 z}\right) + \left(b_0^* e^{-ik_2 z} + b_{-1}^* e^{+ik_1 z}\right) r_R e^{+ik_2 L}\right] \tag{2.19}$$

while the resonance condition from Eq. (2.13) provides

$$k_2 L = (m + N)\,\pi \tag{2.20}$$

with N being the number of unit cells. We note that with our choice of the reference planes for the cavity length L (see Fig. 2.12), an LN cavity consists of N unit cells.

2.4.1 LN cavity with N odd

We start by assuming that N is *odd*. In this case, one finds from Eq. (2.20)

$$e^{+ik_2 L} = \begin{cases} +1, & \text{for } m \text{ odd} \\ -1, & \text{for } m \text{ even} \end{cases} \tag{2.21}$$

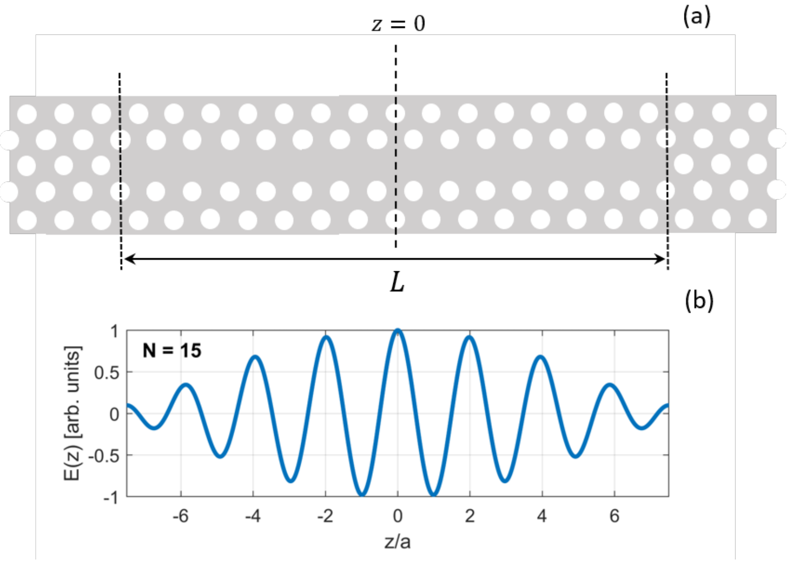

Figure 2.13: (a) LN cavity with $N = 15$ and (b) spatial dependence in arbitrary units of the fundamental mode. The mode is shown between the reference planes delimiting the cavity length L in (a).

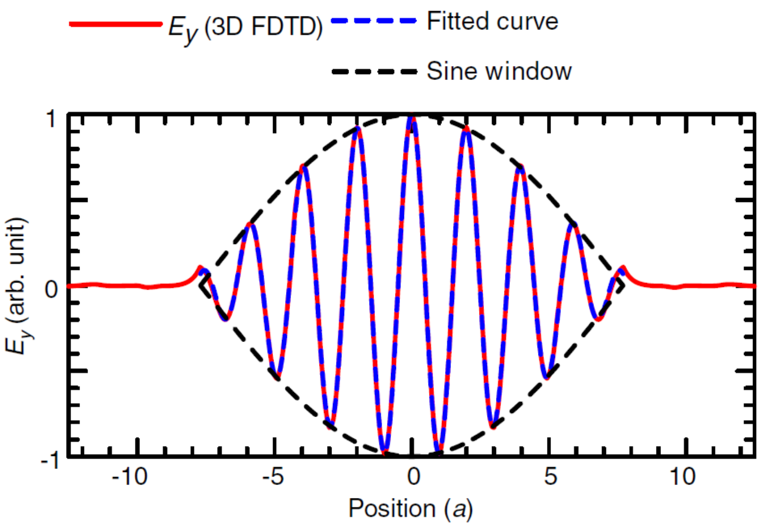

Figure 2.14: Spatial dependence in arbitrary units of the fundamental mode in an LN cavity with 15 unit cells. The figure is reproduced from [118]. According to the reference system used therein, the field component is the *lateral* one.

We assume the right mirror reflection coefficient r_R to have unitary magnitude, which is a reasonable approximation for photonic bandgap mirrors. Concerning the phase, we take it to be equal to zero. We discuss in Sec. 2.4.3 the implications of a phase equal to π.

Since N is odd, the centre of the cavity at $z = 0$ is aligned with a maximum in the magnitude of the Bloch mode $e_+(z)$. In this case, one finds the spatial harmonic b_{-1} to be real and positive. The spatial average b_0 is also found to be real and positive irrespective of N being either odd or even. In light of these considerations, from Eq. (2.19) one finds

$$E(z) = \begin{cases} 2\tilde{F} w(z, L) \left[|b_0| \cos(k_2 z) + |b_{-1}| \cos(k_1 z) \right], & \text{for } m \text{ odd} \\ 2i\tilde{F} w(z, L) \left[|b_0| \sin(k_2 z) - |b_{-1}| \sin(k_1 z) \right], & \text{for } m \text{ even} \end{cases} \tag{2.22}$$

The expressions are consistent with those found in [118] through fitting with FDTD simulations. In particular, $E(z)$ is even (odd) with respect to the centre of the cavity if the order m of the resonant mode is odd (even).

As an example, Fig. 2.13 shows (a) an LN cavity with $N = 15$ and (b) the spatial dependence in arbitrary units of $E(z)$ for the *fundamental* mode (i.e. with $m = 1$). The field is simply computed through Eqs. (2.22) and thus only shown between the reference planes delimiting the cavity length L, where the equation applies. For the sake of comparison, we also include Fig. 2.14, which is reproduced from [118]. It shows the *lateral* component of the electric field in an LN cavity with 15 unit cells, obtained therein through FDTD simulations.

2.4.2 LN cavity with N even

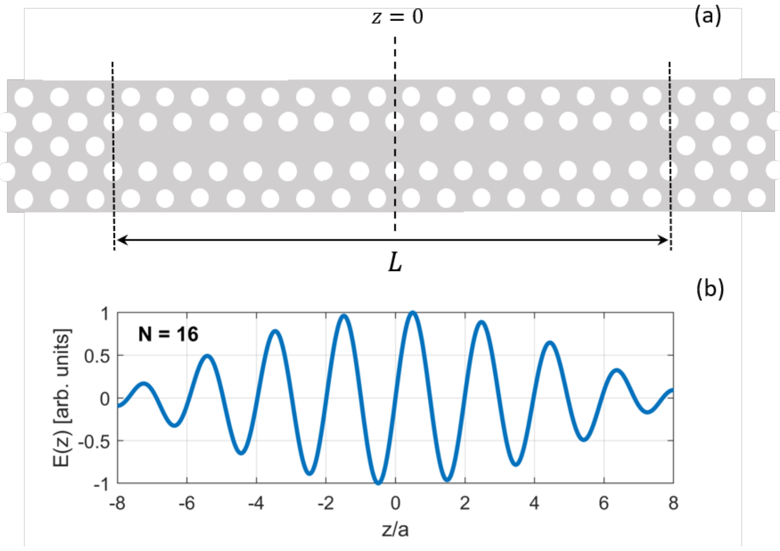

Figure 2.15: (a) LN cavity with $N = 16$ and (b) spatial dependence in arbitrary units of the fundamental mode. The mode is shown between the reference planes delimiting the cavity length L in (a).

We now assume that N is *even*. In this case, one finds from Eq. (2.20)

$$e^{+ik_2 L} = \begin{cases} -1, & \text{for } m \text{ odd} \\ +1, & \text{for } m \text{ even} \end{cases} \tag{2.23}$$

Similarly to Sec. 2.4.1, the right mirror reflection coefficient is assumed to be unitary.

Since N is even, the centre of the cavity at $z = 0$ is aligned with a minimum in the magnitude of the Bloch mode $e_+(z)$. In this case, the spatial harmonic b_{-1} is found to be real and negative. Therefore, from Eq. (2.19) one finds

$$E(z) = \begin{cases} 2i\tilde{F}w(z, L)\left[|b_0|\sin(k_2 z) + |b_{-1}|\sin(k_1 z)\right], & \text{for } m \text{ odd} \\ 2\tilde{F}w(z, L)\left[|b_0|\cos(k_2 z) - |b_{-1}|\cos(k_1 z)\right], & \text{for } m \text{ even} \end{cases} \tag{2.24}$$

which are consistent with [118]. Specifically, $E(z)$ is odd (even) with respect to the centre of the cavity if the order m of the resonant mode is odd (even).

As an example, Fig. 2.13 shows (a) an LN cavity with $N = 16$ and (b) the spatial dependence in arbitrary units of $E(z)$ for the *fundamental* mode (i.e. with $m = 1$). The field is simply computed through Eqs. (2.24).

2.4.3 Phase of photonic bandgap mirrors

As anticipated in relation to Eq. (2.13) in Sec. 2.3, the phase of a photonic bandgap mirror at the reference plane in Fig. 2.12 can be considered to be either zero or π to good approximation. In Sec. 2.4.1 and Sec. 2.4.2, we have assumed this phase to be zero and shown that the resulting spatial dependence of the m-th resonant mode in an LN cavity is consistent with that found in [118].

Assuming the phase of r_R to be π would invert the parity of the mode with respect to the centre of the cavity. In this case, the parity would be inconsistent with the FDTD simulations of [118]. Specifically, for N being odd, the mode would be odd (even) if m is odd (even). Similarly, for N being even, the mode would be even (odd) if m is odd (even). We view this result as a strong hint that the phase of a photonic bandgap mirror at the reference plane in Fig. 2.12 is indeed zero to a good approximation under the assumptions of our modelling framework.

2.5 Fundamental mode

In this section, we focus on the fundamental resonant mode and examine its distribution in the reciprocal space (simply called k-space in the following), that is the spatial Fourier transform. On this basis, we discuss how the radiation loss scales with the cavity length. The same analysis can be easily applied to higher-order modes.

2.5.1 Spatial dependence

The fundamental resonant mode is that with the lowest frequency, that is with $m = 1$. From Eqs. (2.22) and (2.24), the spatial dependence reads

$$E(z) = \begin{cases} 2\tilde{F}w(z,L)\left[|b_0|\cos(k_2 z) + |b_{-1}|\cos(k_1 z)\right], & \text{for } N \text{ odd} \\ 2i\tilde{F}w(z,L)\left[|b_0|\sin(k_2 z) + |b_{-1}|\sin(k_1 z)\right], & \text{for } N \text{ even} \end{cases} \tag{2.25}$$

It is clear from Eq. (2.25) that $E(z)$ results from the interference of two pairs of plane waves, with wavevectors $\pm k_1$ and $\pm k_2$. The amplitude of the plane waves with wavevector $\pm k_2$ ($\pm k_1$) is the magnitude of the spatial average b_0 (the spatial harmonic b_{-1}). Therefore, the ratio $|b_{-1}/b_0|$ represents the relative strength of one pair of plane waves as compared to the other. As the number of unit cells is varied, the resonance frequency changes and the ratio $|b_{-1}/b_0|$ adjusts itself accordingly. This is emphasized by Fig. (2.16), which displays k_2 (left) and $|b_{-1}/b_0|$ (right) versus the number of unit cells.

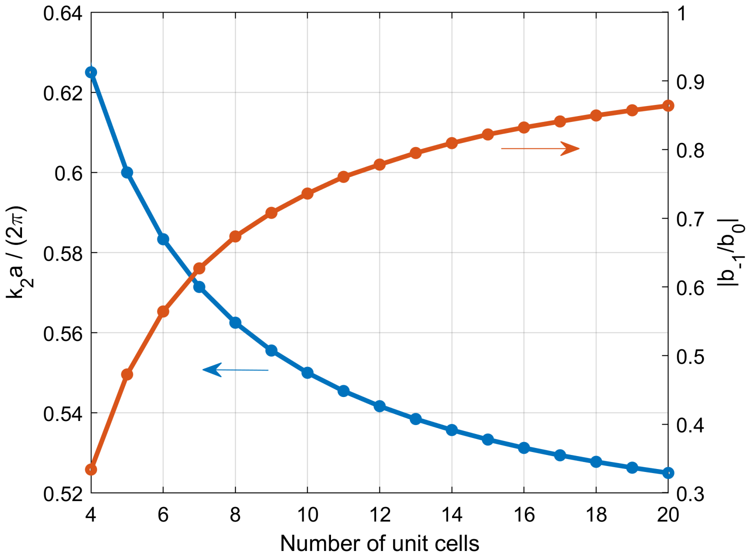

Figure 2.16: Fundamental resonant mode. (left) Normalized wavevector k_2. (right) Magnitude of the ratio between the spatial harmonic b_{-1} and the spatial average b_0.

From Eqs. (2.13) and (2.18), the wavevectors k_1 and k_2 read

$$k_1 = \pi/a - \pi/L \tag{2.26}$$

$$k_2 = \pi/a + \pi/L \tag{2.27}$$

As L increases, both k_1 and k_2 move towards the band edge. Correspondingly, as outlined in Sec. 2.2.2, $|b_{-1}|$ tends to $|b_0|$ and the fundamental mode gradually turns into *DFB-like* according to the definition proposed in [118]. This definition stems from the fact that the mode distribution in a DFB laser is determined by *two* pairs of wavevectors [23]. On the contrary, the shorter the cavity is, the more a single pair of plane waves (that with wavevectors $\pm k_2$) dominates over the other. Therefore, the fundamental mode turns into *FP-like*. Indeed, in a Fabry-Perot (FP) laser the mode distribution is determined by a single pair of plane waves.

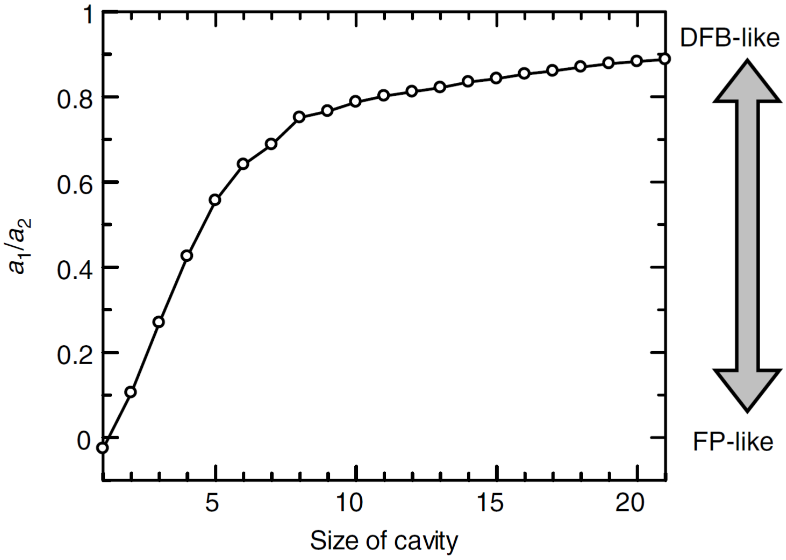

Figure 2.17: Ratio corresponding to $|b_{-1}/b_0|$ computed in [118] through fitting with FDTD simulations of the fundamental resonant mode. Reproduced from [118].

As a comparison, Fig. 2.17 shows the ratio corresponding to $|b_{-1}/b_0|$ computed in [118] for the fundamental resonant mode. The ratio is obtained therein through fitting with FDTD simulations. It is also reported for cavities shorter than 5 unit cells. However, in these cases, the cavity resonant frequency does not lie on the dispersion relation of the associated line-defect waveguide [118]. For this reason, from now on we restrict our analysis to cavities longer than 5 unit cells. By comparing Fig. 2.16 (right axis) with Fig. 2.17 for cavities longer than 5 unit cells, good qualitative agreement is found. This outlines that the analysis carried out in this chapter can capture the main findings of [118]. We emphasize that our approach is not obviously intended as a substitute for FDTD simulations, but rather as an effective tool for elucidating the essential physics of the field distribution in LN cavities and possibly guiding systematic, more rigorous simulations.

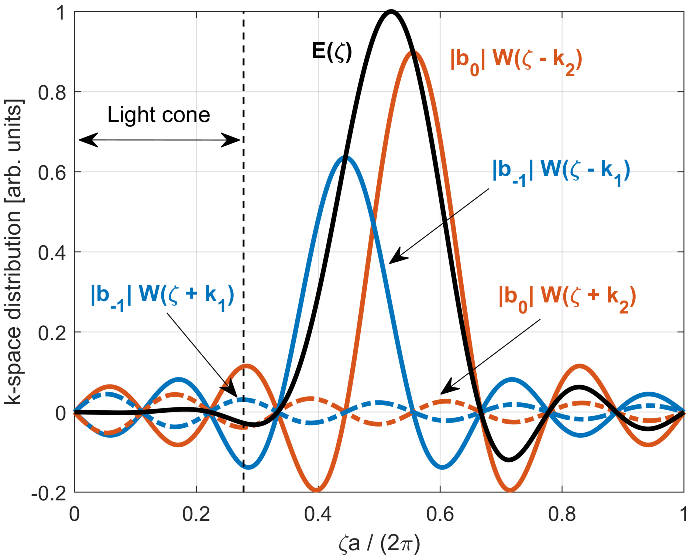

Figure 2.18: Components of the k-space distribution from Eq. (2.28). The blue (red) solid line is for the sinc function centred at $+k_1$ $(+k_2)$. The blue (red) dotted line corresponds to the sinc function centred at $-k_1$ $(-k_2)$. The black solid line is the total spectrum. The black dashed line delimits the light cone. The cavity consists of nine unit cells.

2.5.2 k-space distribution

Having shed light on the spatial dependence of the fundamental mode, we now move to its k-space distribution. From Eq. (2.25), the spatial Fourier transform of $E(z)$ reads

$$\begin{aligned} E(\zeta) = \tilde{F}\big[&|b_0|W(\zeta - k_2) + |b_0|W(\zeta + k_2) \\ &+ |b_{-1}|W(\zeta - k_1) + |b_{-1}|W(\zeta + k_1)\big], \quad \text{for } N \text{ odd} \end{aligned} \tag{2.28}$$

$$\begin{aligned} E(\zeta) = \tilde{F}\big[&|b_0|W(\zeta - k_2) - |b_0|W(\zeta + k_2) \\ &+ |b_{-1}|W(\zeta - k_1) - |b_{-1}|W(\zeta + k_1)\big], \quad \text{for } N \text{ even} \end{aligned} \tag{2.29}$$

where ζ is the spatial angular frequency and $W(\zeta)$ the spatial Fourier transform of $w(z, L)$

$$W(\zeta) = L\frac{\sin(\zeta L/2)}{\zeta L/2} = L\mathrm{sinc}\left(\frac{\zeta L}{2\pi}\right) \tag{2.30}$$

As seen in Sec. 2.1.2, for a given cavity length, the so-called *light cone* or *leaky region* is defined as [3]

$$|\zeta| < \left(\frac{\bar{\omega}}{c}\right) n_{\mathrm{clad}} \tag{2.31}$$

where n_{clad} is the cladding refractive index (in our case, $n_{\mathrm{clad}} = 1$) and $\bar{\omega}$ is the angular frequency of the resonant mode. The spatial frequency components of the field *outside* the light cone are confined to the slab in the vertical direction by total internal reflection. On the other hand, the frequency components *within* the light cone couple to the continuum of radiative modes. We select as an example a cavity with nine unit cells and plot in Fig. 2.18 the various components of the mode spectrum from Eq. (2.28). The blue (red) solid line is for the sinc function centred at $+k_1$ $(+k_2)$, while the blue (red) dotted line corresponds to that centred at $-k_1$ $(-k_2)$. The total spectrum is the black line. Only the positive frequencies are shown due to the symmetry of the spectrum.

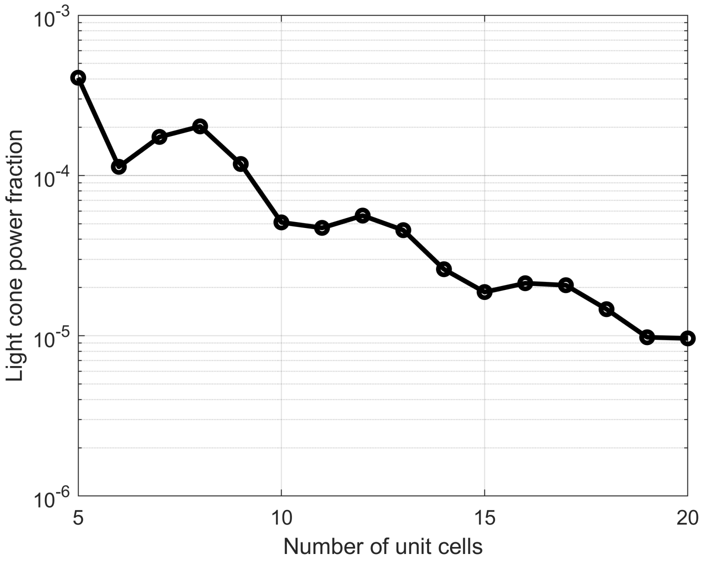

Figure 2.19: Light cone power fraction computed by Eq. (2.32) as a function of the size of the cavity.

We define the *light cone power fraction* as the relative fraction of the electric field intensity within the light cone

$$\eta = \frac{\int_{-\zeta_0}^{+\zeta_0} |E(\zeta)|^2 d\zeta}{\int_{-\infty}^{+\infty} |E(\zeta)|^2 d\zeta} \tag{2.32}$$

where $\zeta_0 = \bar{\omega}/c$ is the upper limit of the light cone for a given cavity length. By computing the light cone power fraction as a function of the cavity length, one obtains an approximate measure of the scaling of the radiation loss with the size of the cavity [178]. The absolute radiation loss rate and, therefore, the Q-factor, may be quantified through more sophisticated approaches [145], but this falls outside the scope of this thesis. The result is illustrated in Fig. 2.19. The light cone power fraction features some local maxima. Overall, it drastically diminishes as the size of the cavity is increased. Depending on the magnitude of the ratio b_{-1}/b_0 between the Bloch modes spatial harmonics, the various components of the field k-space distribution (see Eqs. (2.28) and (2.29)) may *destructively* interfere with more or less effectiveness within the light cone. This is the mechanism behind the local maxima in Fig. 2.19, which we analyze with greater detail in Sec. 2.5.3.

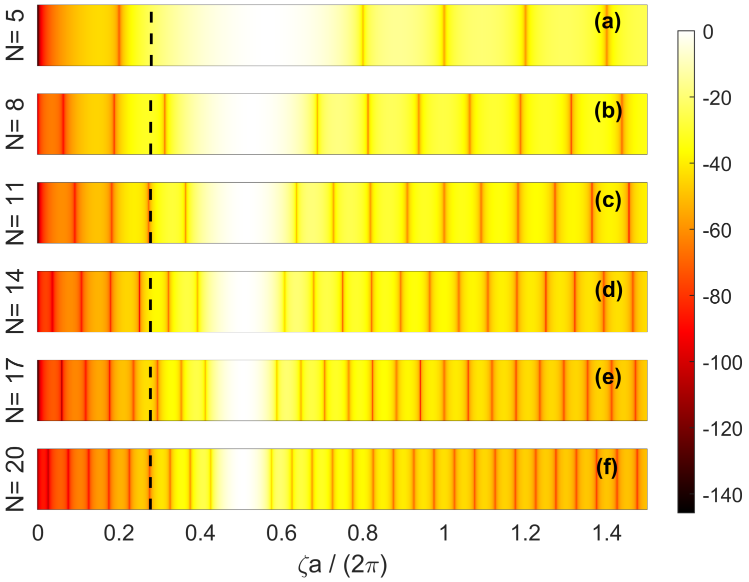

Figure 2.20: Squared magnitude of the electric field k-space distribution in dB normalized to its maximum. The cavity consists of (a) 5, (b) 8, (c) 11, (d) 14, (e) 17 and (f) 20 unit cells. The dashed, vertical line indicates the upper limit of the light cone for each cavity.

The general reduction of the light cone power fraction with increasing cavity length is due to the k-space distribution of the electric field being shifted outside the light cone. This is emphasized by Fig. 2.20, depicting $|E(\zeta)|^2$ in dB normalized to its maximum value, with the number of the cavity unit cells equal to (a) 5, (b) 8, (c) 11, (d) 14, (e) 17 and (f) 20. The spectrum is computed through Eqs. (2.28) and (2.29) and only shown for positive frequencies because of its symmetry. The dashed, vertical line denotes the upper limit of the light cone for each cavity. As the cavity becomes longer, 1) k_1 approaches to π/a in compliance with Eq. (2.26) and 2) the width of each of the sinc functions in Eqs. (2.28) and (2.29) is reduced, owing to the well-known uncertainty principle of the Fourier transform. As a result, the field spectrum departs from the light cone and the light cone power fraction generally decreases.

The dependence of the light cone power fraction on the cavity size reflects that reported in [178], which was obtained through a different approach (briefly summarized in the end of Sec. 2.1.3). For the sake of comparison, we include Fig. 2.21, which is reproduced from [178]. The blue line is the light cone power fraction for the fundamental mode in the absence of disorder, which is the case we are examining. The difference in the absolute values as compared to Fig. 2.19 may be caused by discrepancies in the Bloch modes spatial profiles, as we further speculate in Sec. 2.5.4.

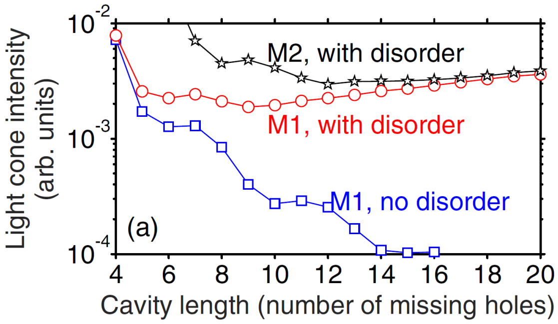

Figure 2.21: Light cone power fraction as a function of the size of the cavity for the fundamental mode M_1 and the second-order mode M_2. The blue line is without disorder related to fabrication imperfections. Reproduced from [178].

We conclude this section with a few comments on the impact of the field penetration length within the mirrors, which we have neglected. A smoother decay of the window function $w(z, L)$ in Eq. (2.25) at the edges of the cavity would reduce the high-frequency components of its Fourier transform $W(\zeta)$. Ultimately, for a given cavity length, this may limit the fraction of the electric field wavevector components within the light cone in compliance to Eqs. (2.28) and (2.29). However, one should also consider that the destructive interference among the various replicas of $W(\zeta)$ also plays a role in determining the light cone power fraction, as discussed in Sec. 2.5.3. Therefore, systematic investigations should be carried out to assess the impact of the field penetration length, which might be the subject of future work.

2.5.3 Local maxima in the light cone power fraction

In the following, we are interested in unveiling the origin of the local maxima in Fig. 2.19. These maxima are also found in [178], as evidenced by Fig. 2.21 (blue line).

For this purpose, we force the ratio $|b_{-1}/b_0|$ to a fixed value and compute the resulting light cone power fraction. The results are shown in Fig. 2.22, where the ratio is set to 1 (blue), 0.6 (red) and 0.4 (yellow). For the sake of comparison, the black line is the light cone power fraction in Fig. 2.19, for which the ratio $|b_{-1}/b_0|$ is that reported in Fig. 2.16. We refer to the black line as to the *intrinsic* light cone power fraction. If $|b_{-1}/b_0|$ is fixed to unity, the light cone power fraction is larger than the intrinsic one, but it still overall decreases with increasing cavity length. On the other hand, smaller values of $|b_{-1}/b_0|$ appear to strongly modify the dependence of the light cone power fraction on the size of the cavity. In these cases, the light cone power fraction decreases (increases) as the cavity becomes longer for short (long) cavities. Therefore, the figure outlines the key role played by the Bloch modes spatial harmonics in the scaling of the light cone power fraction (and so the radiation loss) with the size of the cavity.

For a deeper understanding of the results in Fig. 2.22, a closer inspection is required

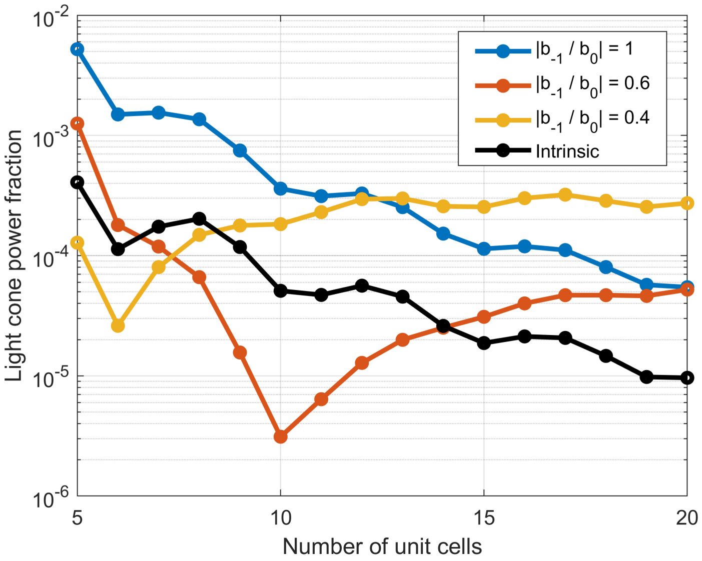

Figure 2.22: Light cone power fraction computed by Eq. (2.32) as a function of the size of the cavity. Each color denotes a different value of the ratio $|b_{-1}/b_0|$, which is forced to 1 (blue), 0.6 (red) and 0.4 (yellow). The black line is the light cone power fraction in Fig. 2.19, for which the ratio $|b_{-1}/b_0|$ is the intrinsic one, reported in Fig. 2.16.

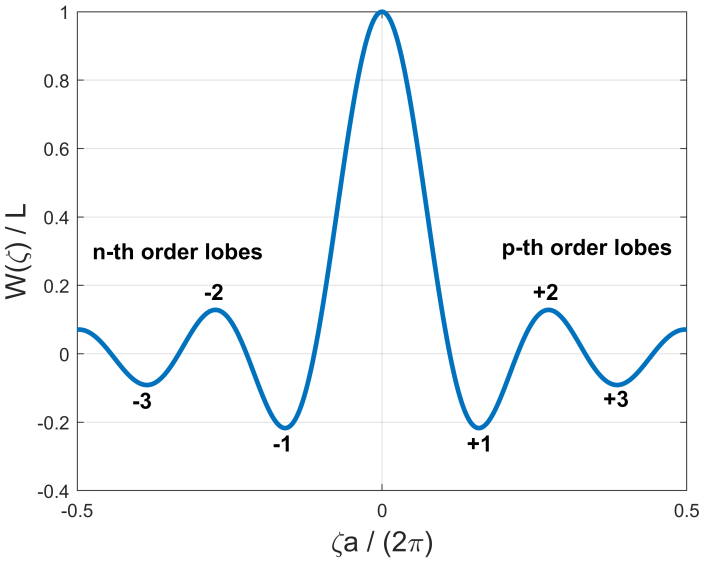

Figure 2.23: Definition of p-th and n-th order side lobes of $W(\zeta)$ from Eq. (2.30). The p-th order (n-th order) side lobes are numbered in order of increasingly positive (negative) detuning from the peak. As an example, the cavity length is set to nine unit cells.

of the various components of the mode k-space distribution in Eqs. (2.28) and (2.29). To facilitate the analysis, we introduce some definitions. Let us consider the sinc function $W(\zeta)$ from Eq. (2.30). In the following, we denote as p-th order (n-th order) side lobes those lying at higher (lower) frequencies with respect to the peak. This is illustrated in Fig. 2.23. The letter p (n) reflects the positive (negative) detuning of a given side lobe from the peak.

Armed with these definitions, we recall Fig. 2.18. This figure highlights a key feature of the k-space distribution, that is the *destructive* interference between the side lobes of the sinc functions denoted in blue and red. As noted in [118], such interference stems from 1) the spectral positions of the zeroes of a sinc function and 2) the detuning between $+k_1$ and $+k_2$ (and, similarly, $-k_1$ and $-k_2$). Indeed, the zeroes of the pair of sinc functions centred at $+k_1$ and $+k_2$ are located at $\zeta a/(2\pi) = k_i a/(2\pi) + n/N$, with $i = 1, 2$ and $n = \pm1, \pm2$, etc.. On the other hand, the detuning $(k_2 - k_1)a/(2\pi)$ is equal to $1/N$ from Eqs. (2.26) and (2.27). This guarantees that the zeroes of the two sinc functions are aligned such that the interfering side lobes have *opposite* sign. A similar reasoning applies to the other pair of sinc functions.

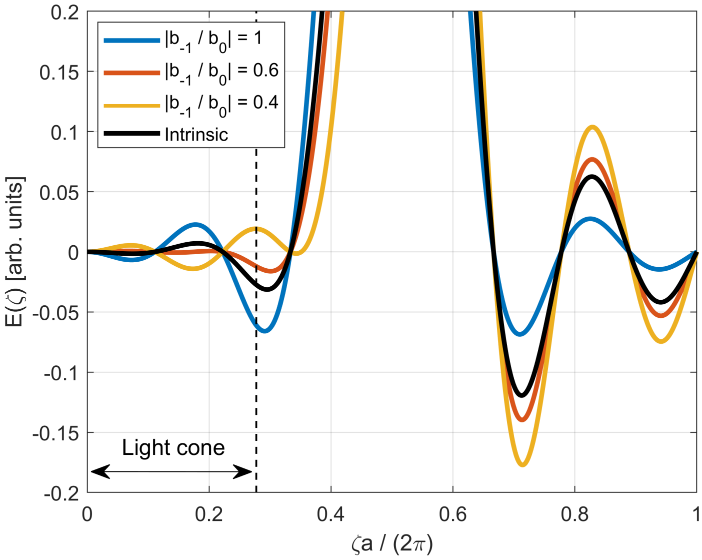

Figure 2.24: Fourier transform of the electric field computed by Eq. (2.28) for a cavity with nine unit cells. Each color denotes a different value of the ratio $|b_{-1}/b_0|$, which is forced to 1 (blue), 0.6 (red) and 0.4 (yellow). The black line coincides with that shown in Fig. 2.18 and corresponds to the intrinsic value of the ratio.

However, as compared to [118], here we emphasize another key feature. For each pair of interfering side lobes, one should consider their *order*, as defined in Fig. 2.23. Fig. 2.24 shows the total spectrum $E(\zeta)$, with the cavity length being nine unit cells. Each colour indicates a different value of the ratio $|b_{-1}/b_0|$, which is set to 1 (blue), 0.6 (red) and 0.4 (yellow). The black line coincides with that shown in Fig. 2.18 and corresponds to the intrinsic value of the ratio. Since the ratio $|b_{-1}/b_0|$ is not larger than unity, the side lobes of $E(\zeta)$, as the ratio is increased, have smaller and smaller intensity (in absolute value) at frequencies *outside* the light cone. In fact, at these frequencies a side lobe of the sinc function centred at $+k_2$, with order p, destructively interferes with a side lobe of the sinc function centred at $+k_1$, with order $(p+1)$ (see Fig. 2.18). The situation is different at frequencies close to or within the light cone. Here, $E(\zeta)$ features side lobes whose absolute intensity does not monotonically vary with the ratio $|b_{-1}/b_0|$, as evidenced by Fig. 2.24. In fact, a side lobe of the sinc function centred at $+k_2$, with order $(n-1)$, destructively interferes with a side lobe of the sinc function centred at $+k_1$, with order n. The former sinc has a peak amplitude equal to $|b_0|$, while the peak amplitude of the latter is $|b_{-1}|$, with $|b_0|$ being larger than $|b_{-1}|$. However, for a sinc function of given peak amplitude, a side lobe of order n has a larger intensity (in absolute value) than one with order $(n-1)$ (see Fig. 2.23). As a result, depending on the ratio $|b_{-1}/b_0|$, the destructive interference between the side lobes within the light cone can be more or less effective. For a given cavity length, an optimum value of this ratio exists, minimizing the light cone power fraction (see Fig. 2.22).

On the other hand, as the cavity length is increased, the total spectrum overall tends to depart from the light cone, as outlined in Sec. 2.5.2 and exemplified by Fig. 2.20. This shift tends to reduce the light cone power fraction. Therefore, the local maxima in Fig. 2.19 stem from the trade-off between this shift and the effectiveness, at a given cavity length, of the side lobe destructive interference within the light cone. We also note that the local maxima are more prominent for short cavities (see Fig. 2.19). This is due to the fact that in short cavities a given variation in the size of the cavity results in a larger variation of the ratio $|b_{-1}/b_0|$ (see Fig. 2.16).

It should be also emphasized that the light cone power fraction for $|b_{-1}/b_0| = 1$ (see Fig. 2.22) closely resembles that reported in [178] without disorder (see Fig. 2.21, blue line). This matching points out a possible reason for the difference in the absolute values between our result in Fig. 2.19 and the corresponding one in [178]. The latter was indeed obtained through an effective index approach, which might have neglected the frequency dependence of the Bloch modes spatial profiles.

2.5.4 Disorder-induced radiation loss: a possible interpretation

In light of Sec. 2.5.3, in the following we briefly speculate on a possible, simple interpretation of the impact of disorder in LN cavities. Essentially, we suggest that the optimum cavity length minimizing the light cone power fraction of the fundamental mode as found in [178] may stem from the trade-off of two factors. On the one hand, a disorder-induced disruption of the side lobe destructive interference within the light cone. On the other hand, the electric field k-space distribution being shifted outside the light cone with increasing cavity length. In particular, we note that our results in Fig. 2.22 with a forced value of the ratio $|b_{-1}/b_0|$ (yellow and red line) somehow mirror that reported in [178] (see Fig. 2.21, red line) in the presence of disorder.

Two considerations are due. Firstly, as shown in [145], a given mode of the *actual* structure (i.e. with disorder) originates from the coupling of the Bloch modes of the *ideal* structure (i.e. without disorder) with different wavevectors and even belonging to different bands. In light of this consideration, one might imagine that a given disorder realization randomly distorts the spatial profiles of the Bloch modes $e_{\pm}(z)$ and *not just* the corresponding amplitudes $c_{\pm}(z)$ (see Eq. (2.7)). As a result of this spatial distortion, the k-space distribution of $e_{\pm}(z)$ would be altered. In particular, a given disorder realization might essentially translate into a random value of the ratio $|b_{-1}/b_0|$. Secondly, it should be emphasized that results reported in Fig. 2.21 in the presence of disorder are obtained from an ensemble average over a certain number of disorder realizations. Therefore, one might view the red line in Fig. 2.21 as resulting from an ensemble average of Eq. (2.32), with a random value of the ratio $|b_{-1}/b_0|$ being forced for each disorder realization. As already evidenced in the end of Sec. 2.2.2, we note that, at least in one-dimensional Bragg gratings, the ratio $|b_{-1}/b_0|$ is directly linked to the grating coupling coefficient and detuning of the operation frequency from the Bragg frequency [23]. Although these quantities are only defined for ideal (i.e. disorder-free) periodic structures, to first approximation one might simply view disorder as affecting the coupling coefficient and/or detuning from the Bragg frequency. In fact, disorder locally adds or removes dielectric. As a consequence, disorder would end up changing the value of the ratio $|b_{-1}/b_0|$ as compared to that of the ideal structure.

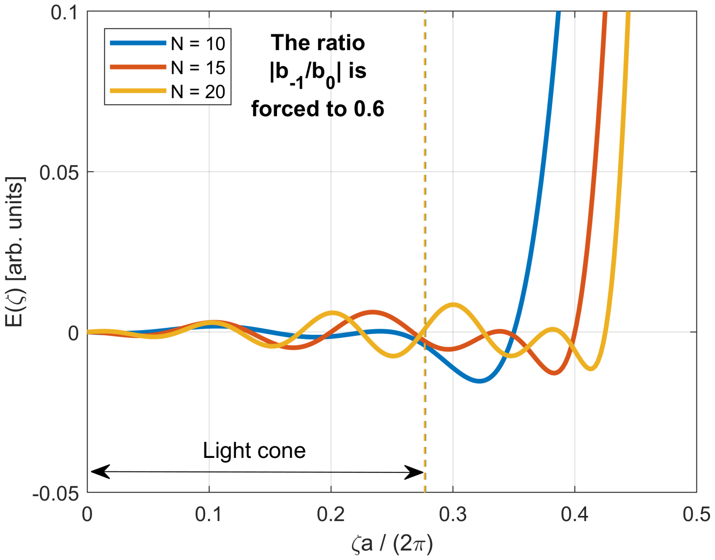

Figure 2.25: Fourier transform of the electric field computed by Eqs. (2.28) or (2.29) for an LN cavity with N equal to 10 (blue), 15 (red) and 20 (yellow). Each dashed, vertical line delimits the light cone for a given N, with the same code of colours (the vertical lines practically overlap). The ratio $|b_{-1}/b_0|$ is forced to 0.6.

To emphasize the impact of a given value of this ratio, we report in Fig. 2.25 the spatial Fourier transform $E(\zeta)$ of the fundamental resonant mode of an LN cavity, with N equal to 10 (blue), 15 (red) and 20 (yellow). Depending on N, the spectrum is computed by Eqs. (2.28) or (2.29). As an example, the ratio $|b_{-1}/b_0|$ is forced to 0.6, which minimizes the light cone power fraction for $N = 10$ (see Fig. 2.22). Each dashed, vertical line in Fig. 2.25 delimits the light cone for a given N, with the light cone boundary computed through Eq. (2.31). For each N, the cavity resonance frequency determining the light cone is that of the ideal (i.e. disorder-free) cavity. This is clearly an approximation, because in practice the resonance frequency is also influenced by disorder [145, 178]. Similarly, we assume for simplicity the wavenumbers k_1 and k_2 to be those of the ideal structure and we compute them via Eqs. (2.26) and (2.27). In practice, they might also vary due to disorder, thus changing the position of the various sinc functions which make up the electric field k-space distribution (see Fig. 2.18). Under these simplifying assumptions, the relative fraction of $E(\zeta)$ within the light cone increases as the cavity becomes longer, as evidenced by Fig. 2.25. This is caused by the disruption of the side lobe destructive interference, which we have thoroughly discussed in Sec. 2.5.3. For $N \geq 10$, this disruption outweighs the benefit of the spectrum $E(\zeta)$ being shifted outside the light cone as N increases. As a result, the light cone power fraction monotonically increases with increasing N for For $N \geq 10$ (see Fig. 2.22).

For the sake of completeness, we note that the disruption of the side lobe destructive interference may only prevail for $|b_{-1}/b_0|$ being smaller than unity. Indeed, by forcing $|b_{-1}/b_0|$ to values larger than unity, we have found the light cone power fraction decreasing overall with increasing cavity length (with a series of local maxima, similar to the blue line in Fig. 2.22). Therefore, a key assumption here is that disorder should lead to a large enough reduction in $|b_{-1}/b_0|$. In addition, it should be recalled that a recent work [15] has investigated the impact of disorder in passive and active LN cavities through FDTD simulations. Disorder has been modelled therein by randomly shifting the centre of each hole. For active cavities, we refer to Sec. 4.4.1. In the case of passive cavities, the Q-factor has been found to be marginally affected by disorder. Therefore, the investigations on passive cavities carried out in [15] equally challenge the interpretation discussed in the current section and that presented in [178]. This certainly calls for further scrutiny. For instance, a possibility is that a specific type of disorder other than that considered in [15] could result in a proper reduction of the ratio $|b_{-1}/b_0|$.

The simplified interpretation which we have discussed is obviously just presented as an hypothesis. It should be assessed by systematic investigations, which are outside the scope of this thesis, but might be the subject of future work. However, if found to be correct, this picture would emphasize the key role of the side lobe destructive interference in suppressing the light cone power fraction. In this case, disorder may be viewed as disturbing this beneficial interference, leading to the increase of the radiation loss beyond a certain cavity length.

2.6 Conclusions

In summary, we have presented a transparent and efficient modelling framework for analyzing the resonant modes of passive LN cavities. These are photonic crystal cavities with N missing holes based on line-defect waveguides, as shown in Fig. 2.12.

In Sec. 2.2, we have discussed dispersion relation and Bloch modes of passive line-defect photonic crystal waveguides. We compute them by the plane wave eigensolver MIT-Photonic-Bands (MPB) [56]. In Sec. 2.4, we have derived simple analytical expressions for the resonant modes, which agree with those reported in [118]. However, the expressions reported therein are obtained by fitting with FDTD simulations. As compared to [118], here we have shown that the modes spatial dependence naturally follows from the expansion of the electric field in the two counter-propagating *Bloch* modes of the waveguide on which the cavity is based.

In Sec. 2.5, we have focused on the fundamental resonant mode. Specifically, in Sec. 2.5.1 we have clarified the physical meaning of the amplitudes of the two pairs of plane waves which determine the mode distribution. The relative strength of these plane waves corresponds to the ratio $|b_{-1}/b_0|$ between the two dominant spatial harmonics of the Bloch modes of the waveguide. As the cavity length is increased, the resonance frequency moves towards the band edge and the ratio $|b_{-1}/b_0|$ correspondingly changes, as summarized by Fig. 2.16. As a result, the resonant mode turns from FP-like into DFB-like, as outlined in [118]. Our analysis has directly traced back this mode change to the frequency dependence of the Bloch modes spatial profiles, thus elucidating the physics. We have then focused on the scaling of the light cone power fraction with the size of the cavity. In Sec. 2.5.2, we have shown that the light cone power fraction strongly diminishes as the size of the cavity is increased, as illustrated by Fig. 2.19. This suggests a similar scaling for the radiation loss. On this regard, our result reflects those obtained in [178] through a different approach.

The following subsections further elaborate on the key role played in this scaling by the Bloch modes spatial harmonics. Sec. 2.5.4 reveals that the spatial and frequency dependence of the Bloch modes influence the local maxima in the light cone power fraction as a function of the cavity length. In particular, for proper values of the ratio $|b_{-1}/b_0|$, the light cone power fraction decreases (increases) as the cavity becomes longer for short (long) cavities, as shown in Fig. 2.22. At a given cavity length, the degree of suppression of the electric field wavevector components within the light cone depends on the effectiveness of the destructive interference among the sinc functions which make up the field k-space distribution. This interference is directly controlled by the ratio $|b_{-1}/b_0|$, as illustrated in Fig. 2.24. The local maxima stem from the trade-off between the effectiveness of this interference and the field spectrum being shifted outside the light cone as the cavity length is increased.

In light of these considerations, in Sec. 2.5.4 we have speculated on the impact of disorder due to unavoidable fabrication imperfections. By comparing the results of Fig. 2.22 with those reported in [178] in the presence of disorder, we have advanced an hypothesis. According to our hypothesis, disorder may be viewed as directly affecting the Bloch modes spatial profiles, thus changing the ratio $|b_{-1}/b_0|$. Specifically, a given disorder realization may be viewed as resulting in a random value of $|b_{-1}/b_0|$. If $|b_{-1}/b_0|$ is smaller than unity, the light cone power fraction may increase with the size of the cavity beyond a certain cavity length, as evidenced by Fig. 2.22 and Fig. 2.25. Therefore, disorder may be viewed as disrupting the destructive interference within the light cone among the sinc functions which make up the field k-space distribution.

Finally, we note that the method we have presented in this chapter should not obviously be intended as a full substitute for more rigorous approaches, such as FDTD simulations. It should be rather viewed as a picklock to clarify the essential physics of the field distribution in passive LN cavities and then guide systematic, more rigorous investigations. In particular, we outline the advantage of our method in terms of efficiency as compared to FDTD simulations. Indeed, a systematic investigation on the optimization of the Q-factor can be performed as a function of the cavity length at the cost of fully solving Maxwell's equations only once (that is, on the supercell of the line-defect waveguide). On the other hand, the FDTD method requires to fully solve Maxwell's equations for each cavity length.

Chapter 3

Active Photonic Crystal Waveguides

In this chapter, we deal with the impact of material gain on the slow-light propagation in active photonic crystal waveguides. In Sec. 3.1, we introduce the research context of slow-light, with a focus on photonic crystal waveguides. Sec. 3.2 and Sec. 3.3 are devoted to a thorough discussion of the modelling framework which we have employed, with detailed mathematical derivations being left to Appendix A and Appendix B. In Sec. 3.4 we cover the impact of material gain and refractive index perturbations on the waveguide dispersion relation, while in Sec. 3.5 we focus on the impact on optical propagation and power flow. Detailed mathematical derivations regarding this section are provided in Appendix C. In Sec. 3.6, we discuss the use of slow-light in compact semiconductor optical amplifiers, with an emphasis on the impact of the linewidth enhancement factor. In Sec. 3.7, we briefly suggest a possible, efficient strategy to model the impact of fabrication imperfections. Finally, conclusions are drawn in Sec. 3.8.

3.1 Introduction and motivation

The *group velocity* v_g is the speed at which the time-domain envelope of a pulse propagates in a dispersive medium with refractive n. It is given by $v_g = c/n_g$, where c is the vacuum light speed and n_g the *group index* defined by [140]

$$n_g = n(\omega_0) + \omega_0 \left.\frac{dn}{d\omega}\right|_{\omega_0} \tag{3.1}$$

Here, ω_0 is the central frequency of the pulse and higher-order dispersion terms are ignored. Eq. (3.1) reveals that the group velocity can be controlled via the refractive index dispersion. If one ensures $v_g \ll c$, then *slow-light* is accomplished and light pulses are significantly delayed.

The refractive index dispersion can be of two types. The first one is *material* dispersion, which may be exploited in many fundamentally different ways [13]. Among these, we cite electromagnetically induced transparency (EIT) [28], usually in a gas of atoms at cryogenic temperatures [45]. This is a quantum interference phenomenon by which a medium can be made transparent in a narrow frequency window via proper photo-excitation. In this window, strong material dispersion leading to slow-light concurrently arises. However, the feasibility of this approach in on-chip room-temperature applications is extremely challenging. Furthermore, due to the narrow frequency window, only slowly-varying pulses can be delayed without distortion.

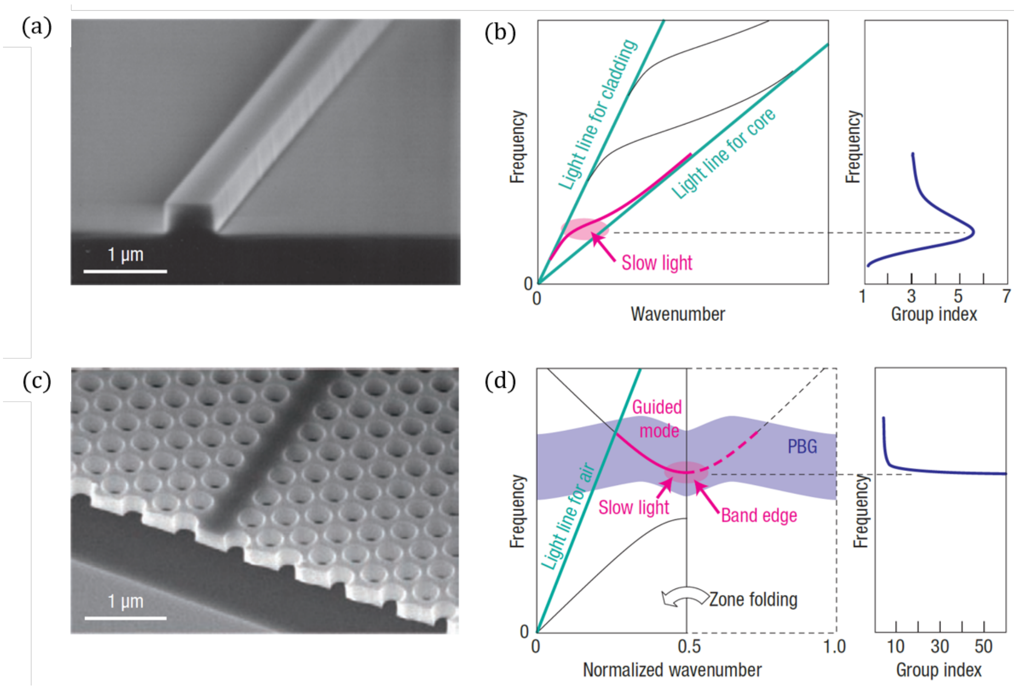

Figure 3.1: (a, c) Scanning electron microscope image and (b, d) schematic band diagram and group index spectrum for (a, b) a silicon photonic-wire waveguide and (c, d) a photonic crystal waveguide. Reproduced from [9].

The other type of dispersion is *structural* dispersion, that is dispersion of the *effective* refractive index of a guided mode within a waveguide. This is the type of dispersion on which we focus in the following. Structural dispersion is usually negligible in conventional dielectric waveguides, where the group index does not deviate significantly from the effective refractive index. In these waveguides, n_g is usually around 3.5. However, by increasing the refractive index contrast between core and cladding, the group index may be also increased, as in silicon photonic-wire waveguides [134]. These are ridge-type waveguides with a silicon core and a cladding made of air or silicon dioxide, as shown by the scanning electron microscope image in Fig. 3.1(a). A schematic representation of the band diagram and group index spectrum is reported in Fig. 3.1(b). In this case, n_g can be as high as 5 or 6. A much larger group index can be achieved in photonic crystal waveguides, which we have already introduced in Sec. 2.1. Fig. 3.1(c) shows an electron microscope image of such a waveguide, while Fig. 3.1(d) provides a schematic representation of the band diagram and group index spectrum. Close to the band edge, the group index ideally diverges to infinity.

There is a number of motivations to pursue slow-light propagation. A first motivation is realizing optical buffers, which can delay and temporarily store information packets in the optical domain directly. This strategy is convenient in terms of energy efficiency and bandwidth because avoids prior conversion to the electrical domain [66]. As compared to current solutions, which are based on long optical fibres, optical buffers exploiting slow-light propagation may be much more compact and thus suited to photonic integrated circuits. A second motivation is that the light-matter interaction is enhanced by slow-light. Linear effects, such as gain and thermo- or electro-optic tuning of refractive index, are enhanced in direct proportion to n_g. Nonlinear effects, such as optical Kerr effect, scale like n_g^2 [65]. Essentially, these enhancements stem from two factors. Firstly, the slower propagation of light makes the interaction time longer. Secondly, if the group velocity dispersion is negligible, a light pulse undergoes *spatial* compression when entering the slow-light regime from a conventional waveguide. This is illustrated by Fig. 3.2, which is reproduced from [65]. The spatial compression occurs because the front of the pulse enters the slow-light regime first as compared to the back. If no energy is lost at the interface, then the pulse intensity increases so as to accommodate the same amount of energy in a smaller volume. As a result of the enhanced light-matter interaction, devices such as switches, amplifiers or lasers become more energy-efficient and potentially more compact, with clear benefits in terms of integration density.

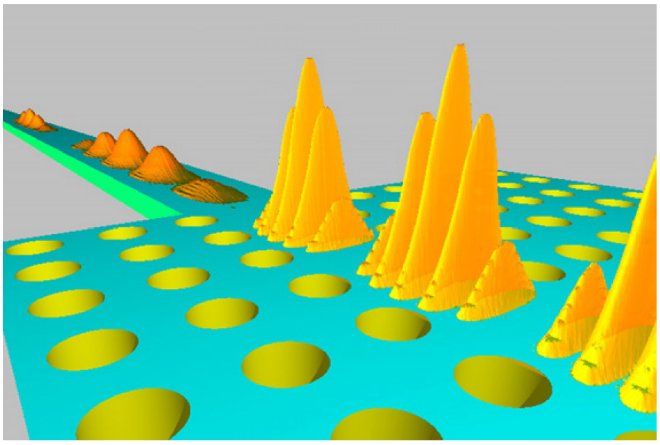

Figure 3.2: Illustration of spatial compression and intensity increase of a pulse after entering the slow light regime under the assumption of negligible group velocity dispersion. Reproduced from [65].

However, slow-light in photonic crystal waveguides is usually accompanied by strong group velocity dispersion, which distorts optical pulses. Two main strategies exist to avoid pulse distortion. The first one is using dispersion-compensated slow-light devices, which essentially combine two photonic crystal waveguides with opposite dispersion characteristics [98, 125]. The second strategy relies on the so-called zero-dispersion slow-light devices. Photonic crystal waveguides can be modified such that the dispersion relation becomes a straight band over a certain frequency range. This dispersion engineering can be accomplished, for instance, by tailoring the diameter of the holes adjacent to the waveguide core [34, 68]. Coupled-resonators optical waveguides (CROWs) [182] are other notable zero-dispersion slow-light devices which are not necessarily based on photonic crystals. A CROW is a cascade of coupled high-Q resonators. As a result of the coupling between adjacent resonators, a transmission band arises where propagation of guided modes is allowed. At the centre of the transmission band, the group velocity dispersion is zero. CROWS based on different types of resonators have been demonstrated, such as microrings on silicon [176] or photonic crystal heterostructure cavities [114]. For an excellent review of CROWs, we refer to [99]. Thorough reviews on the use of slow-light in photonic crystals can be found in [65, 9, 113].

3.1.1 Slow-light gain enhancement

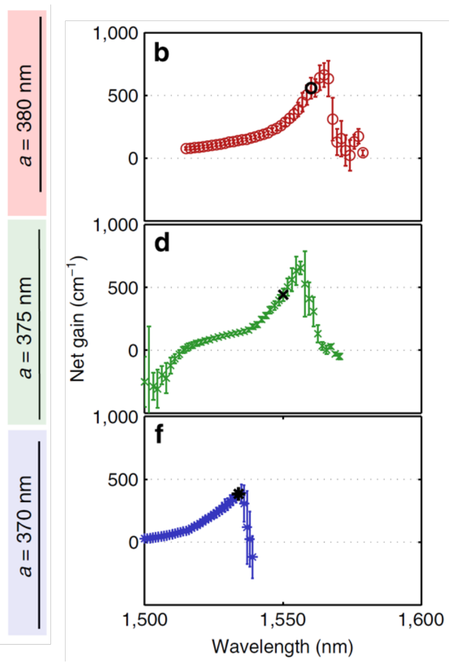

Figure 3.3: Measured net gain coefficient of active photonic crystal waveguides with varying lattice constant *a*. Reproduced from [29].

As already mentioned, the gain coefficient *per unit length* is enhanced by slow-light propagation. An application of this phenomenon to lasers was envisioned in [25], where a so-called photonic band edge laser was proposed. Essentially, they suggested to replace the uniform gain medium in a vertical-cavity surface-emitting laser (VCSEL) with an active medium consisting of alternating gain layers having large refractive index contrast. However, the slow-light enhancement of the gain coefficient was originally pointed out in [174] around 20 years earlier, within the context of DFB lasers. As shown in [174], the gain per unit length of a guided Bloch mode in a periodic medium is enhanced, under the same pumping conditions, as compared to that of a guided mode in a uniform medium. The enhancement factor is given by the ratio between the phase velocity in the uniform medium and the group velocity in the periodic medium. This factor is currently known as *slow-down factor* in the context of photonic crystals. Intuitively, the gain enhancement results from a longer effective length due to the multiple back-and-forth scattering. Importantly, a fundamental question is also addressed in [174] on the impact of slow-light on the gain *per unit time*, that is $P^{-1}(dP/dt)$, with P being the optical power. The gain per unit time is unaffected by slow-light, as later stated in the context of photonic crystals [12, 178] and nanolasers [105]. It should be also emphasized that a large group index does not necessarily translate into an enhancement of gain. Indeed, the evolution with frequency of the shape of the guided mode must be also taken into account. For instance, as shown in [103], an increase of the group index in translationally invariant, weakly-guiding optical fibres is perfectly counterbalanced by a decrease of the optical confinement factor. As a result, in this case the gain per unit length remains unaffected by slow-light.

Recently, the slow-light enhancement of gain has been experimentally verified in active photonic crystal waveguides [29]. This is summarized by Fig. 3.3, which is reproduced from [29]. As the lattice constant a is increased, the band edge is red-shifted and the spectral region of gain enhancement correspondingly moves. The gain decrease at longer wavelengths is ascribed to various phenomena, such as carrier depletion due to amplified spontaneous emission, disorder-induced scattering loss and gain-induced limitation of the slow-down factor. The latter is addressed in [41]. Specifically, it is shown therein that the inclusion of gain significantly alters the dispersion relation of periodic media (such as CROWs, Bragg stacks and photonic crystal waveguides) in the slow-light region, resulting in a reduction and spectral broadening of the group index. This is exemplified by Fig. 3.4, which is reproduced from [41]. However, it should be emphasized that the analysis of [41] applies to Bloch modes of active periodic structures which are assumed to be infinitely long. In practice, the impact of a back-reflected Bloch mode due to the finite device length must be taken into account, as pointed out in [19]. This effect is thoroughly discussed in the following sections.

3.1.2 Disorder-induced loss

A critical limitation to the use of slow-light is represented by scattering losses induced by unavoidable fabrication imperfections, which has received a significant attention

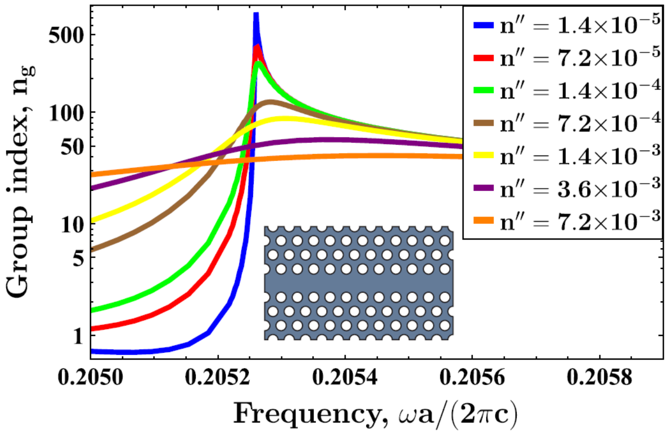

Figure 3.4: Group index of an active photonic crystal waveguide. n'' is the refractive index imaginary part, being proportional to the material gain. Reproduced from [41].

from the research community. For a comprehensive review of this issue in conventional waveguides, photonic crystal waveguides and CROWs, including both theory and experiments, we refer to [93]. In the following, we briefly recall the salient points regarding photonic crystal waveguides.

Fabrication imperfections which inevitably affect real devices are generally indicated as *disorder*. In photonic crystal waveguides, they can be, for instance, roughness at the hole boundary or displacement of holes from the position of the ideal periodic lattice, on the order of few nanometers. Disorder induces two types of loss, as identified in [50]. The first one consists in *radiation loss*, whereby a fraction of power of the guided mode is scattered out-of-plane and coupled to radiation modes. The second type is *backscattering loss*. Essentially, a guided mode propagating in a given direction is partly reflected by the waveguide imperfections, thus losing power due to coupling with guided, counter-propagating modes.

In [50], theoretical expressions for the radiation and backscattering loss are derived. These expressions provide *incoherent ensemble average* loss coefficients per unit cell. They predict the average loss that one may expect when averaging the transmission spectra of many nominally identical structures consisting of a single unit cell. In light of this initial study, an approximate scaling rule for disorder-induced losses has been proposed. According to this, radiation and backscattering loss scale, respectively, in a linear and quadratic fashion with the group index n_g of the ideal (i.e. disorder-free) structure [117], if the group index is sufficiently low.

The main limitations to this scaling rule are two. Firstly, it ignores the evolution of the mode shape with group index, which may result in underestimating the actual loss [124]. Experiments have been carried out on dispersion-engineered waveguides, modified such that they exhibit a flat group index in a given frequency range. In spite of the constant group index, backscattering loss has been found to sharply increase [93], outlining the inconsitency with the approximate scaling rule. Intuitively, this feature stems from the weaker lateral confinement of the Bloch modes in the slow-light region. As a result, the field more strongly interacts with the holes adjacent to the line-defect, thus experiencing a larger backscattering loss.

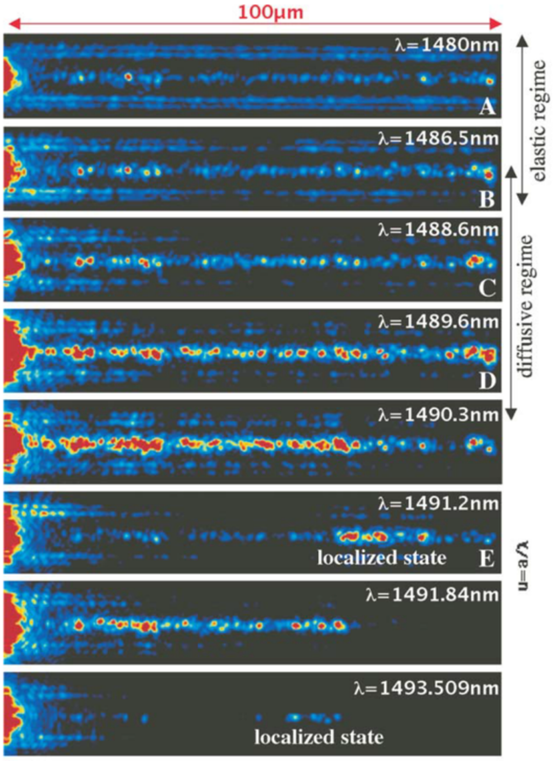

Figure 3.5: Real space images of the infrared field radiated at the top surface of a photonic crystal waveguide at different wavelengths. Reproduced from [72].

The second limitation is that the scaling rule, as already mentioned, is based on an incoherent ensemble average. Several experiments have revealed that transmission spectra of photonic crystal waveguides exhibit strong oscillations close to the band edge. As pointed out in [91], these oscillations are not due to spurious reflections at the waveguide termination facets, but intrinsically related to disorder. They cannot be explained by incoherent scattering models [50, 124], which neglect the multiple-scattering occurring deep in the slow-light region. In the multiple-scattering regime (also known as *diffusive* regime), light is scattered multiple times before exiting the waveguide and interference effects among the various bascattered contributions may severely impact the field propagation. The effect is dramatically illustrated by Fig. 3.5. The figure shows the real space image of the field radiated at the top surface of a photonic crystal waveguide and is obtained experimentally [72]. At shorter wavelengths (i.e. lower group index), the field pattern is almost uniform throughout the waveguide length. However, as the wavelength approaches the band edge and the group index increases, the multiple-scattering of light becomes more and more relevant. As a result, the field pattern tends to become highly non-uniform and localized states may even appear at frequencies below the ideal band edge, where propagation should in theory be inhibited. In the multiple scattering regime, *coherent* scattering models are necessary [90, 123, 122], which can accurately describe the transmission spectrum of real photonic crystal waveguides in the proximity of the band edge.

Being aware of the complexity and challengens of an accurate description of disorder-induced losses in photonic crystal waveguides is obviously important. However, it should be emphasized that, at a given group index n_g and level of disorder, the impact of multiple-scattering effects scales with the waveguide length. For short waveguides, the average dampening of power transmission is captured to a good approximation by Beer-Lambert law, i.e. $P(L) = P_0 e^{-(\alpha_{\mathrm{rad}}+\alpha_{\mathrm{back}})L}$, with P_0 being the input power, L the waveguide length and α_{rad} (α_{back}) the radiation (backscattering) loss coefficient [124]. For L not longer than 50 μm, the approximation is acceptable for n_g up to around 60 and dramatically improves with decreasing n_g and L. In this thesis, we focus on the impact of material gain, the possible applications being compact slow-light semiconductor optical amplifiers (see Sec. 3.6) and photonic crystal lasers (see Chapter 4). The values of L which we consider do not exceed 50 μm and are significantly smaller than this limit in the case of lasers. Therefore, we expect multiple-scattering effects to be negligible in lasers, where radiation losses due to the small size of the cavity probably play a major role (see Sec. 2.5.4). In the case of slow-light amplifiers, we also expect disorder-induced multiple-scattering to be not too severe within the aforementioned limits for n_g and L. Furthermore, as we thoroughly discuss in Sec. 3.6, multiple-scattering due to the gain itself represents a significant limitation to the device performance.

In light of these considerations, in this thesis we model disorder-induced scattering losses through a phenomenological approach based on the aforementioned scaling rule, which represents a good starting point [117], and leave to future work possible refinements. In particular, we note that the coupled-Bloch-mode equations which we introduce in Sec. 3.2 to describe the impact of gain are closely related to the coherent scattering model of [122]. We refer to Sec. 3.7 for further details on this analogy and future perspectives of a simple, but efficient modelling of disorder-induced multiple-scattering. We also note that the scattering matrix formulation which we introduce in Sec. 3.5 is natutally suited to being combined with other rigorous descriptions of disorder [90].

3.1.3 Motivation of this chapter

The main motivation behind the analysis carried out in this chapter is developing an efficient modelling framework to account for the impact of material gain in active photonic crystal waveguides and lasers.

As discussed above, the group index in photonic crystal waveguides may greatly exceed that of conventional, ridge-type waveguides. One of the advantages of slow-light is enhancing the gain per unit length. Experimentally verified [29], this gain enhancement enables the realization of shorter optical amplifiers with promising applications to photonic integrated circuits [87], as well as shorter lasers [178]. However, a fundamental limitation is imposed by the gain itself [41, 19], as already, briefly mentioned.

To properly describe the slow-light enhancement of gain, we start from the coupled-Bloch-mode equations presented in [19]. However, these equations are therein solved numerically, thus not providing important insight on the coupling mechanism. Therefore, a first part of our analysis is devoted to dissecting the physics of these equations. The outcome is an efficient framework, which elucidates the impact of a generally complex refractive index perturbation on the optical propagation in active photonic crystal waveguides. This framework is applied to the analysis of semiconductor photonic crystal optical amplifiers, offering new insights on the impact of the linewidth enhancement factor [139]. The same framework is then utilized in Chapter 4 to analyze slow-light effects in various photonic crystal lasers.

3.2 Coupled-Bloch-mode equations

In this section, we introduce the coupled-Bloch-mode (CBM) equations which we have employed to study active photonic crystal waveguide and lasers throughout this thesis.

In the spirit of coupled-mode theory [181, 46], the electromagnetic state of a photonic crystal line-defect waveguide with a complex refractive index can be represented as [19]

$$\begin{bmatrix}\mathbf{E}(\mathbf{r})\\ \mathbf{H}(\mathbf{r})\end{bmatrix} = c_+(z)\begin{bmatrix}\mathbf{e}_+(\mathbf{r})\\ \mathbf{h}_+(\mathbf{r})\end{bmatrix} + c_-(z)\begin{bmatrix}\mathbf{e}_-(\mathbf{r})\\ \mathbf{h}_-(\mathbf{r})\end{bmatrix} \tag{3.2}$$

In this formulation, the material gain (or absorption) induced by carrier density is viewed as a perturbation to a reference line-defect waveguide with purely real refractive index. In Eq. (3.2), z is the propagation coordinate and $\mathbf{r}$ the position vector. $\mathbf{e}_+$ ($\mathbf{e}_-$) is the forward-propagating (backward-propagating) electric field of the guided *Bloch* mode at the angular frequency ω; similarly, $\mathbf{h}_\pm$ are the magnetic fields. These modes are z periodic, with the period given by lattice constant a. The amplitudes $c_\pm$ generally depend on the perturbation, as well as on z and ω. They are given by $c_\pm(z) = \psi_\pm(z)e^{\pm ik_z z}$, where k_z is the (real) wavenumber of the reference waveguide, while $\psi_\pm$ are slowly-varying spatial envelopes.

At a given ω, by neglecting nonlinear effects, one may derive two coupled differential equations [19]

$$\frac{\partial\psi_+(z)}{\partial z} = i\kappa_{11}(z)\psi_+ + i\kappa_{12}(z)e^{-2ik_z z}\psi_- \tag{3.3a}$$

$$-\frac{\partial\psi_-(z)}{\partial z} = i\kappa_{21}(z)e^{+2ik_z z}\psi_+ + i\kappa_{11}(z)\psi_- \tag{3.3b}$$

which we call coupled-Bloch-mode (CBM) equations. A detailed derivation of these equations and associated coupling coefficients is provided in Appendix A. In the following, we recall the main features. The self- (κ_{11}) and cross-coupling coefficients (κ_{12} and κ_{21}) are given by

$$\kappa_x(z) = \left(\frac{\omega}{c}\right) S \left[i \left(n_i - i\Delta n_b''\right) \Gamma_x^{\text{carrier}}(z) + \Delta n_b' \Gamma_x^{\text{index}}(z)\right] \tag{3.4}$$

with $x = 11, 12, 21$. $S = n_g/n_{\text{slab}}$ is the *slow-down factor*, with n_g being the group index of the reference waveguide and n_{slab} the slab refractive index. n_i is the imaginary refractive index controlled by carrier density in the active layers of quantum wells or quantum dots and $\Delta n_b''$ the associated real refractive index perturbation. The active layers are assumed to undergo spatially uniform pumping. By assuming the material gain to depend linearly on carrier density, $\Delta n_b''$ may be quantified as

$$\Delta n_b'' = \alpha_H n_i \tag{3.5}$$

with α_H being the linewidth enhancement factor [23]. $\Delta n_b'$ accounts instead for any other source of refractive index perturbation (e.g. structural, thermal or electro-optic). The normalized coupling coefficients $\Gamma_x^{\text{carrier}}$ are

$$\Gamma_{11}^{\text{carrier}}(z) = \frac{a \int_A \epsilon_0 n_{\text{slab}}^2 |\mathbf{e}_+(\mathbf{r})|^2 F_{\text{carrier}}^{\text{uniform}}(\mathbf{r}) dA}{\int_V \epsilon_0 n_b^2(\mathbf{r}) |\mathbf{e}_+(\mathbf{r})|^2 \, dV} \tag{3.6a}$$

$$\Gamma_{12}^{\text{carrier}}(z) = \frac{a \int_A \epsilon_0 n_{\text{slab}}^2 \left[\mathbf{e}_-(\mathbf{r}) \cdot \mathbf{e}_+^*(\mathbf{r})\right] F_{\text{carrier}}^{\text{uniform}}(\mathbf{r}) dA}{\int_V \epsilon_0 n_b^2(\mathbf{r}) |\mathbf{e}_+(\mathbf{r})|^2 \, dV} \tag{3.6b}$$

with $\Gamma_{21}^{\text{carrier}} = \left(\Gamma_{12}^{\text{carrier}}\right)^*$ and $*$ denoting the complex conjugate. Here, V is the volume of a supercell and A the cross-section area at position z. $F_{\text{carrier}}^{\text{uniform}}(\mathbf{r})$ is a function taking into account the spatial distribution of the active material within the active waveguide *as if* the active layers entirely filled the slab along the direction orthogonal to the slab. The concept is clarified by Fig. 3.6. Fig. 3.6(a) depicts the reference waveguide, with the reference system adopted throughout this thesis. We denote the x-direction (y-direction) as *lateral* (*vertical*). The z-direction is instead the *longitudinal* direction. Fig. 3.6(b) and (c) illustrate a cross-section and top view of the active waveguide, with the active layers being limited to the line-defect. This implementation reflects photonic crystal lasers based on line-defect waveguides with a buried heterostructure active region [88, 160]. Finally, Fig. 3.6(d) shows the active waveguide in the fictitious case of the material gain assumed to be *homogeneous* throughout the slab along the vertical direction. $F_{\text{carrier}}^{\text{uniform}}(\mathbf{r})$ is unitary within the active region in Fig. 3.6(d) and zero elsewhere. It should be also mentioned that in many of the currently demonstrated active photonic crystal structures [119, 121, 29], the active layers stretch throughout the slab in the lateral direction, as we discuss in Sec. 3.2.1. In these structures, the population inversion

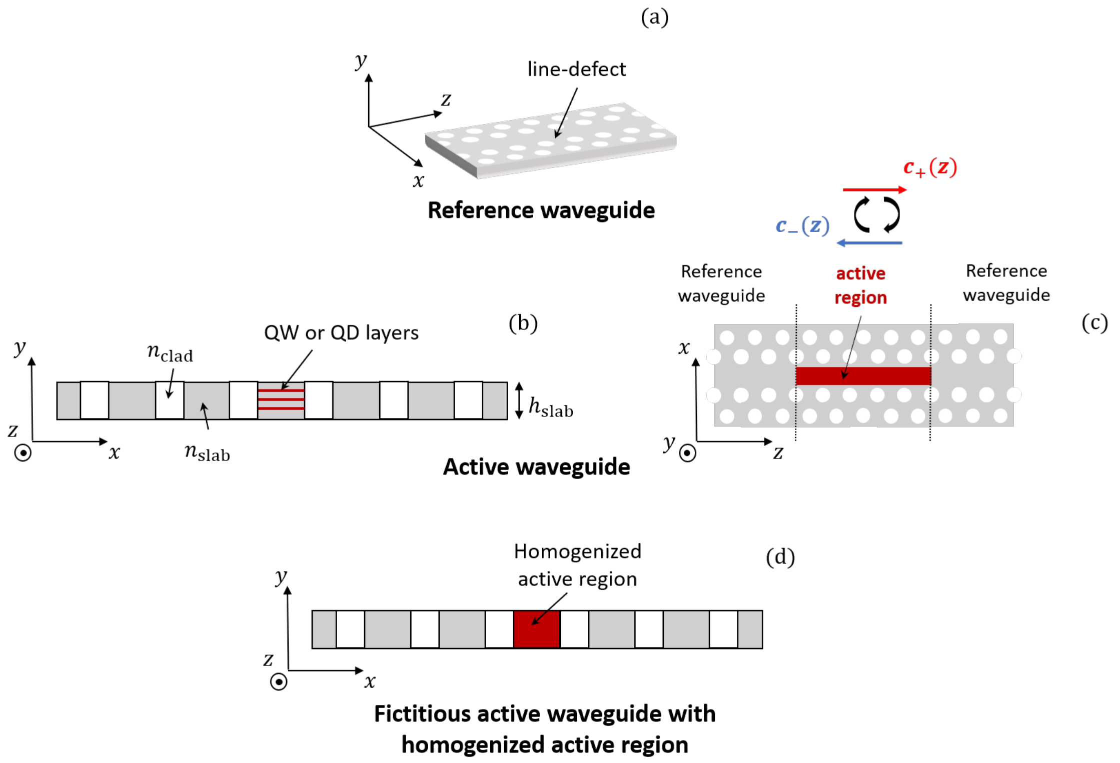

Figure 3.6: (a) Reference photonic crystal waveguide. (b,c) Active photonic crystal waveguide. (d) Fictitious active waveguide with homogenized active region.

extends beyond the line-defect region, owing to the large spot of the optical pump or lack of a structure for lateral carrier confinement. In this case (not shown in Fig. 3.6), $F_{\mathrm{carrier}}^{\mathrm{uniform}}(\mathbf{r})$ is unitary within the slab and zero within holes and cladding. In any case, as mentioned above, we assume the active layers to undergo spatially uniform pumping. Therefore, $\Gamma_{11}^{\mathrm{carrier}}$ and $\Gamma_{12}^{\mathrm{carrier}}$ are 1) frequency-dependent and 2) z periodic, with the period given by the lattice constant a. This is due to the frequency dependence and spatial periodicity of the Bloch modes of the reference waveguide. Furthermore, it should be emphasized that $\Gamma_{11}^{\mathrm{carrier}}$ is real, while $\Gamma_{12}^{\mathrm{carrier}}$ is generally a complex coefficient.

The actual distribution of the active material along the vertical direction is embedded into the imaginary refractive index n_i. Indeed, n_i reflects the *modal* gain coefficient $g_0 = \Gamma_y g_{\mathrm{mat}}$, with

$$n_i = -\frac{1}{2}\left(\frac{c}{\omega}\right)\Gamma_y g_{\mathrm{mat}} \tag{3.7}$$

Here, g_{mat} is the material gain (spatially limited to the active layers) and Γ_y the optical confinement factor within the active layers along the vertical direction. As quantified in Appendix A, this confinement factor is independent of ω and z to a good approximation. For a single active layer being 8 nm thick, limited to the line-defect as in Fig. 3.6(b) and placed in the middle of the slab, Γ_y is around 4%. This approach is convenient because, for a given reference waveguide, the normalized coupling coefficients are only computed once. One can then account for any number of active layers by appropriately scaling Γ_y.

The normalized coupling coefficients $\Gamma_{11}^{\text{index}}$ and $\Gamma_{12}^{\text{index}}$ are obtained, respectively, from Eqs. (3.6a) and (3.6b) by replacing $F_{\text{carrier}}^{\text{uniform}}(\mathbf{r})$ with $F_{\Delta n_b'}(\mathbf{r})$. Similarly, one finds $\Gamma_{21}^{\text{index}} = \left(\Gamma_{12}^{\text{index}}\right)^*$. The distribution function $F_{\Delta n_b'}(\mathbf{r})$ reflects the possible local tuning of refractive index, with $F_{\Delta n_b'} = 1$ ($F_{\Delta n_b'} = 0$) where the refractive index has been tuned (elsewhere). For simplicity, we assume this tuning, if present, to be limited to the slab and to be spatially uniform along z. Therefore, $\Gamma_{11}^{\text{index}}$ and $\Gamma_{12}^{\text{index}}$ are also z periodic, as well as frequency-dependent.

Unless otherwise specified, throughout this thesis we assume for simplicity the material gain to be spectrally flat. However, as shown in Appendix A, incorporating a frequency-dependent material gain is straightforward.

3.2.1 Normalized coupling coefficients

In the following, we focus on the frequency and spatial dependence of the normalized coupling coefficients given by Eqs. (3.6a) and (3.6b). We discuss two possible implementations of the active region, that is 1) active layers extending through out the slab in the lateral direction and 2) active layers limited to the line-defect.

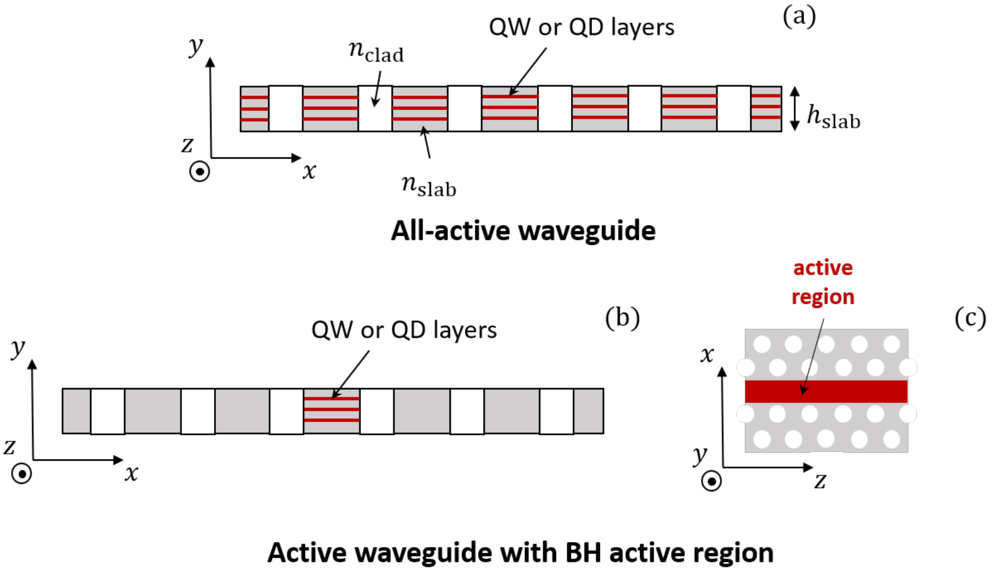

Figure 3.7: Active photonic crystal waveguide with the active layers (a) extending throughout the slab in the lateral direction (all-active waveguide) and (b,c) limited to the line-defect (buried heterostructure active region).

The two structures are shown in Fig. 3.7(a) and (b) respectively. As already mentioned, that in Fig. 3.7(a) reflects the majority of currently demonstrated active photonic crystal structures based on line-defect waveguides. These structures are often optically pumped [119, 29, 177], although not necessarily [121]. We denote this type of waveguide as *all-active*. On the other hand, the structure in Fig. 3.7(b) reflects photonic crystal lasers based on line-defect waveguides with a *buried heterostructure* (BH) active region, which improves the energy efficiency. This type of structure has been demonstrated both under optical [88] and electrical pumping [160]. For simplicity, throughout this thesis we assume the BH, if present, to almost completely fill the line-defect between the innermost holes, as shown in Fig. 3.7(b) and (c). In practice, the exact measures of the BH in the lateral direction obviously depend on the specific, practical realization. However, we expect these deviations not to alter our conclusions and to only lead to minor, quantitative changes.

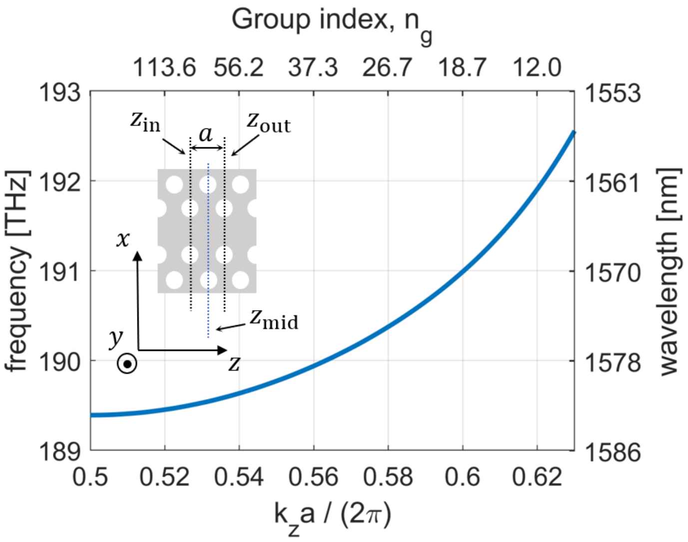

Figure 3.8: Dispersion relation of the reference waveguide for the fundamental guided TE-like mode. The inset shows a top view of the waveguide. The unit cell reference planes along the longitudinal direction are also indicated, with z_{in} corresponding to the input, z_{mid} to the centre and z_{out} to the output.

Fig. 3.8 shows the dispersion relation of the reference waveguide for the fundamental guided TE-like mode. The simulation parameters are summarized in Tab. 2.1. The dispersion relation and Bloch modes of the reference waveguide have been computed by the plane wave eigensolver MIT-Photonic-Bands (MPB), as explained in Sec. 2.2.1. The inset depicts a top view of the waveguide and the unit cell reference planes along the longitudinal direction are also indicated. The input (output) is denoted by z_{in} (z_{out}), while z_{mid} corresponds to the centre.

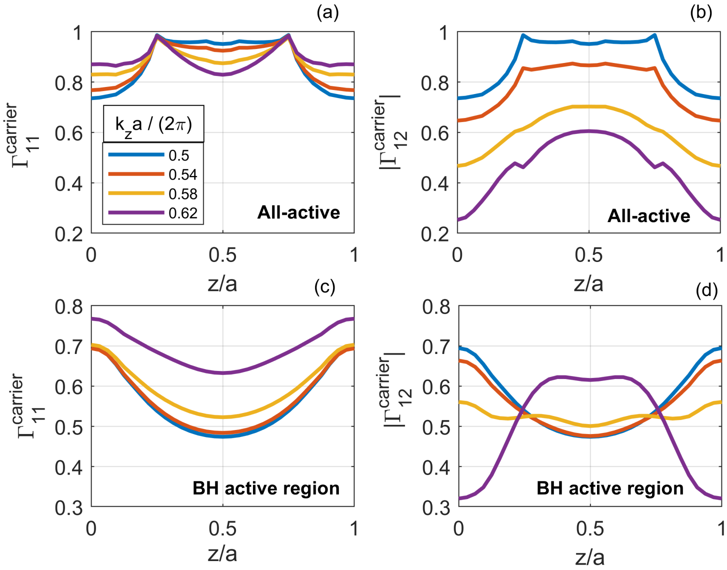

Figure 3.9: Normalized coupling coefficients over a unit cell of (a) and (b) an all-active waveguide and (c) and (d) a waveguide with a BH active region. (a) and (c) report the self-coupling coefficient, (b) and (d) the magnitude of the cross-coupling coefficient. Each colour corresponds to a different value of the wavenumber, as indicated by the legend in (a).

Fig. 3.9 illustrates the normalized coupling coefficients of (a) and (b) an all-active waveguide and (c) and (d) a waveguide with a BH active region. The self-coupling coefficient $\Gamma_{11}^{\text{carrier}}$ is shown in (a) and (c), the magnitude of the cross-coupling coefficient $\Gamma_{12}^{\text{carrier}}$ in (b) and (d). They are reported over a unit cell. Each colour corresponds to a different value of the wavenumber, as indicated by the legend in (a). We note that the spatial average of $|\Gamma_{12}^{\text{carrier}}|$ builds up when the wavenumber moves towards the band edge, with the increase being more pronounced in the all-active waveguide. At the band edge, $\Gamma_{11}^{\text{carrier}}$ and $|\Gamma_{12}^{\text{carrier}}|$ practically coincide. The increase in the average of $|\Gamma_{12}^{\text{carrier}}|$ is a key feature, on which we will return afterwards.

The frequency and spatial dependence of the self-coupling coefficient can be better understood by visualizing the squared magnitude of the electric field. For this purpose, Fig. 3.10 shows $|\mathbf{e}_{+}(\mathbf{r})|^2$ on the waveguide cross-section at two different frequencies, corresponding to (a) and (c) $k_z a/(2\pi) = 0.54$ and (b) and (d) $k_z a/(2\pi) = 0.62$. The longitudinal coordinate is set to (a) and (b) the input and (c) and (d) centre of a unit cell. The vertical (horizontal) white lines define the holes (semiconductor slab). The vertical green lines delimit the lateral extension of the BH active region, if present. When plotting $|\mathbf{e}_{+}(\mathbf{r})|^2$ at a given frequency, we have normalized it to its maximum value over the whole supercell volume. As the frequency approaches the band edge, the mode tends to spread in the lateral direction, with the broadening being more prominent

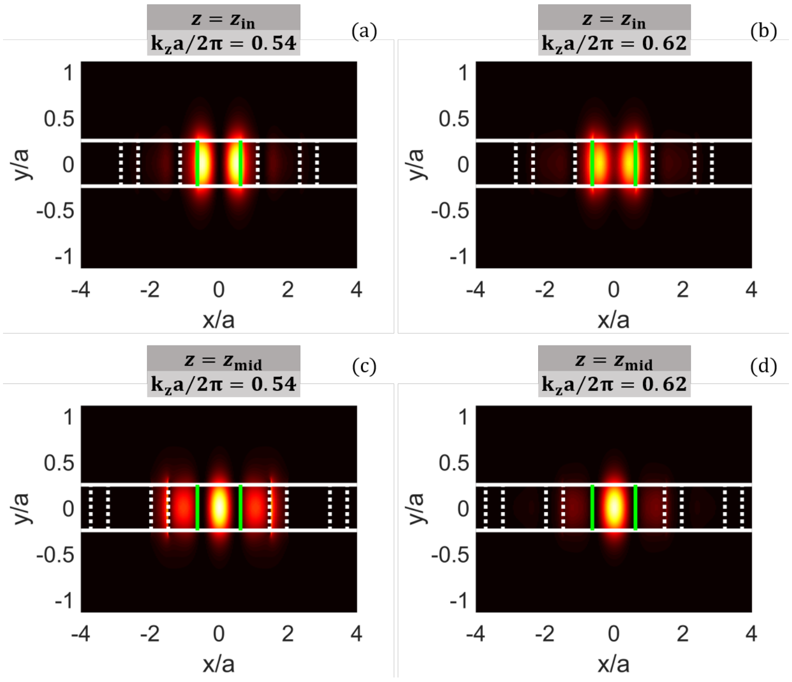

Figure 3.10: Squared magnitude of the electric field $|\mathbf{e}_{+}(\mathbf{r})|^2$ on the waveguide cross-section at (a) and (b) $z = z_{\text{in}}$ and (c) and (d) $z = z_{\text{mid}}$ (see the inset of Fig. 3.8.) The normalized wavenumber $k_z a/(2\pi)$ is (a) and (c) 0.54 and (b) and (d) 0.62. The vertical (horizontal) white lines define the holes (semiconductor slab). The vertical green lines delimit the lateral extension of the BH active region, if present. In these plots, we have normalized $|\mathbf{e}_{+}(\mathbf{r})|^2$ at a given frequency to its maximum value over the whole supercell volume.

at the centre of the unit cell as compared to the input. As a result, in the case of a BH active region, the relative fraction of $|\mathbf{e}_{+}(\mathbf{r})|^2$ within the active region diminishes as compared to the total distribution over the supercell volume. Therefore, the self-coupling coefficient is generally reduced, with a stronger reduction at the centre of the unit cell (see Fig. 3.9(c)). On the other hand, in the case of an all-active waveguide, the self-coupling coefficient decreases (increases) at the input (centre) of a unit cell as the frequency approaches the band edge (see Fig. 3.9(a)). This is due to the smaller (larger) fraction of $|\mathbf{e}_{+}(\mathbf{r})|^2$ within the holes as compared to the total distribution over the supercell volume.

As already mentioned, the coupling coefficients are periodic. Therefore, they can be expanded in a Fourier series

$$\Gamma_x^{\text{carrier}}(z) = \sum_q \Gamma_{x,q}^{\text{carrier}} e^{+iq\frac{2\pi}{a}z} \tag{3.8}$$

with $x = 11,\ 12,\ 21$. The magnitude of the spatial harmonics is reported in Fig. 3.11, in

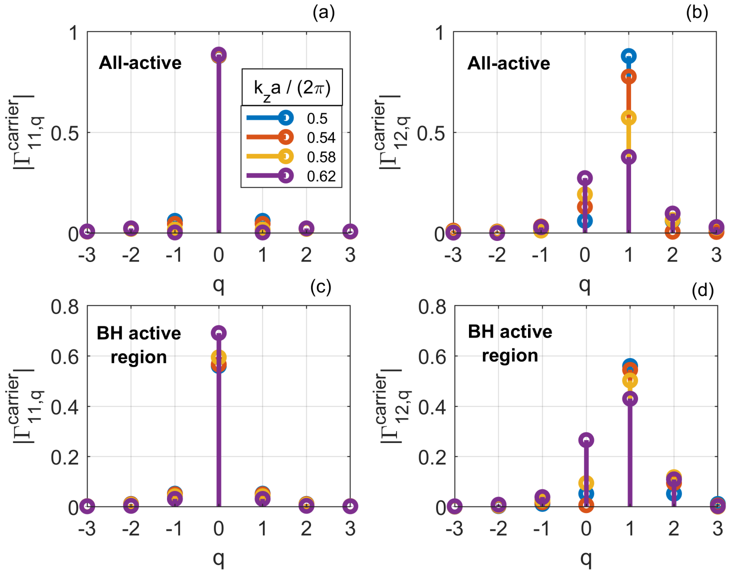

Figure 3.11: Magnitude of the spatial harmonics of the normalized coupling coefficients of (a) and (b) an all-active waveguide and (c) and (d) a waveguide with a BH active region. The spatial harmonics of the self-coupling coefficient are in (a) and (c), those of the cross-coupling coefficient in (b) and (d). Each colour corresponds to a different value of the wavenumber, as indicated by the legend in (a).

the case of (a) and (b) an all-active waveguide and (c) and (d) a waveguide with a BH active region. Each colour corresponds to a different value of the wavenumber, as indicated by the legend in (a). The frequency dependence of the spatial harmonics follows a similar trend in the two structures. In the self-coupling coefficient (see Fig. 3.11(a) and (c)), all harmonics other than the spatial average ($q = 0$) are negligible. In the cross-coupling coefficient $\Gamma_{12}^{\text{carrier}}$ (see Fig. 3.11(b) and (d)), the first-order harmonic ($q = 1$) is the dominant one. Furthermore, its intensity as compared to the average strongly increases as the wavenumber approaches the band edge. This behaviour reflects the variation of the magnitude of $\Gamma_{12}^{\text{carrier}}$ (see Fig. 3.9(b) and (d)) and its phase.

This phase is shown in Fig. 3.12 in the case of an all-active waveguide and (b) a waveguide with a BH active region. The two plots are almost the same. We note that the phase of $\Gamma_{12}^{\text{carrier}}$ approximately varies with z in a linear fashion, with a total phase shift of 2π. Moreover, the closer the wavenumber is to the band edge and the more linear the phase becomes. Therefore, the first-order harmonic of the cross-coupling coefficient is proportional to the spatial average of its magnitude and turns out to be real and *negative* to a good approximation. In fact, on the basis of Fig. 3.12, one may approximate the phase of $\Gamma_{12}^{\text{carrier}}$ with $\frac{2\pi}{a}z - \pi$ and find

$$\Gamma_{12,q=1}^{\text{carrier}} = \frac{1}{a}\int_a \Gamma_{12}^{\text{carrier}}(z)e^{-i\frac{2\pi}{a}z} \approx e^{-i\pi}\langle|\Gamma_{12}^{\text{carrier}}(z)|\rangle \tag{3.9}$$

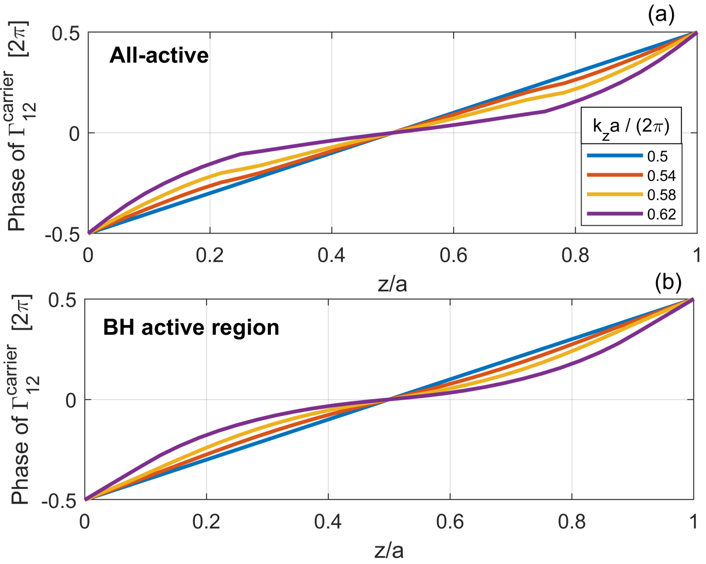

Figure 3.12: Phase of the normalized cross-coupling coefficient of (a) an all-active waveguide and (b) a waveguide with a BH active region plotted over a unit cell. Each colour corresponds to a different value of the wavenumber, as indicated by the legend in (a).

where $\langle\rangle$ indicates the spatial average. Since this average increases as the wavenumber approaches the band edge (see Fig. 3.9(b) and (d)), the magnitude of the first-order harmonic consequently builds up.

The peculiar frequency dependence of the spatial harmonics of the coupling coefficients originates from the compresence of the *two* in-plane electric field components. Indeed, as reviewed in Chapter 2, TE-like modes in line-defect photonic crystal waveguides possess two main electric field components. They are the longitudinal and lateral component. In contrast, TE-like modes in conventional ridge-type waveguides only have a single main component, that is the lateral one. To assess the impact of this additional longitudinal component, we focus on the waveguide with a BH active region. For this structure, we have computed the coupling coefficients by only considering either the lateral or longitudinal component. The magnitude of the spatial harmonics is reported in Fig. 3.13. In (a) and (c) only the longitudinal component has been taken into account. In (b) and (d) we have only considered the lateral component. Each colour corresponds to a different value of the wavenumber, as indicated by the legend in (a). In the self-coupling coefficient (see Fig. 3.13(a) and (b)), the spatial average is the dominant harmonic irrespective of the field component which is taken into account. However, two additional harmonics ($q = \pm 1$) are also present, whose relative strength as compared to the spatial average depends on the field component which is considered (as well as on frequency). Furthermore, we note that the spatial average increases (decreases)

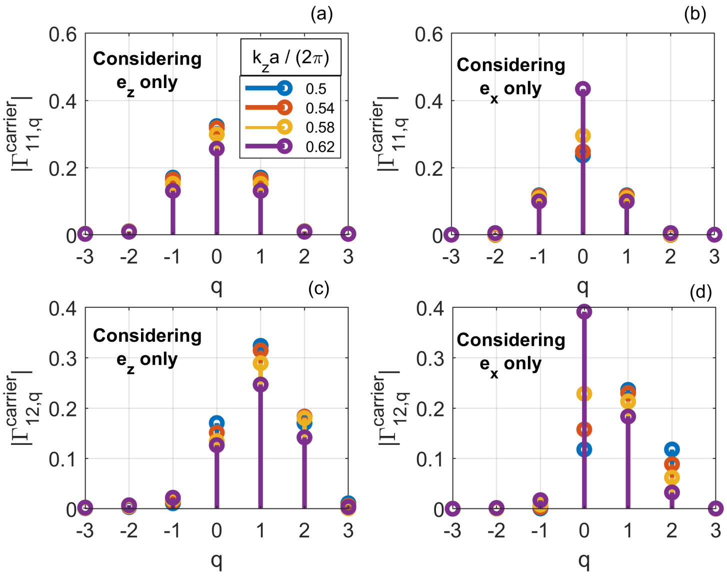

Figure 3.13: Magnitude of the spatial harmonics of the normalized coupling coefficients of a waveguide with a BH active region. The coupling coefficients are computed by only considering the (a) and (c) longitudinal and (b) and (d) lateral component of the electric field. The spatial harmonics of the self-coupling coefficient are in (a) and (b), those of the cross-coupling coefficient in (c) and (d). Each colour corresponds to a different value of the wavenumber, as indicated by the legend in (a).

as the wavenumber approaches the band edge if one only considers the longitudinal (lateral) field component. On the other hand, when both components are accounted for, the average of the normalized self-coupling coefficient decreases towards the band edge (see Fig. 3.11(c)). In the cross-coupling coefficient, the situation is more intricate. Three harmonics are generally relevant, corresponding to $q = 0, 1, 2$. If we only account for the longitudinal component (see Fig. 3.13(c)), the first-order harmonic ($q = 1$) is the dominant one. The more the wavenumber approaches the band edge, the larger the ratio becomes between the first-order harmonic and either of the other two harmonics. However, such increase is much weaker as compared to the case when the lateral field component is also taken into account (see Fig. 3.11(d)). On the other hand, if we only account for the lateral component (see Fig. 3.13(d)), the first-order harmonic is not necessarily the dominant one. In particular, as the wavenumber departs from the band edge, the spatial average ($q = 0$) strongly builds up as compared to the first-order harmonic. This increase is much stronger as compared to the case when the longitudinal field component is also taken into account (again, see Fig. 3.11(d)). We have verified that similar considerations apply to the case of an all-active waveguide. In light of these considerations, we ascribe the frequency dependence and relative strength of the various spatial harmonics of the coupling coefficients to the combined effect of the lateral and longitudinal electric field component.

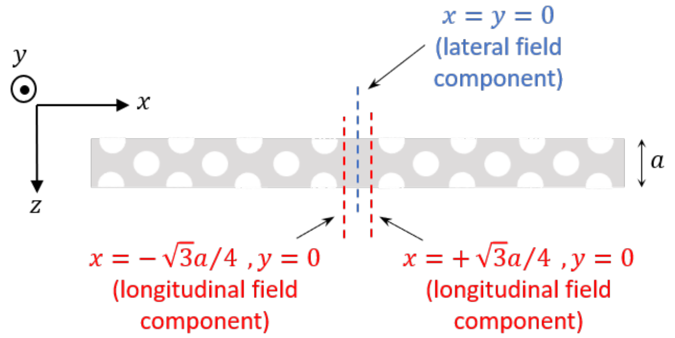

Figure 3.14: Top view of a supercell. When evaluating the coupling coefficients, the major contributions of the lateral (longitudinal) electric field component originate from the blue line (red lines).

The physics of this behaviour can be further elucidated by simple, analytical considerations, elaborated in the following. We wish to derive rough, analytical estimates of the integrals in Eqs. (3.6a) and (3.6b). As evident from Fig. 2.7(b), the lateral electric field component is approximately uniform within the waveguide along the lateral direction. Furthermore, the field is well confined to the slab in the vertical direction, due to the high refractive index contrast between slab and air cladding. Therefore, as illustrated by Fig. 3.14, we may approximate the lateral component by evaluating it along the centerline of the waveguide, namely

$$e_{x,+}(\mathbf{r}) \approx e_{x,+}(x = 0, y = 0, z) \triangleq e_{x,+}(z) \tag{3.10}$$

Here, the subscript x highlights that this is the *lateral* component. Furthermore, based on Eq. (2.5), one finds

$$e_{x,+}(z) \approx b_{x,0} + b_{x,-1} e^{-i\frac{2\pi}{a}z} \tag{3.11}$$

where $b_{x,0}$ and $b_{x,-1}$ are, respectively, the spatial average and first-order harmonic of $e_{x,+}(z)$. By choosing the reference plane $z = 0$ at the interface between two unit cells, one finds $b_{x,0}$ ($b_{x,-1}$) to be real and positive (real and negative), as discussed in Sec. 2.4.2. In particular, $b_{x,-1}$ tends to $b_{x,0}$ as the frequency approaches the band edge. This signifies a transition from a moving to a standing wave, as explained in Sec. 2.2.2. At the band edge, one finds $b_{x,-1} = -|b_{x,0}|$. Therefore, at this frequency, we may approximate the contribution of the lateral field component entering the integrals in Eqs. (3.6a) and (3.6b) as

$$|e_{x,+}(\mathbf{r})|^2 \approx 2|b_{x,0}|^2 - |b_{x,0}|^2 e^{+i\frac{2\pi}{a}z} - |b_{x,0}|^2 e^{-i\frac{2\pi}{a}z} \tag{3.12a}$$

$$e_{x,-}(\mathbf{r}) \left[e_{x,+}(\mathbf{r})\right]^* \approx |b_{x,0}|^2 - 2|b_{x,0}|^2 e^{+i\frac{2\pi}{a}z} + |b_{x,0}|^2 e^{+i\frac{4\pi}{a}z} \tag{3.12b}$$

It is worth emphasizing that Eqs. (3.12a) and (3.12a) are consistent, respectively, with Fig. 3.13(b) and (d). We shall now analyze the contribution of the longitudinal electric field component. As evident from Fig. 2.7(a), this component is zero along the centerline of the waveguide and changes its sign when moving along the lateral direction. In this case, we may write

$$e_{z,+}(\mathbf{r}) \approx e_{z,+}(x = \pm\sqrt{3}a/4, y = 0, z) \triangleq e^{r,l}_{z,+}(z) \tag{3.13}$$

with $e^{l}_{z,+}(z) = -e^{r}_{z,+}(z)$. Here, the subscript z highlights that this is the *longitudinal* component. Furthermore, the subscripts r and l denote, respectively, the position on the right ($x = +\sqrt{3}a/4$) and left ($x = -\sqrt{3}a/4$) of the centerline (see Fig. 3.14). From MPB simulations (not shown here for the sake of brevity), it turns out that only two spatial harmonics are relevant, as previously found for the lateral component. Specifically, we may write

$$e^{r}_{z,+}(z) \approx b^{r}_{z,0} + b^{r}_{z,-1} e^{-i\frac{2\pi}{a}z} \tag{3.14}$$

By choosing, again, the reference plane $z = 0$ at the interface between two unit cells, one finds that $b^{r}_{z,0}$ and $b^{r}_{z,-1}$ are purely imaginary. At the band edge, one finds $b^{r}_{z,-1} = b^{r}_{z,0}$, with $b^{r}_{z,0} = |b^{r}_{z,0}|e^{+i\pi/2}$. Again, this signifies a transition from a moving to a standing wave. In light of these considerations, at the band edge we may write

$$\left|e^{r,l}_{z,+}(\mathbf{r})\right|^2 \approx 2\left|b^{r,l}_{z,0}\right|^2 + \left|b^{r,l}_{z,0}\right|^2 e^{+i\frac{2\pi}{a}z} + \left|b^{r,l}_{x,0}\right|^2 e^{-i\frac{2\pi}{a}z} \tag{3.15a}$$

$$e^{r,l}_{z,-}(\mathbf{r})\left[e^{r,l}_{z,+}(\mathbf{r})\right]^* \approx -\left|b^{r,l}_{z,0}\right|^2 - 2\left|b^{r,l}_{z,0}\right|^2 e^{+i\frac{2\pi}{a}z} - \left|b^{r,l}_{z,0}\right|^2 e^{+i\frac{4\pi}{a}z} \tag{3.15b}$$

Therefore, the contributions stemming from $e^{r}_{z,+}(z)$ and $e^{l}_{z,+}(z)$ add up with the same sign when evaluating the integrals in Eqs. (3.6a) and (3.6b). It should be emphasized that Eqs. (3.15a) and (3.15b) are consistent, respectively, with Fig. 3.13(a) and (c).

By using Eqs. (3.12a) and (3.15a) and recalling the definition of the self-coupling coefficient from Eq. (3.6a), we may write

$$|\mathbf{e}_{+}(\mathbf{r})|^2 \approx |e_{x,+}(\mathbf{r})|^2 + \left|e^{r,l}_{z,+}(\mathbf{r})\right|^2 \approx 4|b_{x,0}|^2 \propto \Gamma^{\text{carrier}}_{11,q=0} \tag{3.16}$$

where we have assumed $\left|b_{x,0}\right| \approx \left|b^{r,l}_{z,0}\right|$ and neglected the vertical electric field component (which is much smaller than the other two components for TE-like modes). Similarly, by using Eqs. (3.12b) and (3.15b) and recalling the definition of the cross-coupling coefficient from Eq. (3.6b), we obtain

$$\begin{aligned}\mathbf{e}_{-}(\mathbf{r}) \cdot \mathbf{e}^{*}_{+}(\mathbf{r}) &\approx e_{x,-}(\mathbf{r})\left[e_{x,+}(\mathbf{r})\right]^* + e^{r,l}_{z,-}(\mathbf{r})\left[e^{r,l}_{z,+}(\mathbf{r})\right]^* \\ &\approx -4|b_{x,0}|^2 e^{+i\frac{2\pi}{a}z} \propto \Gamma^{\text{carrier}}_{12,q=1} e^{+i\frac{2\pi}{a}z}\end{aligned} \tag{3.17}$$

Eqs. (3.16) and (3.17) evidence that, at the band edge, one should expect $\Gamma^{\text{carrier}}_{12,q=1} = -|\Gamma^{\text{carrier}}_{11,q=0}|$, which is indeed what we have found. Overall, these simple considerations emphasize that the physics of coinciding self- and cross-coupling coefficients at the band edge is a transition from a moving to a standing wave.

3.3 Reduced coupled-Bloch-mode equations

On the basis of Sec. 3.2.1 (and, specifically, of the results in Fig. 3.11), we may expand the coupling coefficients in a Fourier series and only retain the spatial average (first-order harmonic) in the expansion of the self-coupling coefficient $\Gamma^{\text{carrier}}_{11}$ (cross-coupling coefficient $\Gamma^{\text{carrier}}_{12}$). Furthermore, since $\Gamma^{\text{carrier}}_{21}$ is the complex conjugate of $\Gamma^{\text{carrier}}_{12}$, one finds $\Gamma^{\text{carrier}}_{21,-q} = \left(\Gamma^{\text{carrier}}_{12,q}\right)^*$. Therefore, we may only retain the harmonic with order $q = -1$ in the expansion of the cross-coupling coefficient $\Gamma^{\text{carrier}}_{21}$. By doing so, from Eqs. (3.3a) and (3.3b) we obtain

$$\frac{\partial \psi_+(z)}{\partial z} = i\kappa_{\text{FF}}\psi_+ + i\kappa_{\text{FB}}e^{+i2\delta z}\psi_- \tag{3.18a}$$

$$-\frac{\partial \psi_-(z)}{\partial z} = i\kappa_{\text{BF}}e^{-i2\delta z}\psi_+ + i\kappa_{\text{FF}}\psi_- \tag{3.18b}$$

which we call *reduced* coupled-Bloch-mode (CBM) equations. The self- (κ_{FF}) and cross-coupling coefficients (κ_{FB} and κ_{BF}) are given by

$$\kappa_x = \left(\frac{\omega}{c}\right) S \left[i \left(n_i - i\Delta n''_b\right) \Gamma_x + \Delta n'_b \Gamma^{\text{index}}_x \right] \tag{3.19}$$

with $x = \text{FF}, \text{FB}, \text{BF}$. Here, one finds $\Gamma_{\text{BF}} = \left(\Gamma_{\text{FB}}\right)^*$ and $\Gamma^{\text{index}}_{\text{BF}} = \left(\Gamma^{\text{index}}_{\text{FB}}\right)^*$. To simplify the notation, we have denoted by Γ_{FF} (Γ_{FB}) the spatial average (first-order harmonic) of $\Gamma^{\text{carrier}}_{11}$ ($\Gamma^{\text{carrier}}_{12}$). Similarly, we have denoted by $\Gamma^{\text{index}}_{\text{FF}}$ ($\Gamma^{\text{index}}_{\text{FB}}$) the spatial average (first-order harmonic) of $\Gamma^{\text{index}}_{11}$ ($\Gamma^{\text{index}}_{12}$). On this regard, we have assumed either of two possible implementations for the distribution function $F_{\Delta n'_b}(\mathbf{r})$ of the local refractive index tuning. A first possibility is a spatially uniform refractive index tuning within the slab and no tuning within holes and cladding. In this case, $F_{\Delta n'_b}(\mathbf{r})$ has the same form as $F^{\text{uniform}}_{\text{carrier}}(\mathbf{r})$ in an all-active waveguide. A second possibility is a spatially uniform refractive index tuning within the waveguide region corresponding to the line-defect and no tuning elsewhere. In this case, $F_{\Delta n'_b}(\mathbf{r})$ coincides with $F^{\text{uniform}}_{\text{carrier}}(\mathbf{r})$ in a waveguide with a BH active region. In either case, we can apply to the normalized coupling coefficients due to refractive index tuning the same considerations made in Sec. 3.2.1 on those due to active material. Therefore, we can neglect all harmonics in the expansion of $\Gamma^{\text{index}}_{11}$ ($\Gamma^{\text{index}}_{12}$) other than the spatial average (first-order harmonic). Finally, we note that δ in Eqs. (3.18a) and (3.18b) is the detuning from the band edge

$$\delta = q\frac{\pi}{a} - k_z, \quad \text{with } q = 1 \tag{3.20}$$

When expanding the cross-coupling coefficients $\Gamma_{12}^{\text{carrier}}$ and $\Gamma_{12}^{\text{index}}$, we have discarded the spatial harmonics with order $q \neq 1$ and justified the approximation on the basis of the relative strength of the first-order harmonic as compared to the others. However, in light of Fig. 3.11(b) and (d), one might question the validity of this approximation when the wavenumber is far from the band edge. In fact, in this case the spatial average ($q = 0$) may be comparable with the first-order harmonic. However, we emphasize that an *additional* reason to discard the harmonics with $q \neq 1$ in the expansion of the cross-coupling coefficient is that they would result in larger values of the detuning δ (see Eq. (3.20)). For a given intensity of the cross-coupling coefficient, the larger this detuning is and the weaker the interaction becomes between the amplitude of the forward- (ψ_+) and backward-propagating mode (ψ_-). This is indeed the basis on which the same approximation is justified in the coupled-mode theory of one-dimensional gratings [79] and DFB lasers [23, 4]. Therefore, we consider our approximation to be acceptable even when the wavenumber is far from the band edge.

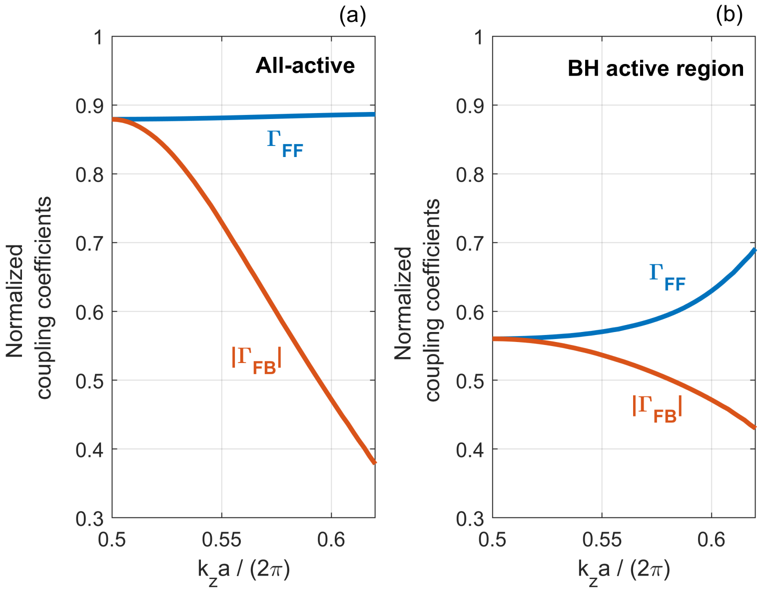

Figure 3.15: Normalized self-coupling coefficient Γ_{FF} (blue) and magnitude of the normalized cross-coupling coefficient Γ_{FB} (red) of (a) an all-active waveguide and (b) a waveguide with a BH active region.

Fig. 3.15 shows the normalized self-coupling coefficient Γ_{FF} (blue) of (a) an all-active waveguide and (b) a waveguide with a BH active region. The magnitude of the normalized cross-coupling coefficient Γ_{FB} is also shown (red). In an all-active waveguide, the normalized self-coupling coefficient is almost independent of frequency. On the other hand, as a result of the broadening of the electric field squared magnitude in the lateral direction (see Fig. 3.10), in a waveguide with a BH active region the normalized self-coupling coefficient decreases towards the band edge. Moreover, in either type of waveguide, a strong cross-coupling coefficient builds up close to the band edge. As thoroughly discussed in Sec. 3.2.1, this is due to the increase in $\langle|\Gamma_{12}^{\text{carrier}}(z)|\rangle$, as well as to the linear z dependence of the phase of $\Gamma_{12}^{\text{carrier}}(z)$.

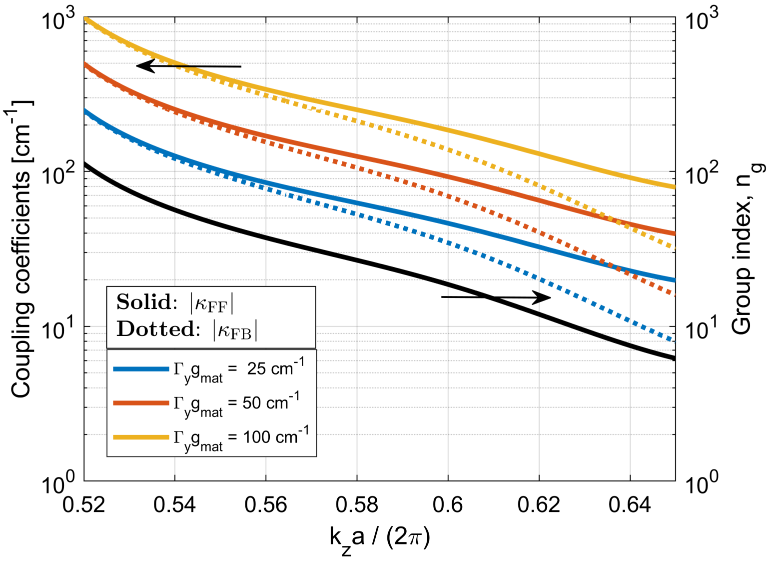

Figure 3.16: (left) Magnitude of the self-coupling coefficient κ_{FF} (solid) and cross-coupling coefficient κ_{FB} (dotted) of a waveguide with a BH active region. Each colour denotes a value of the modal gain $\Gamma_y g_{\text{mat}}$, corresponding to 25 (blue), 50 (red) and 100 (yellow) cm^{-1}. The linewidth enhancement factor is assumed to be zero and no other source of refractive index perturbation is considered. (right) Group index of the reference waveguide.

Fig. 3.16 shows (left) the magnitude of the coupling coefficients of a waveguide with a BH active region and (right) the group index n_g of the reference waveguide. The x-axis reports the normalized wavenumber of the reference waveguide. The self-coupling (cross-coupling) coefficient κ_{FF} (κ_{FB}) is denoted by solid (dotted) line. The modal gain $\Gamma_y g_{\text{mat}}$ is set to 25 (blue), 50 (red) and 100 (yellow) cm^{-1}. For simplicity, the linewidth enhancement factor α_H is assumed to be zero and any other source of refractive index perturbation is neglected. The figure emphasizes that the frequency dependence of the self-coupling coefficient is essentially controlled by n_g. Furthermore, the cross-coupling coefficient becomes increasingly comparable to the self-coupling coefficient as the wavenumber approaches the band edge. The relative strength of κ_{FB} as compared to κ_{FF} is controlled by the normalized coupling coefficients in Fig. 3.15(b). Our results are consistent with [94], where the build-up of a huge cross-coupling coefficient was already pointed out. However, as compared to [94], we have discussed the physical origin of this behaviour in Sec. 3.2.1.

3.4 Dispersion relation

In this section, we analyze the dispersion relation of a line-defect waveguide with generally complex refractive index. Throughout this thesis, we generally denote this waveguide as *perturbed.* If the waveguide contains active material, we may alternatively denote it as *active*, with the two definitions being interchangeable.

In Appendix B, we provide a detailed derivation of the dispersion relation. In the following, we only recal the main features. The electromagnetic state of the perturbed waveguide can be represented as

$$\begin{bmatrix} \mathbf{E}(\mathbf{r}) \\ \mathbf{H}(\mathbf{r}) \end{bmatrix} = \tilde{F} \begin{bmatrix} \tilde{\mathbf{e}}_+(\mathbf{r}) \\ \tilde{\mathbf{h}}_+(\mathbf{r}) \end{bmatrix} e^{+i\tilde{k}_z z} + \tilde{B} \begin{bmatrix} \tilde{\mathbf{e}}_-(\mathbf{r}) \\ \tilde{\mathbf{h}}_-(\mathbf{r}) \end{bmatrix} e^{-i\tilde{k}_z z} \tag{3.21}$$

Here, the electric (magnetic) fields $\tilde{\mathbf{e}}_\pm$ and ($\tilde{\mathbf{h}}_\pm$) are the Bloch modes of the *perturbed* waveguide

$$\tilde{\mathbf{e}}_\pm(\mathbf{r}) = \mathbf{e}_\pm(\mathbf{r}) + r_\pm e^{\mp i \frac{2\pi}{a} z} \mathbf{e}_\mp(\mathbf{r}) \tag{3.22a}$$

$$\tilde{\mathbf{h}}_\pm(\mathbf{r}) = \mathbf{h}_\pm(\mathbf{r}) + r_\pm e^{\mp i \frac{2\pi}{a} z} \mathbf{h}_\mp(\mathbf{r}) \tag{3.22b}$$

with $\tilde{F}$ and $\tilde{B}$ being the amplitudes. The Bloch modes of the perturbed waveguide result from the interference of the forward- and backward-propagating Bloch modes of the reference waveguide, with r_+ and r_- determining the strength of the backward component as compared to the forward one and viceversa. The wavenumber $\tilde{k}_z$ is generally *complex* and given by

$$\tilde{k}_z = \beta_{\text{eff}} - \frac{i}{2} g_{\text{eff}} \tag{3.23}$$

where the effective propagation constant β_{eff} and *net* modal gain g_{eff} are

$$\beta_{\text{eff}} = \text{Re}\left\{\lambda_+\right\} + \frac{\pi}{a} \tag{3.24a}$$

$$g_{\text{eff}} = -2\text{Im}\left\{\lambda_+\right\} \tag{3.24b}$$

Here, λ_+ is given by

$$\lambda_+ = \pm\sqrt{(\kappa_{\text{FF}} - \delta)^2 - \kappa_{\text{FB}}\kappa_{\text{BF}}} \tag{3.25}$$

Eqs. (3.24a) and (3.24b) represent the dispersion relation of the active waveguide. The sign of the square root in Eq. (3.25) is selected such that the mode with amplitude $\tilde{F}$ is forward-propagating. In the presence of optical gain or absorption, this implies that $\mathrm{Im}\left\{\lambda_+\right\}$ and $\mathrm{Im}\left\{\kappa_{\mathrm{FF}}\right\}$ must have the same sign. With a certain abuse of notation and for the sake of simplicity, we always refer to g_{eff} as the effective "gain", even in the presence of a purely real refractive index perturbation (i.e. in the absence of gain or absorption). In this case, it remains understood that g_{eff} simply has the physical meaning of imaginary part of the complex wavenumber $\tilde{k}_z$ and cannot be greater than zero.

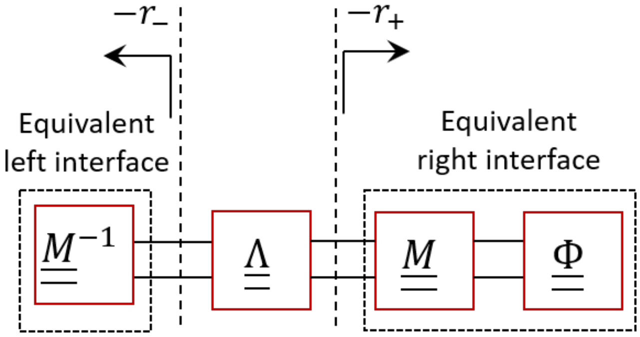

Figure 3.17: Block diagram of an active photonic crystal waveguide.

The coefficients $r_\pm$ in Eqs. (3.22a) and (3.22b) are

$$r_+ = -\frac{\kappa_{\mathrm{BF}}}{(\kappa_{\mathrm{FF}} - \delta) + \lambda_+} \tag{3.26a}$$

$$r_- = -\frac{\kappa_{\mathrm{FB}}}{(\kappa_{\mathrm{FF}} - \delta) + \lambda_+} \tag{3.26b}$$

In Appendix C, we have elucidated their physical meaning by deriving the block diagram in Fig. 3.17. Each block is described by a transmission matrix. By cascading all the blocks, one obtains the transmission matrix of the active waveguide in the basis of the Bloch modes of the reference waveguide. $\underline{\underline{\Lambda}}$ is the transmission matrix in the basis of the Bloch modes of the active waveguide

$$\underline{\underline{\Lambda}} = \begin{bmatrix} e^{+i\lambda_+ L} & 0 \\ 0 & e^{-i\lambda_+ L} \end{bmatrix} \tag{3.27}$$

with L being the waveguide length. While propagating, these modes remain uncoupled, because $\underline{\underline{\Lambda}}$ is diagonal. The matrix $\underline{\underline{\Phi}}\,\underline{\underline{M}}$ accounts for the *mismatch* (i.e. change of basis) between the Bloch modes of the active waveguide and those of the reference waveguide (used as original basis) at the right end. Similarly, $\underline{\underline{M}}^{-1}$ takes into account the mismatch at the left end. These matrices play the role of equivalent dielectric interfaces between the active waveguide and the reference waveguide, which is supposed to extend on either side (cf. Fig. 3.6(c)). The expressions of these matrices are derived in Appendix C. Here, it is important to note that r_+ can be interpreted (within a phase shift of π) as the reflection coefficient of the equivalent right interface indicated in Fig. 3.17. This is the reflection coefficient which the forward-propagating Bloch mode of the active waveguide ”sees” at the right end. Similarly, r_{-} is (within a phase shift of π) the reflection coefficient of the equivalent left interface. This is the reflection coefficient which the backward-propagating Bloch mode of the active waveguide ”sees” at the left end.

It is instructive to derive the dispersion relation in the limiting case of negligible cross-coupling coefficients. This is the case when the operation frequency is far from the band edge, as evident from Fig. 3.15. For simplicity, we assume that there is no source of refractive index perturbation other than due to carrier density. In this case, by forcing $\kappa_{\mathrm{FB}} = \kappa_{\mathrm{BF}} = 0$ in Eq. (3.25), one finds

$$\beta_{\mathrm{eff}} = k_z - S\Gamma_{\mathrm{FF}}\Gamma_y g_{\mathrm{mat}}\alpha_H/2 \tag{3.28a}$$

$$g_{\mathrm{eff}} = S\Gamma_{\mathrm{FF}}\Gamma_y g_{\mathrm{mat}} \tag{3.28b}$$

These equations represent the dispersion relation in the absence of distributed feedback (DFB). In particular, Eq. (3.28b) describes the conventional slow-light enhancement of modal gain by the slow-down factor [29, 178]. As we show in the following sections, our modelling framework based on Eq. (3.21) is more general, as it takes into account in a self-consistent manner the intrinsic limitation to gain enhancement imposed by the gain itself [41, 19].

We also consider the limiting case of a purely real refractive index perturbation and negligible distributed feedback. In this case, again by forcing $\kappa_{\mathrm{FB}} = \kappa_{\mathrm{BF}} = 0$ in Eq. (3.25), one finds

$$\beta_{\mathrm{eff}} = k_z + (\omega/c)S\Gamma_{\mathrm{FF}}\Delta n_b' \tag{3.29a}$$

$$g_{\mathrm{eff}} = 0 \tag{3.29b}$$

In Sec. 3.4.1, we directly compare these equations against results of MPB simulations and show that the inclusion of cross-coupling is essential to reproduce the stopband induced by the refractive index variation.

3.4.1 Real refractive index perturbation

We start by considering a purely real refractive index perturbation $\Delta n_b'$, thus assuming $n_i = \Delta n_b'' = 0$ (see Eq. (3.19)). In this case, we can compare the effective propagation constant from Eq. (3.24a) with that computed by MPB in the case of the slab refractive index being $n_{\mathrm{slab}} + \Delta n_b'$. As an example, we assume the refractive index perturbation to be homogeneous throughout the slab, as in [137]. This implies that $\Gamma_{\mathrm{FF}}^{\mathrm{index}}$ and $\Gamma_{\mathrm{FB}}^{\mathrm{index}}$ in Eq. (3.19) coincide with those shown in Fig. 3.15(a).

Fig. 3.18(a) shows the dispersion relation versus frequency computed by MPB for $n_{\mathrm{slab}} = 3.17$ (black) and $n_{\mathrm{slab}} = 3.17 + \Delta n_b'$, with $\Delta n_b' = -10^{-3}$ (dotted, blue). As the

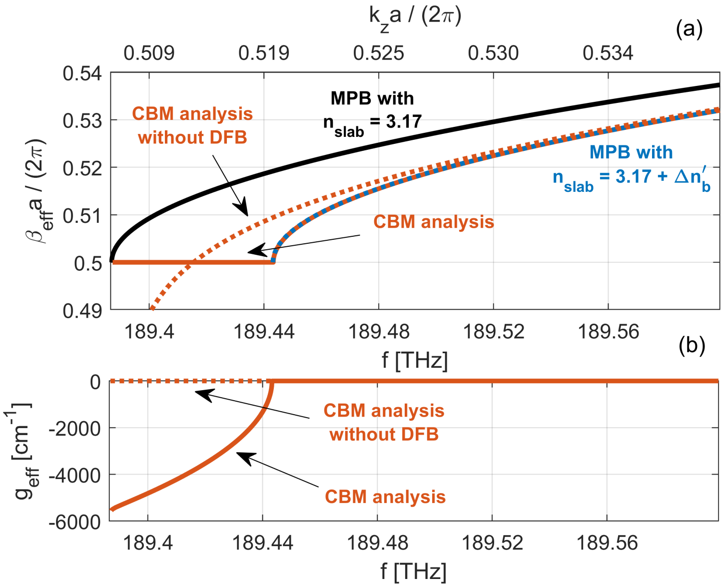

Figure 3.18: Comparison between CBM analysis and MPB in the case of a purely real refractive index perturbation assumed to be homogeneous throughout the slab. (a) Dispersion relation versus frequency computed by MPB for $n_{\text{slab}} = 3.17$ (black) and $n_{\text{slab}} = 3.17 + \Delta n_b'$, with $\Delta n_b' = -10^{-3}$ (dotted, blue). Normalized effective propagation constant computed by Eq. (3.24a) (solid, red) and Eq. (3.29a) (dotted, red) with $\Delta n_b' = -10^{-3}$. The reference waveguide for the CBM analysis is that with $n_{\text{slab}} = 3.17$. The top x-axis reports the normalized wavenumber of this reference waveguide. (b) Effective gain computed by Eq. (3.24b) (solid, red) and Eq. (3.29b) (dotted, red) with $\Delta n_b' = -10^{-3}$.

slab refractive index decreases, the band edge shifts to higher frequencies. This shift is fully captured by our modelling framework with inclusion of the distributed feedback, that is Eq. (3.24a) (solid, red). This is clearly not the case if the distributed feedback is neglected, i.e. Eq. (3.29a) is used (dotted, red). The band edge shift is accompanied by the formation of a stopband. Throughtout this stopband, β_{eff} is equal to π/a, while g_{eff} is negative, signifying that the Bloch modes are *evanescent*. This is outlined by Fig. 3.18(b), which illustrates g_{eff} computed by Eq. (3.24b) (solid, red). On the contrary, Eq. (3.29b), which neglects the distributed feedback, predicts that g_{eff} is identically equal to zero (dotted, red). We note that MPB does not provide the imaginary part of the wavenumber (i.e. g_{eff}) because it solves Maxwell's equations as an eigenproblem by treating the *frequency* as the eigenvalue (see Sec. 2.2.1 in Chapter 2). In other terms, the wavenumber is assumed to be real and the frequency range where no solution is found (i.e. the photonic bandgap) corresponds to the wavenumber being complex and the Bloch modes being evanescent. Therefore, g_{eff} has to be negative within the stopband induced by the refractive index perturbation, where no solution is found by MPB. Overall, this example emphasizes the importance of the distributed feedback in the slow-light region and supports the goodness of our modelling framework.

3.4.2 Complex refractive index perturbation

As a second step, in addition to the real refractive index perturbation, we consider the presence of material gain. Similarly to Sec. 3.4.1, we assume both the refractive index perturbation and material gain to be homogeneous throughout the slab. For simplicity, the linewidth enhancement factor is assumed to be zero. Unless otherwise specified, the distributed feedback is taken into account.

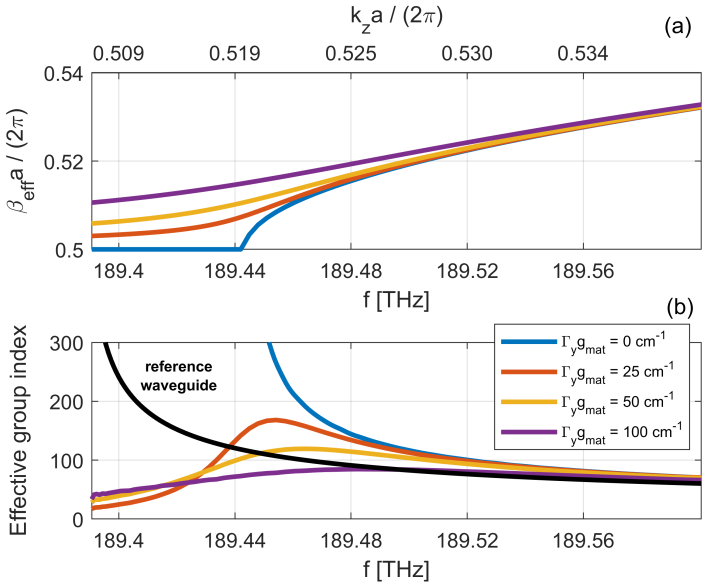

Figure 3.19: (a) Normalized effective propagation constant and (b) effective group index in the case of a complex refractive index perturbation assumed to be homogeneous throughout the slab. Each colour corresponds to a given value of the modal gain $\Gamma_y g_{\text{mat}}$, as indicated by the legend in (b). The black line is the group index of the reference waveguide. The real refractive index perturbation is $\Delta n_b' = -10^{-3}$ and the linewidth enhancement factor is assumed to be zero. The top x-axis reports the normalized wavenumber of the reference waveguide.

Fig. 3.19 shows (a) the normalized effective propagation constant and (b) effective group index versus frequency. The effective group index is defined as $c(d\beta_{\text{eff}}/d\omega)$, with c being the vacuum light speed. Each colour denotes a given value of the modal gain $\Gamma_y g_{\text{mat}}$, as indicated by the legend in (b). The black line is instead the group index of the reference waveguide. The real refractive index perturbation is $\Delta n_b' = -10^{-3}$ as in

Sec. 3.4.1. The top x-axis reports the normalized wavenumber of the reference waveguide. In the absence of gain, the effective group index diverges at the frequency to which the band edge has been shifted by the refractive index perturbation. However, as the gain grows, the slope of the effective propagation constant with respect to frequency steeply diminishes close to the band edge. Consequently, the group index is strongly reduced and gradually broadens over frequency. This reduction and spectral broadening of the group index induced by material gain is consistent with predictions of non-perturbative approaches [41] and supports the effectiveness of our modelling framework.

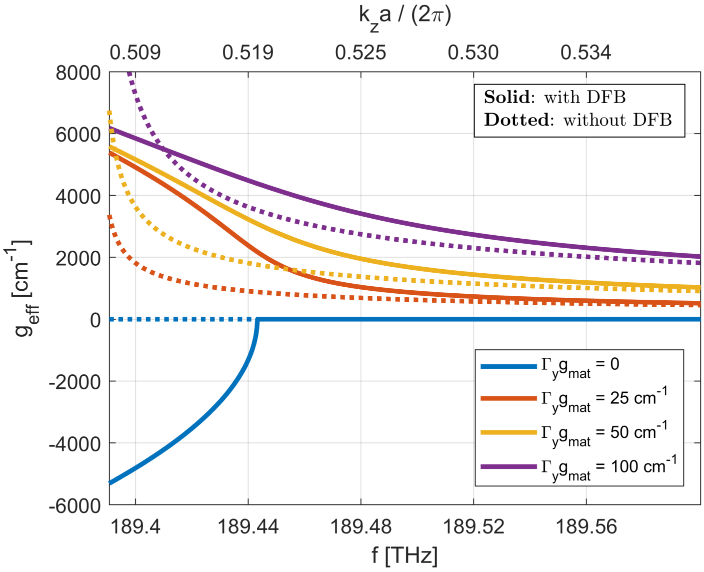

Figure 3.20: Effective gain with distributed feedback (solid) and without it (dotted) in the case of a complex refractive index perturbation assumed to be homogeneous throughout the slab. Each colour corresponds to a given value of the modal gain $\Gamma_y g_{\text{mat}}$, as indicated by the legend. The real refractive index perturbation is $\Delta n_b' = -10^{-3}$ and the linewidth enhancement factor is assumed to be zero. The top x-axis reports the normalized wavenumber of the reference waveguide.

Fig. 3.20 shows the effective gain computed by taking into account the distributed feedback (solid) and neglecting it (dotted). The latter corresponds to forcing $\kappa_{\text{FB}} = \kappa_{\text{BF}} = 0$ in Eq. (3.24b), which results in Eq. (3.28b). This equation predicts the conventional gain enhancement in direct proportion to the group index of the reference waveguide (that is the black line in Fig. 3.19(b)). If the modal gain $\Gamma_y g_{\text{mat}}$ is greater than zero, a frequency range exists, in dependence of the modal gain, where the effective gain is significantly larger with the distributed feedback taken into account. We may provide an *intuitive* interpretation for this feature. Essentially, the refractive index perturbation pushes to higher frequencies the band edge and, concurrently, the slow-light enhancement of gain. By this line of reasoning, one might be tempted to think that the effective gain, at a given value of the modal gain $\Gamma_y g_{\mathrm{mat}}$, is enhanced in direct proportion to the effective group index. However, this is *not* actually the case, as a comparison of Fig. 3.19(b) and Fig. 3.20 clearly reveals. Therefore, we highlight that the impact of a complex refractive index perturbation on the effective gain is more intricate than a simple scaling by the effective group index. Instead, it should be taken into account through Eq. (3.24b). As a measure of the enhancement of the effective gain with respect to the modal gain $\Gamma_y g_{\mathrm{mat}}$, we report their ratio in Fig. 3.21. The ratio is computed at $k_z a/(2\pi) = 0.5195$, that is around the band edge of the active waveguide (see Fig. 3.19(a)). As the modal gain grows, the ratio steeply decreases, emphasizing that the slow-light enhancement of gain is intrinsically limited by the gain itself. Again, this result is consistent with predictions of non-perturbative approaches [41]. However, as compared to [41], in Sec. 3.5 we demonstrate that the effective gain is *not* an exhaustive figure of merit. In fact, a larger effective gain does *not* necessarily imply more transmitted power.

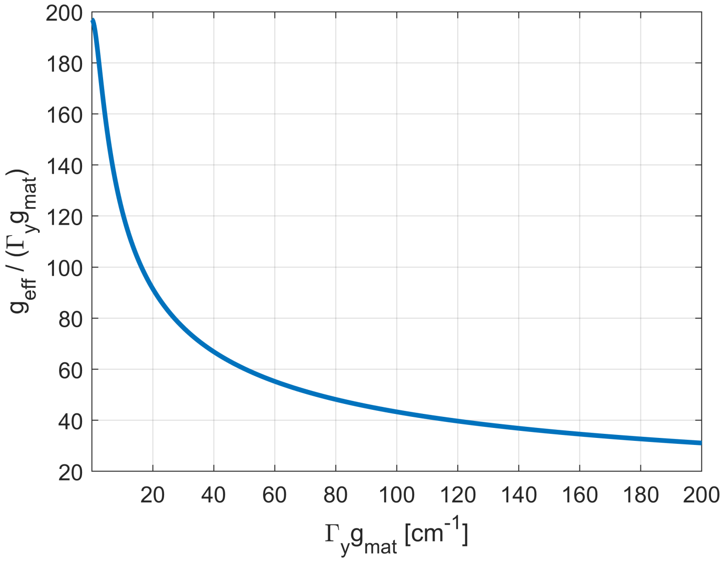

Figure 3.21: Ratio between the effective gain and the modal gain $\Gamma_y g_{\mathrm{mat}}$ in the case of a complex refractive index perturbation assumed to be homogeneous throughout the slab. The real refractive index perturbation is $\Delta n_b' = -10^{-3}$ and the linewidth enhancement factor is assumed to be zero. The ratio is evaluated at $k_z a/(2\pi) = 0.5195$, that is around the band edge of the active waveguide.

It is also instructive to examine the reflection coefficients $r_\pm$ from Eqs. (3.26a) and (3.26b). Fig. 3.22 shows their magnitude. In the absence of gain, the magnitude is unitary within the stopband. In Sec. 3.5, we directly relate this feature to the power flowing

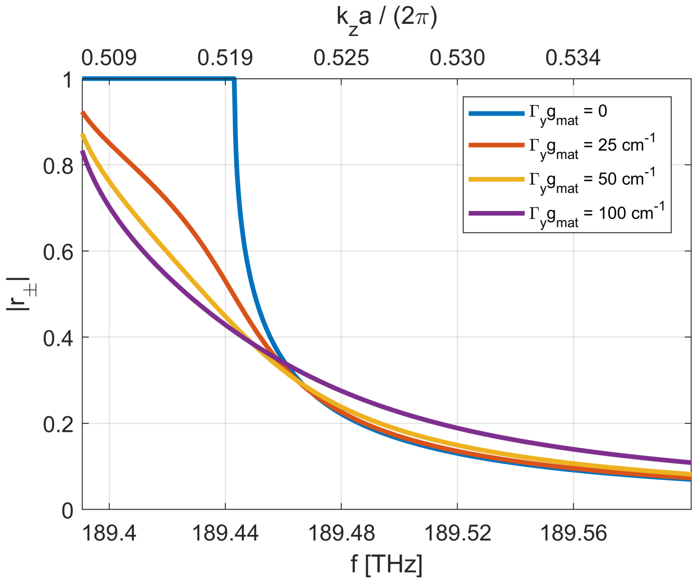

Figure 3.22: Magnitude of the reflection coefficients $r_\pm$ in the case of a complex refractive index perturbation assumed to be homogeneous throughout the slab. Each colour corresponds to a given value of the modal gain $\Gamma_y g_{\text{mat}}$, as indicated by the legend. The real refractive index perturbation is $\Delta n'_b = -10^{-3}$ and the linewidth enhancement factor is assumed to be zero. The top x-axis reports the normalized wavenumber of the reference waveguide.

along the waveguide. If the frequency is detuned from the stopband, the magnitude of $r_\pm$ steeply decreases, because the distributed feedback becomes increasingly less effective. This is due to the smaller cross-coupling coefficients, as well as the larger detuning δ. This feature suggests that, under these conditions, the impact of the equivalent interfaces in Fig. 3.17 may be neglected. As the modal gain grows, the magnitude of $r_\pm$ decreases within the stopband and only slightly increases at higher frequencies, where the impact of the distributed feedback remains limited.

As a final example, we discuss the impact of the linewidth enhancement factor α_H. For this purpose, we assume $\Delta n'_b = 0$, such that the only perturbation is that induced by carrier density. Similarly to the previous examples, we assume the perturbation to be homogeneous throughout the slab. Fig. 3.23 shows (a) the normalized effective propagation constant and (b) effective gain with the modal gain $\Gamma_y g_{\text{mat}}$ being $50\,\text{cm}^{-1}$. The linewidth enhancement factor is 0 (blue), 1.5 (red) and 3 (yellow). As α_H increases, so does the magnitude of the real refractive index perturbation $\Delta n''_b$ induced by carrier density. Therefore, the band edge shifts to higher frequencies, as $\Delta n''_b$ becomes more and more negative. Concurrently, the effective gain g_{eff} at a given frequency increases, because the slow-light enhancement of gain is pushed to higher frequencies. We explore the implications of these features in Sec. 4.4, when analyzing the oscillation condition

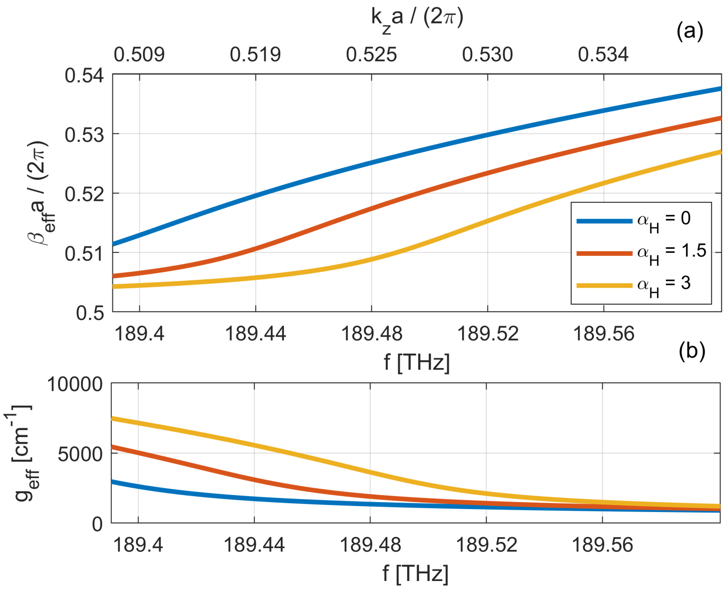

Figure 3.23: (a) Normalized effective propagation constant and (b) effective gain with the modal gain $\Gamma_y g_{\text{mat}}$ being 50 cm^{-1} and the linewidth enhancement factor α_H equal to 0 (blue), 1.5 (red) and 3 (yellow). The perturbation is assumed to homogeneous throughout the slab and the real refractive index perturbation $\Delta n_b'$ is equal to zero. The top x-axis in (a) reports the normalized wavenumber of the reference waveguide.

of photonic crystal lasers with photonic bandgap mirrors.

However, the linewidth enhancement factor not only enhances the effective gain, but it also results in a larger mismatch at the equivalent interfaces in Fig. 3.17. This is outlined by Fig. 3.24, showing the magnitude of the reflection coefficients $r_\pm$. The modal gain $\Gamma_y g_{\text{mat}}$ is 50 cm^{-1} and α_H is equal to 0 (blue), 1.5 (red) and 3 (yellow). As α_H increases, the magnitude of the cross-coupling coefficients grows. Consequently, in compliance with Eqs. (3.26a) and (3.26b), the magnitude of $r_\pm$ at a given frequency increases as well. The implications of this enhanced distributed feedback induced by the linewidth enhancement factor are discussed in Sec. 3.6, dealing with slow-light optical amplification.

We may also consider the complex refractive index perturbation to be spatially limited to the line-defect, as in waveguides with a BH active region. In this case, we have only found a minor, quantitative change of the results. This is because the dispersion relation and reflection coefficients $r_\pm$ are essentially controlled by the relative strength of the normalized cross-coupling coefficient Γ_{FB} as compared to the normalized self-coupling coefficient Γ_{FF}. As evidenced by Fig. 3.15, this relative strength is similar if the perturbation is assumed to be homogeneous throughout the slab (Fig. 3.15(a)) or limited to the line-defect (Fig. 3.15(b)). Therefore, the considerations which we have made on the dispersion relation and reflection coefficients $r_\pm$ equally apply to both cases.

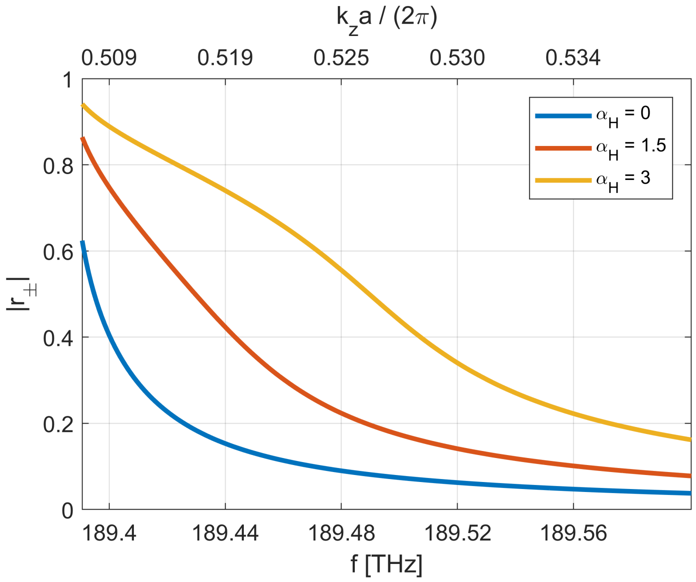

Figure 3.24: Magnitude of the reflection coefficients $r_{\pm}$ with the modal gain $\Gamma_y g_{\text{mat}}$ being $50\,\text{cm}^{-1}$ and the linewidth enhancement factor α_H equal to 0 (blue), 1.5 (red) and 3 (yellow). The perturbation is assumed to homogeneous throughout the slab and the real refractive index perturbation $\Delta n_b'$ is equal to zero. The top x-axis reports the normalized wavenumber of the reference waveguide.

3.5 Optical propagation and power flow

In this section, we focus on the optical propagation and power flow, which we derive in detail in Appendix B. In the following, we recall the main expressions. Furthermore, we recall from Appendix C the scattering matrix by which optical propagation may be described.

The amplitudes $c_{\pm}(z)$ (see Eq. (3.2)) can be conveniently expressed as

$$c_+(z) = e^{+i\frac{\pi}{a}z}\left(\tilde{F}e^{+i\lambda_+ z} + r_-\tilde{B}e^{-i\lambda_+ z}\right) \tag{3.30a}$$

$$c_-(z) = e^{-i\frac{\pi}{a}z}\left(r_+\tilde{F}e^{+i\lambda_+ z} + \tilde{B}e^{-i\lambda_+ z}\right) \tag{3.30b}$$

with the amplitudes $\tilde{F}$ and $\tilde{B}$ depending on the boundary conditions. The *net* power flow $P(z)$ at position z may be expressed in two equivalent manners. The first expressions is

$$P(z) = \underbrace{|c_+(z)|^2 P_0}_{P_+(z)} - \underbrace{|c_-(z)|^2 P_0}_{P_-(z)} \tag{3.31}$$

where P_0 is the power carried by the forward-propagating Bloch mode of the reference waveguide

$$P_0 = \frac{v_g}{2a}\int_V \epsilon_0 n_b^2(\mathbf{r})|\mathbf{e}_+(\mathbf{r})|^2\, dV \tag{3.32}$$

with v_g being the group velocity. In Eq. (3.31), the forward- (P_+) and backward-propagating power (P_-) are coupled and generally *not* monotonic with position z. Importantly, they are proportional to the squared magnitude of the amplitudes $c_\pm(z)$.

As an alternative, by inserting Eqs. (3.30a) and (3.30b) into Eq. (3.31), we may equivalently express the net power flow as

$$P(z) = \tilde{P}_+(z) - \tilde{P}_-(z) + \tilde{P}_{\text{cross}}(z) \tag{3.33}$$

The first two contribution are the forward- (+) and backward-propagating power (−) of the Bloch modes of the *perturbed* waveguide

$$\tilde{P}_+(z) = |\tilde{F}|^2 e^{g_{\text{eff}} z} \left(1 - |r_+|^2\right) P_0 \tag{3.34a}$$

$$\tilde{P}_-(z) = |\tilde{B}|^2 e^{-g_{\text{eff}} z} \left(1 - |r_-|^2\right) P_0 \tag{3.34b}$$

These contributions are obviously monotonic with position z and exponentially increase with the effective net modal gain g_{eff}. However, they are also scaled down by the factor $(1 - |r_\pm|^2)$. Depending on $r_\pm$, this factor might even be zero (see Fig. 3.22). The third contribution is the cross power

$$\tilde{P}_{\text{cross}}(z) = 2\text{Re}\left\{ \tilde{F}\tilde{B}^* e^{2i\beta_{\text{eff}} z} e^{-i\frac{2\pi}{a} z} (r_-^* - r_+) \right\} P_0 \tag{3.35}$$

This contribution is *periodic* with position z. The spatial period is equal to π/δ_{eff}, with the effective detuning δ_{eff} being

$$\delta_{\text{eff}} = \frac{\pi}{a} - \beta_{\text{eff}} \tag{3.36}$$

The cross power arises because the Bloch modes of the perturbed waveguide are generally *not* power orthogonal (see Sec. B.3.2 in Appendix B). In addition, in dependence of $r_\pm$, the cross power is not necessarily negligible as compared to the other two contributions. The important insight of Eq. (3.33) is that a larger g_{eff} does *not* necessarily imply more power. In fact, the impact of the reflection coefficients $r_\pm$, as well as the cross power, should be also taken into account, as we show in the following.

Finally, we recall from Appendix C that the amplitudes $c_\pm$ of the Bloch modes entering and exiting the perturbed waveguide may be related by the scattering matrix $\underline{\underline{S}}$, that is

$$\begin{bmatrix} c_-(0) \\ c_+(L) \end{bmatrix} = \underline{\underline{S}} \begin{bmatrix} c_+(0) \\ c_-(L) \end{bmatrix} \tag{3.37}$$

Here, $z = 0$ ($z = L$) is the input (output) of the perturbed waveguide. The elements of the scattering matrix are [139]

$$S_{11} = \frac{-\left(e^{+2i\lambda_+ L} - 1\right) r_+}{1 - r_+ r_- e^{+2i\lambda_+ L}} e^{-i\frac{2\pi}{a}L} \tag{3.38a}$$

$$S_{12} = S_{21} = \frac{(1 - r_+ r_-) e^{+i\lambda_+ L}}{1 - r_+ r_- e^{+2i\lambda_+ L}} e^{+i\frac{\pi}{a}L} \tag{3.38b}$$

$$S_{22} = \frac{-\left(e^{+2i\lambda_+ L} - 1\right) r_-}{1 - r_+ r_- e^{+2i\lambda_+ L}} e^{+i\frac{2\pi}{a}L} \tag{3.38c}$$

The squared magnitude of S_{12} (or S_{21}) represents the power transmitted to one end normalized to the power injected from the other side. Similarly, the squared magnitude of S_{11} (S_{22}) is the power reflected at the input (output) normalized to the power injected from the input (output).

3.5.1 Distributed feedback effects

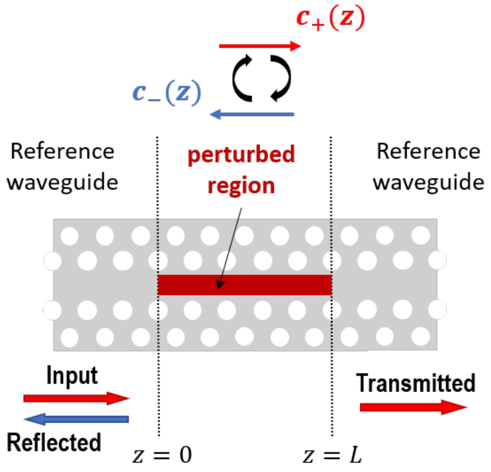

Figure 3.25: Illustration of coupling between the amplitudes of the forward- and backward-propagating Bloch modes of a reference waveguide induced by a complex refractive index perturbation in a region of length L.

In the following, we consider a typical scattering experiment, illustrated by Fig. 3.25. A region of length L of the reference waveguide, denoted as ”perturbed region”, contains a complex refractive index perturbation. The input power is injected from the left-hand side, at $z = 0$. The perturbation induces coupling between the amplitudes of the forward- and backward-propagating Bloch modes of the reference waveguide. As a result, the input power is partly transmitted at $z = L$ (undergoing amplification, if the perturbed region provides optical gain) and partly reflected back at $z = 0$. We assume the perturbation to be limited to the line-defect, as in waveguides with a BH active region. This experiment corresponds to the boundary conditions

$$c_+(z=0) = c_{0_+} \tag{3.39a}$$

$$c_-(z=L) = 0 \tag{3.39b}$$

By applying these conditions to Eqs. (3.30a) and (3.30b), one finds

$$\tilde{F} = \frac{c_{0_+}}{1 - r_+ r_- e^{+2i\lambda_+ L}} \tag{3.40a}$$

$$\tilde{B} = \frac{-r_+ c_{0_+} e^{+2i\lambda_+ L}}{1 - r_+ r_- e^{+2i\lambda_+ L}} \tag{3.40b}$$

We may directly relate c_{0_+} to the input power $P_{\text{in}} = P_+(z=0)$. In this case, from Eq. (3.31) we obtain

$$|c_{0_+}| = \sqrt{\frac{P_{\text{in}}}{P_0}} \tag{3.41}$$

Here, we note that the constraint on the input power does not fix the phase of c_{0_+} (that is, the phase of the forward-propagating field at the waveguide input). For simplicity, we assume this phase to be zero.

In the following, we investigate the spatial evolution of the forward- and backward-propagating power from Eq. (3.31) under various circumstances. By using Eqs. (3.30a) and (3.30b), one finds

$$|c_+(z)|^2 = |\tilde{F}|^2 e^{g_{\text{eff}} z} + |r_-|^2 |\tilde{B}|^2 e^{-g_{\text{eff}} z} + 2\text{Re}\left\{\tilde{F}\tilde{B}^* r_-^* e^{-2i\delta_{\text{eff}} z}\right\} \tag{3.42a}$$

$$|c_-(z)|^2 = |r_+|^2 |\tilde{F}|^2 e^{g_{\text{eff}} z} + |\tilde{B}|^2 e^{-g_{\text{eff}} z} + 2\text{Re}\left\{\tilde{F}\tilde{B}^* r_+ e^{-2i\delta_{\text{eff}} z}\right\} \tag{3.42b}$$

The forward- and backward-propagating power may undergo spatial oscillations, with a period given by π/δ_{eff} (see Eq. (3.36)). This spatial period depends not only on the frequency, but also on the perturbation itself, as governed by the effective propagation constant. The oscillations originate from the beating of the forward- and backward-propagating Bloch modes of the active waveguide.

Real refractive index perturbation

We start by considering a purely real refractive index perturbation $\Delta n_b' = -10^{-3}$ in a region of length $L = 20a$. Fig. 3.26 shows the forward-propagating (blue), backward-propagating (red) and net (black) power flow computed by Eq.(3.31). They are reported in units of the input power P_{in}. As discussed in Sec. 3.4.1, the perturbation leads to the formation of a stopband. The frequency to which the plots refer corresponds to $k_z a/(2\pi) = 0.51$ and lies right within the stopband, where the Bloch modes are evanescent. As a result, the forward (backward) power exponentially decays (grows) in the

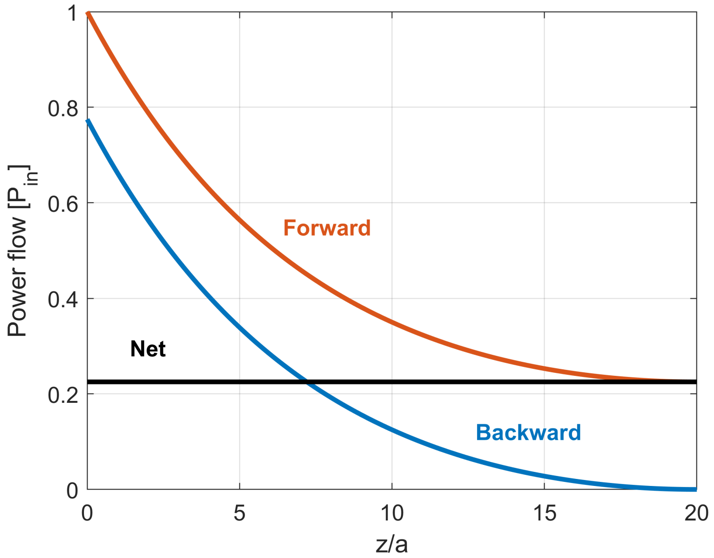

Figure 3.26: Forward-propagating (blue), backward-propagating (red) and net (black) power flow computed by Eq. (3.31) in the case of a purely real refractive index perturbatio. The perturbation is $\Delta n_b' = -10^{-3}$ and is limited to the line-defect. The frequency corresponds to $k_z a/(2\pi) = 0.51$ and lies within the stopband induced by the perturbation. The length of the perturbed waveguide is $L = 20a$. The power flows are in units of the input power P_{in}.

positive (negative) z-direction. Since there is neither gain, nor loss, the forward power diminishes by exactly the same amount by which the backward power grows. Furthermore, the net power entering the waveguide at $z = 0$ is conserved all along the perturbed region, as expected. On this regard, it should be emphasized that this net power is exactly equal to the cross power from Eq. (3.35). In fact, since the magnitude of $r_\pm$ is unitary within the stopband (see Fig. 3.22), the two power contributions from Eqs. (3.34a) and (3.34b) are identically equal to zero, irrespective of g_{eff}. On the other hand, β_{eff} is equal to π/a within the stopband, which results in the cross power being constant with z. This example highlights the physical meaning of the stopband and the important role of the cross power from Eq. (3.35). Furthermore, we notice that the forward- and backward-propagating power do not oscillate in space. In fact, $\beta_{\text{eff}} = \pi/a$ leads to $\delta_{\text{eff}} = 0$.

It is also instructive to inspect the transmistted power as a function of frequency. The left axis in Fig. 3.27 shows the power transmission $|S_{21}|^2$ computed by Eq. (3.38b). The perturbation and length of the perturbed waveguide are the same as in Fig. 3.26. The right axis displays the effective propagation constant normalized to π/L. As the frequency approaches the stopband, the power transmission steeply drops, due to the

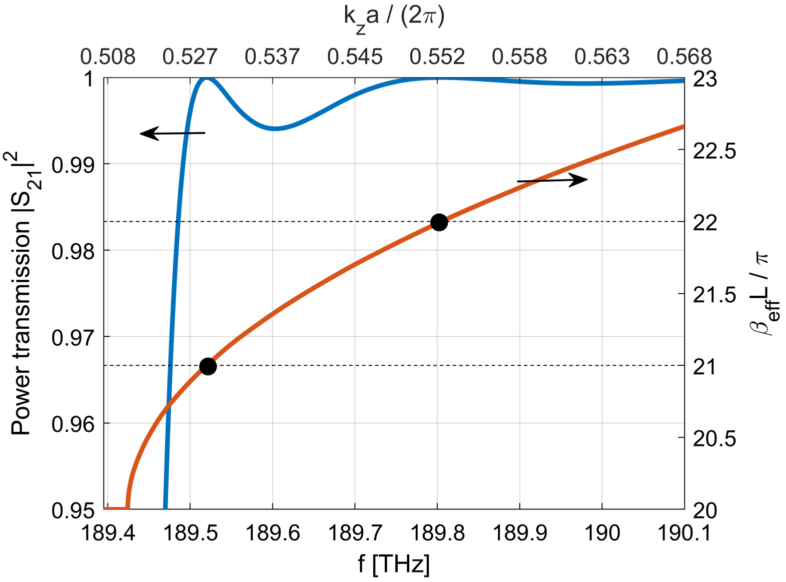

Figure 3.27: Power transmission (left) and effective propagation constant normalized to π/L (right) versus frequency in the case of a purely real refractive index perturbation. The perturbation is $\Delta n_b' = -10^{-3}$ and is limited to the line-defect. The length of the perturbed waveguide is $L = 20a$. The black bullets correspond to frequencies where complete transmission is achieved, with the dashed, black lines being guides to the eye. The top x-axis reports the normalized wavenumber of the reference waveguide.

build-up of a huge reflection. On the other hand, at high frequencies, the power transmission is large, owing to the negligible interaction between the forward and backward wave. At certain frequencies, even complete transmission is achieved. The usage of the Bloch modes as a basis provides a compact expression for these frequencies. They are those for which $\beta_{\mathrm{eff}}L/\pi$ is an integer, as evidenced by the black bullets in Fig. 3.27. In one-dimensional dielectric layered media, this relation between the Bloch modes propagation constant and frequencies of complete transmission is a well-known phenomenon and can be understood as a form of tunnelling [140].

Complex refractive index perturbation

In the following, we consider a complex refractive index perturbation, to elucidate the role of the effective gain in the presence of material gain. To emphasize the distributed feedback effects, we assume the length of the perturbed region in Fig. 3.25 to be 100 lattice constants.

We start by assuming $\Delta n_b' = -10^{-3}$, as well as the presence of material gain. The linewidth enhancement factor is assumed to be zero. Fig. 3.28 shows (a) the forward- and (b) backward-propagating power computed by Eq. (3.31). The modal gain $\Gamma_y g_{\mathrm{mat}}$

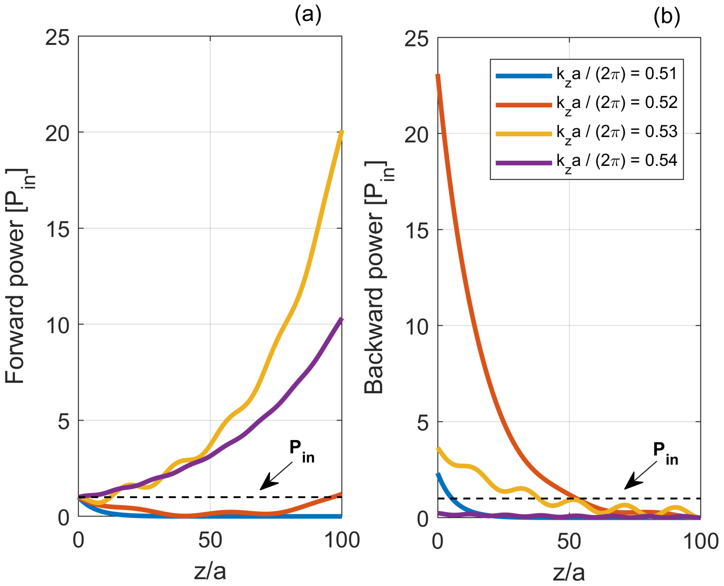

Figure 3.28: (a) Forward- and (b) backward-propagating power computed by Eq. (3.31) in the case of a complex refractive index perturbation limited to the line-defect. The real refractive perturbation is $\Delta n'_b = -10^{-3}$, while the modal gain $\Gamma_y g_{\text{mat}}$ is $50\,\text{cm}^{-1}$. The linewidth enhancement factor is assumed to be zero. The frequency corresponds to the normalized wavenumber $k_z a/(2\pi)$ being 0.51 (blue), 0.52 (red), 0.53 (yellow) and 0.54 (purple), as indicated by the legend in (b). The dashed, black line denotes the level of the input power P_{in}. The length of the perturbed waveguide is $L = 100a$. The power flows are in units of the input power P_{in}.

is $50\,\text{cm}^{-1}$. The frequency corresponds to the normalized wavenumber $k_z a/(2\pi)$ being 0.51 (blue), 0.52 (red), 0.53 (yellow) and 0.54 (purple), as denoted by the legend in (b). The dashed, black line indicates the level of the injected power P_{in}. A number of features can be noted. At $k_z a/(2\pi) = 0.51$, the forward power exponentially decays from P_{in} down to zero, although the modal gain is positive. This signifies that the input power is completely and steeply transferred from the forward to the backward wave by the strong distributed feedback, which by far outweighs the optical amplification. We emphasize that this power transfer occurs in spite of the effective gain g_{eff} being positive (see Fig. 3.20). Therefore, this is another, clear indication of the fact that the effective gain is *not* an exhaustive figure of merit of optical amplification, as already mentioned. On the other hand, the backward power exponentially grows in the negative z direction, rising above P_{in} close to waveguide input. This means that the backward wave is also amplified by the positive modal gain, as well as being fed by the forward wave. At $k_z a/(2\pi) = 0.52$, the forward power is not monotonic with z, indicating a trade-off between the optical amplification and transfer of power from the forward to the backward wave. As compared to the case with $k_z a/(2\pi) = 0.51$, the backward power is strongly enhanced, just because the forward wave undergoes amplification while transferring power. As k_z is further detuned from the band edge, the interaction between the forward and backward wave gradually dies out. At $k_z a/(2\pi) = 0.53$, the optical amplification prevails over the distributed feedback, since the forward power at $z = L$ (that is the transmitted power) is larger than the backward power at $z = 0$ (that is the reflected power). At $k_z a/(2\pi) = 0.54$, the forward wave propagates almost undisturbed, since the backward power remains well below the input power P_{in}. Overall, this example outlines the impact of distributed feedback effects on the optical propagation in active photonic crystal waveguides. Furthermore, it clearly demonstrates that a larger effective gain g_{eff} does *not* necessarily imply more transmitted power. In fact, g_{eff} at a positive value of modal gain monotonically decreases as k_z is detuned from the band edge (see Fig. 3.20). Nevertheless, the transmitted power does not follow this trend, as evidenced by Fig. 3.28(a) at $z = L$.

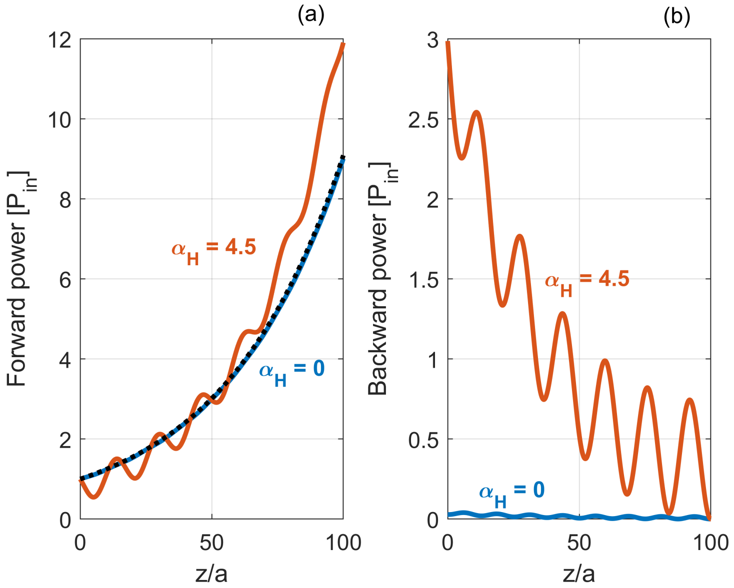

Figure 3.29: (a) Forward- and (b) backward-propagating power computed by Eq. (3.31) with the linewidth enhancement factor α_H being 0 (blue) and 4.5 (red). The modal gain $\Gamma_y g_{\mathrm{mat}}$ is $50\,\mathrm{cm}^{-1}$ and the frequency corresponds to $k_z a/(2\pi) = 0.54$. The black, dotted line in (a) is the forward power with the cross-coupling coefficients forced to zero. The perturbation is assumed to be limited to the line-defect. The length of the perturbed waveguide is $L = 100a$. The power flows are in units of the input power P_{in}.

As a second example, we assume $\Delta n_b' = 0$ and consider the impact of the linewidth enhancement factor α_H. Fig. 3.29 shows (a) the forward- and (b) backward-propagating power computed by Eq. (3.31) with α_H set to 0 (blue) and 4.5 (red). The black, dotted line in (a) is the forward power in the absence of distributed feedback, i.e. with the cross-coupling coefficients forced to zero. The modal gain is $\Gamma_y g_{\mathrm{mat}} = 50\,\mathrm{cm}^{-1}$ and the normalized wavenumber $k_z a/(2\pi) = 0.54$. For $\alpha_H = 0$, the interaction between the forward and backward wave is negligible, as the frequency is sufficiently detuned from the band edge. Therefore, the forward power practically coincides with that computed in the absence of distributed feedback. On this regard, we note that the forward power without distributed feedback is independent of α_H. In fact, between β_{eff} and g_{eff}, only the former depends on α_H (see Eqs.(3.28a) and (3.28b)). Furthermore, since the cross-coupling coefficients are forced to zero, one finds $r_\pm = 0$, resulting in the power $P(z)$ being independent of α_H (as evident from Eq. (3.33)). As the linewidth enhancement factor increases, so does the magnitude of the associated real refractive index perturbation $\Delta n_b''$. Therefore, for $\alpha_H = 4.5$ the distributed feedback is stronger, as evidenced by the oscillations in the forward and backward power in Fig. 3.29, as well as the much larger reflected power. In particular, we note that the transmitted power is enhanced by the larger α_H (see Fig. 3.29(a) at $z = L$), but the relative increase in the reflected power is much higher (see Fig. 3.29(b) at $z = 0$). This important feature stems from the impact of the linewidth enhancement factor on the dispersion relation, discussed in Sec. 3.4.2. In particular, a larger α_H not only makes the effective gain increase (see Fig. 3.23(b)), but it also enhances the magnitude of the reflection coefficients $r_\pm$ (see Fig. 3.24), thus boosting the distributed feedback. The implications are explored in Sec. 3.6.

3.6 Slow-light optical amplification

In this section, we investigate in detail the impact of slow-light on the reflection and transmission properties of active photonic crystal waveguides [139]. Owing to the slow-light enhancement of the gain coefficient, these waveguides are viewed as promising candidates for compact semiconductor optical amplifiers (SOAs) [97, 29]. Our analysis is restricted to the linear regime, i.e. sub-milliwatt power levels [97], appropriate for on-chip interconnects. As compared to previous investigations [97, 18], our modelling framework accounts for the impact of the gain-induced distributed feedback and linewidth enhancement factor. As discussed in Sec. 3.5.1, distributed feedbcak effects are not negligible in the slow-light regime and are further enhanced by the refractive index perturbation induced by carrier density. To focus on the impact of material gain, in the following we neglect any real refractive index perturbation other than due to carrier density, thus assuming $\Delta n_b' = 0$.

To account for the adverse impact of disorder on practical devices, we limit our discussion to modes with group index n_g up to around 60, which have indeed been measured in waveguides with active material [133]. Furthermore, we include the scattering loss through a phenomenological approach, by adding a loss contribution to the self-coupling coefficient, i.e.

$$\kappa_{\text{FF}} = i\left(\frac{\omega}{c}\right) S\left(n_i - i\Delta n_b''\right)\Gamma_{\text{FF}} + \frac{i}{2}\left(\alpha_1 S + \alpha_2 S^2\right) \tag{3.43}$$

where α_1 and α_2 account, respectively, for disorder-induced coupling with radiation modes and backscattering [117]. We assume $\alpha_1 = 5\,\mathrm{cm}^{-1}$ and, for simplicity, $\alpha_2 = 0$, since this effect only gives rise to a minor, quantitative change of the results for realistic [178] values of α_2. We briefly discuss the impact of this parameter in Sec. 3.6.1.

We assume a waveguide with a BH active region and length $L = 100a$, corresponding to 43.8 μm. Furthermore, we consider values of the modal gain $\Gamma_y g_\mathrm{mat}$ not larger than $200\,\mathrm{cm}^{-1}$. As discussed in Appendix A, the optical confinement factor Γ_y is around 4% per active layer. For a typical structure with three active layers, this translates into a maximum material gain around $1600\,\mathrm{cm}^{-1}$, which is reasonable [23]. In the following, the amplifier reflection and gain are computed as the squared magnitude of S_{11} and S_{21} from Eqs. (3.38a) and (3.38b) respectively.

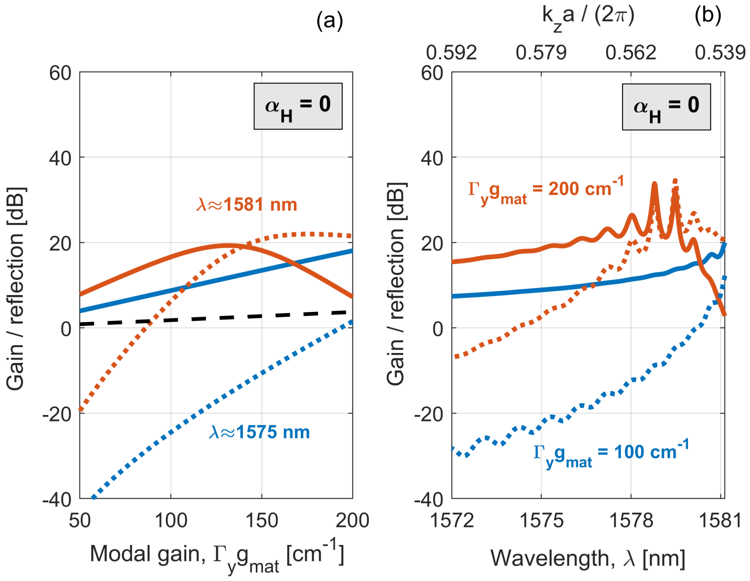

Figure 3.30: Amplifier gain (solid) and reflection (dotted) with $\alpha_H = 0$. They are plotted: (a) versus modal gain, $\Gamma_y g_\mathrm{mat}$, at $\lambda \approx 1575\,\mathrm{nm}$ (blue) and $\lambda \approx 1581\,\mathrm{nm}$ (red); (b) versus wavelength, λ, at $\Gamma_y g_\mathrm{mat} = 100\,\mathrm{cm}^{-1}$ (blue) and $\Gamma_y g_\mathrm{mat} = 200\,\mathrm{cm}^{-1}$ (red). The dashed, black line in (a) is the gain with slow-light effects being neglected.

Fig. 3.30 shows the amplifier gain (solid) and reflection (dotted) with the linewidth enhancement factor α_H set to zero. They are reported versus (a) the modal gain $\Gamma_y g_\mathrm{mat}$ and (b) wavelength λ. The choice $\alpha_H = 0$ reflects an active waveguide with ideal quantum dot layers. Let us focus on Fig. 3.30(a). At $\lambda \approx 1575\,\mathrm{nm}$ (blue), the amplifier gain monotonically increases with the modal gain, while for $\lambda \approx 1581\,\mathrm{nm}$ (red) it achieves a maximum. The appearance of an optimum is explained as resulting from the build-up of a strong reflection. In fact, the closer λ is to the band edge, the stronger the distributed feedback induced by material gain is. This is due to the smaller detuning δ (see Eqs. (3.18a) and (3.18b)), as well as the relative increase of Γ_FB as compared to Γ_{FF} (see Fig. 3.15(b)). As a reference, the amplifier gain with slow-light effects being neglected (i.e. $S = 1$, $\Gamma_{\text{FF}} = 1$ and $\Gamma_{\text{FB}} = 0$) is also shown (dashed, black). Let us now turn our attention to Fig. 3.30(b). In a complementary fashion as compared to Fig. 3.30(a), at $\Gamma_y g_{\text{mat}} = 100\,\text{cm}^{-1}$ (blue) both amplifier gain and reflection increase as the wavelength approaches the band edge, because the slow-down factor grows. However, at $\Gamma_y g_{\text{mat}} = 200\,\text{cm}^{-1}$ (red) the distributed feedback beyond a certain wavelength is large enough to induce a steep decrease in the amplifier gain. These results are consistent with previous investigations [19]. However, as compared to [19] we have elucidated and thoroughly discussed in the previous sections the physics of the gain-induced distributed feedback. Furthermore, we have derived an efficient framework based on Eqs. (3.38a)-(3.38c) to analyze the reflection and transmission properties of active photonic crystal waveguides.

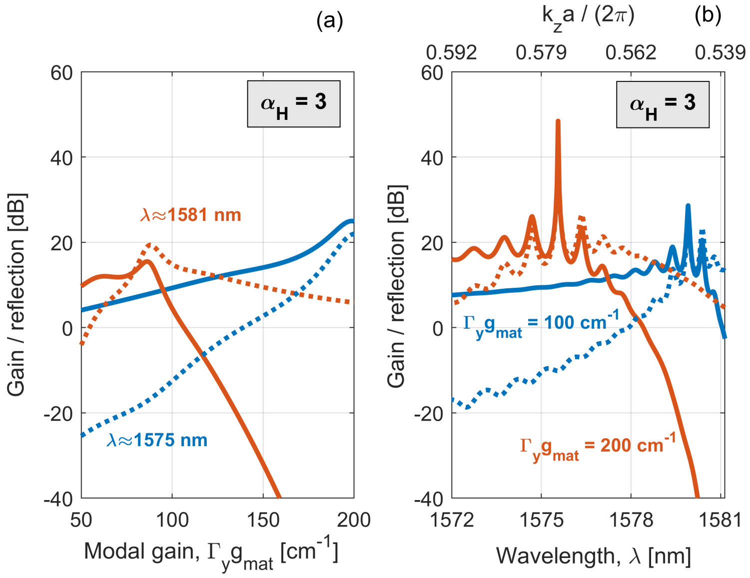

Figure 3.31: Amplifier gain (solid) and reflection (dotted) with $\alpha_H = 3$. They are plotted: (a) versus modal gain, $\Gamma_y g_{\text{mat}}$, at $\lambda \approx 1575\,\text{nm}$ (blue) and $\lambda \approx 1581\,\text{nm}$ (red); (b) versus wavelength, λ, at $\Gamma_y g_{\text{mat}} = 100\,\text{cm}^{-1}$ (blue) and $\Gamma_y g_{\text{mat}} = 200\,\text{cm}^{-1}$ (red).

To explore the impact of the linewidth enhancement factor, in Fig. 3.31 we assume $\alpha_H = 3$, representative of an active waveguide with generic quantum well layers. Again, we report the amplifier gain (solid) and reflection (dotted) versus (a) the modal gain and (b) wavelength. As the modal gain grows (see Fig. 3.31(a)), the band edge shifts to shorter and shorter wavelengths, due to the increasing refractive index perturbation induced by carrier density. Consequently, the amplifier gain at a given wavelength, in dependence of the modal gain, may be slightly enhanced by α_H, as already discussed in relation to Fig. 3.29. However, this enhancement comes at the price of an enhanced reflection, due to the combined effect of gain- and index-induced distributed feedback.

Therefore, the drop in amplifier gain sets in at smaller modal gain values than for $\alpha_H = 0$. Similarly (see Fig. 3.31(b)), it occurs, for a given value of modal gain, at wavelengths more detuned from the band edge. Furthermore, we note that the distributed feedback due to material gain induces strong oscillations in the waveguide transmission and reflection spectra, in a similar fashion as compared to disorder-induced multiple-scattering [91, 123].

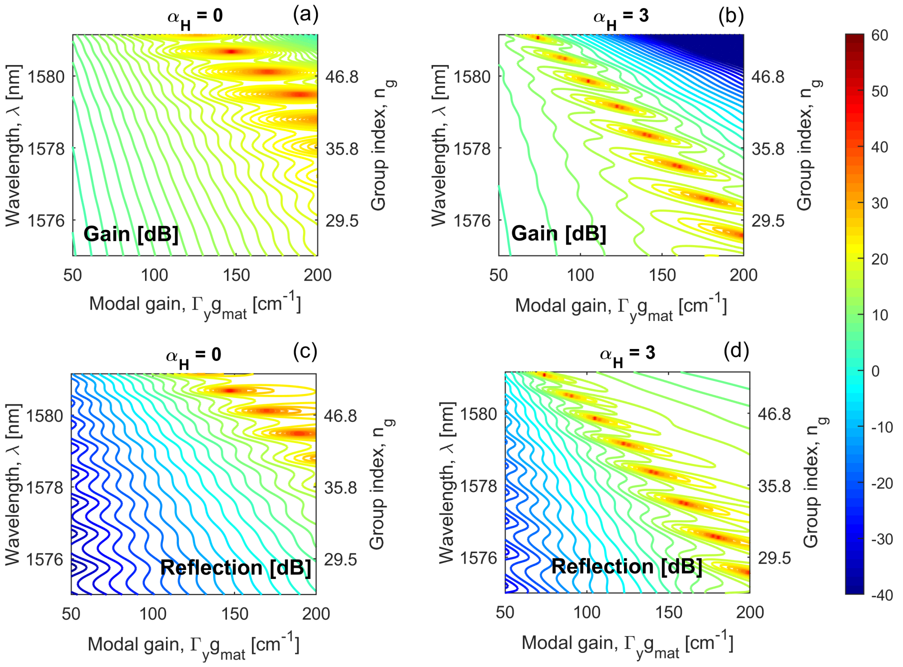

Figure 3.32: (a, b) Amplifier gain and (c, d) reflection with (a, c) $\alpha_H = 0$ and (b, d) $\alpha_H = 3$ versus wavelength, λ, and modal gain, $\Gamma_y g_{\mathrm{mat}}$.

A complete overview is provided by Fig. 3.32, reporting contour plots of (a, b) amplifier gain and (c, d) reflection with (a, c) $\alpha_H = 0$ and (b, d) $\alpha_H = 3$ versus wavelength and modal gain. It is seen that both amplifier gain and reflection diverge for certain combinations of wavelength and modal gain. These points correspond to the poles of the scattering matrix $\underline{\underline{S}}$ (i.e. $r_+ r_- e^{+2i\lambda_+ L} = 1$) and therefore to the onset of lasing, which is genuinely sustained by the *Bloch* modes gain-induced distributed feedback. The peaks corresponding to these poles appear to have finite height in Fig. 3.32 only because of the limited resolution in the wavelength and modal gain. By numerically solving the equation $r_+ r_- e^{+2i\lambda_+ L} = 1$, we have verified that these peaks do correspond to combinations of wavelength and modal gain for which lasing is achieved. In Sec. 4.4.2, we further discuss this feedback-sustained lasing.

The quantification of a maximum amplifier gain depends on the acceptable level of reflection, which varies with the application. As an example, Fig. 3.33 illustrates the gain corresponding to the reflection being smaller than −20 dB. The LEF is (a) $\alpha_H = 0$,

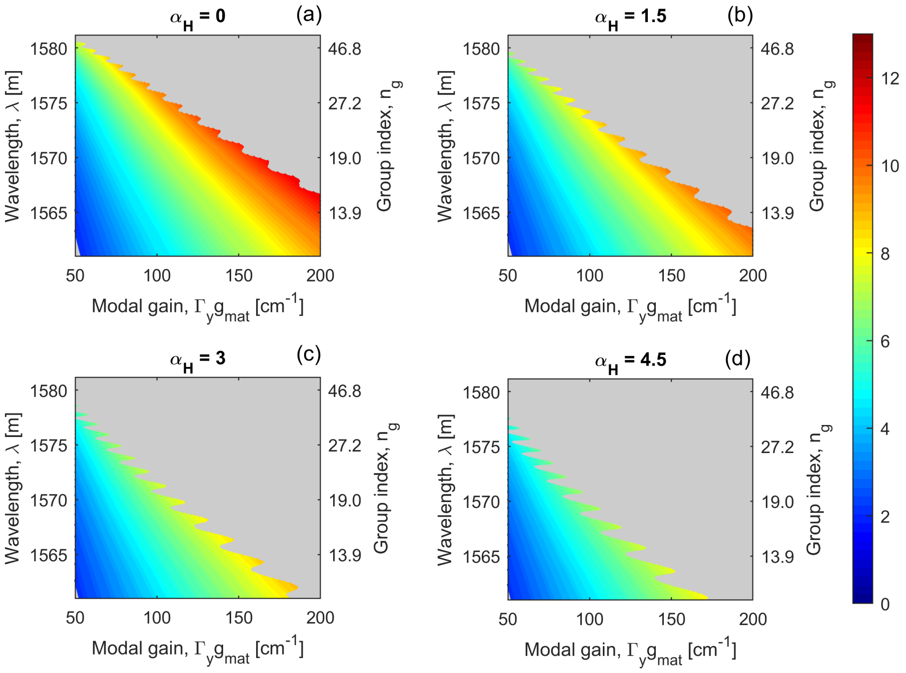

Figure 3.33: Amplifier gain in dB with (a) $\alpha_H = 0$, (b) $\alpha_H = 1.5$, (c) $\alpha_H = 3$ and (d) $\alpha_H = 4.5$. The coloured area corresponds to the reflection being smaller than -20 dB.

(b) $\alpha_H = 1.5$, (c) $\alpha_H = 3$ and (d) $\alpha_H = 4.5$. As α_H grows, one has increasingly less freedom, in terms of wavelength and modal gain, to achieve a certain amplifier gain. For instance, a maximum gain larger than 11 dB can be achieved with $\alpha_H = 0$, but not greater than 8 dB with $\alpha_H = 4.5$. This suggests that, for a given material gain, quantum dots may be more attractive than quantum wells as active layers.

Finally, some comments are due on the saturation of material gain, which we have neglected. The estimate of the saturation power of photonic crystal amplifiers with slow-light effects included is highly non-trivial. As an example, the output saturation power of the amplifiers analyzed in [97] is estimated between 0.1 and 1 mW. However, a conventional rate equations model is therein employed. In [18], a more sophisticated model is presented. Such model essentially amounts to combining the coupled-Bloch-mode equations with a carrier density rate equation. The stimulated emission rate is directly expressed in terms of the total electric field and carrier-induced polarization change, but the gain-induced distributed feedback is neglected. With a group index ranging between 4 and 40, the output saturation power is found to be (approximately) between 0.1 mW and 0.03 mW. These values could serve as rough estimates of the output saturation power. A rigorous assessment of this quantity would require to follow the same approach illustrated in [18] without neglecting the distributed feedback. This is beyond the scope of this thesis, but could be the subject of future work.

3.6.1 Impact of backscattering loss

As already mentioned, we have set $\alpha_2 = 0$ because the impact of this parameter is mostly quantitative, rather than qualitative. A point of attention is that the cross-coupling coefficient is unaffected by α_2, although this loss parameter is representative of a backscattering loss. This implies that the power lost by either the forward- or backward-propagating wave in connection with α_2 is truly lost, rather than recycled back to the counter-propagating wave (which is of course not the case in practice). A more consistent modelling approach could be, for instance, combining our coupled-Bloch-mode equations with the model illustrated in [90]. This possibility is outside the scope of this thesis, but could be the subject of future work. Another possibility is briefly illustrated in Sec. 3.7.

In [133], $\alpha_2 \approx 0.5\,\mathrm{cm}^{-1}$ is estimated from measurements on GaAs-based photonic crystal waveguides, for a range of group index values similar to that which we have considered. In [178], values of α_2 between 1 and $1.5\,\mathrm{cm}^{-1}$ are suggested for InP-based photonic crystal waveguides. As an example, we shall consider below $\alpha_2 = 1.5\,\mathrm{cm}^{-1}$ and discuss its impact.

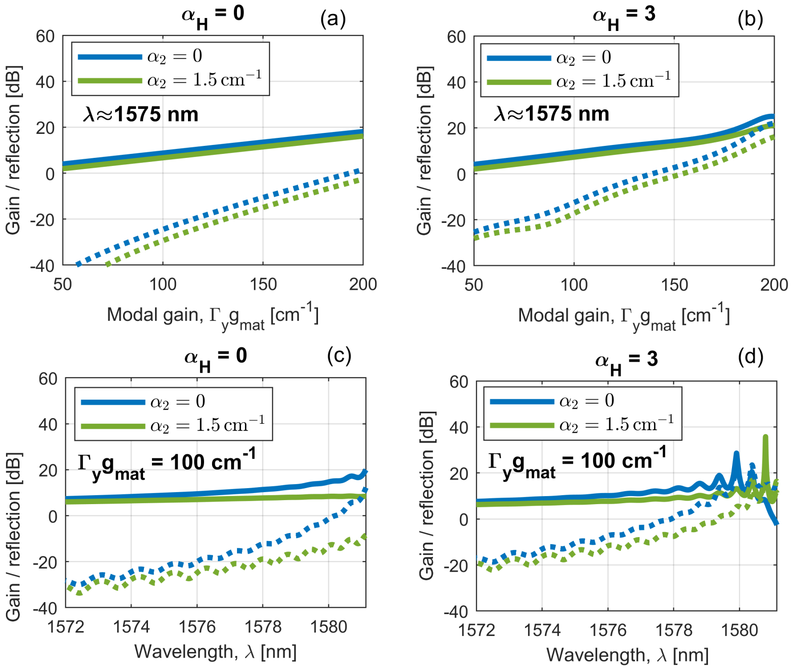

Figure 3.34: Amplifier gain (solid) and reflection (dotted) with (a, c) $\alpha_H = 0$ and (b, d) $\alpha_H = 3$. They are plotted: (a, b) versus modal gain, $\Gamma_y g_{\mathrm{mat}}$, at $\lambda \approx 1575$ nm; (c, d) versus wavelength, λ, at $\Gamma_y g_{\mathrm{mat}} = 100\,\mathrm{cm}^{-1}$. The loss coefficient α_2 is set to 0 (blue) and $1.5\,\mathrm{cm}^{-1}$ (green).

Fig. 3.34 shows the amplifier gain (solid) and reflection (dotted) as a function of (a, b) the modal gain $\Gamma_y g_\mathrm{mat}$, with the wavelength $\lambda \approx 1575\,\mathrm{nm}$, and (c, d) λ, with $\Gamma_y g_\mathrm{mat} = 100\,\mathrm{cm}^{-1}$. The backscattering loss α_2 is set to 0 (blue) and $1.5\,\mathrm{cm}^{-1}$ (green), while the linewidth enhancement factor is (a, c) $\alpha_H = 0$ and (b, d) $\alpha_H = 3$. At $\lambda \approx 1575\,\mathrm{nm}$, the impact of distributed feedback is relatively weak. Consequently, the amplifier gain approximately goes as $e^{g_\mathrm{eff} L}$, with $g_\mathrm{eff} = S\Gamma_\mathrm{FF}\Gamma_y g_\mathrm{mat} - (\alpha_1 S + \alpha_2 S^2)$. Therefore, the vertical shift between the solid blue and green line in Fig. 3.34(a) and (b) is approximately independent of $\Gamma_y g_\mathrm{mat}$ (being proportional to $\alpha_2 S^2 L$). Furthermore, the amplifier reflection is also dampened by α_2, because the power lost by the forward-propagating wave does not feed the backward-propagating one. With $\alpha_H = 0$ and $\Gamma_y g_\mathrm{mat} = 100\,\mathrm{cm}^{-1}$ (see Fig. 3.34(c)), the distributed feedback is also relatively weak at any wavelength. For $\alpha_2 = 1.5\,\mathrm{cm}^{-1}$, the closer λ is to the band edge, the larger the difference is between the blue and green lines, because the slow-down factor increases. With $\alpha_H = 3$ and $\Gamma_y g_\mathrm{mat} = 100\,\mathrm{cm}^{-1}$ (see Fig. 3.34(d)), the distributed feedback close to the band edge is strong enough to make the gain drop if $\alpha_2 = 0$. If $\alpha_2 = 1.5\,\mathrm{cm}^{-1}$, the wavelength at which the gain starts diminishing is moved closer to the band edge, because of the dampening of reflection due to α_2.

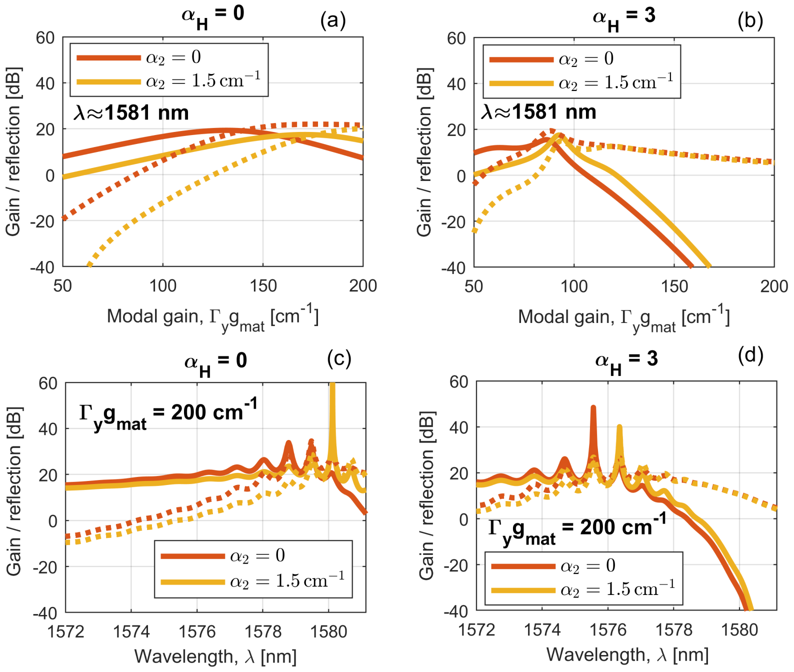

Figure 3.35: Amplifier gain (solid) and reflection (dotted) with (a, c) $\alpha_H = 0$ and (b, d) $\alpha_H = 3$. They are plotted: (a, b) versus modal gain, $\Gamma_y g_\mathrm{mat}$, at $\lambda \approx 1581\,\mathrm{nm}$; (c, d) versus wavelength, λ, at $\Gamma_y g_\mathrm{mat} = 200\,\mathrm{cm}^{-1}$. The loss coefficient α_2 is set to 0 (red) and $1.5\,\mathrm{cm}^{-1}$ (yellow).

This effect is even more evident in Fig. 3.35, reporting the amplifier gain (solid) and reflection (dotted) as a function of (a, b) $\Gamma_y g_\mathrm{mat}$, with $\lambda \approx 1581\,\mathrm{nm}$, and (c, d) λ, with

$\Gamma_y g_{\mathrm{mat}} = 200\,\mathrm{cm}^{-1}$. Similarly to Fig. 3.34, we consider $\alpha_2 = 0$ (red) and $\alpha_2 = 1.5\,\mathrm{cm}^{-1}$ (yellow), while the linewidth enhancement factor is (a, c) $\alpha_H = 0$ and (b, d) $\alpha_H = 3$. If the distributed feedback is relatively weak, the effect of α_2 is just dampening both the amplifier gain and reflection. This occurs for values of $\Gamma_y g_{\mathrm{mat}}$ being sufficiently small or wavelengths sufficiently detuned from the band edge, with the upper bound on $\Gamma_y g_{\mathrm{mat}}$ and λ depending on α_H. When the distributed feedback becomes strong enough, the amplifier gain starts dropping. The effect of α_2 is just shifting to larger values the modal gain or wavelength which triggers this mechanism. We have also checked that values of α_2 as large as 3 or $6\,\mathrm{cm}^{-1}$ do not alter the conclusions above.

3.7 Modelling disorder-induced multiple-scattering

In this section, we briefly outline the analogies between the coupled-Bloch-mode equations which we have utilized and the model discussed by M. Patterson and S. Hughes in [122], describing coherent, optical propagation in passive photonic crystal waveguides affected by disorder. In light of these considerations, we suggest an approach to model disorder by the scattering matrix formulation which we have derived.

The equations presented in [122] exactly coincide with the coupled-Bloch-mode equations introduced in Sec. 3.2, i.e. Eqs. (3.3a) and (3.3b). The differences between the two models are only the following ones:

- In [122], the self-coupling coefficient includes a contribution due to coupling with radiation modes, which we have neglected;

- In [122], the perturbation entering the self- and cross-coupling coefficients is due to disorder, rather than to material gain. The disorder-induced perturbation is $\Delta\epsilon(\mathbf{r})$, corresponding to the difference between the permittivity of the reference, ideal waveguide (i.e. without disorder) and that of the actual waveguide (i.e. with disorder). By replacing with $\Delta\epsilon(\mathbf{r})$ the susceptibility perturbation $\chi_{\mathrm{pert}}(\mathbf{r})$ in the cross-coupling coefficients which we have employed (see Eqs.(A.16b)-(A.16c) in Appendix A), one exactly finds the cross-coupling coefficients of [122]. The same holds for the self-coupling coefficient, minus the contribution due to coupling with radiation modes.

As noted in [123], to a first approximation disorder simply adds and removes dielectric from an unperturbed Bloch mode in a random fashion, thus causing local and random shifts of the dispersion relation along the waveguide. Therefore, by neglecting the radiation loss, one may simply model a certain instance of disorder by randomly dividing the waveguide in a given number of sections and assigning to each section a random refractive index perturbation $\Delta n_b'$. Each section can be described by the scattering matrix formulation which we have derived (see Eqs. (3.38a)-(3.38c)). Finally, the scattering matrix of the waveguide as a whole is obtained by cascading those of the various sections. Since the field is mostly localized within the line-defect region, we may assume $\Delta n_b'$ to be spatially limited to the line-defect, similarly to material gain in the case of a BH active region.

This strategy would allow to model disorder-induced, coherent multiple-scattering in *active* photonic crystal waveguides in a simple, but efficient manner. In particular, it appears to have the following basic ingredients: 1) it naturally accounts for the frequency dependence of the reflection and transmission at a given, disorder-induced scattering site, represented by a random refractive index perturbation (as an example, see Fig. 3.27); 2) it naturally takes into account the interference between multiple, disorder-induced reflections; 3) it self-consistely accounts for the presence of active material. As compared to the inclusion of backscattering loss in the form discussed in Sec. 3.6.1, this approach would allow to investigate the competition between disorder-induced and gain-induced multiple-scattering, for which no descriptions, to the best of our knowledge, are documented so far.

3.8 Conclusions

In summary, we have presented and thorougly discussed an efficient framework for analyzing the reflection and transmission properties of active photonic crystal waveguides. In the following, we recall the salient points.

In Sec. 3.2, we have carefully dissected the coupled-Bloch-mode equations introduced in [19] to model the impact of material gain on the optical propagation. As compared to [19], we have accounted for a generally complex refractive index perturbation. Furthermore, we have thorougly analyzed the frequency and spatial dependence of the coupling coefficients. Specifically, we have carried out this analysis for two possible geometries of the active region and, generally, of the perturbation, even if purely real (see Fig. 3.9). The first one is a so-called all-active waveguide, with active layers extended throughout the waveguide along the lateral direction (see Fig. 3.7(a)). The second geometry is a buried heterostructure (BH) active region, with active layers spatially limited to the line-defect (see Fig. 3.7(b) and (c)). Being periodic, the coupling coefficients can be expanded in a Fourier series. In either type of active region, we have found that the cross-coupling coefficient is increasingly dominated by the first-order spatial harmonic as the frequency approaches the band edge (see Fig. 3.11). This peculiar behaviour is essentially due to the compresence of the lateral and longitudinal electric field components in the TE-like modes of photonic crystal waveguides (see Fig. 3.13).

In light of these considerations, in Sec. 3.3 we have introduced the so-called *reduced* coupled-Bloch-mode equations. They contain all the essential physics of the coupled-Bloch-mode equations, but greatly elucidated. In particular, the optical propagation is governed by two factors: 1) the detuning from the band edge (see Eq. (3.20)) and 2) the relative strength of the cross-coupling coefficient as compared to the self-coupling coefficient (see Fig. 3.15).

Armed with this tool, in Sec. 3.4 we have derived the dispersion relation and Bloch modes of the *active* waveguide. We have also derived a block diagram of the active waveguide, which further elucidates the physics (see Fig. 3.17). According to this diagram, the Bloch modes of the *active* waveguide are backscattered at the equivalent dielectric interfaces on either side of the waveguide, with reflection coefficients given by $r_\pm$ within a phase shift of π (see Eqs. (3.26a) and (3.26b)). These interfaces arise from the mismatch between the Bloch modes of the active waveguide and those of the reference waveguide, which is assumed to extend on either side. In the case of a purely real refractive index perturbation, we have compared our approach against results of MPB simulations and verified that the former well reproduces the frequency shift of the dispersion relation (see Fig. 3.18). We have then analyzed the impact of a complex refractive index perturbation, which we have found to be consistent with previous results [41]. However, as compared to [41] we have clarified that the effective gain (see Fig. 3.20) does *not* simply scale with the group index of the *active* waveguide (see Fig. 3.19(b)), that is the effective group index. Therefore, this effective group index is *not* an exhaustive figure of merit of the slow-light gain enhancement. Moreover, we have analyzed the impact of the linewidth enhancement factor α_H on the dispersion relation. At given values of the modal gain and frequency, the effective gain grows with α_H (see Fig. 3.23(b)). However, the magnitude of the reflection coefficients $r_\pm$ also increases (see Fig. 3.24), signifying an enhanced backscattering of the Bloch modes of the active waveguide.

In Sec. 3.5, we have introduced analytical expressions describing the optical propagation and power flow in the active waveguide. In particular, we have discussed two equivalent formulations of the power flow, which offer alternative and complementary points of view for the interpretation of simulation results. We have also presented compact expressions for the scattering matrix, describing the multiple-scattering induced by the complex refractive index perturbation. Equipped with this theoretical framework, we have analyzed the spatial and frequency dependence of the power flow in response to power injection from the waveguide input. This analysis sheds further light on the physical meaning of the effective propagation constant, effective gain and reflection coefficients $r_\pm$. In particular, a purely real refractive index perturbation causes a band edge shift, accompanied by oscillations in the power transmission spectrum and a steep decrease as the frequency approaches the band edge (see Fig. 3.27). The case of a complex refractive index perturbation emphasizes the non-trivial nature of the induced distributed feedback and clearly reveals that a larger effective gain does *not* necessarily imply more transmitted power (see Fig. 3.28). In addition, we have found that the linewidth enhancement factor slightly enhances the transmitted power, but greatly boosts the backscattered power (see Fig. 3.29).

In Sec. 3.6, we have explored the implications of this last finding in compact slow-light semiconductor optical amplifiers [139]. We have ignored the saturation of material gain and restricted our analysis to the linear regime of the amplifier, i.e. sub-milliwat power levels, appropriate for on-chip interconnects. We have found that the maximum amplifier gain is limited by the buildup of a strong reflection, which increases as the operation wavelength approaches the band edge and/or the material gain grows (see Fig. 3.30). This is consistent with previous results [19] and confirms that the slow-light gain enhancement is intrinsically limited by the gain itself. Furthermore, as compared to [19] we have clarified the impact of the linewidth enhancement factor α_H, which further hampers the achievement of a given amplifier gain. This implies that devices with smaller α_H may offer better performance (see Fig. 3.31 and Fig. 3.33).

Finally, in Sec. 3.7 we have outlined the close analogies between our modelling framework and the model discussed in [122] for disorder-induced coherent, multiple-scattering in passive photonic crystal waveguides. We have suggested a simple, but efficient strategy to model this effect in active photonic crystal waveguides by exploiting our modelling framework.

Chapter 4

Oscillation condition of photonic crystal lasers: slow-light effects

In this chapter, we deal with the impact of slow-light on the oscillation condition of photonic crystal lasers based on line-defect waveguides. In Sec. 4.1, we provide a brief introduction to photonic crystal lasers and motivations for this chapter. In Sec. 4.2, we derive the oscillation condition and in Sec. 4.3 we present a block diagram of the active cavity, which elucidates the role of the gain-induced distributed feedback associated with slow-light. The following sections focus on results. Specifically, Sec. 4.4 and Sec. 4.5 cover lasers with, respectively, photonic bandgap mirrors and photonic heterostructure mirrors. In Sec. 4.6, we investigate the impact of slow-light on the tuning characteristics of a new, recently proposed laser structure, the so-called Fano laser. Finally, in Sec. 4.7 we draw the conclusions.

4.1 Introduction and motivation

As discussed in Chapter 1, photonic crystal lasers are promising candidates as compact and energy-efficient light-sources for computercom applications. In Sec. 2.1, we have discussed the main concepts behind optical guiding and radiation loss in passive line-defect cavities. In the following, we turn our attention to active photonic crystal cavities and briefly review the currently most promising solutions. For thorough reviews of photonic crystal lasers, we refer to [126, 33].

The first demonstration of a photonic crystal laser dates back to around 20 years ago [119]. The laser was made of an LN cavity with optically pumped quantum well (QW) layers stretching throughout the slab (a so-called *all-active* structure, as defined in Chapter 3). Fig. 4.1 illustrates a cross-section view of this type of laser. We have already shown this figure in Sec. 2.1, when introducing photonic crystal cavities. As discussed therein, the field is confined within the plane of periodicity by the photonic band

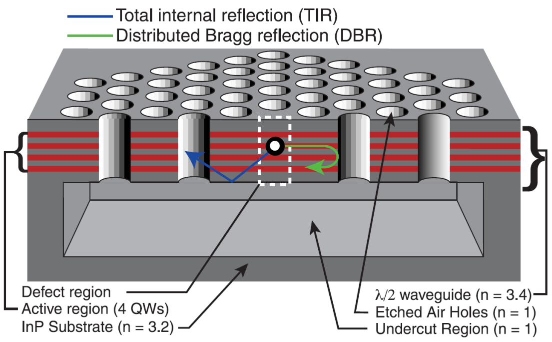

Figure 4.1: Photonic crystal laser based on an LN cavity. Reproduced from [119].

gap (distributed Bragg reflection) and vertically by index guiding (total internal reflection). Since this first demonstration, photonic crystal lasers have attracted significant research interest, flourishing into a large variety of studies and demonstrations. Initially, continuous-wave (CW) room-temperature operation was difficult to achieve, due to heat accumulating in the active region. In the following years, significant progress has been made and room-temperature CW operation has been demonstrated under optical pumping by using LN cavities with embedded quantum dots [109]. As shown in the following, current state-of-the-art photonic crystal lasers are not generally based on LN cavities. However, LN cavities continue to be an attracting platform for fundamental research, such as investigations of thresholdless operation [161], slow-light effects [178] and integration on silicon [187].

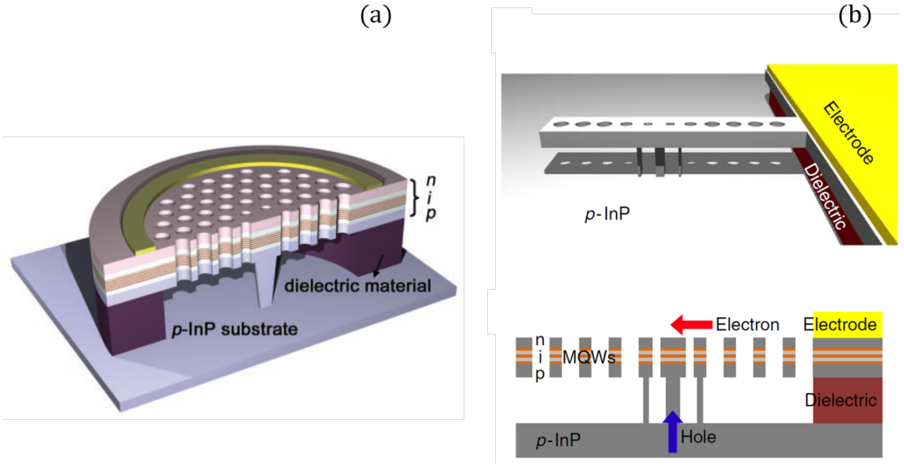

Figure 4.2: Electrically pumped photonic crystal lasers with carrier injection through a nanopillar. (a) and (b) are reproduced from [121] and [54] respectively.

A key requirement for integration into photonic circuits is electrical pumping, for which a few different schemes are currently documented. Owing to the small size of photonic crystal lasers, the challenge here is fabricating contacts without inducing huge optical loss within the metal and ensuring, at the same time, that carriers are efficiently injected into the active region. One solution is carrier injection through a nanopillar placed right below the centre of the cavity, as demonstrated in [121]. This was the first demonstration of an electrically pumped photonic crystal laser. A schematic representation is illustrated in Fig. 4.2(a). The cavity is formed by omitting a single hole in an hexagonal lattice of air holes. The active region consists of QW layers extending throughout the structure and carrier injection is performed through a vertical heterojuction, with electrons (holes) injected from the top electrode (the bottom nanopillar). The same group later proposed a refined design based on a so-called nanobeam cavity [54], which is schematically reported in Fig. 4.2(b). In this case, the cavity is induced by drilling holes in an air-suspended nanobeam, with the hole size gradually varying from the centre towards the left- and right-hand side of the nanobeam. Again, the injection scheme is based on a vertical heterojunction. Importantly, a threshold current as low as 5 μA was measured. However, lasing was only achieved in these studies [121, 54] under pulsed mode. The main issues hindering CW operation are 1) the degradation of the Q-factor due to the nanopillar and 2) the lack of lateral carrier confinement in the active region. Furthermore, integration into photonic circuits appears challenging. In fact, interfacing with output waveguides has not been demonstrated. The output power is collected from vertical (i.e. out-of-plane) light scattering, as in conventional LN cavities.

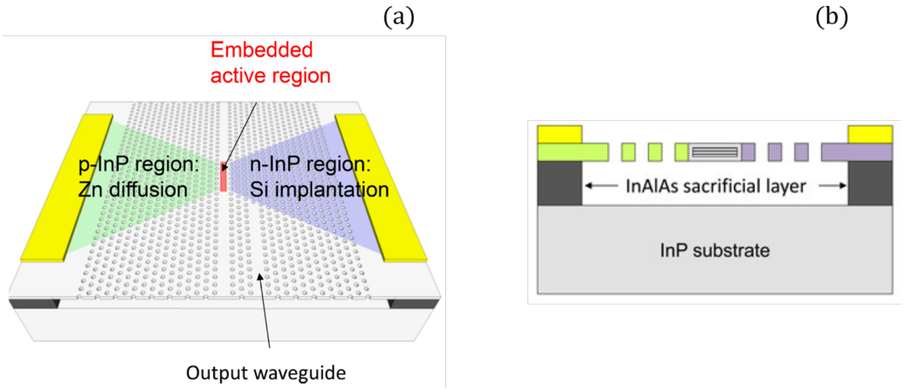

Figure 4.3: (a) Three-dimensional and (b) cross-section view of an electrically pumped LEAP laser. (a) and (b) are reproduced from [142] and [85] respectively.

A major breakthrough in the field of photonic crystal lasers has been the introduction of the so-called lambda-scale-embedded active region photonic crystal laser (LEAP laser). Initially demonstrated under optical pumping [88], this laser has undergone a rapid series of improvements, leading to CW lasing under electrical injection at room temperature. Fig. 4.3 shows (a) a three-dimensional and (b) cross-section view of an electrically pumped LEAP laser. The figures are reproduced from [142] and [85] respectively. The laser is based on an active photonic crystal line-defect waveguide. The active region is a buried heterostructure (BH), which we have already introduced in

Chapter 3 when dealing with active photonic crystal waveguides. It consists of InGaAs QW layers separated by InGaAsP barrier layers, embedded in InP. Carriers are injected into the active region by a lateral heterojunction, already demonstrated in previous studies from a different group [30]. Importantly, the output light is evanescenty coupled from the active region to an in-plane output waveguide (see Fig. 4.3(a)), which is advantageous in the perspective of device integration. The slab hosting the active region is an InP air-suspended membrane (see Fig. 4.3(b)), with an InAlAs sacrificial layer and an InP substrate.

The embedded active region fulfills various functions. Firstly, it forms the laser cavity itself. In fact, the slight refractive index difference between the active region and surrounding InP induces a photonic heterostructure, ensuring a tight confinement of photons in the longitudinal direction. In Sec. 2.1, we have reviewed the general principle of photon confinement in photonic heterostructure cavities. Secondly, as compared to all-active structures, the BH ensures effective confinement of carriers in the lateral (as well as vertical) direction, owing to the larger electronic bandgap of InP as compared to the active region. Therefore, the laser injection efficiency is improved, thereby reducing the threshold current. Thirdly, InP has a much larger thermal conductivity than InGaAsP. Therefore, heat generated in the active region is more efficiently dissipated as compared to air-bridge structures entirely made of InGaAsP [177]. These and other technological advances have culminated in the demonstration of oustanding performance [160]. A threshold current as low as 4.8 μA and an output power of a few μW have been demonstrated under CW operation at room temperature. In the same work, a maximum 3dB modulation bandwidth around 12 GHz and a minimum energy cost of 4.4 fj/bit have been achieved. These values make the LEAP laser a promising candidate as a source for computercom applications. For thorough reviews on the LEAP laser, we refer to [89, 142].

It should be mentioned that recently heterogeneous integration of the LEAP laser on silicon has been also demonstrated [159]. In this case, the laser active region and the silicon-on-insulator (SOI) waveguide are stacked vertically and aligned laterally, with the vertical separation controlling the coupling efficiency. However, the threshold current was around one order of magnitude larger than for LEAP lasers on InP substrate, outlining the necessity of further improvements.

Another notable demonstration of a photonic crystal laser with electrical injection has been achieved in [24] under CW room-temperature operation. It is a so-called hybrid (i.e. heterogeneously integrated) indium phosphide-on-silicon nanolaser diode. Fig. 4.4(a) and (b) illustrate, respectively, a three-dimensional and cross-section view of this device. The laser cavity is a one-dimensional photonic crystal obtained by drilling holes in an InP-based rib waveguide. The lattice constant (i.e. the hole-to-hole distance) gradually increases from the centre towards the sides of the rib. Carriers are injected into the active region (denoted by red) through a vertical n-i-p heterojunction. The n- and p-doped layers are made of InP and InGaAsP respectively, while the active layers are InGaAsP QWs. The n- and p-contacts are indicated in Fig. 4.4(a). The light

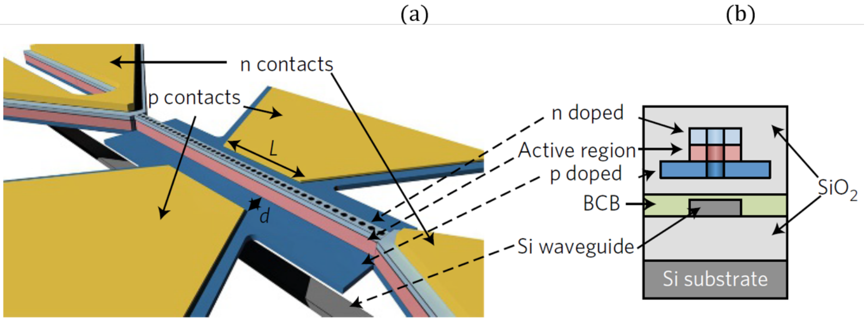

Figure 4.4: Electrically pumped hybrid indium phosphide-on-silicon nanolaser diode. (a) Three-dimensional and (b) cross-section view. Reproduced from [24].

emission generated in the active region is evanescently coupled to the SOI waveguide located below (see Fig. 4.4(b)). Here, the coupling efficiency can be controlled by adjusting the width of the silicon waveguide. In fact, this width determines the effective refractive index of the silicon waveguide, thereby controlling the phase matching condition between the silicon and InP waveguide. The laser structure is encapsulated in silicon dioxide, which improves the mechanical stability and heat sinking properties. Another key parameter is the distance (denoted by d in Fig. 4.4(a)) between the InP rib and the p-contacts. This distance results from the trade-off of various requirements. Essentially, 1) minimizing the electrical resistance encountered by the holes injected from the p-contact and 2) minimizing the optical loss due to the field absorption within the metal. From this trade-off, d is chosen around 1 μm. As compared to the LEAP laser in [160], this hybrid nanolaser shows a larger threshold current (around 100 μA). However, it also emits more power (tens of μW), owing to the larger slope efficiency. In addition, it is heterogeneously integrated on silicon. On the other hand, the dynamic characteristics of this laser [24] have not been explored.

Regarding integration on silicon of photonic crystal lasers, it should be mentioned the recent demonstration of [187]. In this work, a photonic crystal laser based on an LN cavity has been epitaxially grown on silicon. Fig. 4.5(a) illustrates the entire epitaxial structure including the silicon substrate, while Fig. 4.5(b) schematically represents the laser active region. The active region consists of InAs QDs embedded in InGaAs QWs, separated by GaAs barrier layers. This device is still far from the state-of-the-art photonic crystal lasers briefly reviewed above. Indeed, lasing has been only achieved under optical pumping. Moreover, the output power is collected from out-of-plane light scattering, meaning that the laser is not interfaced with output waveguides. However, the demonstration of CW operation at room-temperature in a structure epitaxially grown on silicon certainly constitutes a noteworthy result. Furthermore, it outlines that LN cavities still represent a vivid research field. Incidentally, we note that the epitaxial structure in Fig. 4.5 closely reflects the QD lasers on silicon which we study in Chapter 6.

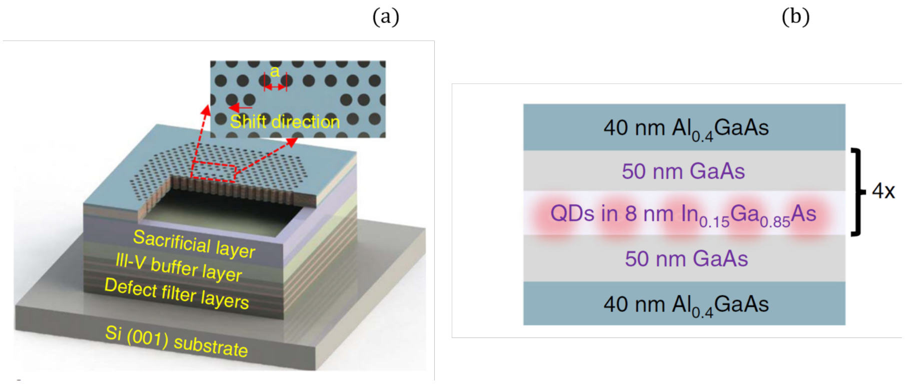

Figure 4.5: Optically pumped photonic crystal laser epitaxially grown on silicon. Schematic view of (a) the entire epitaxial structure and (b) laser active region. Reproduced from [187].

In spite of reflecting different implementations, the photonic crystal lasers discussed above share a common feature. The laser cavity is formed by introducing a *defect* within an otherwise (ideally) perfect photonic crystal structure. For example, in the LEAP laser [160] the perfect structure is represented by a line-defect photonic crystal waveguide. The defect inducing the laser cavity is instead the refractive index modulation introduced by the active region, thereby forming a photonic heterostructure (see Sec. 2.1). In the hybrid indium phospide-on-silicon nanolaser diode [24], the perfect structure is a one-dimensional photonic crystal obtained from a rib waveguide by drilling holes with a fixed lattice constant. The defect is induced by modulating the lattice constant from the centre towards the right- and left-hand side of the rib. In light of this consideration, the lasers reviewed above can be collectively denoted by *microcavity-based photonic crystal lasers* [126]. To a first approximation, these lasers can be viewed as effective Fabry-Perot resonators for the *Bloch* modes of the region corresponding to the defect [70].

As anticipated in Chapter 1, it should be mentioned that another category of photonic crystal lasers exists, which we briefly recall in the following lines. These lasers can be generally labeled as *slow-light based photonic crystal lasers* or *DFB-like photonic crystal lasers* [126]. Essentially, the lasing operation is achieved by usage of modes of a photonic crystal structure with low group velocity and is sustained by the strong distributed feedback throughout the periodic lattice. A further classification is possible, by distinguishing DFB-like photonic crystal lasers for *surface* and *in-plane* emission. The former [11, 36, 135] predominantly emit light in the direction orthogonal to the plane of the photonic crystal lattice. In the latter, most of the light remains instead confined within the plane of periodicity. In particular, this in-plane emission can be either achieved in a perfectly periodic lattice [69] or in line-defect photonic crystal waveguides [1, 60, 43]. As already mentioned, these DFB-like photonic crystal lasers are outside the scope of this thesis, with a single exception. For this case, we refer to Sec. 4.4.2.

4.1.1 Motivation of this chapter

In this chapter, we focus on specific types of microcavity-based photonic crystal lasers. In particular, as shown in Chapter 3, line-defect photonic crystal waveguides support significant slow-light, with possible enhancement of optical gain [29]. This effect could be exploited for the realization of lasers with shorter cavity length or lower threshold gain [105].

However, slow-light in microcavity-based photonic crystal lasers has not received much attention beyond the conventional picture [105, 178] of a simple reduction of the mirror loss. In particular, as thoroughly discussed in Chapter 3, slow-light operation in active photonic crystal waveguides does *not* automatically ensure gain enhancement, since a gain-induced distributed feedback sets in [19, 139]. Therefore, it appears natural to investigate the impact of the same effect in the case of microcavity-based photonic crystal lasers.

With this motivation in mind, in this chapter we extend to the case of photonic crystal lasers based on line-defect waveguides the theoretical framework developed in Chapter 3.

4.2 Oscillation condition

In this section, we derive the oscillation condition of photonic crystal lasers based on line-defect waveguides. Slow-light effects are accounted for through the model thoroughly discussed in Chapter 3.

In the following, we follow the approach illustrated in [157] for DFB lasers. From Eq. (3.21), the electric field in the active region reads

$$\begin{aligned} E(z) = {} & e^{+i\frac{\pi}{a}z}\left[\tilde{F}e^{+i\lambda_+ z} + r_-\tilde{B}e^{-i\lambda_+ z}\right]e_+(z) \\ & + e^{-i\frac{\pi}{a}z}\left[r_+\tilde{F}e^{+i\lambda_+ z} + \tilde{B}e^{-i\lambda_+ z}\right]e_-(z) \end{aligned} \tag{4.1}$$

Here, we are considering for simplicicity the electric field to be a scalar quantity. $E(z)$ in Eq. (4.1) may correspond to the electric field lateral component along the centerline of the cavity, as discussed in Sec. 2.3. The quantities appearing in Eq. (4.1) have been already introduced in Chapter 3, but are briefly reviewed for the sake of convenience. $e_\pm$ are the forward (+) and backward (-) Bloch modes of a *reference* waveguide with purely real refractive index. $\tilde{F}$ ($\tilde{B}$) is the amplitude of the forward (backward) Bloch mode of the *active* waveguide, with λ_+ being the complex propagation constant from Eq. (3.25). $r_\pm$ are computed by Eqs. (3.26a) and (3.26b). They are coefficients determining the composition of the Bloch modes of the active waveguide in terms of those of the reference waveguide, in compliance with Eqs.(3.22a) and (3.22b). Finally, a is the lattice constant.

We denote by r_L (r_R) the left (right) mirror reflection coefficient in the basis of the Bloch modes of the reference waveguide. Depending on the specific type of cavity, these reflection coefficients have different forms, as discussed in the following sections. We assume the left (right) mirror to be placed at $z = 0$ ($z = L$) and consequently express the boundary conditions as

$$\begin{aligned} & r_R e^{+i\frac{\pi}{a}L}\left[\tilde{F}e^{+i\lambda_+ L} + r_-\tilde{B}e^{-i\lambda_+ L}\right]e_+(L) \\ & \quad = e^{-i\frac{\pi}{a}L}\left[r_+\tilde{F}e^{+i\lambda_+ L} + \tilde{B}e^{-i\lambda_+ L}\right]e_-(L) \end{aligned} \tag{4.2a}$$

$$r_L\left[r_+\tilde{F} + \tilde{B}\right]e_-(0) = \left[\tilde{F} + r_-\tilde{B}\right]e_+(0) \tag{4.2b}$$

By making use of the fact that e_- is the complex conjugate of e_+ [120, 141], Eqs. (4.2a) and (4.2b) can be reformulated as

$$\left(r_+ - r_F\right)e^{+2i\lambda_+ L}\tilde{F} + (1 - r_F r_-)\tilde{B} = 0 \tag{4.3a}$$

$$\left(1 - r_+ r_B\right)\tilde{F} + (r_- - r_B)\tilde{B} = 0 \tag{4.3b}$$

where r_F and r_B are given by

$$r_F = r_R e^{+i\frac{2\pi}{a}L}e^{+2i\phi_+(L)} \tag{4.4a}$$

$$r_B = r_L e^{-2i\phi_+(0)} \tag{4.4b}$$

and ϕ_+ is the phase of e_+. For the laser to oscillate, a solution other than the trivial $\tilde{F} = \tilde{B} = 0$ must exist. By enforcing the determinant of the coefficient matrix to be zero, we obtain the oscillation condition

$$\underbrace{\frac{r_B - r_-}{1 - r_+ r_B}}_{r_{L_{eq}}}\underbrace{\frac{r_F - r_+}{1 - r_- r_F}}_{r_{R_{eq}}}e^{+2i\lambda_+ L} = 1 \tag{4.5}$$

Eq. (4.5) can be interpreted as the oscillation condition of a Fabry-Perot laser where the left (right) mirror reflection coefficient is $r_{L_{eq}}$ ($r_{R_{eq}}$) and the (complex) propagation constant is λ_+. Unless otherwise specified, we assume for simplicity that the active region consists of an integer number of unit cells and embed any possible deviation into the phase of r_L or r_R. In this case, one finds $\phi_+(0) = \phi_+(L) = 0$ [136], as discussed in Sec. 2.2.2. Eq. (4.5) can be separated into magnitude and phase, leading to

$$g_{\text{eff}} = \frac{1}{L}\ln\left(\frac{1}{|r_{L_{eq}}||r_{R_{eq}}|}\right) \tag{4.6a}$$

$$2\left(\beta_{\text{eff}} - \frac{\pi}{a}\right)L + \phi_{L_{eq}} + \phi_{R_{eq}} = 2\pi m \tag{4.6b}$$

where $\phi_{L_{eq}}$ ($\phi_{R_{eq}}$) is the phase of $r_{L_{eq}}$ ($r_{R_{eq}}$) and m is an integer. β_{eff} and g_{eff} are the effective propagation constant and *net* modal gain of the Bloch modes of the active waveguide. In contrast to conventional Fabry-Perot lasers, the amplitude and phase conditions are strongly coupled by the gain-induced distributed feedback, even in the ideal case of zero linewidth enhancement factor. In particular, the material gain does not only couple β_{eff} and g_{eff}. Indeed, through r_+ and r_-, the equivalent mirrors also depend on the threshold gain and oscillation frequency in a non-trivial manner.

If the threshold gain is small enough and/or the oscillation frequency sufficiently detuned from the band edge, the impact of the distributed coupling is negligible. In this limiting case, one finds $r_\pm \approx 0$, as outlined in Sec. 3.4. Therefore, $r_{L_{eq}}$ ($r_{R_{eq}}$) is reduced to r_L (r_R). Furthermore, β_{eff} is reduced to $k_z - S\Gamma_{\text{FF}}\Gamma_y g_{\text{mat}}\alpha_H/2$ and g_{eff} to $S\Gamma_{\text{FF}}\Gamma_y g_{\text{mat}} - (\alpha_1 S + \alpha_2 S^2)$, with S being the slow-down factor. As discussed in Sec. 3.6, here α_1 and α_2 account, respectively, for disorder-induced coupling with radiation modes and backscattering [117]. The amplitude and phase condition are only coupled through the linewidth enhancement factor α_H and Eqs. (4.6a) and (4.6b) are reduced to

$$\Gamma_{\text{FF}}\Gamma_y g_{\text{mat}} = \alpha_1 + \alpha_2 S + \frac{1}{SL}\ln\left(\frac{1}{|r_L||r_R|}\right) \tag{4.7a}$$

$$2\left(k_z - \frac{1}{2}S\Gamma_{\text{FF}}\Gamma_y g_{\text{mat}}\alpha_H - \frac{\pi}{a}\right)L + \phi_L + \phi_R = 2\pi m \tag{4.7b}$$

where ϕ_L (ϕ_R) is the phase of r_L (r_R). These equations describe the oscillation condition of a Fabry-Perot laser with effective gain (or, equivalently, mirror loss) enhanced (reduced) by the slow-down factor [178]. Here, we emphasize that Eqs.(4.6a) and (4.6b) are more general, as they also account for the gain-induced distributed feedback.

4.3 Block diagram of the active cavity

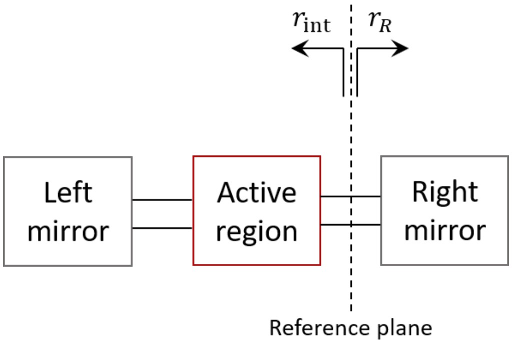

Figure 4.6: Reference plane for the internal reflection coefficient r_{int}

An equivalent approach to express the oscillation condition is computing the complex loop gain of the laser cavity at a given reference plane and enforcing it to be unitary. This formulation requires that the field inside the cavity has to reproduce itself after a roundtrip. If we assume the reference plane to be between the active region and the right mirror (see Fig. 4.6), the oscillation condition reads

$$r_{\mathrm{int}} r_R = 1 \tag{4.8}$$

where r_{int} is the effective reflection coefficient for the backward-propagating field at the reference plane. This *internal* reflection coefficient encompasses both the left mirror r_L and roundtrip gain, with the latter including the gain-induced distributed feedback in the active region.

To better understand the impact of distributed feedback on the oscillation condition, in this section we analyze how the internal reflection coefficient r_{int} depends on frequency and gain. For this purpose, it is useful to derive a block diagram of the active cavity, which further elucidates the physics.

4.3.1 Block diagram

In Sec. 3.4, we have already discussed a convenient block diagram (see Fig. 3.17) to describe the optical propagation in an active photonic crystal waveguide. This diagram is derived in detail in Sec. C.3.

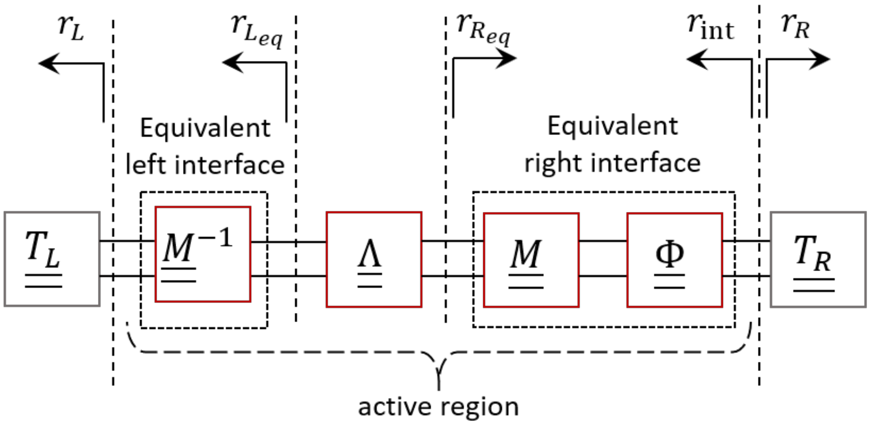

Figure 4.7: Block diagram of a photonic crystal laser. The internal reflection coefficient r_{int} is indicated.

Therefore, we can readily replace the active region in Fig. 4.6 with the block diagram from Fig. 3.17. By doing so, we obtain the convenient representation in Fig. 4.7. Here, $\underline{\underline{T}}_L$ ($\underline{\underline{T}}_R$) is the left (right) mirror transmission matrix in the basis of the Bloch modes of the *reference* waveguide. The left and right mirror reflection coefficient are r_L and r_R respectively. We denote by $S_{l_{ij}}$ ($S_{r_{ij}}$) the scattering parameters of the equivalent left (right) interface in Fig. 4.7, with $i, j = \{1,2\}$. These parameters are derived in Sec. C.3. We use those expressions by assuming that the active region consists of an integer number of unit cells. As a result, the reflection coefficient $r_{L_{eq}}$ of the equivalent left mirror reads

$$r_{L_{eq}} = S_{l_{22}} + \frac{S_{l_{12}} r_L S_{l_{21}}}{1 - r_L S_{l_{11}}} = \frac{r_L - r_-}{1 - r_L r_+} \tag{4.9}$$

Similarly, one finds the reflection coefficient $r_{R_{eq}}$ of the equivalent right mirror

$$r_{R_{eq}} = S_{r_{11}} + \frac{S_{r_{21}} r_R S_{r_{12}}}{1 - r_R S_{r_{22}}} = \frac{r_R - r_+}{1 - r_- r_R} \tag{4.10}$$

Under the assumption of L/a being an integer, the expressions of $r_{L_{eq}}$ and $r_{R_{eq}}$ from Eq. (4.5) consistently coincide with those from Eqs. (4.9) and (4.10).

4.3.2 Internal reflection coefficient

The cascade of blocks denoted by "active region" in Fig. 4.7 is described by the scattering parameters from Eqs. (3.38a)-(3.38c) (see Sec. 3.5). Here, we denote these parameters by $S_{\text{act}_{ij}}$, with $i, j = \{1,2\}$. With this notation, the internal reflection coefficient r_{int} reads

$$r_{\text{int}} = S_{\text{act}_{22}} + \frac{S_{\text{act}_{12}} r_L S_{\text{act}_{21}}}{1 - r_L S_{\text{act}_{11}}} \tag{4.11}$$

Unless otherwise specified, the general approach we follow in this thesis is solving the oscillation condition $r_{\text{int}} r_R = 1$ with r_{int} given by Eq. (4.11). This approach is equivalent to solving Eqs. (4.6a) and (4.6b) derived in Sec. 4.2, the difference only being the reference plane at which the complex loop gain is computed. Indeed, by evaluating the loop gain at the plane where $r_{R_{eq}}$ is defined (see Fig. 4.7), the oscillation condition in the form of Eq. (4.5) is readily obtained. The two approaches provide alternative lines of reasoning for interpreting the results in the following sections.

Eq. (4.11) can be considerably simplified if the active region consists of an integer number of unit cells. In this case, one finds

$$r_{\text{int}} = \frac{r_- + r_{L_{eq}} e^{2i\lambda_+ L}}{1 - (-r_+) r_{L_{eq}} e^{2i\lambda_+ L}} \tag{4.12}$$

As an example, Fig. 4.8 illustrates r_{int} in (a) magnitude and (b) phase for different values of the modal gain $\Gamma_y g_{\text{mat}}$. The bottom x-axis reports the wavenumber k_z of the reference waveguide normalized to the lattice constant a, while the top x-axis in (a) shows the group index n_g of the reference waveguide. The solid (dotted) line is with (without) gain-induced distributed feedback and the length of the active region is $L = 6.57\ \mu\text{m}$, corresponding to 15 unit cells. We have assumed $r_L = 1$, $\alpha_1 = 5\ \text{cm}^{-1}$, $\alpha_2 = 0$, $\alpha_H = 1.5$

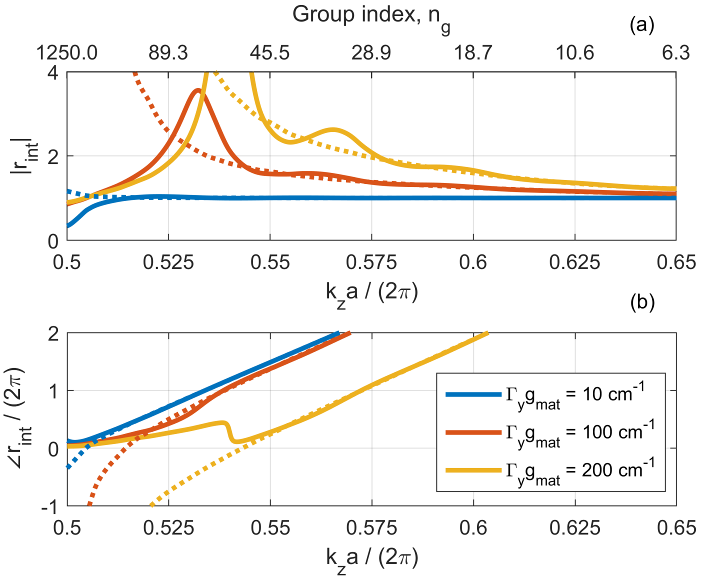

Figure 4.8: Internal reflection coefficient r_{int} as a function of the normalized wavenumber of the reference waveguide in (a) magnitude and (b) phase. The different colors denote different values of the modal gain $\Gamma_y g_{\mathrm{mat}}$. The solid (dotted) line is with (without) gain-induced distributed feedback. The length of the active region is $L = 6.57\ \mu$m, corresponding to 15 unit cells. The top x-axis in (a) reports the group index of the reference waveguide.

and the optical gain to be limited to the line-defect, as allowed by the buried heterostructure (BH) technology [160]. The parameters of the reference waveguide are summarized in Tab. 2.1 in Sec. 2.2.1.

Without distributed feedback, the magnitude of the internal reflection coefficient steadily increases as k_z approaches the band edge, as dictated by the growing group index n_g. Indeed, as anticipated in connection with Eqs. (4.7a) and (4.7b), neglecting the distributed feedback implies $r_{\pm} = 0$ and, consequently, $r_{L_{eq}} = r_L$, $\beta_{\mathrm{eff}} = k_z - S\Gamma_{\mathrm{FF}}\Gamma_y g_{\mathrm{mat}}\alpha_H/2$ and $g_{\mathrm{eff}} = S\Gamma_{\mathrm{FF}}\Gamma_y g_{\mathrm{mat}} - (\alpha_1 S + \alpha_2 S^2)$, with S being the slow-down factor. Therefore, in this case one easily finds from Eq. (4.12) a strong and monotonic increase towards the band edge in the magnitude of r_{int} (if α_2 is zero and $\Gamma_{\mathrm{FF}}\Gamma_y g_{\mathrm{mat}}$ larger than α_1). From the numerical point of view, this increase in only limited by the numerical computation of $(dk_z/d\omega)^{-1}$ at the band edge, which provides a finite value for n_g, however large.

On the contrary, if one includes the distributed feedback, the trend is non-monotonic and decreasing towards the band edge for k_z greater than a given value, depending on the gain. The location of the maximum depends on the impact of the distributed feedback in a complicated manner, as governed by Eq. (4.12). Nevertheless, we can recognize some general features. Overall, the feedback intensifies as k_z approaches the band edge and/or the modal gain $\Gamma_y g_\text{mat}$ grows, as discussed in Chapter 3. The stronger the feedback becomes, the more detuned from the band edge the value of k_z is at which the magnitude of r_int starts diminishing. Furthermore, the number and intensity of the resonant peaks (see, e.g., the red and yellow lines in Fig. 4.8(a)) also increase with the feedback strength. The resonant peaks are caused by the resonant term appearing in the denominator of Eq. (4.12). This terms stems from the reflection which the Bloch modes of the active region undergo at the equivalent right interface (that is $-r_+$), as well as from the general dependence on frequency and gain of the equivalent left mirror reflection coefficient. This mirror accounts for the mismatch between the Bloch modes of the active region and those of the reference waveguide at the left equivalent interface (see Fig. 4.7).

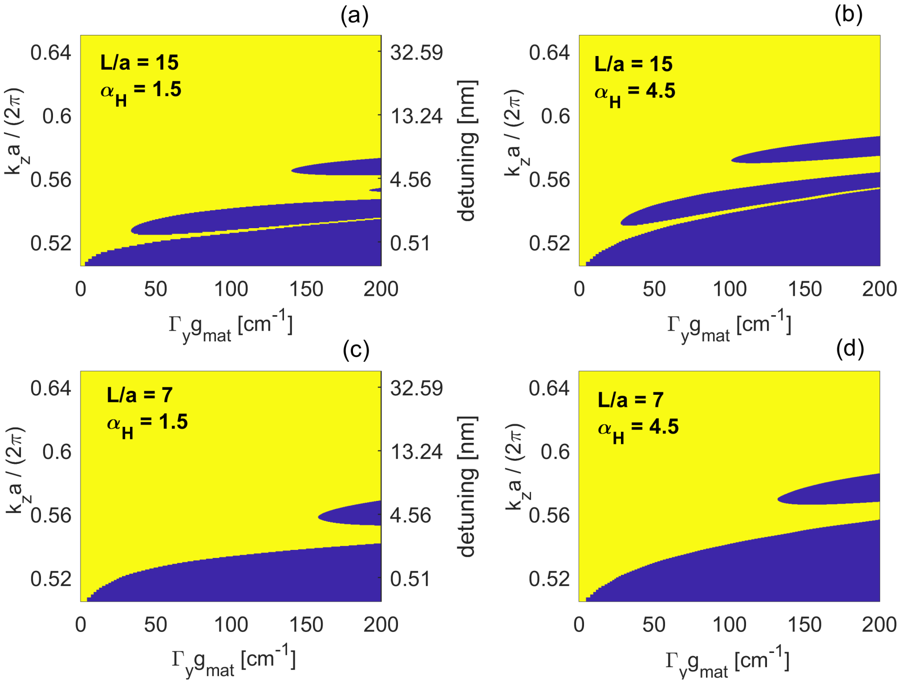

Figure 4.9: Maps showing conditions under which the relative error in the magnitude of the internal reflection coefficient r_int is smaller (yellow) and larger (blue) than 10 %. This is the error which one would commit as compared to the full model by neglecting the distributed feedback. The cavity length corresponds to (a, b) 15 unit cells and (c, d) 7 unit cells. The linewidth enhancement factor is equal to (a, c) 1.5 and (b, d) 4.5. The right y-axis in (a, c) reports the detuning from the band edge.

The relative error which one would commit as compared to the full model by neglecting the distributed feedback clearly depends on the feedback strength. This varies with detuning from the band edge and modal gain, but it also depends, for instance, on the cavity length and linewidth enhancement factor. As an example, Fig. 4.9 illustrates when the error is smaller (yellow) and larger (blue) than 10 %, as a function of detuning from the band edge and modal gain. The cavity is (a, b) 15 and (c, d) 7 lattice constants long, while the linewidth enhancement factor is equal to (a, c) 1.5 and (b, d) 4.5. At given values of detuning and modal gain, the longer the cavity is and the more relevant the distributed feedback becomes, thus restricting the ranges of detuning and modal gain where neglecting the distributed feedback would be acceptable. A similar trend is found when the linewidth enhancement factor is increased. This is expected, since the carrier-induced refractive index perturbation enhances the backscattered power, as discussed in Chapter 3.

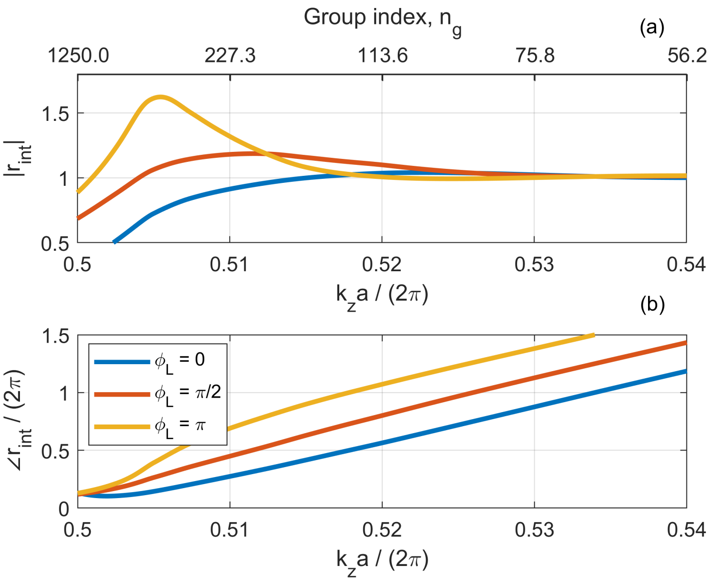

Figure 4.10: Internal reflection coefficient r_{int} as a function of the normalized wavenumber of the reference waveguide in (a) magnitude and (b) phase. The different colors denote different values of the left mirror phase ϕ_L. The modal gain is $\Gamma_y g_{\text{mat}} = 10\,\text{cm}^{-1}$ and the length of the active region $L = 6.57\,\mu$m, corresponding to 15 unit cells. The top x-axis in (a) reports the group index of the reference waveguide.

Close to the band edge, the trend in the internal reflection coefficient also strongly depends on 1) the phase of the cross-coupling coefficient (entering r_+ and r_-) and 2) the phase of the left mirror, ϕ_L. The former is determined by the phase of Γ_{FB}. As outlined by Eq. (3.9) in Sec. 3.2, the phase of Γ_{FB} is approximately equal to π according to our choice of the unit cell reference planes. Concerning the phase of the left mirror, Fig. 4.10 shows, as an example, (a) the magnitude and (b) phase of the internal reflection coefficient close to the band edge for ϕ_L equal to 0 (blue), $\pi/2$ (red) and π (yellow). The modal gain is $\Gamma_y g_{\text{mat}} = 10\,\text{cm}^{-1}$ and the other parameters are the same as in Fig. 4.8. As ϕ_L changes from zero to π, the resonant peak moves closer to the band edge. At the same time, the value of k_z at which the phase of r_{int} is an integer multiple of 2π shifts to the same direction. This suggests that, by engineering the phase of the left mirror (as well as that of the right mirror), one may leverage the resonance and possibly optimize the threshold gain. This possibility is briefly explored in Sec. 4.4 (see Fig. 4.14), but systematic investigations are outside the scope of this thesis. Unless otherwise specified, in the following we assume ϕ_L to be zero. This assumption is supported by the analysis carried out in Chapter 2 (see, in particular, Sec. 2.4.3). The implications of a non-zero value for the left mirror phase are relevant in the study of the Fano laser tuning characteristics in Sec. 4.6.2 and are discussed therein.

To conclude this section, some comments are appropriate on the internal reflection coefficient as compared to the group index of the *active* waveguide, analyzed in Chapter 3. It is important to note how the trend in the amplitude of the internal reflection coefficient somehow resembles the gain-induced reduction and spectral broadening of the group index of the active waveguide [41, 137], to which it can be *intuitively* and *qualitatively* correlated. With regard to this, see, for instance, Fig. 3.4 in Sec. 3.1.1 or Fig. 3.19(b) in Sec. 3.4.2. The physical argument, in this case, would be that of an *effective* slow-down factor, scaling with the group index of the *active* waveguide. On this basis, one could be tempted to consider the impact of gain in the slow-light regime to be well described by this effective slow-down factor. However, the appearance of multiple resonances in the magnitude of r_{int} (see Fig. 4.8(a)) and the strong coupling with the phase (see Fig. 4.8(b) and Fig. 4.10(b)) clearly indicate that the impact of gain in the slow-light region is actually more intricate and generally requires to take into account the nature of the active cavity as summarized by Fig. 4.7. This confirms that the effective group index (i.e. the group index of the active waveguide) is *not* an exhaustive figure of merit of slow-light gain enhancement, as already, thoroughly discussed in Chapter 3.

4.4 Lasers with photonic bandgap mirrors

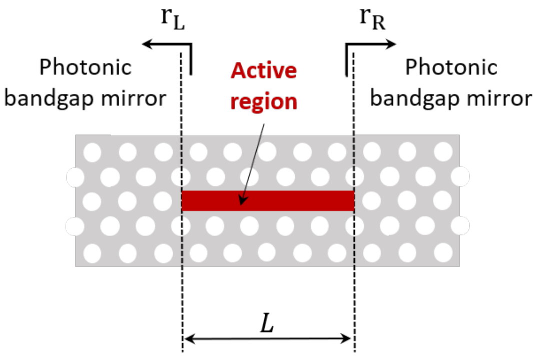

Figure 4.11: Laser with photonic bandgap mirrors.

Armed with the understandings of the previous sections, we can now move to the solution of the oscillation condition for various types of photonic crystal lasers based on line-defect waveguides. In this section we focus on conventional line-defect lasers with photonic bandgap mirrors, as that shown in Fig. 4.11. These mirrors are broadband and generally have high reflectivity [70].

In the following, we assume for the reference waveguide the parameters in Tab. 2.1 in Sec. 2.2.1. The slab refractive index n_{slab} is set to 3.17, representative of the InP platform. The lattice constant a is 438 nm, with the hole radius being $0.25a$. The slab is 250 nm thick and assumed to be suspended in air. Unless otherwise specified, the other parameters are $r_L = 1$, $\alpha_H = 1.5$, $\alpha_1 = 5\,\text{cm}^{-1}$ and $\alpha_2 = 0$. The impact of the loss coefficient α_2 is discussed in Sec. 4.4.1. Furthermore, we assume the optical gain to be limited to the line-defect and we consider different values of the right mirror reflection coefficient.

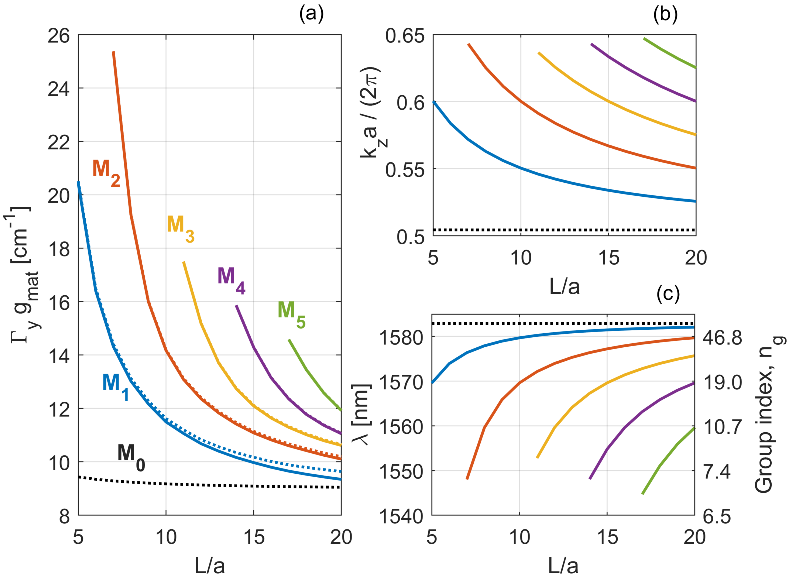

Figure 4.12: Oscillation condition of lasers with photonic bandgap mirrors. (a) Modal gain $\Gamma_y g_{\text{mat}}$, (b) wavenumber and (c) wavelength at the lasing threshold of the various longitudinal modes with $r_R = 0.99$. Each color corresponds to a different longitudinal mode. The solid (dotted) line is with (without) the gain-induced distributed feedback. The solid and dotted lines in (b) and (c) practically overlap.

We start by considering the case $r_R = 0.99$ [178]. Fig. 4.12 shows (a) the modal gain $\Gamma_y g_{\text{mat}}$, (b) wavenumber and (c) wavelength at the lasing threshold of the various longitudinal modes, with each color corresponding to a different mode. The modes are numbered according to the threshold gain, the lowest order mode being that with the smallest gain. The solid (dotted) lines are obtained by taking into account (neglecting) the gain-induced distributed feedback. A number of features can be noted.

First of all, without distributed feedback the lasing mode is M$_0$, which is very close to the band edge. On the contrary, if one takes the distributed feedback into account, M$_0$ is missing and the lasing mode is M$_1$. In the following lines, we focus on all modes other than M_0. For these modes, the impact of distributed feedback appears to be limited, because they are far from the band edge. Indeed, the solid and dotted lines in Fig. 4.12(b) and (c) practically overlap. In this case, the wavenumber simply obeys Eq. (4.7b). This equation dictates that, for a given mode order m, an increase in the cavity length should be compensated by a smaller detuning of k_z from π/a in order to continue to fulfill the phase condition. This easily explains why the oscillation frequency moves towards the band edge, as experimentally observed [178] and predicted by finite-difference time-domain simulations [15]. Regarding the threshold gain, the strong decrease with increasing cavity length is due to the slow-light reduction of the mirror loss, as prescribed by Eq. (4.7a). As already evidenced, this equation reflects a Fabry-Perot laser with effective modal gain enhanced by the slow-down factor. The simple increase in the cavity length plays a minor role in reducing the threshold gain. In fact, the threshold gain decrease is limited in the case of M_0, whose lasing wavelength is practically constant.

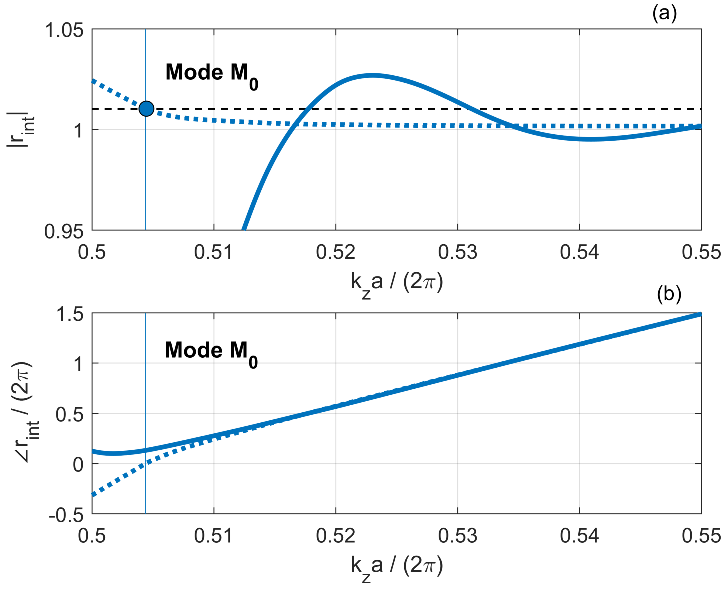

Figure 4.13: Oscillation condition of lasers with photonic bandgap mirrors. (a) Magnitude and (b) phase of the internal reflection coefficient at the lasing threshold of mode M_0 for the laser in Fig. 4.12 with 15 lattice constants. The solid (dotted) line is with (without) the gain-induced distributed feedback. The horizontal, dashed line indicates the level $1/r_R$, while the vertical line denotes the wavenumber at the oscillation frequency.

We now turn our attention to M_0 to better understand why this mode is missing if distributed feedback is taken into account. As an example, we select the cavity with 15 lattice constants. Fig. 4.13 shows (a) the magnitude and (b) phase of the internal reflection coefficient at the lasing threshold of mode M_0 with (solid line) and without (dotted line) distributed feedback. The horizontal, dashed line indicates the level $1/r_R$, while the vertical line denotes the wavenumber at the oscillation frequency. This figure highlights that, in the presence of distributed feedback, 1) the magnitude of r_{int} strongly decreases towards the band edge and 2) the phase condition cannot be fulfilled. On the other hand, without distributed feedback magnitude and phase condition allow for lasing close to the band edge. In this case, the detuning of the lasing frequency from the band edge is only due to the non-zero linewidth enhancement factor, as understood from Eq. (4.7b).

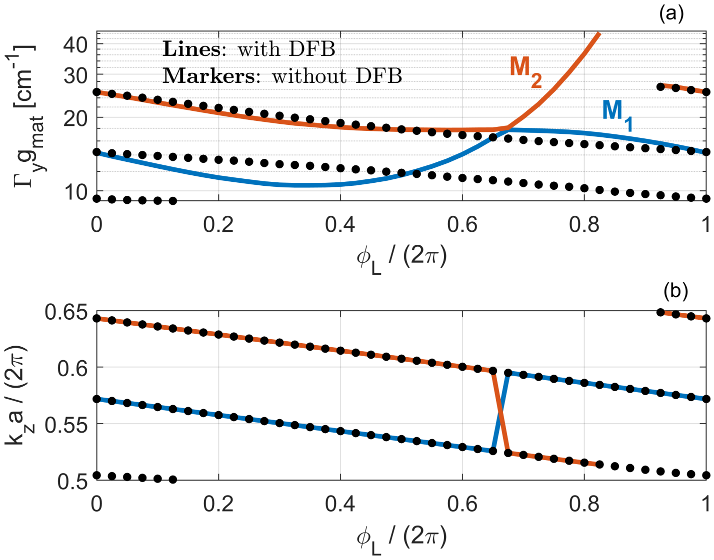

Figure 4.14: Oscillation condition of lasers with photonic bandgap mirrors. (a) Modal gain $\Gamma_y g_{\text{mat}}$ and (b) wavenumber at the lasing threshold of mode M_1 (blue) and M_2 (red) versus the phase of the left mirror, with the cavity being 7 lattice constants long. The magnitude of the left mirror reflection coefficient is fixed to unity, while the right mirror reflection coefficient is $r_R = 0.99$. The black markers are the solutions of the oscillation condition in the absence of distributed feedback.

We emphasize that the reason for the absence of lasing close to the band edge in the presence of distributed feedback is not simply the fact that the phase condition cannot be fulfilled. Instead, the reason is the impossibility to simultaneously and efficiently fulfil the phase and magnitude condition, owing to their strong coupling caused by the distributed feedback. To corroborate this interpretation, we report in Fig. 4.14 (a) the modal gain and (b) wavenumber at the lasing threshold of mode M_1 (blue) and M_2 (red) versus the phase of the left mirror. The magnitude of the left mirror reflection coefficient is fixed to unity, while the right mirror reflection coefficient is $r_R = 0.99$. The cavity is 7 lattice constants long. As usually done throughout this thesis, the modes are numbered according to the threshold gain, with M_1 being the lasing mode. The black markers are the solutions of the oscillation condition in the absence of distributed feedback. It is seen that, by properly tuning the left mirror phase, one can indeed push the lasing frequency towards the band edge. Without distributed feedback, this tuning results in a trivial, monotonic decrease of the threshold gain. On the contrary, in the presence of distributed feedback, only initially the threshold gain decreases as the lasing frequency approaches the band edge. Below a given detuning, the distributed feedback is more and more relevant and the threshold gain starts increasing, until lasing far from the band edge becomes more convenient. This mode hopping corresponds to the crossing of the blue and red lines in Fig. 4.14(a). The optimum mirror phase stems from a non-trivial trade-off between two effects. On the one hand, the slow-light reduction of the mirror loss. On the other hand, the feedback-induced reduction of the round-trip gain close to the band edge. This reduction also depends, at given frequency and detuning, on the value of the left mirror phase. The origin of the optimum is further explained

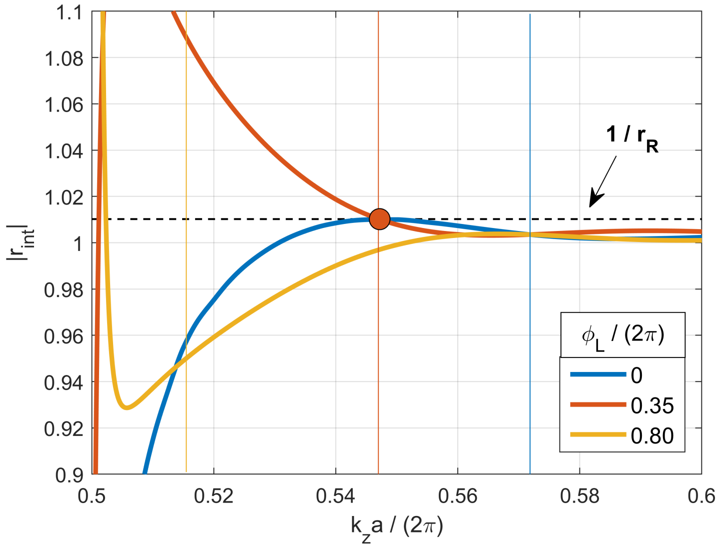

Figure 4.15: Magnitude of the internal reflection coefficient versus the wavenumber. Cavity length, right mirror and magnitude of the left mirror reflection coefficient are the same as in Fig. 4.14. The different colors denote different values of the left mirror phase ϕ_L, with $\phi_L/(2\pi) = 0.35$ being the optimum phase of Fig. 4.14. In all cases, the modal gain is fixed to the value of the minimum threshold gain of mode M_1 in that figure. The horizontal, dashed line indicates the level $1/r_R$. The vertical, blue (red) line denotes the lasing frequency of mode M_1 in Fig. 4.14 for $\phi_L = 0$ ($\phi_L/(2\pi) = 0.35$). The vertical, yellow line indicates the lasing frequency of mode M_2 in Fig. 4.14 for $\phi_L/(2\pi) = 0.8$.

by Fig. 4.15, showing the magnitude of r_{int} with the modal gain being the optimum threshold gain of mode M_1 in Fig. 4.14. Cavity length, right mirror and magnitude of the left mirror reflection coefficient are the same as therein. The different colors denote different values of the left mirror phase ϕ_L, with $\phi_L/(2\pi) = 0.35$ being the optimum phase of Fig. 4.14. The horizontal, dashed line indicates the level $1/r_R$, corresponding to lasing. The vertical, blue (red) line denotes the lasing frequency of mode M_1 for $\phi_L = 0$ ($\phi_L/(2\pi) = 0.35$). The vertical, yellow line indicates the lasing frequency of mode M_2 for $\phi_L/(2\pi) = 0.8$. Fig. 4.15 emphasizes that, depending on the left mirror phase, the distributed feedback may strongly reduce the round-trip gain at the lasing frequency, thus forcing the modal gain to grow in order to achieve lasing. This is the case, e.g., for $\phi_L/(2\pi) = 0.8$. Overall, Fig. 4.14 and Fig. 4.15 demonstrate that an intrinsic limitation to lasing close to the band edge is posed by the gain-induced distributed feedback. It should be emphasized, though, that in practice disorder due to unavoidable fabrication imperfections would also jeopardize the possibility of lasing in the slow-light region (see Sec. 4.4.1). From an experimental point of view, distinguishing between the two effects would probably not be trivial.

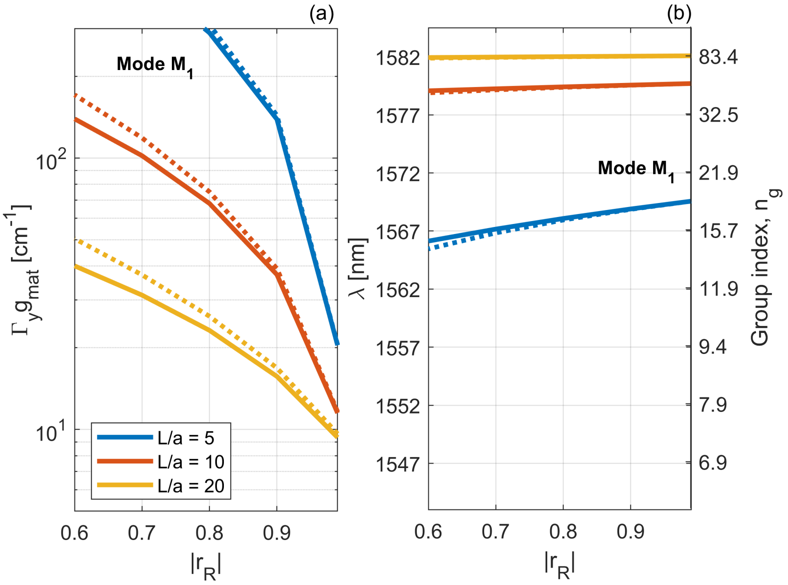

Figure 4.16: Oscillation condition of lasers with photonic bandgap mirrors. (a) Modal gain $\Gamma_y g_{\mathrm{mat}}$ and (b) wavelength at the lasing threshold of mode M_1 with (solid) and without (dotted) gain-induced distributed feedback versus the right mirror reflection coefficient. The colors denote different cavity lengths, with 5 (blue), 10 (red) and 20 (yellow) unit cells.

It is interesting to investigate the impact of distributed feedback in the case of higher threshold gain, as one would expect it to become more and more relevant as the gain increases. For this purpose, Fig. 4.16 illustrates (a) the modal threshold gain $\Gamma_y g_{\mathrm{mat}}$ and (b) corresponding wavelength for mode M_1 versus the right mirror reflection coefficient. In principle, this coefficient can be varied, for instance, by tuning the radius and/or position of the hole at the interface between the waveguide and the mirror [144, 2]. The solid (dotted) line is with (without) gain-induced distributed feedback. The cavity consists of 5 (blue), 10 (red) and 20 (yellow) unit cells. As r_R decreases, the threshold gain grows and the wavelength departs from the slow-light region. The distributed feedback does not have a great influence on the wavelength, as evident from Fig. 4.16(b). Therefore, the wavelength shift can be simply understood from Eq. (4.7b) and is due to the non-zero linewidth enhancement factor. On the oher hand, the distributed feedback appears to reduce the threshold gain. The reason for this reduction is not trivial and deserves closer inspection.

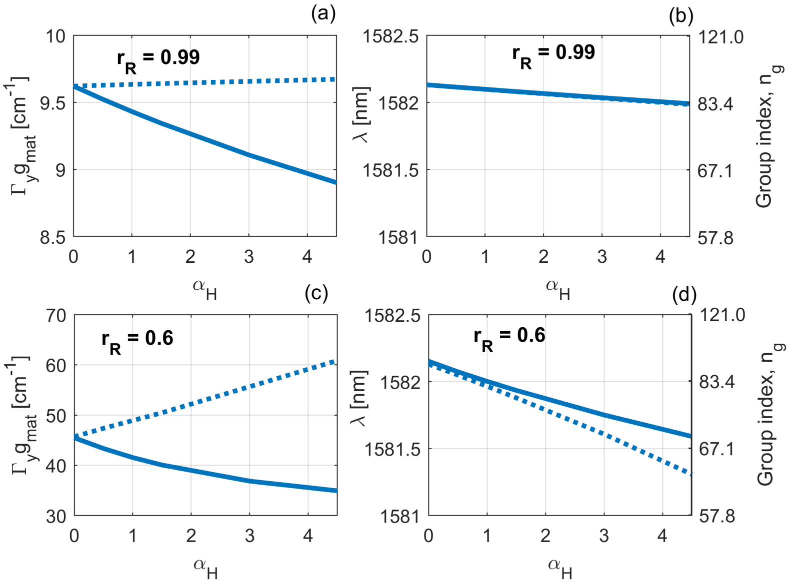

Figure 4.17: Oscillation condition of lasers with photonic bandgap mirrors. (a) and (c) Modal gain $\Gamma_y g_{mat}$ and (b) and (d) wavelength at the lasing threshold of mode M_1 with (solid) and without (dotted) gain-induced distributed feedback versus the linewidth enhancement factor. The right mirror reflection coefficient is (a) and (b) $r_R = 0.99$ and (c) and (d) $r_R = 0.6$. The cavity length is 8.76 μm, corresponding to 20 unit cells.

Thus, we select as an example the cavity with 20 lattice constants. In Fig. 4.17, we report for mode M_1 (a) and (c) the threshold gain and (b) and (d) corresponding wavelength versus the linewidth enhancement factor α_H. The solid (dotted) line is with (without) distributed feedback. The right mirror reflection coefficient is (a) and (b) $r_R = 0.99$ and (c) and (d) $r_R = 0.6$. Without distributed feedback, the wavelength is gradually detuned from the slow-light region as α_H increases. Therefore, the gain correspondingly grows, owing to the diminishing slow-down factor. On the contrary, a larger α_H reduces the threshold gain in the presence of distributed feedback, with the relative reduction enhanced by a smaller r_R. We emphasize that this occurs in spite of the wavelength shifting to the same direction with and without distributed feedback. Therefore, the non-zero linewidth enhancement factor appears to be responsible for the reduction of threshold gain enabled by distributed feedback and emphasizes the non-trivial nature of this phenomenon.

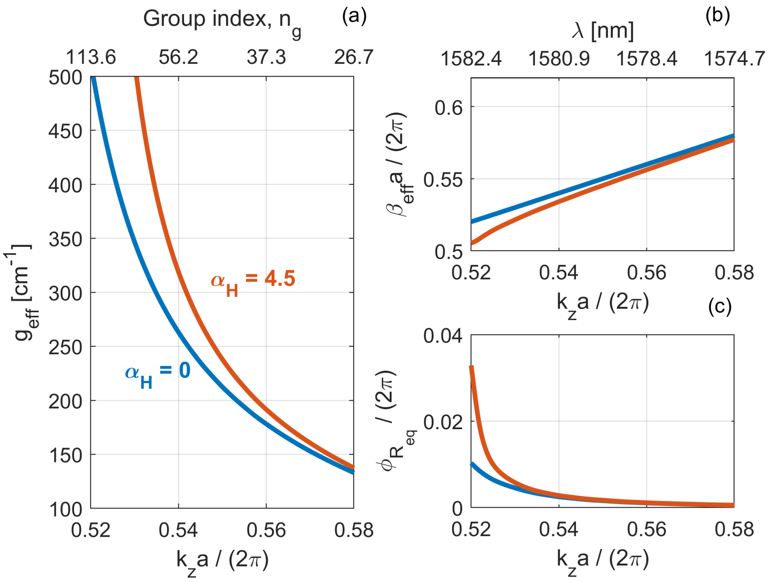

Figure 4.18: (a) Effective net modal gain, (b) effective propagation constant and (c) phase of the equivalent right mirror for $\alpha_H = 0$ (blue) and $\alpha_H = 4.5$ (red) in the presence of the gain-induced distributed feedback. The cavity length is 8.76 μm, corresponding to 20 unit cells. The modal gain is $\Gamma_y g_{\text{mat}} = 34.93\,\text{cm}^{-1}$, corresponding to the lasing threshold for $\alpha_H = 4.5$ and $r_R = 0.6$.

An interpretation is possible in light of Eqs. (4.6a) and (4.6b). Essentially, in the presence of distributed feedback and for a given value of the modal gain $\Gamma_y g_{\text{mat}}$, the net *effective* modal gain g_{eff} increases with the linewidth enhancement factor, as already discussed in Sec. 3.4.2. The larger g_{eff} enables lasing with a smaller value of $\Gamma_y g_{\text{mat}}$ in compliance with Eq. (4.6a). As an example, Fig. 4.18 depicts g_{eff} with distributed feedback for $\alpha_H = 0$ (blue) and $\alpha_H = 4.5$ (red). The cavity length corresponds to 20 unit cells and the modal gain to the lasing threshold for $\alpha_H = 4.5$ and $r_R = 0.6$. On the other hand, the peculiar impact of distributed feedback on the phase condition (see Eq. (4.6b)) dictates that the wavelength should depart from the band edge. Indeed, the decrease in the effective propagation constant β_{eff} at a given frequency with increasing α_H is counteracted by the increase in the phase of the equivalent right mirror $\phi_{R_{eq}}$. This mechanism is exemplified by Fig. 4.18(b) and (c), illustrating (b) the normalized effective propagation constant and (c) phase of the equivalent right mirror.

To summarize, the larger the linewidth enhancement factor, the greater the reduction of threshold gain enabled by distributed feedback. This result genuinely stems from Eqs. (4.7a) and (4.7b), which we have derived, and cannot be reproduced by Eqs.(4.6a) and (4.6b). It reveals that the gain-induced distributed feedback may be beneficial under certain circumstances, although the impact is negligible for realistic values of the right mirror reflection coefficient ($r_R \approx 0.99$). Furthermore, this result is somehow in contrast with our previous discussion in Chapter 3 on slow-light amplifiers. In fact, in Sec. 3.6 we have shown that, for a given material gain, amplifiers based on active photonic crystal waveguides with smaller linewidth enhancement factor α_H may offer better performance [139]. However, in that context one is interested in achieving a reasonable amplifier gain with negligible distributed reflection. Therefore, the amplifier is chosen to be much longer as compared to the laser cavities which we are considering in this chapter. Consequently, the amplifier gain at a given wavelength may indeed be enhanced by α_H, as already noted in Sec. 3.6. However, as a result of the long device length, the benefit is outperformed by the build-up of a huge reflection, which renders larger values of α_H detrimental rather than beneficial.

4.4.1 Impact of disorder

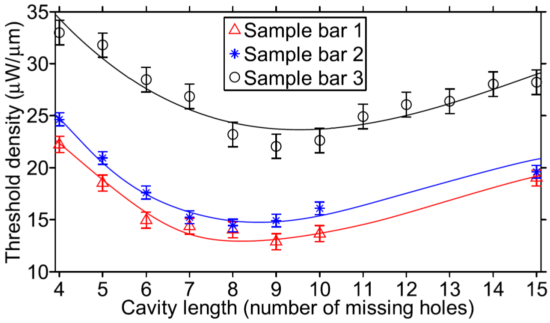

Figure 4.19: Oscillation condition of lasers with photonic bandgap mirrors. Measured threshold pump power density versus cavity length. Reproduced from [178].

In [178], quantum dot photonic crystal lasers with photonic bandgap mirrors have been characterized. A peculiar scaling of threshold gain as a function of cavity length has been reported and ascribed to the impact of disorder-induced losses due to unavoidable fabrication imperfections [178]. Specifically, an optimum cavity length has been found, which minimizes the threshold gain. This is illustrated in Fig. 4.19, which is reproduced from [178]. Furthermore, the wavelength of the lasing mode has been found to move towards the band edge in a *continuous* fashion with increasing cavity length, similarly to Fig. 4.12(c). Therefore, in the following we briefly investigate the impact of disorder.

As outlined in Sec. 3.6, α_1 and α_2 are phenomenological parameters which account for disorder-induced losses due to out-of-plane scattering and backscattering respectively [117]. We assume $\alpha_2 = 1.5\,\mathrm{cm}^{-1}$ [178] and $r_R = 0.99$ and solve the oscillation condition for the various longitudinal modes. For each mode, Fig. 4.20 reports (a) the

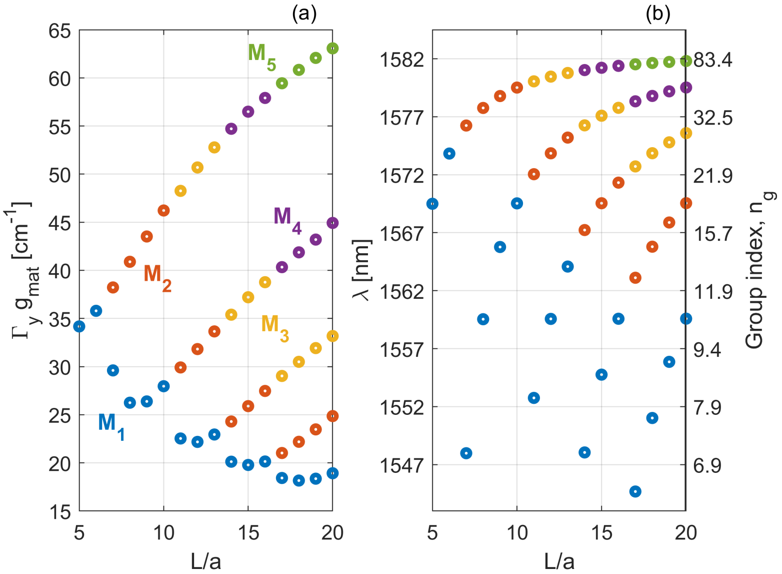

Figure 4.20: Oscillation condition of lasers with photonic bandgap mirrors in the presence of disorder. (a) Modal gain $\Gamma_y g_{\text{mat}}$ and (b) wavelength at the lasing threshold of the various longitudinal modes with $r_R = 0.99$ and $\alpha_2 = 1.5\,\text{cm}^{-1}$. Each color corresponds to a different longitudinal mode.

modal gain $\Gamma_y g_{\text{mat}}$ and (b) wavelength at the lasing threshold with gain-induced distributed feedback included. Neglecting the distributed feedback has no impact, revealing that it does not play a role in this case. Therefore, the results can be interpreted on the basis of Eqs. (4.7a) and (4.7b). The modes are numbered such that M_1 possesses the smallest threshold gain, with higher order modes having increasingly larger gain. In contrast to Fig. 4.12(a), the threshold gain of M_1 does not monotonically decrease as the cavity becomes longer. It features instead a succession of local minima, with each minimum stemming from the trade-off between slow-light enhancement of disorder-induced backscattering loss and slow-light reduction of the mirror loss. Indeed, these contributions scale, respectively, in direct and inverse proportion to the slow-down factor (see Eq. (4.7a)). However, as the cavity length increases, the phase condition pushes the wavelength closer to the band edge (see Eq. (4.7b)). Therefore, the lasing wavelength around a gain minimum and beyond a certain cavity length *discontinuously* jumps farther from the slow-light region, where lasing becomes more convenient (see the blue markers in Fig. 4.20(b)). This feature highlights that the phenomenological model of disorder based on α_2 cannot fully capture the experimental findings of [178], where no mode jump was observed.

To assess if the gain-induced distributed feedback may influence the solution of the oscillation condition with a non-zero value of α_2, we report in Fig. 4.21 (a) the modal

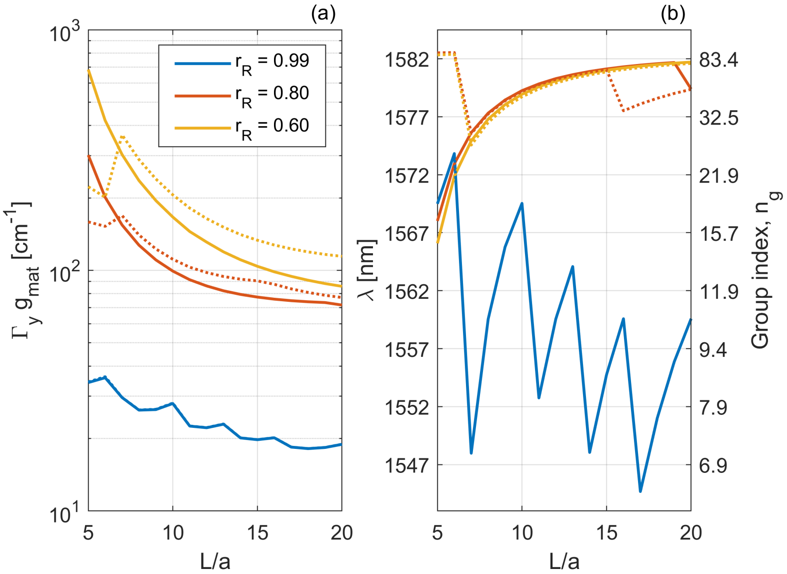

Figure 4.21: Oscillation condition of lasers with photonic bandgap mirrors in the presence of disorder. (a) Modal gain $\Gamma_y g_{\mathrm{mat}}$ and (b) wavelength of the lasing mode with $\alpha_2 = 1.5\,\mathrm{cm}^{-1}$. The colors denote different values of the right mirror reflection coefficient r_R. The solid (dotted) line is with (without) gain-induced distributed feedback.

gain $\Gamma_y g_{\mathrm{mat}}$ and (b) wavelength of the *lasing* mode with $\alpha_2 = 1.5\,\mathrm{cm}^{-1}$ and different values of r_R. The solid (dotted) line is with (without) gain-induced distributed feedback. Firstly, we note that lasing close to the band edge (i.e. mode M_0) is forbidden even without distributed feedback, owing to the strong disorder-induced losses. Secondly, as r_R decreases, the distributed feedback becomes more and more relevant. Eventually, the scaling of threshold gain with cavity length in the presence of distributed feedback becomes monotonic and no discontinuous jump in the lasing wavelength is observed. On the contrary, without distributed feedback discontinuous jumps in the lasing wavelength occur irrespective of how small r_R is. We have verified that larger values of α_2 and/or smaller values of r_R do not qualitatively alter this framework. This suggests that a competition exists between the gain-induced distributed feedback and the mechanism of disorder-induced loss governed by α_2, with the former eventually prevailing if the threshold gain is large enough.

To conclude, it should be mentioned that the interpretation of the experimental results of [178] is currently controversial. In fact, a recent investigation [15] employing a self-consistent Maxwell-Bloch model of quantum dot photonic crystal lasers has not come up with a definite conclusion. As already mentioned in Sec. 2.5.4, finite-difference time-domain simulations of passive cavities in [15] have not found a strong dependence of the quality factor on disorder. This clearly challenges the role of disorder as a major cause for the optimum in Fig. 4.19. On the other hand, the simulations of [15] in the presence of optical gain have not been able to fully reproduce the experimental findings of [178]. The inhomogeneous broadening of the quantum dot ensemble [146] has been taken into account. Various, possible positions for the frequency corresponding to the gain peak have been considered. Furthermore, simulations have been carried out with and without disorder. Nonetheless, the threshold gain has been essentially found to reach a plateau for long cavity lengths and no clear optimum has been observed. Therefore, we note that the sole inhomogeneous broadening of the quantum dot ensemble cannot explain the experimental findings of [178], as already noted therein.

4.4.2 Feedback-sustained lasing

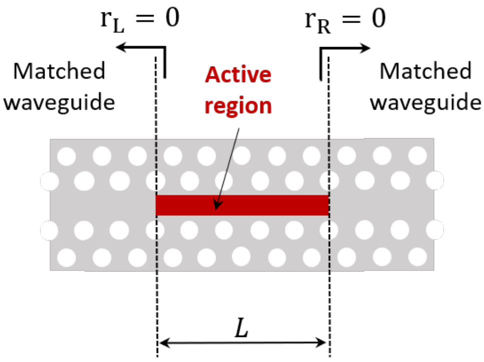

Figure 4.22: Laser with matched output waveguides.

From the principle point of view, it is interesting to investigate whether the sole gain-induced distributed feedback can sustain lasing with reasonable threshold gain. In Sec. 3.6, we have already noted that proper combinations of wavelength and modal gain may lead to feedback-sustained lasing (see Fig. 3.32). However, the active region in that case was longer as compared to the laser cavities investigated in the current chapter.

In the following, we examine the structure in Fig. 4.22, with L between 5 and 20 lattice constants. The optical gain is assumed to be limited to the line-defect. The left (right) mirror reflection coefficient r_L (r_R) is set to zero. From Eq. (4.5), the oscillation condition with $r_L = r_R = 0$ reads

$$r_+ r_- e^{+2i\lambda_+ L} = 1 \tag{4.13}$$

This equation corresponds to an effective Fabry-Perot resonator with complex propagation constant λ_+ and a left (right) facet with reflection coefficient r_- (r_+). Eq. (4.13) intuitively explains why we could expect lasing even for $r_L = r_R = 0$. Ideally, r_L and r_R are zero if 1) perfect refractive index matching is achieved at the interface with the active region and 2) the waveguides at either side of the active region are matched at the output. In practice, identically zero reflection coefficients cannot be achieved. However, various solutions have been proposed to approach the second condition, such as simple tapers [166] or more elaborated adapters [51]. Remarkably, the latter solution enables efficient coupling with conventional ridge waveguides even for extremely low group velocities.

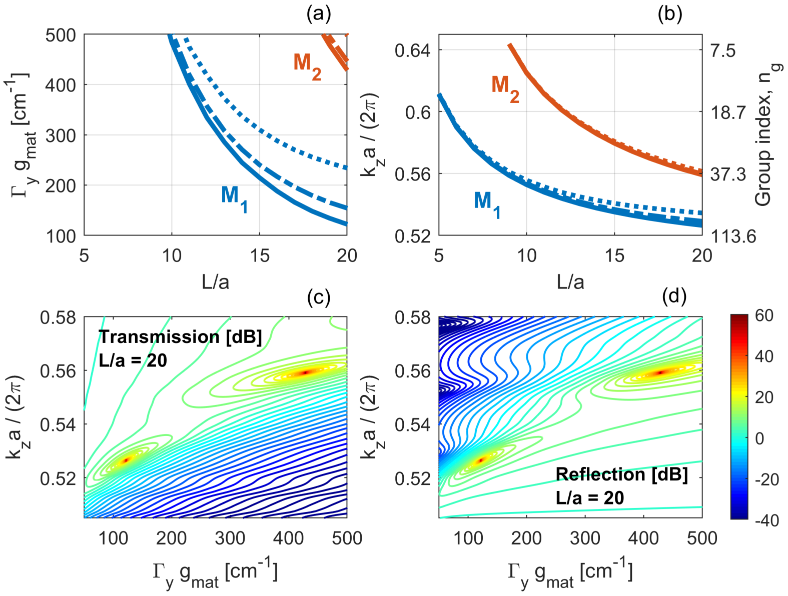

Figure 4.23: Oscillation condition of lasers with matched output waveguides. (a) Modal gain $\Gamma_y g_{\mathrm{mat}}$ and (b) wavenumber at the lasing threshold of the lasing mode (blue) and second-order mode (red) for the laser in Fig. 4.22. The loss coefficient α_2 is set to 0 (solid), 1.5 cm^{-1} (dash-dotted) and 6 cm^{-1} (dotted). (c) Transmission and (d) reflection spectra of the laser in Fig. 4.22 with the active region consisting of 20 unit cells and the loss coefficient α_2 set to 0.

Fig. 4.23 illustrates (a) the modal gain $\Gamma_y g_{\mathrm{mat}}$ and (b) wavenumber at the lasing threshold for the laser in Fig. 4.22. We have assumed $\alpha_1 = 5$ cm^{-1} and $\alpha_H = 1.5$. Only the lasing (blue) and second-order mode (red) are reported. The different line styles correspond to different values of the disorder-induced backscattering loss, with $\alpha_2 = 0$ (solid), 1.5 cm^{-1} (dash-dotted) and 6 cm^{-1} (dotted). The right y-axis in Fig. 4.23(b) reports the group index n_g of the reference waveguide. The figure highlights that long cavities can indeed achieve lasing with reasonable values of threshold gain and, importantly, group index. Indeed, group indices up to around 100 [112] or even larger [170] have been measured, albeit on silicon rather than InP. The threshold gain is considerably higher as compared to the structures with photonic bandgap mirrors. However, the output coupling efficiency is also much larger, being (ideally) unitary on either side.

As already noted in Sec. 3.6, the onset of lasing is accompanied by peaks in the laser transmission and reflection spectra. Fig. 4.23(c) and (d) show, respectively, the laser transmission ($|S_{12}|^2$) and reflection ($|S_{11}|^2$), versus the modal gain $\Gamma_y g_{\mathrm{mat}}$ and normalized wavenumber. The active region is 20 lattice constants long and the loss coefficient α_2 is set to 0. The position of the peaks in the transmission and reflection spectra is consistent with the modal gain and wavenumber at the lasing threshold reported, respectively, in Fig. 4.23(a) and (b). This clearly confirms that the peaks do correspond to the onset of lasing.

4.5 Lasers with photonic heterostructure mirrors

As already discussed in Sec. 2.1.1, a so-called *photonic* heterostructure is a connection in series of two or more photonic crystal waveguides with different *photonic* bandgaps [154]. The photonic band gap can be engineered by different techniques, such as tuning the lattice constant [155, 143], the waveguide width [162] or the slab refractive index [115]. In particular, the latter is the physical principle behind the effective longitudinal confinement of photons in LEAP lasers [160]. Specifically, a smaller (larger) refractive index results in blue-shift (red-shift) of the waveguide band edge.

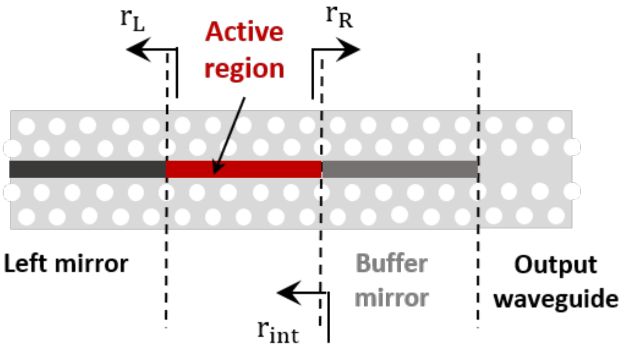

Figure 4.24: Laser with photonic heterostructure mirrors based on refractive index modulation.

Inspired by this principle, in this section we investigate the laser structure in Fig. 4.24 [137], consisting of four sections with slightly different values of the slab refractive index along the line-defect. By going from the left side to the right side, the first section is passive and has the smallest refractive index, thus acting as a left, broad-band mirror. The second section has a larger refractive index as compared to the first and includes the active region. The third section is passive, with a larger or smaller refractive index as compared to the active section. This third section connects the active region with the output waveguide, thus acting as a right, buffer mirror. Finally, the fourth section is the output waveguide, with the largest refractive index. According to the refractive index of the buffer mirror, we identify two configurations, namely Type I and Type II, as shown in Fig. 4.25. For each section, the pass-band (stop-band) frequency region is denoted in blue (red). As compared to the active section, the buffer mirror has a smaller

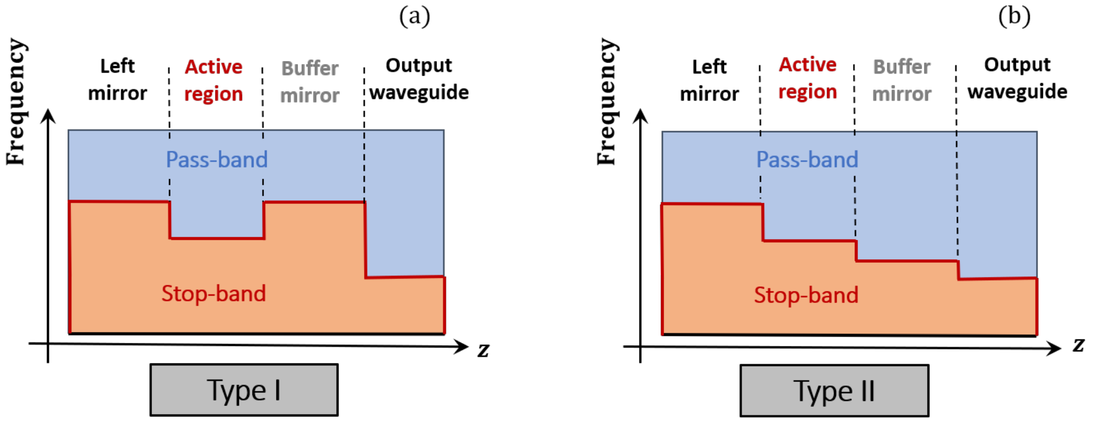

Figure 4.25: Laser with photonic heterostructure mirrors. (a) Type I and (b) Type II photonic heterostructure. As compared to the active section, the buffer mirror has a smaller (larger) refractive index in Type I (Type II).

(larger) refractive index for Type I (Type II). We note that Type I is similar to the configuration on which LEAP lasers are based (see Fig. 4.3(a)). The difference is that in a LEAP laser a single refractive index variation is present, with the active region having a smaller refractive index than the surroundings. Furthermore, in a LEAP laser the waveguide collecting the output power is not placed in line with the active region itself, but is laterally shifted. In the following, we solve the laser oscillation condition upon variation of the buffer mirror length, to emphasize how differently the two configurations behave in terms of threshold gain and output coupling efficiency. A similar investigation is carried out in [148] by finite-difference time-domain simulations, with qualititavely similar results. In that case, the heterostructure is formed by modulating the waveguide width.

We consider the output waveguide to be the reference waveguide of our modelling framework, for which we assume the parameters in Tab. 2.1 in Sec. 2.2.1. With respect to this waveguide, the other sections are viewed as perturbed, in the real and/or imaginary part of the slab refractive index. For the perturbed sections, we assume similar parameters as compared to [137]. The perturbation to the real part is $\Delta n_r = -0.002$ ($\Delta n_r = -0.001$) for the left mirror (active region). The left mirror (active region) length is 13.14 μm (4.38 μm), corresponding to 30 (10) lattice constants. The loss coefficients are $\alpha_1 = 5\,\text{cm}^{-1}$ and $\alpha_2 = 0$. Concerning the buffer mirror, the refractive index perturbation is $\Delta n_r = -0.002$ ($\Delta n_r = -0.0005$) for a Type I (Type II) heterostructure, while the length is varied from 5 to 30 lattice constants. For the linewidth enhancement factor of the active region, we assume $\alpha_H = 0$ as in [137]. A larger value of α_H would lead to the same qualitative results, provided that one also adjusts accordingly the refractive index perturbations of the various sections.

Fig. 4.26 shows (a) the power reflectivity and (b) phase of a buffer mirror being 30

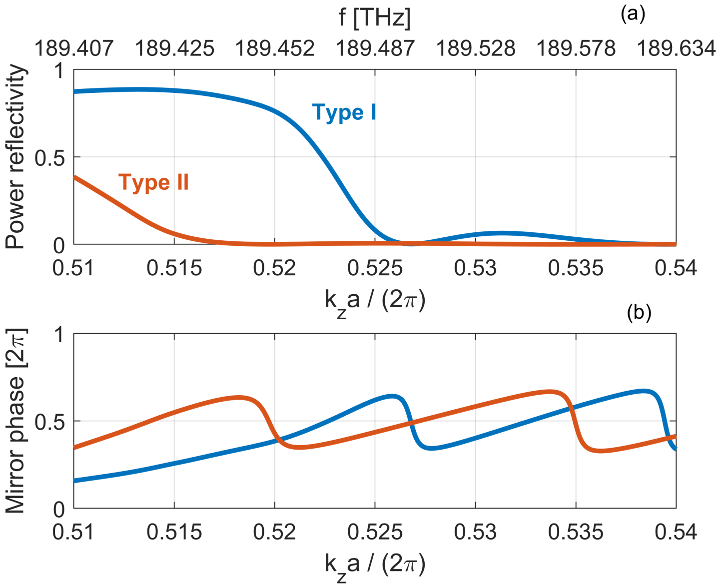

Figure 4.26: (a) Power reflectivity and (b) phase of the buffer mirror in Fig. 4.24 for a Type I (blue) and Type II (red) photonic heterostructure. The mirror is assumed to be 30 lattice constants long.

lattice constants long. The blue (red) line is for a Type I (Type II) heterostructure. As discussed in Sec. 3.4.1, the negative refractive index perturbation blue-shifts the band edge of the waveguide dispersion relation and induces a stopband, where the reflectivity is high. The larger the absolute perturbation is, the wider the stopband becomes and the higher the reflectivity.

For each section, the scattering parameters are computed by Eqs. (3.38a)-(3.38c) (see Sec. 3.5). The results on the oscillation condition are summarized in Fig. 4.27, reporting (a) the modal gain $\Gamma_y g_{\text{mat}}$, (b) wavenumber and (c) wavelength at the lasing threshold versus the length of the buffer mirror. The blue (red) line is for Type I (Type II) heterostructure. Higher-order modes are not reported, since they have a much larger threshold gain. For the Type I heterostructure, the lasing process is dominated by the reflections from the mirrors, with both of them generally providing high reflectivity. As the buffer becomes longer, its reflectivity increases and the laser threshold gain is monotonically reduced. On the other hand, the gain-induced distributed feedback strongly affects the lasing process for the Type II heterostructure, leading to the non-monotonic variation in the threshold gain as a function of the buffer length. In the following lines, we briefly examine this peculiarity with greater detail.

First of all, we note that the buffer mirror reflectivity for the Type II heterostructure is generally low, as understood from Fig. 4.26. Overall, this explains the larger threshold gain as compared to Type I (see Fig. 4.27(a)). The larger gain enhances the distributed feedback in the active region, leading to a strong and narrow resonance

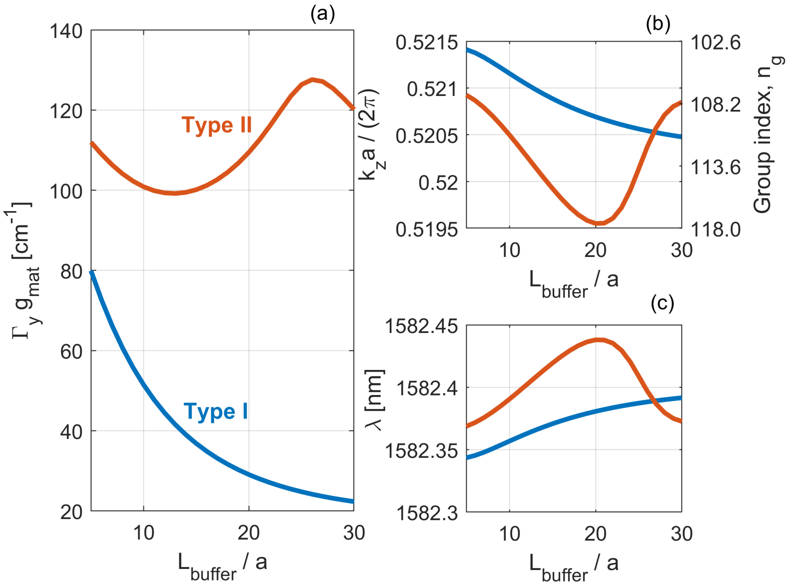

Figure 4.27: Oscillation condition of lasers with photonic heterostructure mirrors. (a) Modal gain $\Gamma_y g_{\mathrm{mat}}$, (b) wavenumber and (c) wavelength at the lasing threshold for a Type I (blue) and Type II (red) photonic heterostructure versus the length of the buffer mirror.

peak in the spectrum of the internal reflection coefficient r_{int}, as defined in Fig. 4.24. As the buffer length changes, its reflectivity generally remains low. Therefore, its impact on the threshold gain variation is negligible. However, the variation in the *phase* of the buffer reflection coefficient forces the laser frequency to adjust itself accordingly, in order to continue to fullfil the phase condition. The non-monotonic variation in the threshold gain stems from the oscillation frequency changing around the resonance peak of the internal reflection coefficient. Depending on the position of the oscillation frequency relative to the resonance peak, the threshold gain can either decrease or increase as the buffer length is varied. In fact, the variation in the oscillation frequency is limited (see Fig. 4.27(b) and (c)), but the resonance is narrow. As an example, Fig. 4.28 shows the magnitude of the internal reflection coefficient in the case of the buffer length equal to (a) 10 and (b) 20 lattice constants. For each case, the various colors denote different values of the modal gain $\Gamma_y g_{\mathrm{mat}}$. To show the evolution of the internal reflection coefficient from below the lasing threshold up to the threshold itself, blue, red an yellow correspond, respectively, to 80%, 90% and 100% of the threshold gain.

The Type II configuration has a larger threshold gain as compared to Type I, but also a greater output coupling efficiency, as already noted in [148]. Fig. 4.29 shows the power output coupling efficiency versus the length of the buffer mirror for the Type I (blue) and Type II (red) heterostructure. It has been computed as the power transmission through the buffer mirror at the lasing threshold. It is clear that the coupling

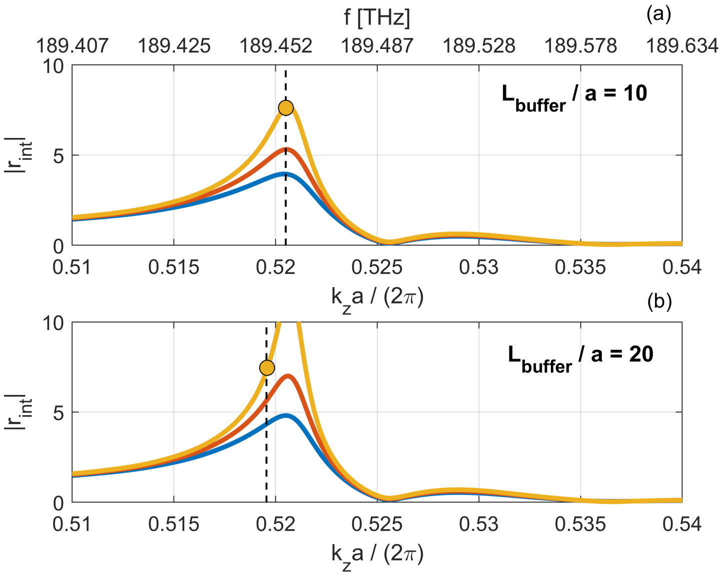

Figure 4.28: Magnitude of the internal reflection coefficient for a Type II heterostructure and the buffer being (a) 10 and (b) 20 lattice constants long. For a given buffer length, the blue, red an yellow line correspond, respectively, to 80%, 90% and 100% of the threshold gain. The black, vertical line denotes the oscillation frequency and the bullet the lasing point.

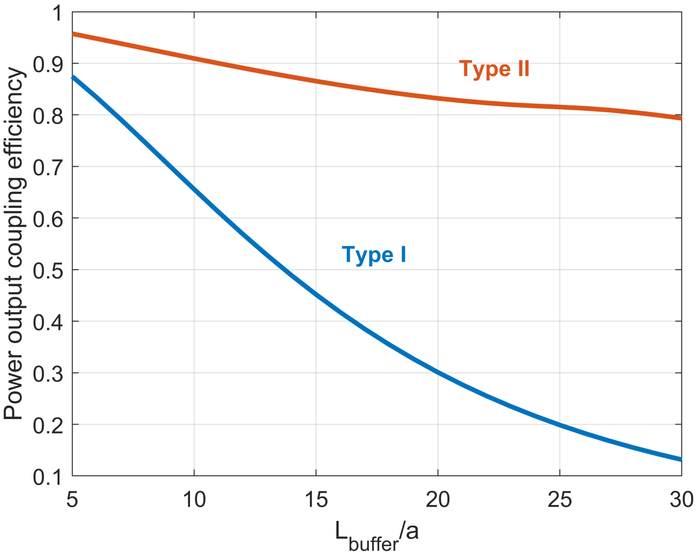

Figure 4.29: Power output coupling efficiency for a Type I (blue) and Type II (red) photonic heterostructure versus the length of the buffer mirror.

efficiency is generally higher for the Type II heterostructure and only slightly degrades as the buffer becomes longer. On the contrary, it strongly decreases for the Type I heterostructure, due to the steep increase in the reflectivity of the buffer mirror.

4.6 Fano laser

In this section, we investigate a new, recently proposed laser structure, the so-called Fano laser. A comprehensive review of the theory and current experimental status can be found in [102].

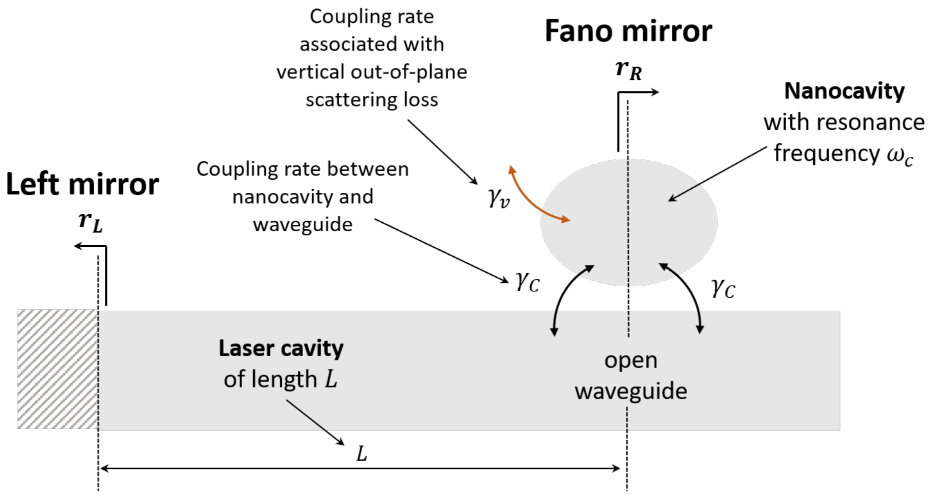

Figure 4.30: Schematic representation of a Fano laser.

The essence of this laser is the mirror, realized through coupling of the waveguide with a nanocavity located adjacently. A schematic representation is shown in Fig. 4.30. The Fano resonance is a general wave interference phenomenon [32, 96, 75]. The Fano mirror reflection does not arise from a discontinuity in refractive indices, but rather from the interference between two light paths: the direct waveguide path and the indirect waveguide-nanocavity-waveguide path. Around the nanocavity resonance frequency, the interference of these two paths is *destructive*. As a result, a narrowband reflection spectrum arises.

The current implementation of the Fano laser is based on the photonic crystal platform [184]. Therefore, the opportunities offered by the photonic crystal technology are combined with the rich physics of the Fano mirror. A comprehensive review of various optical signal processing applications exploiting the Fano resonance on the photonic crystal platform (thus not limited to lasers) is presented in [10]. Among the intriguing properties of the Fano laser (still to be fully explored), we cite ultrafast frequency modulation [100, 129], increased stability against external optical feedback [131], as well as passive [184] and active Q-switching [128].

To understand these features, it is of interest to examine the oscillation condition and tuning characteristics of the laser, i.e. in dependence of the cavity length or nanocavity resonance frequency. This is useful for both general design purposes and more specific applications. For instance, the Fano laser can be modulated via the mirror, by dynamically changing the nanocavity resonance frequency. The response of the threshold gain and oscillation frequency to variations of the nanocavity resonance frequency gives important indications on the on- and off-state of the laser (and transition from one to the other) in switching applications.

The current Fano laser models do not account for waveguide dispersion and, consequently, slow-light effects. In particular, a major assumption is that the Bloch modes travelling in the laser cavity are only coupled at the mirrors [132], thus neglecting the gain-induced distributed feedback associated with slow-light. The assumption is valid if the laser operates far from the band edge of the waveguide dispersion relation. This can be ensured by designing the nanocavity such that its resonance frequency lies far enough from the slow-light region.

However, there is a number of reasons to investigate how slow-light would affect the Fano laser characteristics. As for conventional line-defect lasers, the enhancement of the modal gain per unit length would positively impact on the device compactness and energy efficiency. Furthermore, owing to the extreme sensitivity of the oscillation condition to variations of the cavity length and/or nanocavity resonance frequency [132, 102], the additional strong coupling of the amplitude and phase conditions introduced by slow-light is likely to influence both the static and dynamic characteristics of the laser. For instance, slow-light would change the photon lifetime, which in turn would affect the relaxation resonance frequency and damping rate. An additional example is the likely effect on the tuning range required to switch on and off the laser in Q-switching applications.

The necessary starting point to assess the nature of such effects (and leverage them, if possible) is studying the Fano laser oscillation condition with proper inclusion of slow-light. This section presents the preliminary work carried out on this regard in collaboration with T. Rasmussen and J. Mørk during my stay at DTU Fotonik from January, 2020 to July, 2020.

4.6.1 Fano mirror

The Fano mirror can be modeled by temporal coupled-mode theory [46, 31]. The most general implementation of the Fano mirror on the photonic crystal platform may include a blocking air hole in the waveguide below the nanocavity (a so-called PTE, partially transmitting element) [185]. This PTE renders the mirror spectrum asymmetric with respect to the nanocavity resonance frequency, which can be useful in various applications [10, 128]. By displacing the PTE from the mirror plane, the parity of the resonance can also be controlled, thus blue- or red-shifting the reflection maximum as compared to the minimum.

In the following, we focus on the simplest implementation, without a PTE. In this case, one finds [100]

$$r_R(\omega) = \frac{-\gamma_c}{i(\omega_c - \omega) + \gamma_T} \tag{4.14}$$

Here, ω_c is the nanocavity resonance frequency and γ_c the coupling rate between nanocavity and waveguide, while γ_T is the total decay rate of the field in the nanocavity

$$\gamma_T = \gamma_c + \gamma_v + \gamma_p \tag{4.15}$$

This rate accounts for coupling with the waveguide (γ_c), vertical out-of-plane scattering loss (γ_v) and possible coupling to other ports (γ_p), if present. For each coupling rate, the corresponding Q-factor is defined as $Q_x = \omega_c/(2\gamma_x)$, with $x = T, c, v, p$. From Eq. (4.14), the maximum reflectivity is

$$|r_{R_{\max}}| = \frac{\gamma_c}{\gamma_T} = \frac{Q_T}{Q_c} \tag{4.16}$$

and achieved at ω_c. Therefore, it is clear that the peak reflectivity approaches unity for $Q_c \ll Q_T$. Since the waveguide can be strongly coupled to the nanocavity by reducing the distance between the two, this condition can be easily realized in practice.

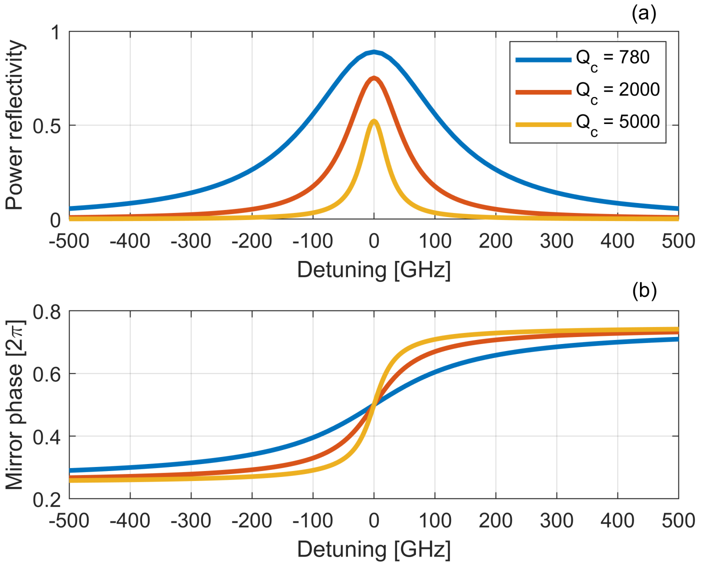

Figure 4.31: (a) Power reflectivity and (b) phase for a Fano mirror with $Q_v = 100000$ and $Q_p = 15000$ and different values of Q_c versus detuning from the resonance frequency. The assumed resonant wavelength is $\lambda_c = 1571$ nm.

The inclusion of another output port above the nanocavity, a so-called *cross-port* (not shown in Fig. 4.30), is not strictly necessary, but useful if one desires to improve the laser differential quantum efficiency [102]. In fact, if the laser operates around the nanocavity resonance frequency and no cross-port is included (i.e. $\gamma_p = 0$), the Fano mirror reflection is high and low power is coupled out to the waveguide below the nanocavity, the so-called *through-port*. If instead the cross-port is included, the total quality factor of the nanocavity is reduced somewhat, but the reduction is negligible if one ensures $Q_c \ll Q_v, Q_p$. The cross-port differential quantum efficiency is approximately proportional to [102]

$$\eta = \frac{Q_v}{Q_v + 2Q_p} \tag{4.17}$$

and can be easily maximized by simply ensuring $Q_p \ll Q_v$. Therefore, one obtains the practical design rule $Q_c \ll Q_p \ll Q_v$.

Fig. 4.31 shows (a) the power reflectivity and (b) phase of a Fano mirror with $Q_v = 100000$ and $Q_p = 15000$ and different values of Q_c. These are typical Fano mirror parameters [129]. As the coupling between nanocavity and waveguide weakens, the peak reflectivity decreases and the mirror bandwidth shrinks. Indeed, from Eq. (4.14) the full width at half maximum (FWHM) of the power reflectivity is given by $2\gamma_T/(2\pi)$, thus diminishing with decreasing γ_c. For the sake of convenience, γ_T is denoted in the following as the Fano mirror linewidth.

4.6.2 Tuning characteristics

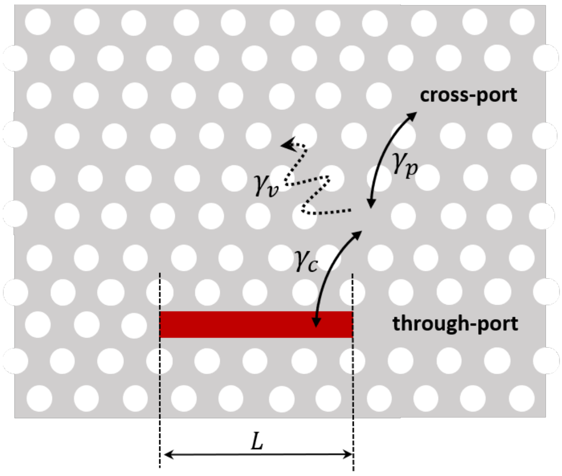

Figure 4.32: Fano laser implementation on the photonic crystal platform including the cross-port. The active region is denoted in red.

Fig. 4.32 shows the implementation of the Fano laser concept on the photonic crystal platform. The active region is denoted in red and limited to the line-defect part of the waveguide. The left mirror is a conventional photonic bandgap mirror.

In the following, we solve the laser oscillation condition upon variation of the cavity length L and nanocavity resonance frequency ω_c with slow-light effects included and the right mirror reflection coefficient r_R given by Eq. (4.14). We follow the approach of [132] and assume that the laser oscillates at a reference frequency ω_r when 1) the nanocavity resonance frequency ω_c coincides with ω_r and 2) the cavity length L is set to a reference value L_r. Therefore, for given L_r and ω_r, the left mirror phase ϕ_L is chosen such that a longitudinal mode lies at ω_r for the *cold* cavity. Then, we let either ω_c or L vary and solve for each value the oscillation condition.

To appreciate the impact of slow-light, we proceed in stages and make comparisons with the current modeling approaches [132, 129], which 1) neglect the gain-induced distributed feedback and 2) assume a fixed value for the group index. For this purpose, we consider the waveguide complex propagation constant with α_2 set to zero and *without* distributed feedback

$$\tilde{\beta}_{\text{eff}}(\omega, g_{\text{mat}}) = k_z(\omega) - \frac{i}{2}\frac{n_g(\omega)}{n_{\text{slab}}}\left[\Gamma_{\text{FF}}(\omega)\Gamma_y g_{\text{mat}}(1 - i\alpha_H) - \alpha_1\right] \tag{4.18}$$

By Taylor-expanding k_z to first order around ω_r and evaluating n_g at ω_r, we obtain

$$\tilde{\beta}_r(\omega, g_{\text{mat}}) = k_z(\omega_r) + \frac{\omega - \omega_r}{c} n_g(\omega_r) - \frac{i}{2}\frac{n_g(\omega_r)}{n_{\text{slab}}}\left[\Gamma_{\text{FF}}(\omega_r)\Gamma_y g_{\text{mat}}(1 - i\alpha_H) - \alpha_1\right] \tag{4.19}$$

which employs fixed values for the group index and confinement factor Γ_{FF}. The difference as compared to [132, 129] is just that these values are directly evaluated from the waveguide dispersion relation and not set a priori. In the following, Eq. (4.19) is our benchmark without slow-light.

Unless otherwise specified, we assume $|r_L| = 1$, $\alpha_1 = 5\,\text{cm}^{-1}$, $\alpha_2 = 0$ and $\alpha_H = 1.5$. The reference wavelength λ_r is 1571 nm, corresponding to a moderate group index n_g around 20. The reference cavity length is $L_r = 8.76\,\mu$m, corresponding to 20 unit cells. The Q-factors defining the Fano mirror are $Q_v = 100000$, $Q_p = 15000$ and $Q_c = 780$.

Tuning the resonance frequency

The photonic crystal platform provides several options to tune the nanocavity resonance frequency. The design parameters determining the resonance frequency are the membrane thickness, the hole radius, the lattice constant, the cavity geometry and the local refractive index [55]. In particular, the refractive index can be tuned by different approaches, such as thermally [170], electrically [44] or optically. Optical control through an out-of-plane excitation is well documented in the literature. In essence, by focusing an optical pulse on the nanocavity, the refractive index undergoes a nonlinear change. Such change is due to, e.g., plasma dispersion from excitation of free carriers by two photon absorption [35, 162] or optical Kerr effect. The latter is usually weaker, but can be strongly enhanced by embedding a bow-tie pattern inside the nanocavity, leading to extreme field confinement [48, 173]. Excitation schemes based on in-plane optical pulses have been also suggested [128], with clear benefits in terms of device

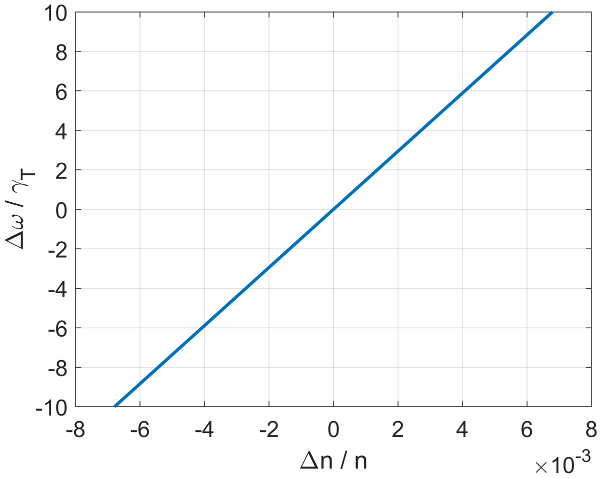

Figure 4.33: Nanocavity resonance frequency change normalized to the Fano mirror linewidth versus relative refractive index change.

integration. The relative refractive index change, $\Delta n/n$, necessary to induce a variation $\Delta\omega$ in the nanocavity resonance frequency, ω_r, can be estimated as [35]

$$\frac{\Delta n}{n} = \frac{\Delta\omega}{\omega_r} = \frac{\Delta\omega/\gamma_T}{2Q_T} \tag{4.20}$$

Fig. 4.33 shows the change in the nanocavity resonance frequency, normalized to the Fano mirror linewidth, as a function of the relative refractive index change. The Q-factor Q_T approximately amounts to 736, as resulting from the values of Q_v, Q_p and Q_c.

In the following, we set the cavity length L to the reference length L_r and solve the oscillation condition upon tuning of the resonance frequency. In the following figures, the x-axis reports the detuning of ω_c from ω_r, normalized to the Fano mirror linewidth γ_T. The modes are numbered in order of increasing threshold gain and denoted by different colors.

Firstly, we neglect slow-light and solve the oscillation condition by using Eq. (4.19) for the waveguide complex propagation constant. Fig. 4.34 shows (a) the modal gain $\Gamma_y g_{\text{mat}}$ and (b) effective detuning of ω_c from the oscillation frequency ω_s, normalized to the Fano mirror linewidth. Both the lasing mode (in blue) and second-order mode (in red) are reported. A number of features can be noted. The modal gain shows a succession of minima, occurring where ω_c (and thus the Fano mirror peak) aligns with a longitudinal mode of the laser cavity. The spacing of these modes is determined by the free spectral range of the cold cavity (within a small correction due to the linewidth enhancement factor). Since the group index is fixed, the minima are equally spaced. This is confirmed by Fig. 4.34(b), showing that the minima do correspond to zero effective detuning. The gain and effective detuning are periodic, with the same periodicity.

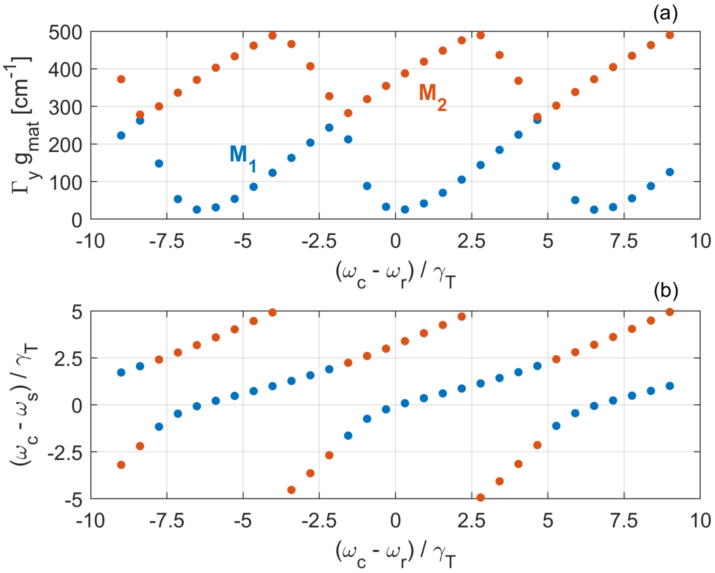

Figure 4.34: Frequency tuning characteristics of Fano lasers without slow-light effects. (a) Modal gain $\Gamma_y g_{\text{mat}}$ and (b) effective detuning of the nanocavity resonance frequency ω_c from the oscillation frequency ω_s, normalized to the Fano mirror linewidth γ_T. The x-axis reports the detuning of the nanocavity resonance frequency from the reference frequency, normalized to the mirror linewidth. The lasing mode M_1 is in blue, the second-order mode M_2 in red.

As ω_c departs from a gain minimum, the threshold gain increases, because the oscillation frequency is detuned from the mirror peak. However, the gain increases more strongly in one detuning direction as compared to the other. The asymmetry is due to the non-zero linewidth enhancement factor and can be understood from the following argument [129]. As the oscillation frequency is detuned from the mirror peak and the gain grows, the contribution to the phase condition associated with the linewidth enhancement factor α_H always has the same sign, irrespective of the detuning direction. On the contrary, since the Fano mirror phase is an anti-symmetric function of detuning (see Fig. 4.31(b)), its contribution can either enhance that resulting from α_H or partially compensate for it. Consequently, the oscillation frequency will be forced to a larger or smaller detuning from the mirror peak (see Fig. 4.34(b)), with a corresponding higher or lower gain (see Fig. 4.34(a)). Finally, we note that the lasing mode is always the closest to the Fano mirror peak and nearly tracks the nanocavity resonance frequency within few mirror linewidths, as evident from Fig. 4.34(b).

We can now make a step forward and include the group index dispersion, but still neglecting the gain-induced distributed feedback. This amounts to using Eqs. (4.7a) and (4.7b) as amplitude and phase condition respectively. Fig. 4.35 shows (a) the threshold gain and (b) effective detuning for the lasing mode (in blue) and two higher-order

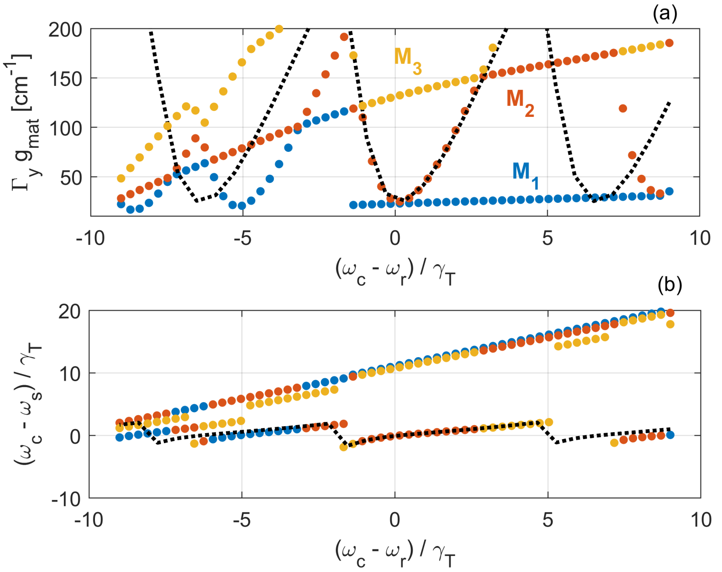

Figure 4.35: Frequency tuning characteristics of Fano lasers with group index dispersion, but without gain-induced distributed feedback. (a) Modal gain $\Gamma_y g_{\mathrm{mat}}$ and (b) effective detuning of the nanocavity resonance frequency ω_c from the oscillation frequency ω_s, normalized to the Fano mirror linewidth. The lasing mode M_1 is in blue. M_2 (red) and M_3 (yellow) are higher-order modes. The lasing mode without slow-light effects from Fig. 4.34 is also shown (dotted, black line).

modes. Additional modes do exist, but are not shown for the sake of clarity. The dotted, black line is the lasing mode without slow-light effects (from Fig. 4.34). The inclusion of the full waveguide dispersion triggers a strong competition among the various longitudinal modes, resulting in relevant differences as compared to Fig. 4.34. First of all, the lasing mode is not necessarily the least detuned from the Fano mirror peak. In particular, since the group index strongly increases towards the slow-light region, the amplitude condition suggests that the lasing mode may even not be the closest to the mirror peak, but the closest to the band edge (if the phase condition can be simultaneously fulfilled). This is indeed the case for a wide range of detuning values (all those for which the blue markers in Fig. 4.35(b) are far from zero effective detuning). Secondly, the level of the gain minima, irrespective of their location, decreases as ω_c moves to lower frequencies. In fact, the deeper ω_s falls into the slow-light region and the larger the enhancement of the modal gain per unit length is. We also note that the gain minima are not equally spaced. The spacing shrinks as ω_c approaches the band edge, owing to the decrease of the free spectral range. Finally, it should be highlighted how the solution without slow-light effects fundamentally captures the response of M_2 around the reference frequency (which makes sense), but cannot reproduce the competition with the other modes, especially close to the band edge.

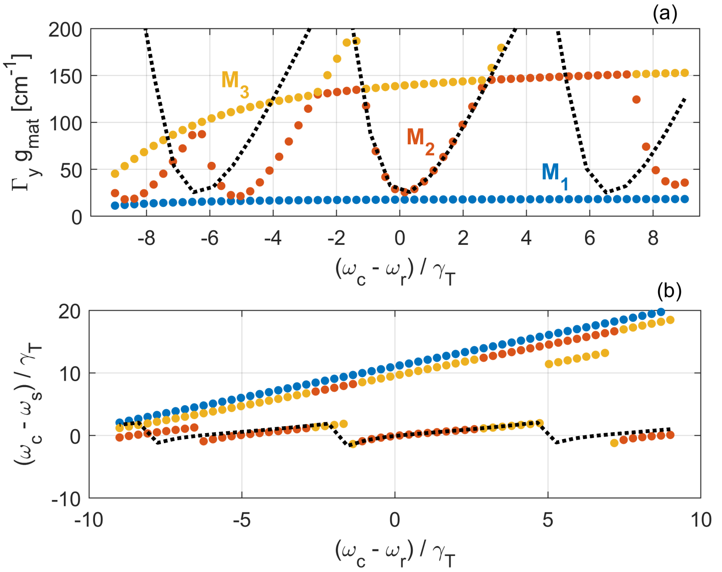

Figure 4.36: Frequency tuning characteristics of Fano lasers with group index dispersion and gain-induced distributed feedback. (a) Modal gain $\Gamma_y g_{\text{mat}}$ and (b) effective detuning of the nanocavity resonance frequency ω_c from the oscillation frequency ω_s, normalized to the Fano mirror linewidth. The lasing mode M_1 is in blue. M_2 (red) and M_3 (yellow) are higher-order modes. The lasing mode without slow-light effects from Fig. 4.34 is also shown (dotted, black line).

We are now ready to include the gain-induced distributed feedback in addition to group index dispersion, that is using Eqs. (4.6a) and (4.6b) for the amplitude and phase condition respectively. The results are summarized in Fig. 4.36, showing (a) the threshold and (b) effective detuning. For the sake of clarity, the first three modes are only shown. The solid, black line is the lasing mode without slow-light effects from Fig. 4.34. As compared to Fig. 4.35, a striking difference can be noticed. The lasing mode is always the closest to the band edge, rather than to the Fano mirror peak. This result is somewhat counterintuitive. In fact, from the discussions on the impact of distributed feedback on lasers with photonic bandgap mirrors in Sec. 4.4 (see, in particular, Fig. 4.12 and Fig. 4.13), one would probably expect the distributed feedback to inhibit the mode deep in the slow-light region. However, the difference here is that we have finely tuned the phase of the left mirror ϕ_L to align a longitudinal mode of the cold cavity with the Fano mirror peak. As a side effect, owing to the distributed feedback, the non-zero value of ϕ_L results in a resonant peak in the magnitude of the internal reflection coefficient r_{int}. On this regard, see the brief discussion in Sec. 4.3.2 in relation to Fig. 4.10. Around this resonance, the amplitude and phase condition can be simultaneously fulfilled, leading to mode M_1 in Fig. 4.36. This example emphasizes the non-trivial nature of distributed feedback.

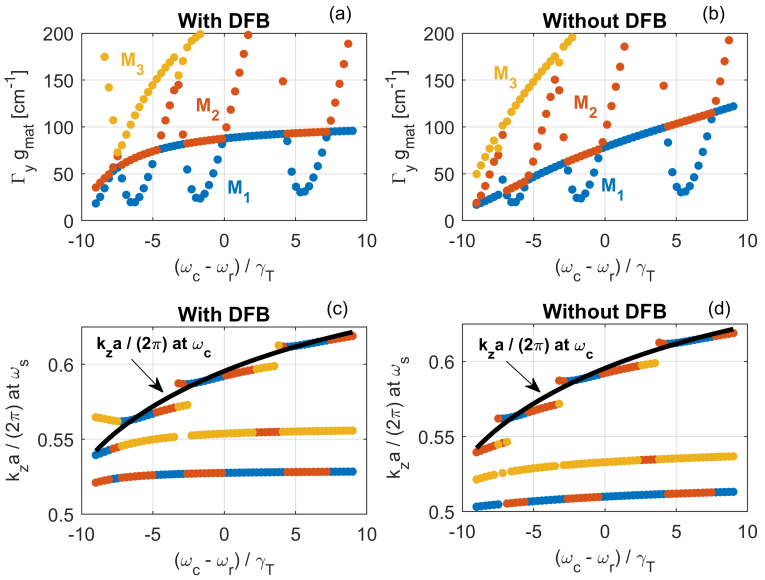

Figure 4.37: Frequency tuning characteristics of Fano lasers with group index dispersion and without adjustment of the left mirror phase. (a) and (b) Modal gain $\Gamma_y g_{\mathrm{mat}}$ and (c) and (d) wavenumber k_z at the lasing threshold of mode M_1 (blue), M_2 (red) and M_3 (yellow). (a) and (c) are with distributed feedback, (b) and (d) without it. The solid, black line in (c) and (d) is k_z evaluated at the nanocavity resonance frequency ω_c.

However, one should consider that the group index n_g corresponding to mode M_1 in Fig. 4.36 is extremely large (around 1000) and such huge values have not been reported experimentally. In addition, it is not clear how the fine tuning of the left mirror phase leading to mode M_1 could be accomplished in practice. Finally, it should be emphasized that if the application requires to control the laser via the Fano mirror, lasing on mode M_1 is obsviously undesirable. For these reasons, it is interesting to investigate the case without adjustment of the left mirror phase (similarly to Sec. 4.4) by leaving the other parameters unchanged. This is in fact the case of practical interest.

Therefore, we report in Fig. 4.37 the frequency tuning characteristics with group index dispersion included and ϕ_L set to zero. Fig. 4.37 (a) and (c) include the gain-induced distributed feedback, which is instead neglected in (b) and (d). Fig. 4.37(a) and (b) show the modal gain $\Gamma_y g_{\mathrm{mat}}$ at the lasing threshold of mode M_1 (blue), M_2 (red) and M_3 (yellow). The corresponding wavenumber k_z is depicted in Fig. 4.37(c) and (d), while the solid, black line is k_z evaluated at the nanocavity resonance frequency. Since the left mirror phase is not adjusted, the reference frequency has no special role in this case and no gain minimum occurs when ω_c is around ω_r (see Fig. 4.37(a) and (b)). However, all the minima correspond to lasing close to the Fano mirror peak, as evident from Fig. 4.37(c) and (d). Furthermore, we note that oscillation close to the band edge is indeed suppressed by the distributed feedback. On the contrary, lasing close to the band edge can still occur if the distributed feedback is neglected. We also note that the distributed feedback generally improves the gain margin, defined as the difference between the threshold gain of M_2 and M_1.

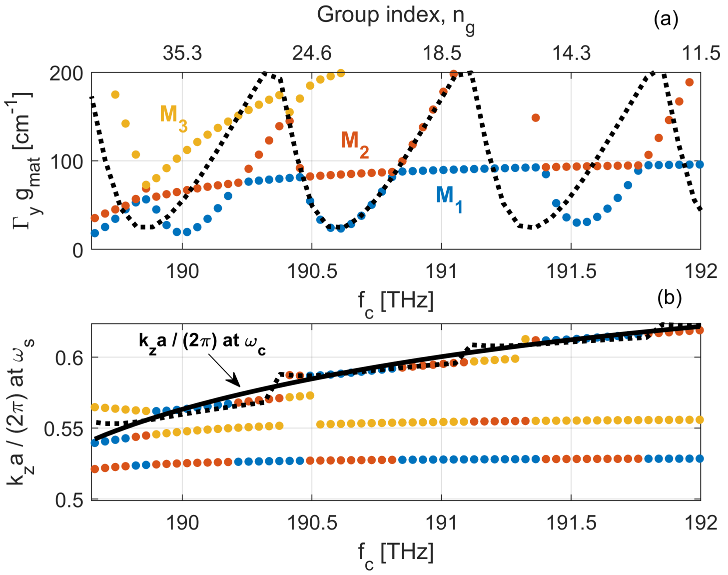

Figure 4.38: Frequency tuning characteristics of Fano lasers with group index dispersion, gain-induced distributed feedback and without adjustment of the left mirror phase. (a) Modal gain $\Gamma_y g_{\mathrm{mat}}$ and (b) wavenumber k_z at the lasing threshold of mode M_1 (blue), M_2 (red) and M_3 (yellow). The bottom x-axis reports the nanocavity resonance frequency $f_c = \omega_c/(2\pi)$. The top x-axis in (a) shows instead the group index n_g. The lasing mode without slow-light effects from Eq. (4.19) is also included (dotted, black line), with the reference frequency for the Taylor expansion set to around 190.6 THz. The solid, black line in (b) is k_z evaluated at the nanocavity resonance frequency.

To summarize, we report again in Fig. 4.38 the frequency tuning characteristics with group index dispersion, gain-induced distributed feedback and without adjustment of the left mirror phase. This time, the bottom x-axis shows the absolute value of the nanocavity resonance frequency in THz, while the top x-axis in (a) reports the group index n_g. Fig. 4.38(a) illustrates the modal gain $\Gamma_y g_{\mathrm{mat}}$ at the lasing threshold of mode M_1 (blue), M_2 (red) and M_3 (yellow). Similarly, Fig. 4.38(b) shows the wavenumber k_z at the lasing threshold of these three modes. The solid, black line in (b) is instead k_z evaluated at the nanocavity resonance frequency. Furthermore, in both Fig. 4.38(a) and (b) we have included the lasing mode without slow-light effects from Eq. (4.19) (dotted, black line). In this case, the reference frequency for the Taylor expansion is set to around 190.6 THz, corresponding to one of the gain minima. Fig. 4.38 compares the ”full” model, given by Eqs. (4.6a) and (4.6b), with the ”approximate” model, based on

Eq. (4.19). The latter essentially corresponds to the modelling approach so far documented in the literature [129]. The threshold gain features a succession of minima, with each minimum corresponding to the alignment of the nanocavity resonance frequency (i.e. the Fano mirror peak) with a mode of the laser cavity. As expected, the two models agree well close to the reference frequency used for the Taylor expansion. However, Eqs. (4.6a) and (4.6b) generally reveal a much stronger competition between the lasing mode and higher-order modes. As a result of this competition, a much smaller detuning from a gain minimum than predicted by Eq. (4.19) is sufficient to induce lasing far from the Fano mirror peak. In particular, the competition intensifies as the nanocavity resonance frequency is detuned towards the slow-light region. Therefore, operation with moderate slow-light may be advantageous, because the threshold gain would benefit from the slow-light reduction of mirror loss. However, operation deep in the slow-light region should be avoided if one wishes to control the laser via the Fano mirror.

Tuning the cavity length

The cavity length is usually changed in integer steps of the photonic crystal lattice constant. However, it should be emphasized that the electric field has a non-zero penetration depth within the left mirror. In addition, perfect control of the phase of none of two mirrors is achievable in practice. Therefore, in the following we allow fractional variations of L in terms of the photonic crystal lattice constant as in [129] and interpret L as an *effective* cavity length.

We set ω_c to ω_r and solve the oscillation condition upon tuning of the cavity length. In the following figures, the x-axis reports the cavity length L normalized to the reference cavity length L_r. Again, the modes are numbered in order of increasing threshold gain and denoted by different colors.

First of all, we neglect slow-light effects, thus using Eq. (4.19) for the waveguide complex propagation constant. Fig. 4.39 summarizes the results which one obtains in this case. The lasing mode is in blue, the second-order (third-order) mode in red (yellow). Fig. 4.39(a) reports the modal threshold gain $\Gamma_y g_{\mathrm{mat}}$, which shows a succession of minima similarly to Fig. 4.34(a). As the cavity length is varied, the oscillation frequency has to change as well, in order to continue to fulfill the phase condition. The gain minima occur whenever the oscillation frequency aligns with the nanocavity resonance frequency, where the Fano mirror reflectivity is maximum. This is confirmed by Fig. 4.39(b), reporting the effective detuning of the nanocavity resonance frequency ω_c from the oscillation frequency ω_s, normalized to the Fano mirror linewidth. The asymmetry in the response arises from the non-zero linewidth enhancement factor, similarly to what observed above in connection with the frequency tuning characteristics. We also note that the threshold gain at each minimum decreases with increasing cavity length, which is hard to see on the figure due to the scale. Finally, it should be emphasized the extreme sensitivity of the response to length tuning [129]. A variation of 1% of L with respect to L_r is enough to more than double the threshold gain as compared

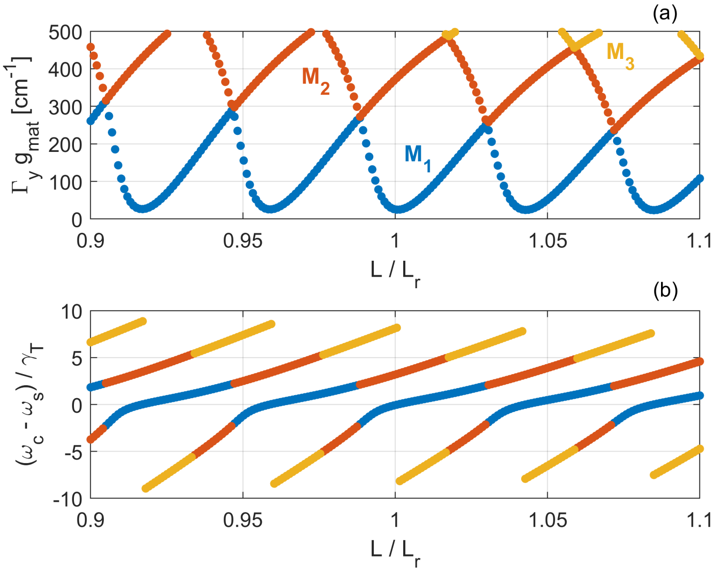

Figure 4.39: Length tuning characteristics of Fano lasers without slow-light effects. (a) Modal gain $\Gamma_y g_{\mathrm{mat}}$ and (b) effective detuning of the nanocavity resonance frequency ω_c from the oscillation frequency ω_s, normalized to the Fano mirror linewidth γ_T. The x-axis reports the ratio between the cavity length and reference cavity length. The lasing mode is in blue, the second-order (third-order) mode in red (yellow).

to one minimum.

We now include the group index dispersion, but still neglect the distributed feedback. Fig. 4.40 depicts (a) the threshold and (b) effective detuning of ω_c from ω_s. The dotted, black line is the lasing mode without slow-light effects from Fig. 4.39. Similarly to Fig. 4.35, the modes deep into the slow-light region strongly compete for lasing with that close to the Fano mirror peak. As L departs from L_r, the detuning of the oscillation frequency from the mirror peak (required to fulfill the phase condition) may become so large that lasing close to the band edge is instead more convenient. If lasing occurs there, the threshold gain strongly diminishes with increasing L. This is because the oscillation frequency gradually moves closer to the band edge and the mirror loss is increasingly reduced by slow-light (similarly to what happens for lasers with photonic bandgap mirrors). As expected, the mode competition is not captured by the black, dotted line.

We finally also include the gain-induced distributed feedback. The results are illustrated in Fig. 4.41, with (a) threshold gain and (b) effective detuning. The lasing mode without slow-light effects (dotted, black line) only captures the response around the Fano mirror peak. Interestingly, the mode competition appears even more complicated than in Fig. 4.36. Indeed, the response shows several additional branches (see

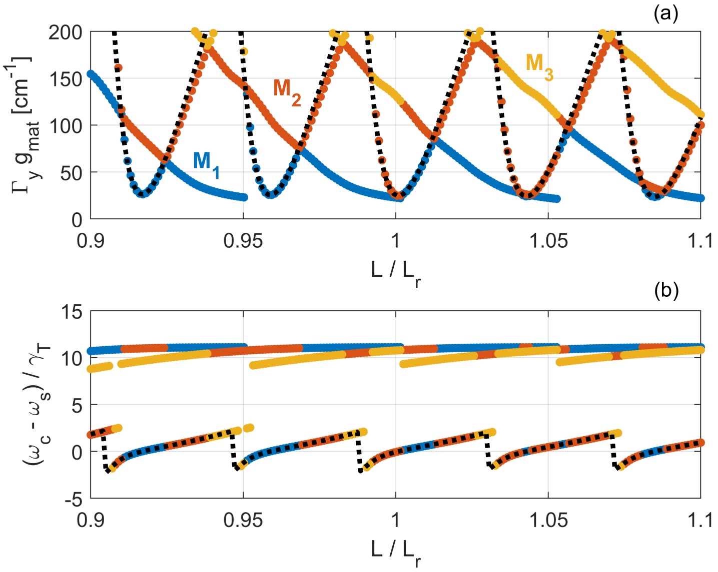

Figure 4.40: Length tuning characteristics of Fano lasers with group index dispersion, but without gain-induced distributed feedback. (a) Modal gain $\Gamma_y g_{\text{mat}}$ and (b) effective detuning of the nanocavity resonance frequency ω_c from the oscillation frequency ω_s, normalized to the Fano mirror linewidth. The lasing mode M$_1$ is in blue. M$_2$ (red) and M$_3$ (yellow) are higher-order modes. The lasing mode without slow-light effects from Fig. 4.39 is also shown (dotted, black line).

Fig. 4.41(a)), with local gain minima other than those reproduced without slow-light effects. The threshold gain variation around each of these additional minima corresponds to changes in the oscillation frequency *far away* from the mirror peak (see Fig. 4.41(b)). Therefore, these minima cannot be ascribed to variations in the Fano mirror reflectivity. On the contrary, they stem from lasing around narrow resonances due to the gain-induced distributed feedback. Therefore, they appear to be a peculiar slow-light effect, which deserves closer inspection.

As an example, we select one of these branches with gain minima far away from the mirror peak and report it in Fig. 4.42, with (a) modal gain and (b) normalized effective detuning. Any other branch would only lead to quantitative changes, with the qualitative analysis being the same. We note how the excursion of the oscillation frequency along the branch (see Fig. 4.42(b)) is quite limited. Interestingly, a slight increase in the cavity length is sufficient to approximately double the threshold gain (see Fig. 4.42(a)). To better understand this behaviour, we depict in Fig. 4.43 the amplitude of the cavity complex loop gain, with the cavity length set to the three values denoted by arrows in Fig. 4.42. The different colors correspond to L equal to L_1 (blue), L_2 (red) and L_3 (yellow). The modal gain $\Gamma_y g_{\text{mat}}$ corresponds to the lasing threshold for $L = L_1$. The black, vertical line denotes the oscillation frequency for this value of cavity length and

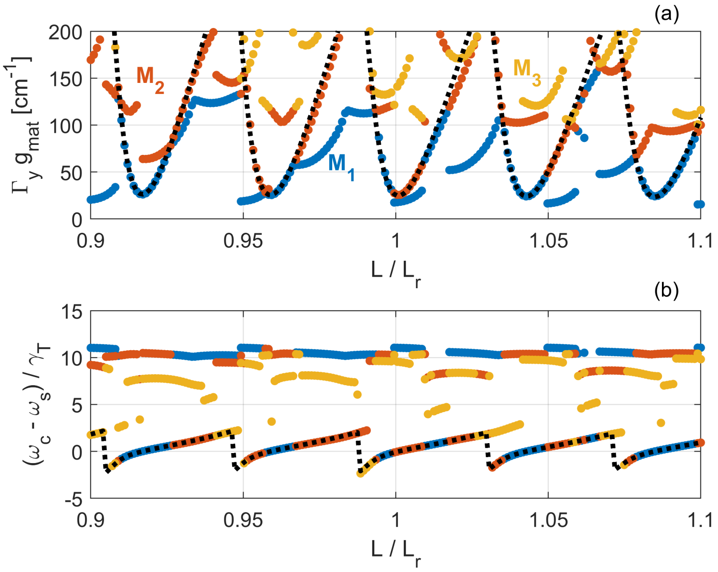

Figure 4.41: Length tuning characteristics of Fano lasers with group index dispersion and gain-induced distributed feedback. (a) Modal gain $\Gamma_y g_{\mathrm{mat}}$ and (b) effective detuning of the nanocavity resonance frequency ω_c from the oscillation frequency ω_s, normalized to the Fano mirror linewidth. The lasing mode M_1 is in blue. M_2 (red) and M_3 (yellow) are higher-order modes. The lasing mode without slow-light effects from Fig. 4.39 is also shown (dotted, black line).

the bullet the lasing point, where the loop gain is unitary. The figure reveals that a cavity length increase reduces the intensity of the resonance peak around the oscillation frequency for a given value of modal gain. Thus, the modal gain for which L_1 achieves lasing is insufficient to make L_2 or L_3 lase. In fact, the loop gain does not reach unity in these two cases. Consequently, the modal gain is forced to grow in order to fullfil the oscillation condition, which explains the increase in Fig. 4.42(a). The slight variation in the oscillation frequency (see Fig. 4.42(b)) is dictated by the necessity to simultaneously fulfill the condition on the phase of the complex loop gain (for simplicity, not shown here). This slow-light effect is somehow analogous to the non-monotonic variation of threshold gain which we have discussed in Sec. 4.5, in the case of the Type II photonic heterostructure (see Fig. 4.27 in Sec. 4.5). In that case, as a result of tuning of the buffer mirror length, the oscillation frequency moves around a resonance caused by the gain-induced distributed feedback. Thus, an optimum buffer length exists which minimizes the threshold gain.

Finally, it should be emphasized that the intricate charateristics of Fig. 4.41, with multiple and possibly non-monotonic gain branches far away from the Fano mirror peak, appear to be a genuine distributed feedback effect, irrespective of the phase of the left mirror. Indeed, without adjustment of the left mirror phase, i.e. by setting

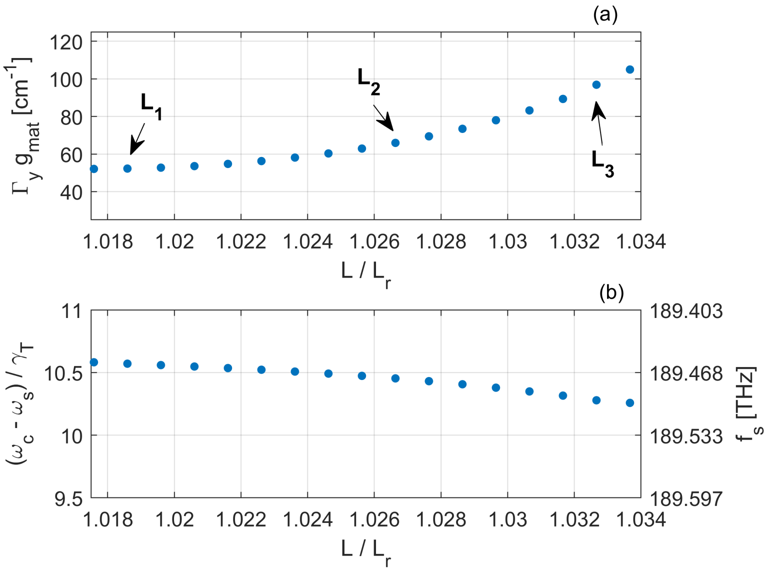

Figure 4.42: Length tuning characteristics of Fano lasers with group index dispersion and gain-induced distributed feedback. (a) Modal gain and (b) normalized effective detuning (right) and absolute oscillation frequency (left) for one of the branches in Fig. 4.41 with oscillation frequency far from the Fano mirror peak. The arrows denote the values of cavity length for which the complex loop gain in Fig. 4.43 is shown.

$\phi_L = 0$, we have only found quantitative, but not qualitative changes.

4.7 Conclusions

To summarize, we have investigated the impact of slow-light and gain-induced distributed feedback on the oscillation condition of photonic crystal lasers based on line-defect waveguides. This analysis extends to lasers the theoretical framework developed in Chapter 3.

In the presence of slow-light, the oscillation condition is described by Eqs. (4.6a) and (4.6b), derived in Sec. 4.2. These equations account for the gain-induced distributed feedback intrinsically associated with slow-light. Thus, they generalize Eqs. (4.7a) and (4.7b), which are conventionally employed to model the oscillation condition of slow-light photonic crystal lasers [178].

Equivalently, the oscillation condition may be expressed by Eq. (4.8) in Sec. 4.3, where the internal reflection coefficient r_{int} is generally given by Eq. (4.11). This is the reflection coefficient of the backward-propagating Bloch mode at the reference plane between the active region and right mirror (see Fig. 4.6). Therefore, r_{int} encompasses both the left mirror reflection coefficient and roundtrip gain, with the latter including the

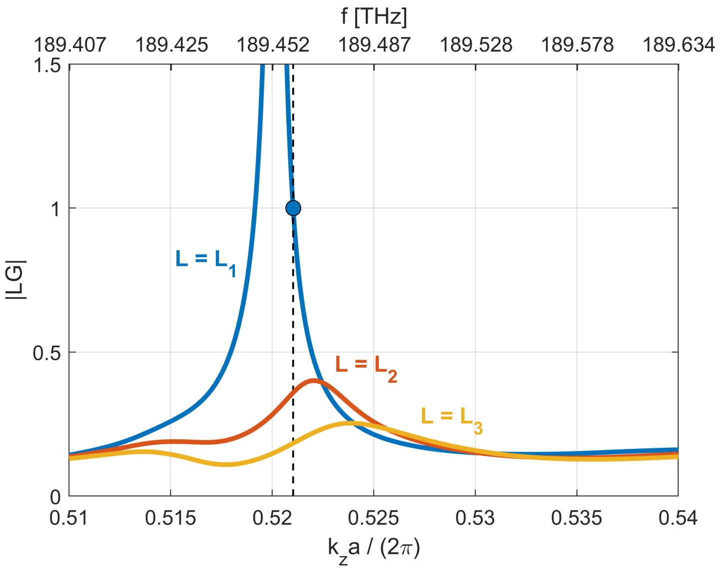

Figure 4.43: Length tuning characteristics of Fano lasers with group index dispersion and gain-induced distributed feedback. Amplitude of the cavity complex loop gain, with the cavity length set to L_1 (blue), L_2 (red) and L_3 (yellow) indicated in Fig. 4.42(a). The modal gain $\Gamma_y g_{\text{mat}}$ corresponds to the lasing threshold of the cavity with $L = L_1$. This modal gain is insufficient to make L_2 or L_3 lase. The black, vertical line denotes the oscillation frequency for $L = L_1$ and the bullet the lasing point.

gain-induced distributed feedback in the active region. As a result, the internal reflection coefficient shows a complicated dependence on frequency and gain, with a strong coupling between amplitude and phase (see Fig. 4.8). Deep into the slow-light region, the magnitude shows multiple resonances and eventually decreases if the group index is sufficiently high. This behaviour reflects the block diagram of the laser cavity in Fig. 4.7.

In Sec. 4.4, we have investigated lasers with photonic bandgap mirrors. As the cavity length increases, the oscillation wavelength moves towards the band edge and the threshold gain strongly decreases, mainly because of the slow-light reduction of the mirror loss (see Fig. 4.12). The distributed feedback suppresses the mode closest the band edge, which would otherwise be the lasing one (see Fig. 4.13 and Fig. 4.14). Furthermore, larger values of the linewidth enhancement factor, α_H, may significantly reduce the threshold gain if the distributed feedback is strong enough (see Fig. 4.17). In fact, the effective net modal gain, g_{eff}, may be enhanced, at a given frequency, by larger values of α_H, under the same pumping conditions (see Fig. 4.18). Therefore, on the one hand quantum dots may offer better performance in slow-light semiconductor optical amplifiers (as discussed in Sec. 3.6), where the goal is achieving a reasonable amplifier gain with minimum backreflection. On the other hand, quantum wells may contribute to reduce the threshold gain in lasers with photonic bandgap mirrors. In Sec. 4.4.1, we have studied the impact of disorder. Indeed, an optimum cavity length which minimizes the threshold gain has been found in [178] (see Fig. 4.19). This optimum has been ascribed therein to disorder due to unavoidable fabrication imperfections. We have modelled the disorder-induced backscattering loss by a phenomenological approach [117, 178], already introduced in Sec. 3.6. This approach, irrespective of whether or not the distributed feedback is included, cannot fully capture the experiments of [178] (see Fig. 4.20). On the other hand, as we have briefly discussed, the interpretation of those experimental findings currently remains controversial [15]. Finally, in Sec. 4.4.2 we have studied the oscillation condition in the event that the left and right mirror reflection coefficient are zero. We have shown that lasing may be possible with reasonable threshold gain if the active region is long enough (see Fig. 4.23). In this case, lasing is entirely sustained by the gain-induced distributed feedback.

In Sec. 4.4, we have focused on the laser in Fig. 4.24 [137]. In this laser, the left and right mirror are photonic heterostructure mirrors, induced by a refractive index structural modulation. We have investigated two possible configurations in dependence of the length of the buffer mirror. The two configurations, namely Type I and Type II, differ in the refractive index change of the buffer mirror relative to the active region (see Fig. 4.25). Interestingly, for Type II an optimum buffer length has been found, which minimizes the threshold gain (see Fig. 4.27). The optimum stems from the oscillation frequency changing around a resonance of the internal reflection coefficient r_{int} (see Fig. 4.28). Therefore, this optimum is a peculiar distributed feedback effect.

In Sec. 4.6, we have discussed the impact of slow-light on the tuning characteristics of Fano lasers [102]. This laser is essentially formed by an open waveguide coupled to a nanocavity. The Fano mirror arises from the destructive interference around the nanocavity resonance frequency between two light paths: the direct waveguide path and the indirect waveguide-nanocavity-waveguide path. Current models of Fano lasers [132, 129] completely neglect slow-light effects. Firstly, we have discussed the case of frequency tuning. In this case, the oscillation condition is solved as a function of the nanocavity resonance frequency, as illustrated in Fig. 4.38. The threshold gain features a succession of minima, with each minimum occurring when the resonance frequency aligns with a longitudinal mode of the laser cavity. This case is of practical interest as the laser may be modulated via the mirror [129, 128]. As compared to current models, the inclusion of slow-light and gain-induced distributed feedback reveals a strong competition among the various longitudinal modes, which intensifies as the group index increases. As a result, lasing may even occur away from the Fano mirror peak. Therefore, operation too deep into the slow-light region should be avoided. However, moderate slow-light may beneficial to reduce the threshold gain. Secondly, we have analyzed the length tuning characteristics. In this case, the oscillation condition is solved as a function of the cavity length, which may be of interest for design purposes. In the presence of slow-light and gain-induced distributed feedback, the threshold gain shows an intricate behaviour (see Fig. 4.41), revealing the extreme sensitivity of the oscillation condition to length tuning. This reflects somehow the sensitivity of the frequency tuning characteristics to the left mirror phase, which we have also discussed.

Overall, these features emphasize that cavity length and phases of both mirrors should be well controlled to pursue operation of Fano lasers in the slow-light region. In addition, we also expect changes in the left and right mirror phase to affect the threshold gain of lasers with photonic bandgap mirrors, as suggested by Fig. 4.14. This sensitivity stems from the influence of the mirror phase on the internal reflection coefficient, as evidenced by Fig. 4.15. Therefore, pursuing experiments with systematic tuning of the mirror phases might be interesting in the slow-light region, even for lasers with photonic bandgap mirrors.

Chapter 5

Rate equation model of photonic crystal lasers with slow-light

In this chapter, we derive a rate equation model of photonic crystal lasers which self-consistently accounts for slow-light and gain-induced distributed feedback. The starting point is the laser oscillation condition, thoroughly discussed in Chapter 4 for various types of photonic crystal lasers based on line-defect waveguides. The field rate equation and carrier rate equation, presented in Sec. 5.1 and Sec. 5.2 respectively, are general, meaning that no particular assumption is made on the left and right mirror. Thus, the approach presented in this chapter may be extended to self-consistently account for slow-light effects in photonic crystal Fano lasers. In Sec. 5.3, we focus on lasers with photonic bandgap mirrors. We derive analytical expressions for the static and small-signal characteristics and present some preliminary results. Finally, in Sec. 5.4 we draw the conclusions.

5.1 Field rate equation

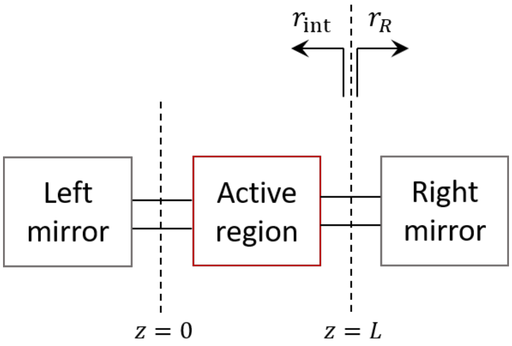

Figure 5.1: Reference plane for the internal reflection coefficient r_{int}

Fig. 5.1 shows the schematic drawing of a laser cavity, already introduced in Sec. 4.3. From Eq. (3.2) in Sec. 3.2, we may express the electric field in the frequency-domain as

$$\mathbf{E}(\mathbf{r},\omega) = c_+(z,\omega)\mathbf{e}_+(\mathbf{r},\omega) + c_-(z,\omega)\mathbf{e}_-(\mathbf{r},\omega) \tag{5.1}$$

Here, $\mathbf{e}_\pm$ are the forward- (+) and backward-propagating (−) electric field of the guided Bloch mode of a *reference* waveguide with purely real refractive index. As explained in Sec. 3.2, the active waveguide on which the laser cavity is based is viewed as perturbed as compared to this reference waveguide. The perturbation is represented by the material gain induced by carrier density. The Bloch fields $\mathbf{e}_\pm$ are z periodic, with the period given by the lattice constant a. The complex amplitudes $c_\pm(z)$ reflect the spatial dependence which the Bloch fields acquire within the laser cavity. On the left hand side of the right mirror (see Fig. 5.1), the boundary conditions are

$$c_-(L,\omega) = c_+(L,\omega)r_R \tag{5.2a}$$

$$c_-(L,\omega) = c_+(L,\omega)/r_{\text{int}} \tag{5.2b}$$

Here, L is the length of the active region and r_R the right mirror reflection coefficient, while r_{int} is the internal reflection coefficient discussed in Sec. 4.3.2. Around the lasing threshold, we may expand $1/r_{\text{int}}$ in a first-order Taylor series [167]

$$\begin{aligned}\frac{1}{r_{\text{int}}(\omega,N)} \approx \frac{1}{r_{\text{int}}(\omega_s,N_s)} - \frac{\left(\frac{\partial r_{\text{int}}}{\partial\omega}\right)\Big|_{(\omega_s,N_s)}}{r^2_{\text{int}}(\omega_s,N_s)}(\omega-\omega_s)\\ - \frac{\left(\frac{\partial r_{\text{int}}}{\partial N}\right)\Big|_{(\omega_s,N_s)}}{r^2_{\text{int}}(\omega_s,N_s)}(N-N_s)\end{aligned} \tag{5.3}$$

where ω_s and N_s are, respectively, the oscillation angular frequency and threshold carrier density. By inserting Eq. (5.3) into Eq. (5.2b), one finds

$$\begin{aligned}r_{\text{int}}(\omega_s,N_s)c_+(L,\omega) + \Bigg\{ i\left[i\left(\omega-\omega_s\right)\right]\left(\frac{\partial r_{\text{int}}}{\partial\omega}\right)\Bigg|_{(\omega_s,N_s)}\\ -\left(N-N_s\right)\left(\frac{\partial r_{\text{int}}}{\partial N}\right)\Bigg|_{(\omega_s,N_s)}\Bigg\} c_+(L,\omega) = r^2_{\text{int}}(\omega_s,N_s)c_-(L,\omega)\end{aligned} \tag{5.4}$$

In the time-domain, the forward- and backward-propagating fields at $z = L$ are defined as the inverse Fourier transform of the amplitudes $c^\pm(L,\omega)$, namely

$$\mathscr{E}^\pm(L,t) = \frac{1}{2\pi}\int_{-\infty}^{+\infty} c_\pm(L,\omega)e^{-i\omega t}d\omega \tag{5.5}$$

Since $\mathscr{E}^{\pm}(L,t)$ is a real quantity, one finds $c_+(L,-\omega) = \left[c_+(L,\omega)\right]^*$. Thus, $\mathscr{E}^{\pm}(L,t)$ may be expressed as

$$\mathscr{E}^{\pm}(L,t) = \mathrm{Re}\left\{\mathscr{E}^{\pm}_{\mathscr{A}}(L,t)\right\} = \frac{1}{2}\mathscr{E}^{+}_{\mathscr{A}}(L,t) + c.c. \tag{5.6}$$

with $c.c.$ denoting the complex conjugate. Here, the complex, time-domain field $\mathscr{E}^{\pm}_{\mathscr{A}}(L,t)$ is given by

$$\mathscr{E}^{\pm}_{\mathscr{A}}(L,t) = \frac{1}{\pi}\int_0^{+\infty} c_{\pm}(L,\omega)e^{-i\omega t}d\omega \tag{5.7}$$

By multiplyng both sides of Eq. (5.4) by the unitary step function and subsequently taking the inverse Fourier transform, we obtain

$$\begin{aligned}
&r_{\mathrm{int}}(\omega_s,N_s)\mathscr{E}^{+}_{\mathscr{A}}(L,t) + i\left(\frac{\partial r_{\mathrm{int}}}{\partial\omega}\right)\Bigg|_{(\omega_s,N_s)}\left[-\frac{d\mathscr{E}^{+}_{\mathscr{A}}(L,t)}{dt} - i\omega_s\mathscr{E}^{+}_{\mathscr{A}}(L,t)\right] \\
&-\left(N-N_s\right)\left(\frac{\partial r_{\mathrm{int}}}{\partial N}\right)\Bigg|_{(\omega_s,N_s)}\mathscr{E}^{+}_{\mathscr{A}}(L,t) = r^2_{\mathrm{int}}(\omega_s,N_s)\mathscr{E}^{-}_{\mathscr{A}}(L,t)
\end{aligned} \tag{5.8}$$

We shall now assume that the laser oscillates in a single longitudinal mode, with a slowly-varying time-domain envelope $\mathscr{A}^+(t)$, namely

$$\frac{1}{2}\mathscr{E}^{\pm}_{\mathscr{A}}(L,t) = \mathscr{A}^{\pm}(t)e^{-i\omega_s t} \tag{5.9}$$

By inserting Eq. (5.9) into Eq. (5.8) and letting the carrier density N to be time-dependent, one finds

$$\frac{d\mathscr{A}^+(t)}{dt} = i\zeta\left[N(t)-N_s\right]\mathscr{A}^+(t) + \gamma_L\left[\mathscr{A}^-(t)r_{\mathrm{int}}(\omega_s,N_s) - \mathscr{A}^+(t)\right] \tag{5.10}$$

Here, ζ and γ_L are

$$\zeta = \left(\frac{\partial r_{\mathrm{int}}/\partial N}{\partial r_{\mathrm{int}}/\partial\omega}\right)\Bigg|_{(\omega_s,N_s)} \tag{5.11a}$$

$$\gamma_L = i\frac{r_{\mathrm{int}}(\omega_s,N_s)}{\left(\partial r_{\mathrm{int}}/\partial\omega\right)\big|_{(\omega_s,N_s)}} \tag{5.11b}$$

It is instructive to explicitly derive ζ and γ_L for a conventional Fabry-Perot laser [167]. In this case, the forward and backward field are only coupled at the mirrors and the internal reflection coefficient reads $r_{\mathrm{int}} = r_L e^{2i\beta L}e^{\left(\Gamma g_{\mathrm{mat}}-\alpha_i\right)L}$. Here, r_L is the left mirror reflection coefficient, which is assumed to be non-dispersive. β is the propagation constant and g_{mat} the material gain, while Γ and α_i are the optical confinement factor and modal intrinsic loss respectively. In this case, consistently with [167], one finds

$$\zeta = -\frac{i}{2} G_N \frac{1 - i\alpha_H}{1 - \frac{i}{2} G_\omega} \tag{5.12a}$$

$$\gamma_L = \frac{1}{\frac{2L}{v_g}\left(1 - \frac{i}{2} G_\omega\right)} \tag{5.12b}$$

Here, α_H is the linewidth enhancement factor and v_g the group velocity at the oscillation frequency, while G_N and G_ω are given by

$$G_N = v_g \left. \frac{\partial\left(\Gamma g_{\mathrm{mat}} - \alpha_i\right)}{\partial N} \right|_{(\omega_s, N_s)} \tag{5.13a}$$

$$G_\omega = v_g \left. \frac{\partial\left(\Gamma g_{\mathrm{mat}} - \alpha_i\right)}{\partial \omega} \right|_{(\omega_s, N_s)} \tag{5.13b}$$

If the net modal gain dispersion at the lasing threshold is negligible, then γ_L is equal to $1/\tau_{\mathrm{in}}$ [129], with $\tau_{\mathrm{in}} = 2L\,/\,v_g$ being the roundtrip time. In addition, one finds

$$\zeta' = -\frac{1}{2}\alpha_H G_N \tag{5.14a}$$

$$\zeta'' = -\frac{1}{2} G_N \tag{5.14b}$$

where ζ' and ζ'' are, respectively, the real and imaginary part of ζ.

On the other hand, if the forward and backward field undergo distributed coupling (such as in conventional DFB lasers), ζ and γ_L should be computed via Eqs. (5.11a) and (5.11b), which are more general. In particular, in this case there is no obvious definition of a roundtrip time and γ_L is a kind of complex roundtrip frequency [167].

Some comments are due on limitations to the applicability of Eq. (5.10). Since the equation is based on a Taylor expansion around the lasing threshold, the accuracy worsens as the frequency and carrier density depart from the expansion point. This means that large-signal dynamics are not well described. In particular, the maximum frequency variation is limited by the roundtrip time, namely $\omega - \omega_s \ll 1/\tau_{\mathrm{in}}$ [127]. This can be easily understood by assuming the left mirror to be non-dispersive, as well as neglecting both the gain-induced distributed feedback *and* modal gain dispersion (i.e. $G_\omega = 0$). In this case, one may expand in a first-order Taylor series the sole argument of the exponential in the expression of r_{int} [131], instead of expanding $1/r_{\mathrm{int}}$ as a whole. Thus, one finds that $\mathscr{A}^+(t)$ evolves in steps of the rountrip time [131]. Therefore, it simply follows from Nyquist sampling theorem that the maximum bandwidth of $\mathscr{A}^+(t)$ is limited by the inverse of the sampling time, i.e. the inverse of the roundtrip time.

Physically, this means that the frequency deviation from the expansion point should be much smaller than the laser free spectral range. Deep into the slow-light region of photonic crystal lasers, the roundtrip time may significantly increase, thus jeopardizing the applicability of Eq. (5.10). To roughly give some numbers, for a typical cavity length $L = 6.5\,\mu$m, the roundtrip time would be around 150 fs for a group index n_g of 3.5 and it would increase up to around 4 ps for $n_g = 100$.

To overcome the limitation imposed by the rountrip time, an artificial, multi-section discretization scheme has been proposed [130]. Essentially, the laser active region is spatially discretized in various nodes (i.e. sub-sections), separated one from another by a distance ΔL. The field at each node is updated as the field from the previous node arrives. The time step by which the field at each node is updated is given by $\Delta L/v_g$, which is the time it takes the field to travel from one node to the other. Therefore, one can improve the temporal resolution by just increasing the number of points in space where the field is tracked. It should be emphasized, though, that this scheme can be derived *only if* the following conditions are met simultaneously: 1) the expression of r_{int} has the form of $r_L e^{2i\beta L} e^{(\Gamma g_{\text{mat}} - \alpha_i)L}$, i.e. the distributed feedback is neglected; 2) the modal gain dispersion is neglected, i.e. $G_\omega = 0$; 3) the left mirror is assumed to be non-dispersive. Otherwise, one cannot derive a simple iterative equation whereby the field is updated in steps of the roundtrip time (on which the multi-section scheme of [130] is ultimately based). This means that the multi-section scheme cannot be used if one accounts for slow-light and gain-induced distributed feedback. It should be noted that even the simple inclusion of slow-light would be problematic. In fact, as a result of the slow-light gain enhancement, one could not assume $G_\omega = 0$, as the effective modal gain would be strongly dispersive (see Eq. (5.23) in Sec. 5.2.1). Furthermore, if one takes the distributed feedback into account, there is no obvious definition of a rountrip time [167] (as already noted above). Therefore, one should come up with other discretization schemes, a task which is beyond the scope of this thesis.

However, these considerations do not imply that Eq. (5.10) is useless. On the contrary, it can be used to determine the small-signal response (see Sec. 5.3.2 and Sec. 5.3.3) and, in general, dynamics with limited deviation from the lasing threshold. The caveat is that large-signal dynamics and ultra-fast dynamics are not well described. Future work could be devoted to overcome this limitation.

5.1.1 Broadband right mirror

If the right mirror is frequency-independent, from Eq. (5.2a) one finds

$$\mathscr{A}^-(t) = r_R \mathscr{A}^+(t) \tag{5.15}$$

This is a valid approximation in the case of lasers with photonic bandgap mirrors, which are broadband (as discussed in Sec. 4.4). By inserting Eq. (5.15) into Eq. (5.10) and exploiting the fact that $r_R r_{\text{int}}(\omega_s, N_s)$ is equal to unity, we obtain

$$\frac{d\mathscr{A}^+(t)}{dt} = i\zeta\left[N(t) - N_s\right]\mathscr{A}^+(t) \tag{5.16}$$

It should be emphasized that if the right mirror is not broadband, Eq. (5.10) should be used. In this case, an additional equation is necessary which couples $\mathscr{A}^+(t)$ and $\mathscr{A}^-(t)$ by accounting for the right mirror frequency dependence. Formally, this equation is obtained by taking the inverse Fourier transform of Eq. (5.2a). In the case of Fano lasers, it can be simply derived from the rate equation of the field inside the nanocavity located adjacently to the laser cavity, as shown in [132]. Since in Sec. 5.3 we focus on lasers with photonic bandgap mirrors, we will not further discuss this additional field rate equation.

5.2 Carrier rate equation

Similarly to [167], we ignore the spatial distribution of the carrier density and describe it via the following rate equation

$$\frac{dN(t)}{dt} = \eta_i \frac{J(t)}{qd} - R\left[N(t)\right] - \frac{R_{\text{st}}(t)}{V_{\text{act}}} \tag{5.17}$$

Here, the carrier density N is the number of carriers normalized to the volume of the active region, V_{act}. η_i is the injection efficiency, J is the current density, q is the electron charge and d the active region thickness. $R\left[N(t)\right]$ is the spontaneous recombination rate per unit volume, accounting for radiative and non-radiative recombination. $R_{\text{st}}(t)$ is the stimulated emission rate, defined as the number of carriers per unit time undergoing stimulated recombination.

5.2.1 Stimulated emission rate

The stimulated recombination rate $R_{\text{st}}(t)$ in photonic crystal lasers is derived in detail in Appendix D. Essentially, it is derived by integrating over the laser cavity the *local* stimulated emission rate, which is directly proportional to the electric field squared magnitude in Eq. (5.1). The derivation accounts for slow-light and gain-induced distributed coupling. In the following, we briefly review the final result.

Fig. 5.2 shows the block diagram of a photonic crystal laser in the presence of slow-light and gain-induced distributed coupling. This diagram has been already discussed in Sec. 4.3.1. $\underline{\underline{T_L}}$ ($\underline{\underline{T_R}}$) is the left (right) mirror transmission matrix in the basis of the Bloch modes of the *reference* waveguide. The left and right mirror reflection coefficient are r_L and r_R respectively. For a detailed discussion on the group of blocks denoted by

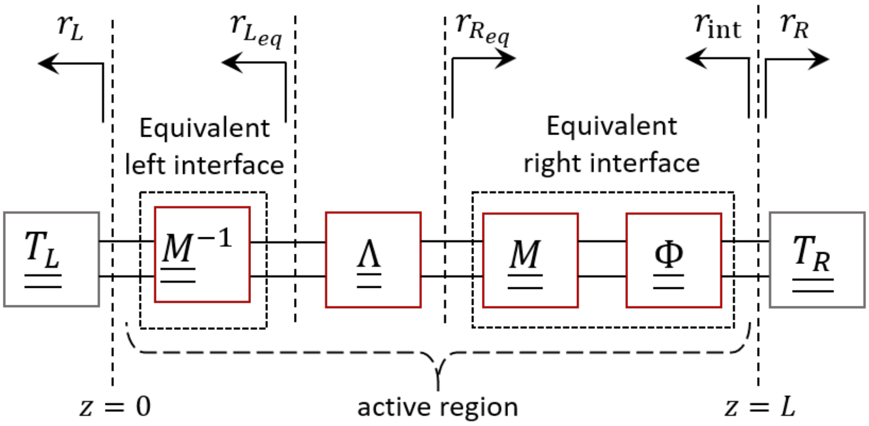

Figure 5.2: Block diagram of a photonic crystal laser with slow-light and gain-induced distributed coupling.

”active region”, we refer to Sec. C.3. Here, it is sufficient to know that $\underline{\underline{\Lambda}}$ is the transmission matrix in the basis of the Bloch modes of the *active* waveguide. Owing to the gain-induced distributed feeback associated with slow-light, equivalent dielectric interfaces originate at the left- and right-hand side of the active region. These interfaces account for the mismatch between the Bloch modes of the active waveguide and those of the reference waveguide. As a result, the Bloch modes of the active waveguide experience an *equivalent* right (left) mirror reflection coefficient $r_{R_{eq}}$ ($r_{L_{eq}}$). By assuming the material gain to be linear with the carrier density, the stimulated emission rate reads

$$R_{\text{st}}(t) = \frac{8W_e}{\hbar\omega_s}\left(\frac{c}{n_{\text{slab}}}\right)\Gamma_y g_N\left[N(t) - N_{\text{tr}}\right]\frac{\xi}{a}\left|\mathscr{A}^+(t)\right|^2 \tag{5.18}$$

where $g_N = \partial g_{\text{mat}}/\partial N$ is the differential gain and N_{tr} the transparency carrier density. Here, c is the vacuum light speed, n_{slab} is the slab refractive index and a the photonic crystal lattice constant, while Γ_y accounts for the vertical optical confinement in the active layers (see Eq. (A.38a) in Sec. A.3.1). W_e is the time-averaged electric field energy stored in a supercell at the oscillation frequency

$$W_e = \frac{1}{4}\int_V \epsilon_0 n_b^2(\mathbf{r})|\mathbf{e}_\pm(\mathbf{r},\omega_s)|^2\, dV \tag{5.19}$$

with V being the volume of the supercell and n_b the background refractive index. ξ is a parameter reflecting the spatial distribution of the electric field squared magnitude, $|\mathbf{E}(\mathbf{r})|^2$, at the lasing threshold. It should be emphasized that the electric field squared magnitude is directly computed from Eq. (5.1). Thus, ξ not only accounts for the longitudinal spatial dependence of the amplitudes, $c_\pm(z)$, but also for the transverse and longitudinal spatial dependence of the Bloch modes, $\mathbf{e}_\pm(\mathbf{r})$. Specifically, ξ reads

$$\xi = \xi_{\text{exp}} + \xi_{\text{cos}} \tag{5.20}$$

with ξ_{exp} and $\xi_{\cos}$ given by

$$\xi_{\text{exp}} = \Gamma_{\text{FF}}\left[1 + |r_{\pm}|^2 - 2\frac{|\Gamma_{\text{FB}}|}{\Gamma_{\text{FF}}}|r_{\pm}|\cos\left(\phi_{\pm}\right)\right]\frac{\left(1 - |r_{L_{eq}}||r_{R_{eq}}|\right)\left(|r_{L_{eq}}| + |r_{R_{eq}}|\right)}{g_{\text{eff}}|r_{L_{eq}}|\left|1 + r_{R_{eq}}r_{-}\right|^2} \tag{5.21a}$$

$$\xi_{\cos} = \Gamma_{\text{FF}}\left[2|r_{\pm}|\cos\left(\phi_{\pm}\right) - \frac{|\Gamma_{\text{FB}}|}{\Gamma_{\text{FF}}}\left(1 + |r_{\pm}|^2\right)\right]\frac{|r_{R_{eq}}|\left[\sin\left(\phi_{L_{eq}}\right) + \sin\left(\phi_{R_{eq}}\right)\right]}{\delta_{\text{eff}}\left|1 + r_{R_{eq}}r_{-}\right|^2} \tag{5.21b}$$

Here, Γ_{FF} and Γ_{FB} are, respectively, the normalized self- and cross-coupling coefficient discussed in Sec. 3.3 (see, in particular, Fig. 3.15 in Sec. 3.3). r_+ (r_-) is, within a phase shift of π, the reflection coefficient of the sole right (left) equivalent dielectric interface, as discussed in Sec. 3.4 (see Fig. 3.17 in Sec. 3.4). $\phi_{\pm}$ is the phase of $r_{\pm}$, while $\phi_{L_{eq}}$ ($\phi_{R_{eq}}$) is the phase of $r_{L_{eq}}$ ($r_{R_{eq}}$). The effective detuning δ_{eff} is given by $\frac{\pi}{a} - \beta_{\text{eff}}$, while g_{eff} is the effective net modal gain. Here, β_{eff} and g_{eff} are the effective propagation constant and effective net modal gain of the Bloch modes of the active waveguide (see Sec. 3.4). We note that all quantities in Eqs. (5.21a) and (5.21b) are evaluated at the lasing threshold.

It is instructive to elaborate on the stimulated emission rate in the absence of gain-induced distributed feedback. In this case, one finds $\Gamma_{\text{FB}} = 0$ and $r_{\pm} = 0$, as the equivalent dielectric interfaces in Fig. 5.2 simply disappear. Therefore, $\xi_{\cos}$ is identically equal to zero, while $r_{L_{eq}}$ and $r_{R_{eq}}$ are reduced, respectively, to r_L and r_R. Thus, ξ_{exp} is reduced to

$$\xi_{\text{exp}} = \Gamma_{\text{FF}}\frac{\left(1 - |r_L||r_R|\right)\left(|r_L| + |r_R|\right)}{g_{\text{eff}}|r_L|} \tag{5.22}$$

By neglecting the disorder-induced backscattering loss, the effective net modal gain reads

$$g_{\text{eff}} = S\left(\Gamma_{\text{FF}}\Gamma_y g_{\text{mat}_s} - \alpha_1\right) \tag{5.23}$$

Here, $S = n_g/n_{\text{slab}}$ is the slow-down factor, with n_g being the group index of the reference waveguide. g_{mat_s} is the material gain at the lasing threshold, while α_1 accounts for disorder-induced loss due to coupling with radiation modes [117]. It should be emphasized that g_{eff} in Eq. (5.23) is evaluated at the lasing threshold. Consequently, it is equal to the mirror loss $\frac{1}{L}\ln\left(\frac{1}{|r_L||r_R|}\right)$ (see Eq. (4.7a)). Therefore, the stimulated emission rate turns out to be *unaffected* by the slow-light reduction of the group velocity, consistently with [178, 101]. It is convenient to introduce the quantity

$$\begin{aligned}\Phi(t) &= \frac{8W_e}{\hbar\omega_s}\frac{S}{\Gamma_{\mathrm{FF}}}\frac{\xi}{a}\left|\mathscr{A}^+(t)\right|^2 \\ &= \frac{1}{2}\frac{1}{\hbar\omega_s}\frac{\left(1-|r_L||r_R|\right)\left(|r_L|+|r_R|\right)}{a\,|r_L|\left(\Gamma_{\mathrm{FF}}\Gamma_y g_{\mathrm{mat}_s}-\alpha_1\right)}\left|\mathscr{A}^+(t)\right|^2\int_V \epsilon_0 n_b^2(\mathbf{r})|\mathbf{e}_\pm(\mathbf{r},\omega_s)|^2\,dV\end{aligned} \tag{5.24}$$

With this definition, Eq. (5.18) is reduced to

$$R_{\mathrm{st}}(t) = \left(\frac{c}{n_g}\right)\Gamma_{\mathrm{FF}}\Gamma_y g_N\left[N(t)-N_{\mathrm{tr}}\right]\,\Phi(t) \tag{5.25}$$

Formally, this is the familiar expression of the stimulated emission rate employed in conventional rate equation models [23], with $\Phi(t)$ clearly playing the role of the photon number. Furthermore, the total optical confinement factor is $\Gamma_{\mathrm{FF}}\Gamma_y$. In order to exactly mimic the formulation of [23], we may define the mode volume

$$V_\Phi = \frac{V_{\mathrm{act}}}{\Gamma_{\mathrm{FF}}\Gamma_y} \tag{5.26}$$

Therefore, the normalized stimulated emission rate $R_{\mathrm{st}}(t)/V_{\mathrm{act}}$ in Eq. (5.17) becomes

$$\bar{R}_{\mathrm{st}}(t) = \frac{R_{\mathrm{st}}(t)}{V_{\mathrm{act}}} = \left(\frac{c}{n_g}\right)g_N\left[N(t)-N_{\mathrm{tr}}\right]\frac{\Phi(t)}{V_\Phi} \tag{5.27}$$

with $\Phi(t)/V_\Phi$ being the photon density.

5.3 Lasers with photonic bandgap mirrors

In the following, we focus on lasers with photonic bandgap mirrors. In this case, the laser is described by Eqs. (5.16) and (5.2). It is convenient to separate the slowly-varying envelope $\mathscr{A}^+(t)$ into magnitude and phase

$$\mathscr{A}^+(t) = |\mathscr{A}^+(t)|e^{-i\phi(t)} \tag{5.28}$$

By inserting Eq. (5.28) into Eq. (5.16), we obtain

$$\frac{d|\mathscr{A}^+(t)|}{dt} = -\zeta''\left[N(t)-N_s\right]|\mathscr{A}^+(t)| \tag{5.29a}$$

$$\frac{d\phi(t)}{dt} = -\zeta'\left[N(t)-N_s\right] \tag{5.29b}$$

where ζ' and ζ'' are, respectively, the real and imaginary part of ζ.

5.3.1 P-I characteristic

In the steady-state, the carrier density rate equation reads

$$0 = \eta_i \frac{J}{qd} - R\left[N_s\right] - \frac{R_{\text{st}}}{V_{\text{act}}} \tag{5.30}$$

where the stimulated emission rate is

$$R_{\text{st}} = \frac{8W_e}{\hbar\omega_s}\left(\frac{c}{n_{\text{slab}}}\right)\Gamma_y g_N\left[N_s - N_{\text{tr}}\right]\frac{\xi}{a}\left|\mathscr{A}^+_{\omega_s}\right|^2 \tag{5.31}$$

Below threshold, we assume $|\mathscr{A}^+_{\omega_s}| = 0$ (spontaneous emission coupled to the lasing mode is neglected). By setting $R_{\text{st}} = 0$ in Eq. (5.30), we find the threshold current density

$$J_{\text{th}} = \frac{qd}{\eta_i} R\left[N_s\right] \tag{5.32}$$

Above threshold, by combining Eq. (5.31) and Eq. (5.30), one finds

$$\begin{aligned}\left|\mathscr{A}^+_{\omega_s}\right|^2 &= \frac{R_{\text{st}}}{\frac{8W_e}{\hbar\omega_s}\left(\frac{c}{n_{\text{slab}}}\right)\Gamma_y g_N\left[N_s - N_{\text{tr}}\right]\frac{\xi}{a}} \\ &= \frac{\eta_i V_{\text{act}}}{qd}\frac{J - J_{\text{th}}}{\frac{8W_e}{\hbar\omega_s}\left(\frac{c}{n_{\text{slab}}}\right)\Gamma_y g_N\left[N_s - N_{\text{tr}}\right]\frac{\xi}{a}}\end{aligned} \tag{5.33}$$

To compute the output power, firstly we recall from Sec. 3.5 (see, in particular, Eqs. (3.31) and (3.32)) that the forward-propagating power on the left-hand side of the right mirror is $P^+(z = L) = |c_+(L)|^2 P_0$, with $P_0 = 2W_e v_g/a$. Secondly, we note that $\mathscr{A}^+_{\omega_s} = \frac{1}{2}c_+(L)$ (see Appendix D). Therefore, the forward-propagating power on the left-hand side of the right mirror may be expressed as

$$P^+(z = L) = \frac{8W_e v_g}{a}\left|\mathscr{A}^+_{\omega_s}\right|^2 \tag{5.34}$$

From here, the power exiting the right mirror reads

$$\begin{aligned}P_{\text{out}} &= (1 - |r_R|^2)P^+(z = L) \\ &= \eta_i \frac{\hbar\omega_s}{q}\frac{v_g}{(c/n_{\text{slab}})}\frac{1 - |r_R|^2}{\Gamma_y g_N\left[N_s - N_{\text{tr}}\right]\xi}\left(I - I_{\text{th}}\right)\end{aligned} \tag{5.35}$$

where $I = (V_{\text{act}}/d)J$ is the current and I_{th} the threshold current. The slope efficiency is given by

$$\text{SE} = \frac{q}{\hbar\omega_s}\frac{dP_{\text{out}}}{dI} = \eta_i \frac{v_g}{(c/n_{\text{slab}})}\frac{1 - |r_R|^2}{\Gamma_y g_N\left[N_s - N_{\text{tr}}\right]\xi} \tag{5.36}$$

It is instructive to elaborate on the slope efficiency in the absence of gain-induced distributed feedback and disorder-induced backscattering loss. In this case, by recalling that $\xi = \xi_{\text{exp}}$ and inserting Eqs. (5.22) and (5.23) into Eq. (5.36), one finds

$$\text{SE} = \eta_i \frac{\alpha_m}{\alpha_m + \alpha_i} \frac{\left(1 - |r_R|^2\right) |r_L|}{\left(1 - |r_L||r_R|\right) \left(|r_L| + |r_R|\right)} \tag{5.37}$$

where the mirror (intrinsic) loss α_m (α_i) is

$$\alpha_m = \frac{1}{SL} \ln \left(\frac{1}{|r_L||r_R|} \right) \tag{5.38a}$$

$$\alpha_i = \alpha_1 \tag{5.38b}$$

To derive Eq. (5.37), we have also made use of Eq. (4.7a) from Sec. 4.2, which provides the threshold modal gain. Eq. (5.37) reveals that, in the absence of gain-induced distributed feedback, slow-light reduces the slope efficiency. In the presence of gain-induced distributed feedback, the impact is generally non-trivial, as Eq. (5.36) should be used.

5.3.2 Intensity modulation response

To analyze the laser under small-signal conditions, we follow the approach of [23]. For this purpose, inspired by Eqs. (5.24) and (5.27), we generally define the number of photons as

$$\Phi(t) = \frac{8 W_e}{\hbar \omega_s} \frac{S}{\Gamma_{\text{FF}}} \frac{\xi}{a} \left| \mathscr{A}^+(t) \right|^2 \tag{5.39}$$

regardless of whether or not the gain-induced distributed feedback is accounted for. By this definition, Eqs. (5.29a) and (5.17) become

$$\frac{d\Phi(t)}{dt} = G_{N_{\text{eq}}} \left[N(t) - N_s \right] \Phi(t) \tag{5.40a}$$

$$\frac{dN(t)}{dt} = \eta_i \frac{I(t)}{q V_{\text{act}}} - R\left[N(t)\right] - v_g g_N \left[N(t) - N_{\text{tr}} \right] \frac{\Phi(t)}{V_\Phi} \tag{5.40b}$$

where the parameter $G_{N_{\text{eq}}}$ is given by

$$G_{N_{\text{eq}}} = -2\zeta'' \tag{5.41}$$

and $V_\Phi = V_{\text{act}} / \left(\Gamma_{\text{FF}} \Gamma_y\right)$ is the mode volume (already defined in Eq. (5.26)). We note that these definitions of photon number and mode volume are somewhat arbitrary in the presence of distributed feedback and are simply introduced for the sake of analogy with conventional rate equation models. For instance, one may also conceive a different proportionality factor linking the number of photons to $\left|\mathscr{A}^+(t)\right|^2$. However, the modulation response is independent of this proportionality factor and thus uniquely defined (as shown below by Eq. (5.47)).

The parameter $G_{N_{\mathrm{eq}}}$ replaces $G_N = v_g \Gamma g_N$ from Eq. (5.13a), which would show up in the case of conventional [23] rate equation models. On the one hand, $G_{N_{\mathrm{eq}}}$ accounts somehow for the *effective* differential gain. In addition to the differential gain g_N, this effective differential gain also reflects the non-linear dependence of the effective net modal gain on carrier density, stemming from the gain-induced distributed feedback. Yet, this is not the whole story. In fact, $G_{N_{\mathrm{eq}}}$ is basically the imaginary part of ζ, which generally accounts for the differential dependence of the internal reflection coefficient on both carrier density and frequency (see Eq. (5.11a)). In particular, even in the simple case of a conventional Fabry-Perot laser, the imaginary part of ζ not only reflects the differential gain, but also the net modal gain dispersion at the oscillation frequency, if present (see Eqs. (5.12a) and (5.13b)). In the case of photonic crystal lasers in the slow-light region, the effective net modal gain is certainly dispersive, mainly because of the strong frequency dependence of the group index. This is the case even if one neglects the gain-induced distributed feedback, by forcing to zero the cross-coupling coefficients (see, for instance, Eq. (3.28b) in Sec. 3.4). In the presence of distributed feedback, things are even more complicated and the frequency dependence of the internal reflection coefficient is highly non-trivial (see, in particular, Fig. 4.8 in Sec. 4.3.2).

To simplify the calculations, we model the spontaneous carrier recombination rate via a carrier lifetime τ_s, namely

$$R\left[N(t)\right] = \frac{N(t)}{\tau_s} \tag{5.42}$$

We now assume that the injected current sinusoidally vary with time at an angular frequency $\tilde{\omega}$, with a small peak-to-peak amplitude, I_1, as compared to the bias point, I_{bias}. Under small-signal conditions, photons and carriers respond similarly. Thus, one finds [23]

$$I(t) = I_{\mathrm{bias}} + I_1 e^{i\tilde{\omega}t} \tag{5.43a}$$

$$\Phi(t) = \Phi_{\mathrm{bias}} + \Phi_1 e^{i\tilde{\omega}t} \tag{5.43b}$$

$$N(t) = N_s + N_1 e^{i\tilde{\omega}t} \tag{5.43c}$$

where Φ_{bias} is the number of photons at the bias point, while Φ_1 is the corresponding perturbation. N_1 is the perturbation to the threshold carrier density N_s. By inserting Eqs. (5.43a)-(5.43c) into Eqs. (5.40a) and (5.40b) and neglecting second-order perturbation terms, we obtain the linear system

$$\begin{bmatrix} \gamma_{\mathrm{NN}_{\mathrm{eq}}} + i\tilde{\omega} & \gamma_{\mathrm{NP}_{\mathrm{eq}}} \\ -\gamma_{\mathrm{PN}_{\mathrm{eq}}} & \gamma_{\mathrm{PP}_{\mathrm{eq}}} + i\tilde{\omega} \end{bmatrix} \begin{bmatrix} N_1 \\ \Phi_1 \end{bmatrix} = \eta_i \frac{I_1}{qV_{\mathrm{act}}} \begin{bmatrix} 1 \\ 0 \end{bmatrix} \tag{5.44}$$

where the matrix elements are

$$\gamma_{\mathrm{NN}_{\mathrm{eq}}} = \frac{1}{\tau_s} + v_g g_N \frac{\Phi_{\mathrm{bias}}}{V_\Phi} \tag{5.45a}$$

$$\gamma_{\mathrm{NP}_{\mathrm{eq}}} = \frac{v_g g_N \left(N_s - N_{\mathrm{tr}}\right)}{V_\Phi} \tag{5.45b}$$

$$\gamma_{\mathrm{PN}_{\mathrm{eq}}} = -2\zeta''\Phi_{\mathrm{bias}} \tag{5.45c}$$

$$\gamma_{\mathrm{PP}_{\mathrm{eq}}} = 0 \tag{5.45d}$$

The element $\gamma_{\mathrm{PP}_{\mathrm{eq}}}$ is identically equal to zero because we have neglected the spontaneous emission coupled to the lasing mode, as well as the gain compression [23]. By solving the linear system, one finds the photon perturbation

$$\Phi_1(\tilde{\omega}) = \eta_i \frac{I_1}{qV_{\mathrm{act}}} \frac{\gamma_{\mathrm{PN}_{\mathrm{eq}}}}{\omega^2_{R_{\mathrm{eq}}}} H_{\mathrm{eq}}(\tilde{\omega}) \tag{5.46}$$

where $\omega_{R_{\mathrm{eq}}}$ is the relaxation resonance (angular) frequency, while $H_{\mathrm{eq}}(\tilde{\omega})$ defines the intensity modulation response

$$H_{\mathrm{eq}}(\tilde{\omega}) = \frac{\Phi_1(\tilde{\omega})}{\Phi_1(\tilde{\omega} \to 0)} = \frac{\omega^2_{R_{\mathrm{eq}}}}{\omega^2_{R_{\mathrm{eq}}} - \tilde{\omega}^2 + i\tilde{\omega}\gamma_{\mathrm{eq}}} \tag{5.47}$$

Here, γ_{eq} is the damping rate. The relaxation resonance frequency and damping rate are given by

$$\omega_{R_{\mathrm{eq}}} = \sqrt{\gamma_{\mathrm{NP}_{\mathrm{eq}}}\gamma_{\mathrm{PN}_{\mathrm{eq}}} + \gamma_{\mathrm{NN}_{\mathrm{eq}}}\gamma_{\mathrm{PP}_{\mathrm{eq}}}} = \sqrt{\frac{v_g g_N \left(\Phi_{\mathrm{bias}}/V_\Phi\right)}{\tau_{p_{\mathrm{eq}}}}} \tag{5.48a}$$

$$\gamma_{\mathrm{eq}} = \gamma_{\mathrm{NN}_{\mathrm{eq}}} + \gamma_{\mathrm{PP}_{\mathrm{eq}}} = \mathrm{K}_{\mathrm{eq}} \left[\omega^2_{R_{\mathrm{eq}}}/(4\pi^2)\right] + \frac{1}{\tau_s} \tag{5.48b}$$

Here, the equivalent photon lifetime $\tau_{p_{\mathrm{eq}}}$ is

$$\tau_{p_{\mathrm{eq}}} = \frac{1}{G_{N_{\mathrm{eq}}}\left(N_s - N_{\mathrm{tr}}\right)} \tag{5.49}$$

The equivalent K-factor, K_{eq}, is related to the equivalent photon lifetime by

$$\mathrm{K}_{\mathrm{eq}} = 4\pi^2\tau_{p_{\mathrm{eq}}} \tag{5.50}$$

With these definitions, the 3-dB direct modulation bandwidth can be computed from the relaxation resonance frequency and damping rate via the usual [23] relationship (see Eq. (1.10) in Sec. 1.2). In particular, the K-factor is an important parameter, as it determines the maximum possible bandwidth [23]

$$f_{3\mathrm{dB}_{\max}} = \sqrt{2}\frac{2\pi}{\mathrm{K}_{\mathrm{eq}}} \tag{5.51}$$

It is instructive to directly express the relaxation resonance frequency as a function of the injected current. For this purpose, by using Eqs. (5.39) and (5.33), one may express the photon number at the bias point as

$$\Phi_{\mathrm{bias}} = \eta_i \frac{1}{v_g \Gamma_{\mathrm{FF}} \Gamma_y g_N \left(N_s - N_{\mathrm{tr}}\right)} \frac{I - I_{\mathrm{th}}}{q} \tag{5.52}$$

which, upon insertion into Eq. (5.48a), provides

$$\omega_{R_{\mathrm{eq}}} = \sqrt{\frac{1}{\tau_{p_{\mathrm{eq}}}} \frac{N_s}{N_s - N_{\mathrm{tr}}} \frac{I/I_{\mathrm{th}} - 1}{\tau_s}} \tag{5.53}$$

This equation reveals that, if the threshold carrier density is sufficiently larger than the transparency carrier density, the relaxation resonance frequency, at a given ratio between the injected current and threshold current and for a given carrier lifetime, is essentially determined by the equivalent photon lifetime.

Photon lifetime

A few words are due on the definition of a photon lifetime. In the presence of slow-light and neglecting the disorder-induced backscattering loss, the photon lifetime is conventionally defined as [105, 178]

$$\tau_p = \frac{1}{\left(\frac{c}{n_g}\right)\left[\frac{1}{L}\ln\left(\frac{1}{|r_L||r_R|}\right) + \alpha_1\left(\frac{n_g}{n_{\mathrm{slab}}}\right)\right]} = \frac{1}{\left(\frac{c}{n_{\mathrm{slab}}}\right)\Gamma g_{\mathrm{mat}_s}} \tag{5.54}$$

where Γ is the optical confinement factor. This definition is basically a statement that the slow-light enhancement of the gain per unit length equivalently manifests itself as a reduction of the cavity loss per unit time (i.e. a longer photon lifetime). From this definition, the Q-factor is obtained as

$$Q = \tau_p \omega_s \tag{5.55}$$

Here, we note that the equivalent photon lifetime from Eq. (5.49) is more general. In particular, Eq. (5.49) is reduced to Eq. (5.54) if 1) the gain-induced distributed feedback and 2) the dispersion of the effective net modal gain are neglected. In other words,

Symbol	Parameters	Values
a	Photonic crystal lattice constant [nm]	438
n_{slab}	Slab refractive index	3.17
n_{clad}	Cladding refractive index	1
r	Hole radius [a]	0.25
h_{slab}	Slab thickness [nm]	250
r_L	Left mirror reflection coefficient	1
r_R	Right mirror reflection coefficient	0.6
α_1	Disorder-induced radiation loss [cm^{-1}]	5
α_2	Disorder-induced backscattering loss [cm^{-1}]	0
α_H	Linewidth enhancement factor	1.5
τ_s	Effective carrier lifetime [ns]	0.5
d	Active region thickness [nm]	18
w	Active region width [nm]	500
η_i	Injection efficiency	0.4
Γ_y	Vertical optical confinement factor	12%
g_N	Differential gain [cm^2]	10^{-16}
N_{tr}	Transparency carrier density [cm^{-3}]	10^{18}
V_{b_0}	Built-in bias voltage [V]	0.6

Table 5.1: Parameters for the rate equation analysis of photonic crystal lasers with photonic bandgap mirrors. The active region is a buried heterostructure.

one should assume $\Gamma_{\text{FB}} = 0$, as well as $\partial\Gamma_{\text{FF}}/\partial\omega = 0$ and $\partial n_g/\partial\omega = 0$. Under these conditions, one finds

$$\zeta'' = -\frac{1}{2}\frac{\partial g_{\text{eff}}/\partial N}{\partial\beta_{\text{eff}}/\partial\omega} = -\frac{1}{2}\left(\frac{c}{n_{\text{slab}}}\right)\Gamma_{\text{FF}}\Gamma_y g_N \tag{5.56}$$

From here, $G_{N_{\text{eq}}}$ in Eq. (5.41) is reduced to $(c/n_{\text{slab}})\Gamma_{\text{FF}}\Gamma_y g_N$. Thus, $\tau_{p_{\text{eq}}}$ in Eq. (5.49) is reduced to τ_p in Eq. (5.54) with $\Gamma = \Gamma_{\text{FF}}\Gamma_y$.

Preliminary results

In the following, we present some preliminary results. The parameters which we have employed are summarized in Tab. 5.1. The parameters of the reference waveguide are the same assumed throughout this thesis (already summarized in Tab. 2.1 in Sec. 2.2.1 and included in Tab. 5.1 for the sake of convenience). For the laser, we assume a buried heterostructure active region. In addition, we note that the active region thickness and vertical optical confinement factor listed in Tab. 2.1 globally account for all the active layers.

Fig. 5.3 shows (a) modal gain $\Gamma_y g_{\text{mat}}$, (b) wavelength, (c) normalized self-coupling coefficient and (d) Q-factor at the lasing threshold of mode M_1 with (solid) and without

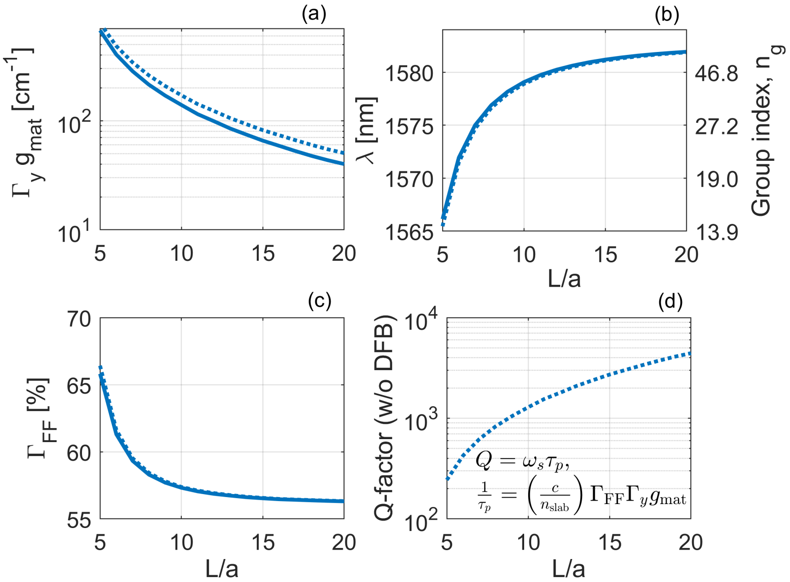

Figure 5.3: Threshold characteristics of photonic crystal lasers with photonic bandgap mirrors as a function of the cavity length. (a) Modal gain $\Gamma_y g_{\rm mat}$, (b) wavelength, (c) normalized self-coupling coefficient and (d) Q-factor at the lasing threshold of mode M_1 with (solid) and without (dotted) gain-induced distributed feedback. The right axis in (b) shows the group index of the reference waveguide.

(dotted) gain-induced distributed feedback, as a function of cavity length. From our discussion in Sec. 4.4, we recall that in the absence of gain-induced distributed feedback, M_1 is not the lasing mode, as M_0 possesses a smaller threshold gain (see Fig. 4.12 in Sec. 4.4). In the presence of gain-induced distributed feedback, M_0 is instead suppressed (see Fig. 4.13 in Sec. 4.4) and M_1 is indeed the lasing mode. Therefore, for a fair comparison, we apply the rate equation model to mode M_1, regardless of whether or not the gain-induced distributed feedback is taken into account. As discussed in Sec. 4.4, the threshold modal gain $\Gamma_y g_{\rm mat}$ is slightly smaller in the presence of distributed feedback (see Fig. 5.3(a)), as the non-zero linewidth enhancement factor improves the effective net modal gain (see Fig. 4.17 and Fig. 4.18 in Sec. 4.4). The oscillation wavelength is almost the same with and without distributed feedback (see Fig. 5.3(b)). As a result, the normalized self-coupling coefficient $\Gamma_{\rm FF}$ is almost unaffected by distributed feedback (see Fig. 5.3(c)). As discussed in Sec. 3.2 and Sec. 3.3, $\Gamma_{\rm FF}$ accounts for the optical confinement in the active region as if the active layers uniformly extended throughout the slab along the vertical direction. In the case of a buried heterostructure active region, $\Gamma_{\rm FF}$ decreases as the wavelength moves deeper into the slow-light region, owing to the lateral spreading of the Bloch modes (see Fig. 3.10 in Sec. 3.2.1 and Fig. 3.15(b) in Sec. 3.3). This explains why $\Gamma_{\rm FF}$ decreases with increasing cavity length. The vertical optical confinement is instead taken into account via Γ_y. As discussed in Sec. A.3.1, Γ_y

is weakly dependent on frequency as compared to Γ_{FF} and thus assumed to be fixed. In the absence of distributed feedback, the Q-factor is obtained from Eqs. (5.54) and (5.55), with the optical confinement factor Γ in Eq. (5.54) being set to $\Gamma_{\text{FF}}\Gamma_y$. An open point is how the Q-factor should be defined in the presence of distributed feedback, which is not unambiguous. Therefore, we omit this case in Fig. 5.3(d).

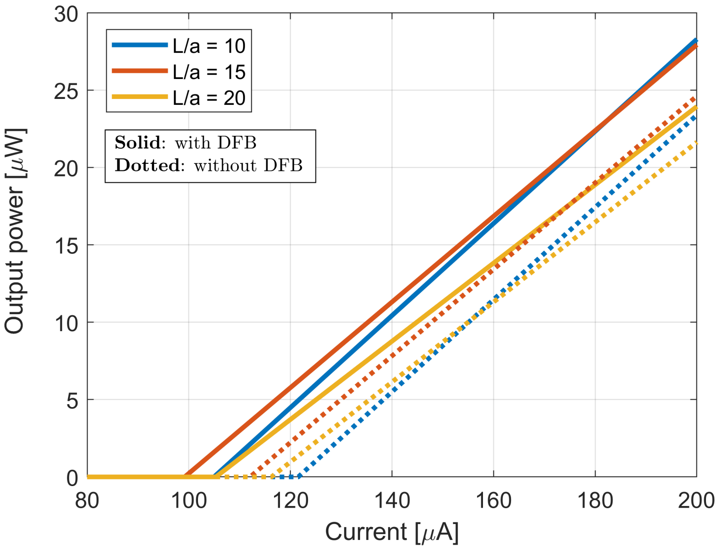

Figure 5.4: P-I characteristic of photonic crystal lasers with photonic bandgap mirrors with (solid) and without (dotted) gain-induced distributed feedback. The cavity length is equal to 10 (blue), 15 (red) and 20 (yellow) lattice constants.

The threshold carrier density is obtained from the value of $\Gamma_y g_{\text{mat}}$ at the lasing threshold by knowing Γ_y, differential gain g_N and transparency carrier density. Subsequently, the threshold current is computed. Fig. 5.4 shows the output power versus injected current with the cavity length being 10 (blue), 15 (red) and 20 (yellow) lattice constants. These values correspond to 4.38 μm, 6.57 μm and 8.76 μm respectively. The solid (dotted) line is with (without) gain-induced distributed feedback. The distributed feedback improves the threshold current, owing to the smaller threshold gain, while the slope efficiency is almost unaffected. For the same cavity lengths, Fig. 5.5(a) shows the 3dB modulation bandwidth as a function of the ratio between injected current and threshold current, with (solid) and without (dotted) gain-induced distributed feedback. The distributed feedback slightly improves the bandwidth, owing to the smaller equivalent photon lifetime $\tau_{p_{\text{eq}}}$. This is reported in Fig. 5.5(b) versus cavity length. In this respect, it should be emphasized that, in spite of the reduced threshold carrier density, $\tau_{p_{\text{eq}}}$ (see Eq. (5.49)) is indeed smaller in the presence of distributed feedback. This is because the distributed feedback also enhances the value of $G_{N_{\text{eq}}}$, as we have verified. Therefore, $G_{N_{\text{eq}}}$ appears to be a key parameter. A point of attention here is that, even

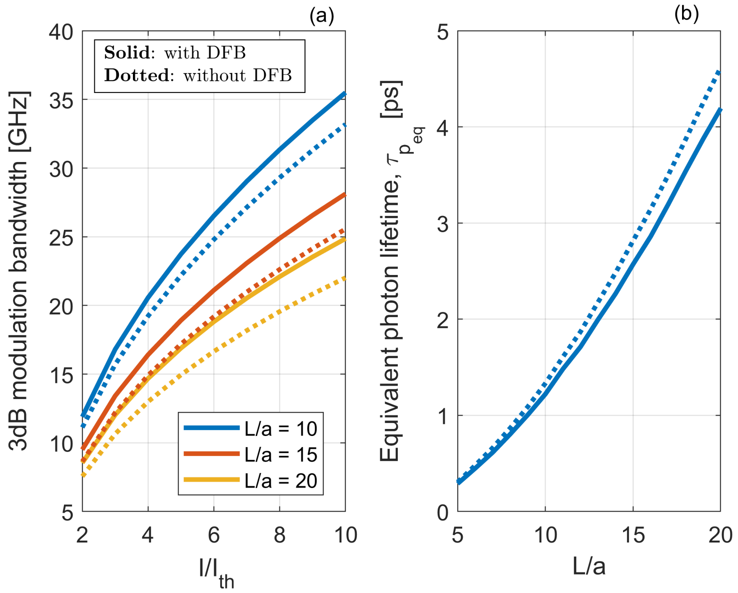

Figure 5.5: Small-signal characteristics of photonic crystal lasers with photonic bandgap mirrors with (solid) and without (dotted) gain-induced distributed feedback. (a) 3dB modulation bandwidth as a function of the ratio between injected current and threshold current with the cavity length being 10 (blue), 15 (red) and 20 (yellow) lattice constants. (b) Equivalent photon lifetime versus cavity length.

in the absence of distributed feedback, $\tau_{p_{eq}}$ is *not* reduced to τ_p. This is because, as discussed above, the two definitions are only equivalent if one assumes $\partial\Gamma_{FF}/\partial\omega = 0$ and $\partial n_g/\partial\omega = 0$, as well as $\Gamma_{FB} = 0$.

Finally, Fig. 5.6 shows the energy cost as a function of the modulation bandwidth with the cavity length being 10 (blue), 15 (red) and 20 (yellow) lattice constants. The energy cost is computed via Eq. (1.14) in Sec. 1.2, by neglecting for simplicity the series electrical resistance. Owing to the larger modulation bandwidth and smaller threshold current, the gain-induced distributed feedback (solid line) appears to reduce the energy cost as compared to the case when it is neglected (dotted line). In addition, we note that, regardless of whether or not the distributed feedback is accounted for, the optimum bandwidth which minimizes the energy cost increases as the cavity becomes shorter. This is due to the larger threshold carrier density (see Eq. (1.18) in Sec. 1.2).

5.3.3 Frequency modulation response

By starting from the phase rate equation, namely Eq. (5.29b), one can also derive the frequency modulation response. The instantaneous frequency is defined as

$$\nu(t) = \frac{\omega_s}{2\pi} + \frac{1}{2\pi}\frac{d\phi(t)}{dt} \tag{5.57}$$

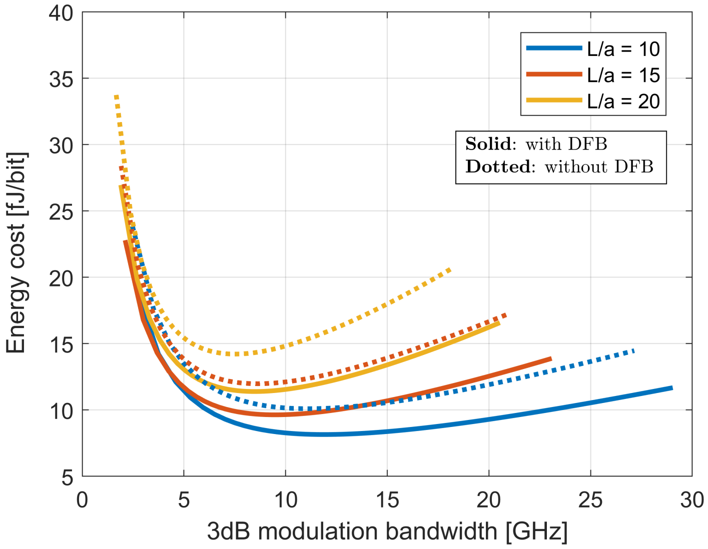

Figure 5.6: Energy cost of photonic crystal lasers with photonic bandgap mirrors with (solid) and without (dotted) gain-induced distributed feedback. The cavity length is equal to 10 (blue), 15 (red) and 20 (yellow) lattice constants.

Under small-signal conditions, $\nu(t)$ responds to the time-harmonic current modulation as

$$\nu(t) = \nu_{\text{bias}} + \nu_1 e^{i\tilde{\omega}t} \tag{5.58}$$

Here, the frequency at the bias point, ν_{bias}, is $\omega_s/(2\pi)$, while the frequency chirp, $\nu_1 e^{i\tilde{\omega}t}$, is $\frac{1}{2\pi} d\phi/dt$. By inserting the frequency chirp, as well as the carrier density from Eq. (5.43c), into Eq. (5.29b), one finds

$$\nu_1 = -\frac{\zeta'}{2\pi} N_1 \tag{5.59}$$

The carrier density perturbation, N_1, is obtained by solving the linear system in Eq. (5.44). Thus, one finds the frequency modulation response

$$\frac{q\nu_1(\tilde{\omega})}{I_1} = -\frac{1}{2\pi}\frac{\eta_i \zeta'}{V_{\text{act}}}\frac{\gamma_{\text{PP}_{\text{eq}}} + i\tilde{\omega}}{\omega_{R_{\text{eq}}}^2} H_{\text{eq}}(\tilde{\omega}) \tag{5.60}$$

This equation extends the conventional expression of the frequency modulation response [23] by accounting for slow-light and gain-induced distributed feedback. Here, it should be emphasized that ζ' is generally different from zero even in the ideal case of a zero linewidth enhancement factor. If one neglects 1) the gain-induced distributed feedback and 2) the dispersion of the effective net modal gain, ζ' is reduced to

$$\zeta' = \frac{\partial\beta_{\text{eff}}/\partial N}{\partial\beta_{\text{eff}}/\partial\omega} = -\frac{1}{2}\left(\frac{c}{n_{\text{slab}}}\right)\alpha_H \Gamma_{\text{FF}} \Gamma_y g_N \tag{5.61}$$

In this case, one finds the conventional expression of the frequency modulation response. As a future perspective, it could be interesting to investigate the impact of slow-light on the frequency chirp as predicted by Eq. (5.60).

5.4 Conclusions

To summarize, we have derived a rate equation model of photonic crystal lasers which self-consistently accounts for slow-light and gain-induced distributed feedback.

The starting point is the laser oscillation condition, thoroughly discussed in Chapter 4. Specifically, the model consists of a field rate equation coupling the amplitudes of the forward- and backward-propagating fields (see Eq. (5.10)) and a carrier rate equation (see Eq. (5.17)). The field rate equation is derived from a first-order Taylor expansion of the oscillation condition around the lasing threshold, by following the approach of [167]. The stimulated emission rate (see Eq. (5.18)) coupling the field and carrier rate equation is derived in detail in Appendix D, by integrating over the laser cavity the local stimulated emission rate. Therefore, the stimulated emission rate in Eq. (5.18) effectively accounts for the longitudinal and transverse spatial dependence of the electric field in the laser cavity, given by Eq. (5.1). An additional field rate equation should be included within the model if the right mirror is frequency-dependent. Formally, this equation is given by the inverse Fourier transform of the right mirror boundary condition (see Eq. (5.2a)). In the case of Fano lasers, it can be derived as shown in [132]. Therefore, the rate equation model presented in this chapter may be extended to Fano lasers to investigate the impact of slow-light.

We have applied the model to lasers with photonic bandgap mirrors, which are broadband. Therefore, no additional field rate equation is required in this case. We have obtained analytical expressions for the P-I characteristic (see Eq. (5.35)), the intensity modulation response (see Eq. (5.47)) and the frequency modulation response (see Eq. (5.60)). In particular, the intensity modulation response retains the familiar expression of conventional [23] rate equation models, with equivalent relaxation resonance frequency and damping rate. These can be expressed in terms of an equivalent photon lifetime (see Eq. (5.49)). This equivalent photon lifetime depends on the threshold carrier density and a small-signal parameter, $G_{N_{\text{eq}}}$. This parameter reflects the differential dependence of the internal reflection coefficient on both carrier density and frequency, as discussed in Sec. 5.3.2. Preliminary results show that the gain-induced distributed feedback may improve, albeit slightly, threshold current (see Fig. 5.4), 3dB modulation bandwidth (see Fig. 5.5(a)) and energy cost (see Fig. 5.6).

Further investigations would be certainly required to explore if the impact of the gain-induced distributed feedback may be more significant. In lasers with photonic bandgap mirrors, this could be the case, for instance, in dependence of the linewidth enhancement factor. In fact, as the linewidth enhancement factor increases, the distributed feedback may considerably reduce the threshold modal gain (see Fig. 4.17 in

Sec. 4.4). In addition, as discussed in Sec. 4.3.2, the internal reflection coefficient strongly depends on the phase of the left mirror. Tuning of this phase would certainly affect both the static and small-signal characteristics. Exploring the frequency modulation response could be also interesting, to assess the impact of slow-light on the frequency chirp.

Chapter 6

QD lasers on silicon: impact of carrier transport

In this chapter, we deal with quantum dot lasers epitaxially grown on silicon. To describe the laser operation, we employ a drift-diffusion transport model, augmented with conventional rate equations for photons and carriers in the quantum dot layers. These rate equations for carriers govern the intersubband transitions involved into simultaneous ground-state and excited-state lasing. The model is described in Sec. 6.2, while results are presented in Sec. 6.3. In particular, we focus on three mechanisms affecting the laser operation. In Sec. 6.3.1, we analyze the impact of threading dislocations on the laser threshold current. In Sec. 6.3.2, we show that the asymmetric transport of carriers explains the ground-state power quenching above the excited-state lasing threshold. In Sec. 6.3.3, we investigate the physics behind an optimum p-type modulation doping which minimizes the ground-state threshold current. Finally, in Sec. 6.4 we draw the conclusions.

6.1 Introduction and motivation

Energy-efficient and low-cost silicon photonics technologies for CMOS-compatible optical interconnects are a very attractive solution for low-power, high-speed data links in data centres and supercomputers. In this context, quantum dot (QD) laser diodes, already considered the most promising lasers for optical communications [107], are attracting strong interest for direct epitaxial growth on silicon. This monolithic integration [17, 147, 76] is the ultimate solution to minimize the complexity and cost of the fabrication process and improve the integration density of the silicon photonic integrated circuit.

However, the mismatch in the lattice constant and thermal expansion coefficients causes the generation of threading dislocations (TDs), which act as non-radiative recombination centres and degrade the laser performance. As an example, Fig. 6.1 shows

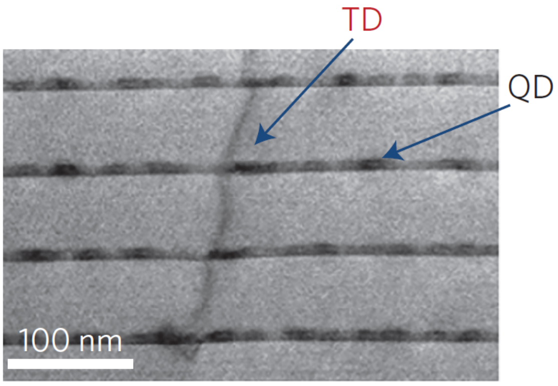

Figure 6.1: Electron microscope image showing the interaction between a threading dislocation (TD) and QD layers. Reproduced from [17].

an electron microscope image of a threading dislocation interacting with QD layers. Despite the significant progress made recently [110, 172, 77, 58], the achievable TD density is still around $10^5 - 10^6$ cm^{-2}. At such high densities, quantum well (QW) lasers either show very poor performances or do not even lase [78]. On the contrary, quantum dots (QDs) have proved to be more tolerant to TDs, due to 3D carrier localization within the QDs [37, 80]. Apart from this feature, QD lasers on silicon share several similarities

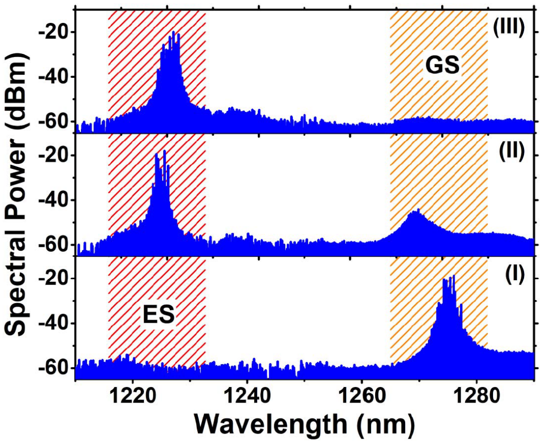

Figure 6.2: Optical spectrum measured for a QD laser epitaxially grown on silicon: (I) above the GS threshold, (II) just above the ES threshold, and (III) well-above the ES threshold. Reproduced from [49].

with ordinary QD laser diodes on GaAs. Among these, we cite the double state lasing from both ground state (GS) and excited state (ES) and the fast hole thermalization in the QD confined states of the valence band [84, 21]. A detrimental effect related to double state emission is the GS power quenching taking place above the ES threshold [38, 63, 49]. Fig. 6.2 exemplies this phenomenon for a QD laser epitaxially grown on silicon

[49], by showing the optical spectrum measured (I) above the GS threshold, (II) just above the ES threshold, and (III) well-above the ES threshold. The hole thermalization, which increases the laser threshold and reduces the differential gain, is usually cured via p-type modulation doping [151, 64, 73], which has been recently employed also for QD lasers on silicon [186]. Experimental results [186] have demonstrated that an optimum doping level exists, as an excessive doping can degrade the GS optical power and threshold current. Fig. 6.3 shows the threshold current density measured [186] for a QD laser epitaxially grown on silicon with varying p-type modulation doping density. This effect is a matter of debate and has been attributed to different phenomena, such as the enhanced free carrier absorption [64] or the increase in the defect-assisted recombination with the doping level [186].

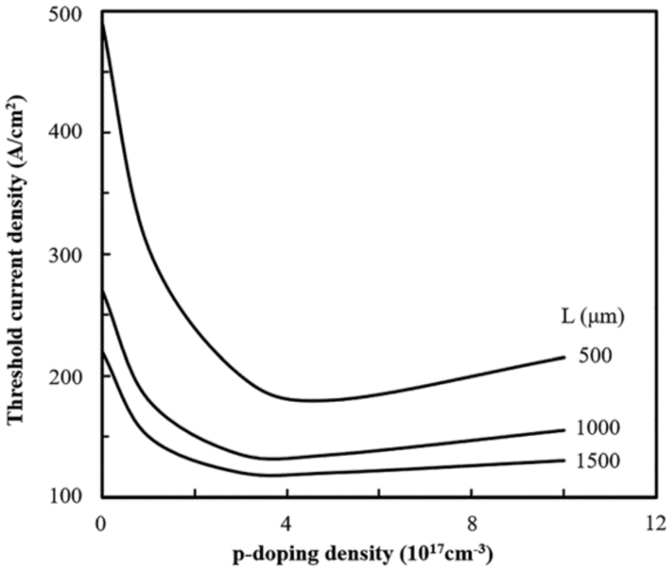

Figure 6.3: Threshold current density measured for a QD laser epitaxially grown on silicon with varying p-type modulation doping density. Reproduced from [186].

6.1.1 Motivation of this chapter

To achieve deeper understanding of the device operation, modelling can be an instrumental platform. In this context, most of the literature relies on lumped rate equations describing the interaction of carriers and photons in each energy state. Although such approaches provide an appropriate picture of the intersubband interactions, they reduce the model of the separate-confinement heterostructure (SCH) to phenomenological capture terms [80, 38], neglecting carrier transport and electrostatic effects. On the contrary, in this chapter we present an investigation based on a drift-diffusion model [39, 16, 40], with the aim at providing a more solid interpretation.

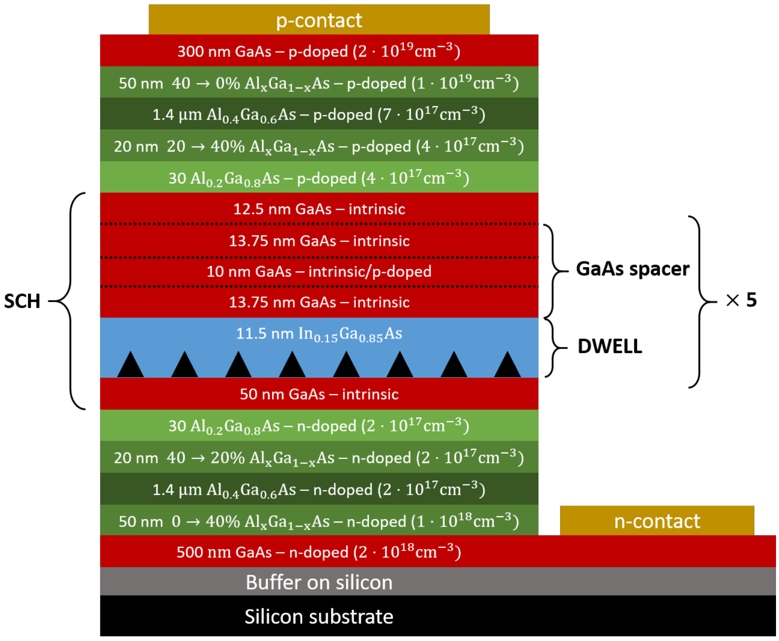

Figure 6.4: Schematic representation of the epitaxial structure of the studied QD lasers, similar to those in [57, 52]. The growth direction is from the bottom to the top.

In particular, the model is applied to characterize the continuous wave (CW) performance of QD lasers on silicon with InAs/GaAs self-assembled QDs emitting at 1.3 μm. We focus on three issues: 1) the impact of TDs on the laser P-I characteristic; 2) the role of carrier transport in the barrier states in reproducing the simultaneous GS and ES lasing and competition; and 3) the existence of an optimum p-type modulation doping which minimizes the laser threshold current.

6.2 Method

6.2.1 Device under study

A schematic drawing of the epitaxial structure of the investigated QD lasers is illustrated in Fig. 6.4. The structure is similar to others reported in the literature [57, 52]. In these devices, the layers grown immediately above the silicon substrate act as buffers and dislocation filters reducing the density of TDs in the n-type cladding and SCH region. The n-type electrical contact is positioned on top of a GaAs n-doped buffer layer, thus avoiding carrier injection through the much more defective layers located below. For this reason, we have not simulated transport through the silicon substrate and buffer and we have assumed that electrons are directly injected through the 500 nm n-doped GaAs layer. The active region includes five layers of InAs QDs each grown in a 11.5 nm-thick In$_{0.15}$Ga$_{0.85}$As QW, thus forming a dot-in-a-well (DWELL) structure. In each of the 37.5 nm-thick GaAs spacers separating a DWELL layer from another, the central 10 nm-thick region can either be intrinsic or p-type doped.

6.2.2 Model

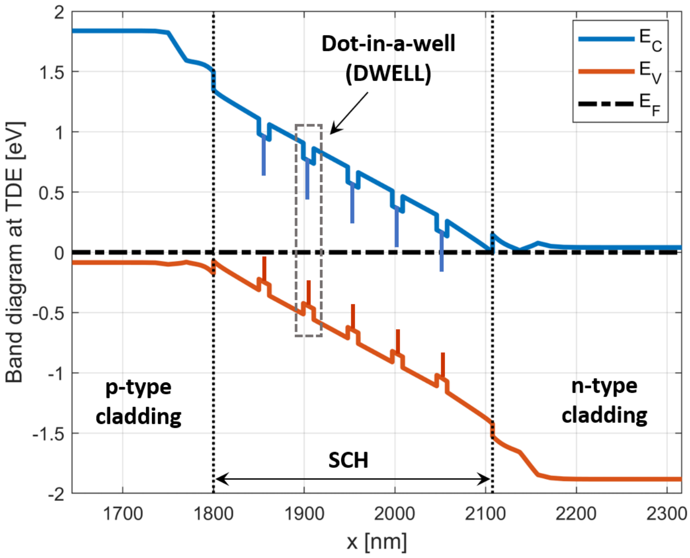

Figure 6.5: Band diagram at thermodynamic equilibrium, with the conduction band (blue), the valence band (red) and the Fermi level (dashed, black). The dotted, vertical lines delimit the SCH region.

The simulation framework consists of an in-house developed [165] Poisson-drift-diffusion system augmented with carrier and photon rate equations of the localized states. The code requires as input a detailed description of the layer stack (material composition, doping) and QD characteristic parameters, listed in Tab. 6.1. These parameters have been taken from previous studies [38] or extracted from literature experimental data representative of QD lasers on silicon.

Fig. 6.5 shows the calculated energy band diagram under thermodynamic equilibrium for the device sketched in Fig. 6.4, with x being the growth direction. The carrier continuity equations are formulated within a drift-diffusion-Poisson formalism as:

$$\frac{\partial n}{\partial t} = \frac{1}{q}\frac{\partial J_n}{\partial x} - U^{\mathrm{B}} - \sum_i \left(R_{n,\mathrm{CAP}}^{\mathrm{B}\to\mathrm{WL},i} - R_{n,\mathrm{ESC}}^{\mathrm{WL},i\to\mathrm{B}} \right) \delta(x - x_i) \tag{6.1a}$$

$$\frac{\partial^2 \phi}{\partial x^2} = -\frac{q}{\epsilon}\left[p - n + N + \sum_{k,i} \left(p_{k,i} - n_{k,i} \right) \delta(x - x_i) \right] \tag{6.1b}$$

here, J_n is the electron current density, U^{B} is the net band-to-band recombination rate including Shockley-Read-Hall (SRH) and radiative processes and N is the net doping.

Parameters	Values
ΔE_n^k, $k = \mathrm{WL, ES, GS}$ [meV]	177.7, 30, 41.1 [38]
ΔE_p^k, $k = \mathrm{WL, ES, GS}$ [meV]	166.3, 25, 25 [38]
$\tau_{n,\mathrm{CAP}}^{\mathrm{B}\to\mathrm{WL}}$, $\tau_{n,\mathrm{CAP}}^{\mathrm{WL}\to\mathrm{ES}}$, $\tau_{n,\mathrm{CAP}}^{\mathrm{ES}\to\mathrm{GS}}$ [ps]	0.1, 1, 1 [116]
$\tau_{p,\mathrm{CAP}}^{\mathrm{B}\to\mathrm{WL}}$, $\tau_{p,\mathrm{CAP}}^{\mathrm{WL}\to\mathrm{ES}}$, $\tau_{p,\mathrm{CAP}}^{\mathrm{ES}\to\mathrm{GS}}$ [ps]	0.1, 0.1, 0.1 [116]
τ_{rad}^k, $k = \mathrm{WL, ES, GS}$ [ns]	1, 1, 1 [80, 16]
$\tau_{n,\mathrm{SRH}}^k$, $k = \mathrm{ES, GS}$ [ns]	1, 1 [80, 16]
$\tau_{p,\mathrm{SRH}}^k$, $k = \mathrm{ES, GS}$ [ns]	1, 1 [80, 16]
QD sheet density $N_{\mathrm{QD},i}$ [cm^{-2}]	4.9×10^{10}
GS (ES) degeneracy μ_{GS} (μ_{ES})	2 (4)
Gain coefficient G_0^{GS} (G_0^{ES}) [cm^{-1}]	433 (779.4)
Electron (hole) effective mass m_n^* (m_p^*) [m_0]	0.054 (0.49)
Optical confinement factor Γ_i	$\sim 2\%$
Intrinsic loss α_i [cm^{-1}]	5
Waveguide width [μm]	3.5
Facet reflection coefficient	0.32
Spontaneous emission factor β_{sp}	10^{-4}
Group index	3.56
GaAs D_n, D_p [cm^{2}s^{-1}]	221, 10
In$_{0.15}$Ga$_{0.85}$As D_n, D_p [cm^{2}s^{-1}]	181, 10
Temperature [K]	300

Table 6.1: QD laser simulations parameters

$R_{n,\mathrm{CAP}}^{\mathrm{B}\to\mathrm{WL},i}$ and $R_{n,\mathrm{ESC}}^{\mathrm{WL},i\to\mathrm{B}}$ are, respectively, the capture and escape rates between the barrier and the i-th QD layer (located in the node x_i). For the sake of brevity, drift-diffusion and carrier rate equations are reported here for electrons only, but a similar set of equations is implemented also for holes.

Fig. 6.6 illustrates the model employed for the dynamics in each QD layer. The rate equations governing the electron dynamics in the i-th QD layer are

$$\begin{aligned}\frac{\partial n_{k,i}}{\partial t} &= \left(R_{n,\mathrm{CAP}}^{k+1,i\to k,i} - R_{n,\mathrm{ESC}}^{k,i\to k+1,i}\right) \\ &\quad - \left(R_{n,\mathrm{CAP}}^{k,i\to k-1,i} - R_{n,\mathrm{ESC}}^{k-1,i\to k,i}\right) - U^{k,i} - R_{\mathrm{st}}^{k,i}\end{aligned} \tag{6.2}$$

where $U^{k,i}$ accounts for SRH and radiative recombination and $R_{\mathrm{st}}^{k,i}$ is the stimulated recombination rate. $R_{n,\mathrm{CAP}}^{k,i\to k-1,i}$ and $R_{n,\mathrm{ESC}}^{k-1,i\to k,i}$ are the capture and escape rates between the states k-th and $(k-1)$-th, with $k = \mathrm{B, WL, ES}$ and $(k-1) = \mathrm{WL, ES, GS}$, computed as in [39, 165], where WL indicates the wetting layer state including both the 2D well states and the upper continuum of the QDs. The capture rate depends on the capture

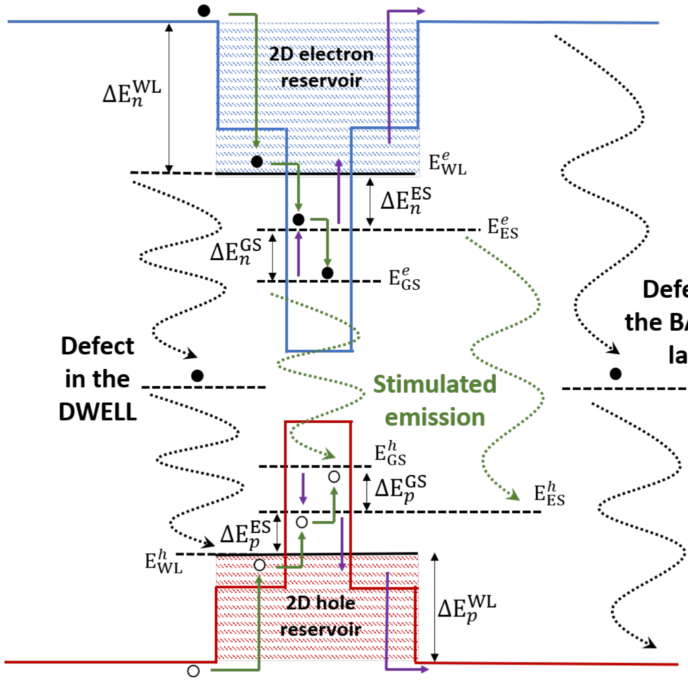

Figure 6.6: Schematic representation of the QD energy states and intersubband transitions.

time ($\tau_{n,\mathrm{CAP}}^{k\to k-1}$) from the state with higher energy (k) to the state with lower energy ($k-1$), whereas the escape rate is dependent on the escape time that leads the system to equilibrium in the absence of any injection current or recombination rate [39]. These equations put in relation the 3D carrier volume densities (n, p) with the electrostatic potential ϕ and the carrier sheet densities ($n_{k,i}$, $p_{k,i}$) of the k-th QD energy level of the i-th QD layer.

The net recombination rate $U^{k,i}$ is given by $U^{k,i} = U_{\mathrm{rad}}^{k,i} + U_{\mathrm{SRH}}^{k,i}$. Here, $U_{\mathrm{rad}}^{k,i}$ is the net radiative recombination rate modelled as

$$U_{\mathrm{rad}}^{k,i} = B_{\mathrm{rad}}^{k}\left(n_{k,i}p_{k,i} - n_{k0,i}p_{k0,i}\right) \tag{6.3}$$

where $n_{k0,i}$ and $p_{k0,i}$ are the electron and hole sheet density in the k-th energy level at thermal equilibrium, respectively, and $B_{\mathrm{rad}}^{k,i}$ is a radiative recombination coefficient related to the radiative time τ_{rad}^{k} [39]. The net SRH recombination rate is modelled as

$$U_{\mathrm{SRH}}^{k,i} = \frac{n_{k,i}p_{k,i} - n_{k0,i}p_{k0,i}}{\tau_{n,\mathrm{SRH}}^{k}\left(p_{k,i} + p_{k0,i}\right) + \tau_{p,\mathrm{SRH}}^{k}\left(n_{k,i} + n_{k0,i}\right)} \tag{6.4}$$

where $\tau_{n,\mathrm{SRH}}^{k}$ and $\tau_{p,\mathrm{SRH}}^{k}$ are SRH lifetimes for electrons and holes, respectively. The SRH lifetime in the barrier and DWELL ($k = \mathrm{B},\ \mathrm{WL}$) is reduced by the presence of TDs according to [180, 6]

$$\frac{1}{\tau_{n(p),\mathrm{SRH}}} = \frac{1}{\tau^0_{n(p),\mathrm{SRH}}} + \frac{\pi^3 D_{n(p)}\mathrm{TDD}}{4} \tag{6.5}$$

with $\tau^0_{n(p),\mathrm{SRH}}$ being the typical (doping-dependent) lifetime of dislocation free GaAs [82] and TDD the TD density. The WL stimulated emission rate is assumed to be negligible. The GS and ES stimulated emission rates are given by

$$R^{k,i}_{\mathrm{st}} = \upsilon_g G^k_0 \Gamma_i \left(\rho^{k,i}_n + \rho^{k,i}_p - 1 \right) S^k \tag{6.6}$$

with $k = \mathrm{ES}, \mathrm{GS}$. Here, S^k is the photon density emitted by the GS or ES ($k = \mathrm{GS}, \mathrm{ES}$) and υ_g the group velocity, while $\rho^{k,i}_{n(p)}$ is the occupation probability of electrons (holes) k-th energy level of the i-th QD layer. The coefficient G^k_0 is the saturated material gain (i.e.: the material gain if the electron and hole k-th state were fully filled) of the QD layer. Γ_i is the optical confinement factor of the TE fundamental mode in the i-th QD layer and it has been computed from the fundamental TE mode profile of the epitaxial structure with no optical gain. The rate equation for the photon density S^k is governed by:

$$\frac{dS^k}{dt} = \beta_{\mathrm{sp}} R^k_{\mathrm{sp}} + \upsilon_g G^{\mathrm{mod}}_k S^k - \frac{S^k}{\tau_p} \tag{6.7}$$

where $R^{\mathrm{k}}_{\mathrm{sp}}$ is the spontaneous emission rate, given by $R^k_{\mathrm{sp}} = \sum_i U^{k,i}_{\mathrm{rad}}$. G^{mod}_k is the GS (ES) modal gain, β_{sp} is the spontaneous emission factor and τ_p is the photon lifetime [23], which accounts for the intrinsic and mirror loss. The GS and ES modal gain are given by

$$\begin{aligned} G^{\mathrm{mod}}_k &= G^k_0 \sum_i \Gamma_i \left(\rho^{k,i}_n + \rho^{k,i}_p - 1 \right) \\ &= \underbrace{G^k_0 \sum_i \Gamma_i \rho^{k,i}_n}_{G^{\mathrm{mod},n}_k} + \underbrace{G^k_0 \sum_i \Gamma_i \rho^{k,i}_p}_{G^{\mathrm{mod},p}_k} - G^k_0 \sum_i \Gamma_i \end{aligned} \tag{6.8}$$

with $k = \mathrm{ES}, \mathrm{GS}$. The coefficient G^{GS}_0 has been estimated to be $\sim 433\,\mathrm{cm}^{-1}$ through a fitting of the measured modal gain versus current reported in [57] (see Fig. 6.7), resulting in $G^{\mathrm{GS}}_0 \sum_i \Gamma_i \sim 52.4\,\mathrm{cm}^{-1}$, where $\Gamma_i \sim 2\%$. The coefficient G^{ES}_0 has been set to $1.8\, G^{\mathrm{GS}}_0$ to account for the ES degeneracy. Unless otherwise specified, the main simulation parameters employed in this work are summarized in Tab. 6.1. The separation between GS and ES energy levels is taken from [38] and corresponds to a difference in GS and ES recombination energy of 55 meV, similar to that reported in [49]. The values of carrier capture and relaxation times are in line with [116], where ultra-fast hole dynamics and picosecond or sub-picosecond electron dynamics have been measured. All the simulations assume isothermal conditions and ambient temperature.

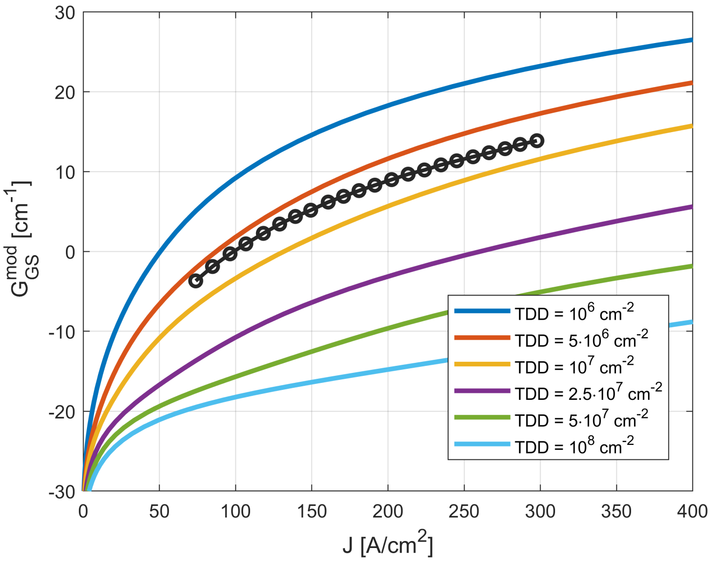

Figure 6.7: Calculated GS modal gain versus current density for different levels of threading dislocation density TDD and experimental gain (circles) from [57].

6.3 Results and discussion

6.3.1 Impact of threading dislocations

We investigate the impact of SRH recombination due to TDs, both in the DWELL and barrier layers. Fig. 6.7 shows the modal gain of the device under study for different values of TDD. In the TDD range $5 \times 10^{16} - 10^{17}$ cm^{-3}, the calculated gain is similar to the experimental one in [57]. For a qualitative comparison with experimental results, we consider a Fabry-Perot laser with mirror loss $\alpha_m = 8.6\,\text{cm}^{-1}$ (corresponding to a Fabry-Perot cavity length $L = 1325\,\mu$m), to guarantee lasing on the GS only [57].

To disentangle the impact of TDs in the barrier and DWELL layers, Fig. 6.8(a) and (c) show simulation results when TDs are present in the barrier only, whereas Fig. 6.8(b) and (d) consider the more realistic situation of similar TDD in the barrier and DWELL layers. The GS threshold current density (Fig. 6.8(a)) and P − I characteristic (Fig. 6.8(c)) are marginally affected by the lifetime degradation induced by TDs in the barrier layers.

On the other hand, recombination mediated by TDs in the DWELL layers affects the laser performance significantly. Fig. 6.8(b) shows the threshold current density (blue) and slope differential efficiency (red) as a function of TDD, taking into account the SRH lifetime reduction according to Eq. (6.5) both in the barrier and DWELL layers. The slope efficiency is defined as $(q/\hbar\omega) \cdot (dP/dI)$, with ω being the GS emission angular frequency, and it has been evaluated just above the laser threshold. In this case, as the TDD in the DWELL layers increases, the effective injection efficiency into the QDs diminishes, causing increased threshold current and reduced slope efficiency. This is

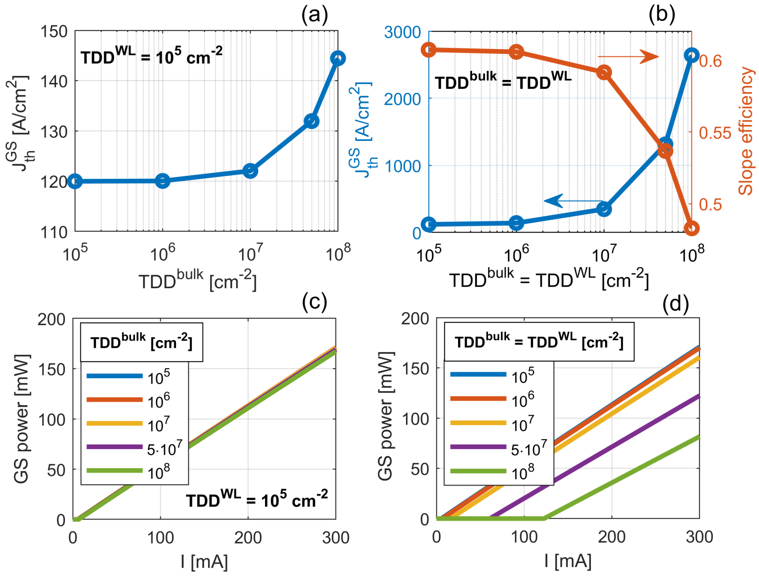

Figure 6.8: (a) GS threshold current density and (c) optical power as a function of the bulk threading dislocation density TDD$^{\text{bulk}}$, for fixed DWELL SRH lifetime (corresponding to TDD$^{\text{WL}}$ = 10^5 cm^{-2}). (b) GS threshold current density and slope efficiency and (d) optical power as a function of the threading dislocation density in the barrier and DWELL layers (TDD$^{\text{WL}}$ = TDD$^{\text{bulk}}$).

also evident from the light-current characteristics in Fig. 6.8(d) calculated for different values of TDD. Therefore, the TDs in the DWELL layers are those responsible for the degradation of the laser performance. Similar scaling of threshold current with TDD has been observed experimentally in [59], where devices of different generations have been compared, having TDD in the same range of Fig. 6.8(b) and (d). These results also support the hypothesis that the degradation mechanisms limiting the long-term reliability could be correlated to a gradual propagation of TDs towards the DWELL layers of the device active region [14].

6.3.2 Impact of carrier transport on double-state lasing and GS power quenching

In this section, we discuss the influence on the CW performance of the asymmetry in the transport of electrons and holes across the barrier, owing to the different electron and hole low-field mobility in the GaAs layers. We demonstrate that this asymmetry is at the basis of the GS power quenching after the ES lasing threshold. For this purpose, we have set the mirror loss to $\alpha_m = 26.6\,\text{cm}^{-1}$ (corresponding to $L = 428\,\mu$m). In this case, dual state emission occurs at a reasonable ES threshold current. All results reported in this section are calculated for a TDD of $5 \cdot 10^6$cm^{-2}.

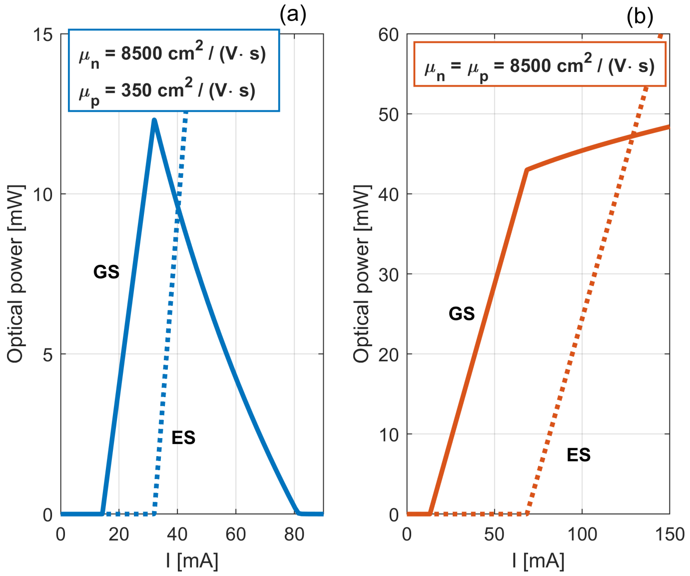

Figure 6.9: GS (solid) and ES (dotted) optical power with (a) $\mu_\mathrm{n} = 8500\,\mathrm{cm}^2/(\mathrm{Vs})$ and $\mu_\mathrm{p} = 350\,\mathrm{cm}^2/(\mathrm{Vs})$ and (b) $\mu_\mathrm{n} = \mu_\mathrm{p} = 8500\,\mathrm{cm}^2/(\mathrm{Vs})$ in the SCH region.

Fig. 6.9(a) shows the optical power emitted on the GS (solid) and ES (dotted) when the mobility of electrons and holes in the SCH region is set to conventional room temperature values, corresponding to $\mu_\mathrm{n} = 8500\,\mathrm{cm}^2/(\mathrm{Vs})$ and $\mu_\mathrm{p} = 350\,\mathrm{cm}^2/(\mathrm{Vs})$. In this case, the GS power decreases as the current overcomes the ES threshold and it is completely quenched at sufficiently high currents. To highlight the impact of the unbalance of electron and hole mobility, Fig. 6.9(b) shows the GS (solid) and ES (dotted) optical power by forcing $\mu_\mathrm{n} = \mu_\mathrm{p} = 8500\,\mathrm{cm}^2/(\mathrm{Vs})$. In this case, the GS power is not quenched when the ES turns on, demonstrating that quenching can be ascribed to the different mobilities. The same conclusion can be drawn by forcing $\mu_\mathrm{n} = \mu_\mathrm{p} = 350\,\mathrm{cm}^2/(\mathrm{Vs})$ (not reported in this work), which only causes a larger separation between GS and ES threshold currents.

The asymmetry in the transport of electrons and holes reflects into the rate at which carriers are filling the various QD layers. This is emphasized in Fig. 6.10(a), showing the net capture rate of carriers from the bulk states to the WL with $\mu_\mathrm{n} = 8500\,\mathrm{cm}^2/(\mathrm{Vs})$ and $\mu_\mathrm{p} = 350\,\mathrm{cm}^2/(\mathrm{Vs})$. Each colour corresponds to a different QD layer, with layer 1 (5) being the closest to the p- (n-) contact. Layers located farthest from the p-contact are filled by holes at a smaller rate. On the contrary, if electron and hole mobilities are equal, holes are more evenly distributed and all the QD layers are filled at a similar rate, which increases linearly with the injected current. This is presented in Fig. 6.10(b), reporting the net capture rate of carriers from the bulk states to the WL with $\mu_\mathrm{n} = \mu_\mathrm{p} = 8500\,\mathrm{cm}^2/(\mathrm{Vs})$. This last case is in line with the exciton rate equation approach that, neglecting carrier transport and hole dynamics, was initially used

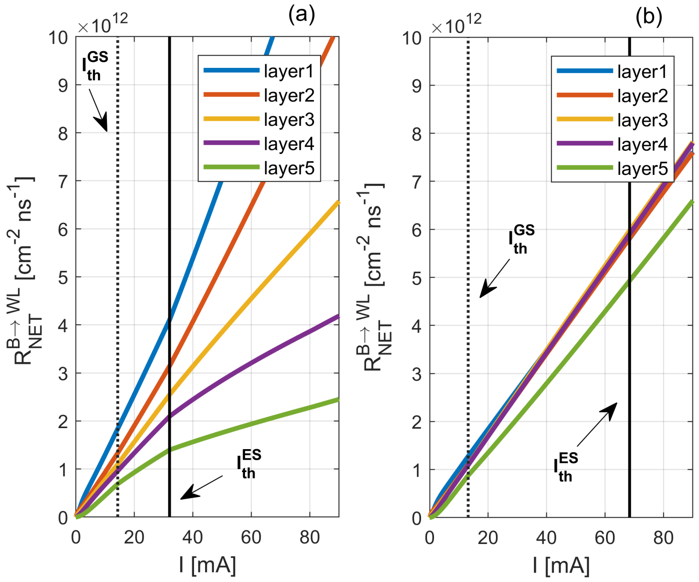

Figure 6.10: Net capture rate from the bulk states to the WL with (a) $\mu_\mathrm{n} = 8500\,\mathrm{cm^2/(Vs)}$ and $\mu_\mathrm{p} = 350\,\mathrm{cm^2/(Vs)}$ and (b) $\mu_\mathrm{n} = \mu_\mathrm{p} = 8500\,\mathrm{cm^2/(Vs)}$. Layer 1 (5) is the closest to the p- (n-) contact.

to model double state lasing in QDs [83]. Indeed, the power-current characteristic in Fig. 6.9(b) mirrors the results which one would obtain in the exciton approximation [83], which is unable to reproduce the GS quenching. On the other hand, several experiments have shown that double state lasing is often characterized by the GS quenching, as reproduced in Fig. 6.9(a) by our transport model with realistic material parameters. This provides a physical background to the results presented in [38]. In that work, a phenomenological fitting parameter was ad-hoc introduced to mimic the asymmetric electron/hole transport.

It should be mentioned that the onset of the GS quenching is characterized by an optical threshold. By varying the mirror loss in the asymmetric transport case, we have found that the reduction of the GS power above the ES threshold is only observable for $\alpha_m > 20\ \mathrm{cm^{-1}}$. On the contrary, in the symmetric transport case, regardless of high or low mobility, the GS power quenching is never reproduced whatever the value of α_m is.

In order to achieve deeper insight into the dual-state competition, it is convenient to inspect the overall, separate contributions of electrons ($G_\mathrm{GS}^{\mathrm{mod},n}$) and holes ($G_\mathrm{GS}^{\mathrm{mod},p}$) to the GS modal gain (see Eq. (6.8)). For the sake of brevity, we only discuss explicitly the case with $\mu_\mathrm{n} = 8500\,\mathrm{cm^2/(Vs)}$ and $\mu_\mathrm{p} = 350\,\mathrm{cm^2/(Vs)}$. As the injected current grows between the GS and ES threshold current, $G_\mathrm{GS}^{\mathrm{mod},n}$ decreases (see Fig. 6.11(a)) due to the spectral hole burning of GS electrons that are injected from ES at a slower rate than they recombine. The electron gain compression due to spectral hole burning is compensated by the growth of hole contribution to keep the lasing threshold gain. Indeed, $G_\mathrm{GS}^{\mathrm{mod},p}$

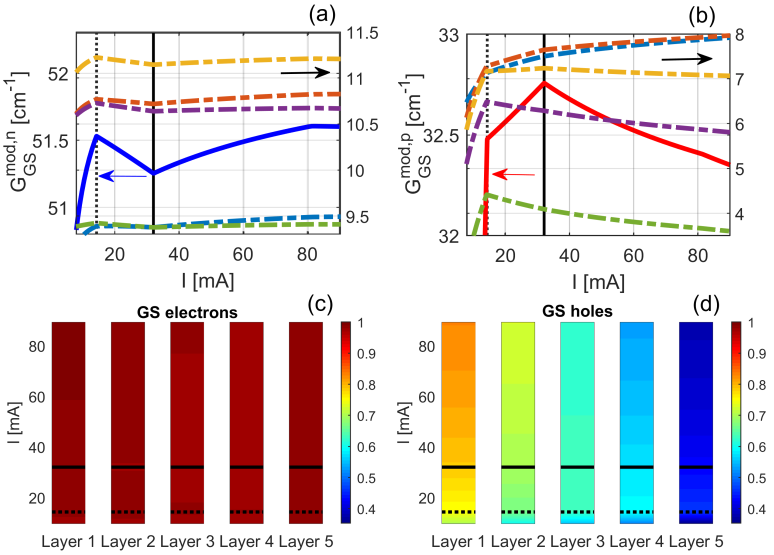

Figure 6.11: Contribution of (a) electrons and (b) holes to the GS modal gain: solid line is the overall contribution, whereas colored dashed lines are the contribution of the different layers (the colour legend is the same as in Fig. 6.10). The vertical lines indicate the GS and ES threshold currents. (c) GS electrons and (d) holes occupation probability. The mobility of electrons and holes in the SCH region are $\mu_n = 8500\,\mathrm{cm^2/(Vs)}$ and $\mu_p = 350\,\mathrm{cm^2/(Vs)}$. Layer 1 (5) is the closest to the p- (n-) contact.

increases (see Fig. 6.11(b)), such that the GS modal gain remains clamped. The dashed curves in Fig. 6.11(a) and (b) quantify how electrons and holes of the various layers contribute to the overall gain in solid line. We see that only the GS holes of the two layers closest to the p-side contribute with increasing gain, thereby compensating for the gain reduction in all the other layers. In contrast, in the case of symmetric mobility $\mu_n = \mu_p = 8500\,\mathrm{cm^2/(Vs)}$ we have found that the hole contribution is always increasing for any current injection.

At the ES threshold current, the ES stimulated emission turns on and starts recombining the ES electrons and holes. This mechanism competes with the relaxation rate from the ES to the GS. Now, the contribution of the GS holes is not enough to compensate for the electron spectral hole burning. As a consequence, the GS electron population has to increase such that $G_{\mathrm{GS}}^{\mathrm{mod},n}$ can maintain the GS threshold condition. Then, the net transition rate of electrons from the ES to the GS decreases due to Fermi blocking. This rate balances the GS stimulated emission rate until the GS optical power is eventually quenched [38]. This mechanism can be simply understood by considering Eq. (6.2) for the GS above the GS lasing threshold, where radiative and non-radiative recombination may be neglected as compared to stimulated recombination. In this case, Eq. (6.2) under steady-state conditions reads

$$0 \approx \left(R_{n,\mathrm{CAP}}^{\mathrm{ES},i \to \mathrm{GS},i} - R_{n,\mathrm{ESC}}^{\mathrm{GS},i \to \mathrm{ES},i} \right) - R_{\mathrm{st}}^{\mathrm{GS},i} \tag{6.9}$$

The first term on the right-hand side is the net transition rate of electrons from the ES to the GS in the i-th QD layer. By summing over the various layers, one obtains the aforementioned balance between the total net rate and the GS optical power. The trends in Fig. 6.11(a) and (b) are also supported by the electron and hole GS occupation probability of the various QD layers. As shown in Fig. 6.11(c) and (d), the GS is almost completely filled with electrons, whereas it is populated scarcely and unevenly by holes.

In summary, the reduction with increasing current of the hole gain contribution in the layers closest to the n-side is caused by the slow hole transport and it is therefore an additional mechanism, besides spectral hole burning, causing gain compression. Spatial hole burning or other gain compression effects are not directly included in the model, but could be taken into account by introducing a phenomenological compression factor parameter [23]. The quantification of the effective gain compression coefficient requires, however, the simulation of the laser intensity modulation response [26], which is outside the scope of this work.

6.3.3 Impact of p-type modulation doping

In order to analyze the impact of modulation doping on dual state emission, we set the mirror loss to $\alpha_m = 26.6\,\mathrm{cm}^{-1}$. All results reported in this section are calculated for $\mathrm{TDD} = 5 \cdot 10^6 \mathrm{cm}^{-2}$.

In this context, the aim of p-type doping is reducing the GS threshold current and increasing that of the ES, such that the GS power is optimized. To focus on the role of doping in terms of electrostatics and transport, in the analysis we intentionally neglect possible additional loss due to free carrier absorption caused by the extra holes in the barrier layers. In addition, we note that the SRH lifetimes calculated according to Eq. (6.5) are dominated by the effect of the TDs. In fact, the doping-dependent, dislocation-free SRH lifetime $\tau^0_{n(p),\mathrm{SRH}}$ in GaAs [82] is by far larger than $\frac{4}{\pi^3 D_{n(p)} \mathrm{TDD}}$. On the other hand, it should be emphasized that Eq. (6.4) inherently includes any change in the SRH recombination rate due to the enhanced hole density in the WL and barrier layers induced by the doping.

Modulation doping is implemented by 10 nm thick doped layers, with doping density N_A, placed as in Fig. 6.4. Fig. 6.12 shows the optical power emitted on the GS (solid) and ES (dotted) with N_A equal to (a) 0, (b) $5 \times 10^{17}\,\mathrm{cm}^{-3}$ and (c) $3 \times 10^{18}\,\mathrm{cm}^{-3}$. These doping levels correspond to 0, 10 and 60 extra holes per QD. Adding 10 extra holes per QD is beneficial, as the GS power quenching is cured and the GS threshold current is reduced. However, 60 extra holes turn out to be excessive, as the previous benefits are partially undermined.

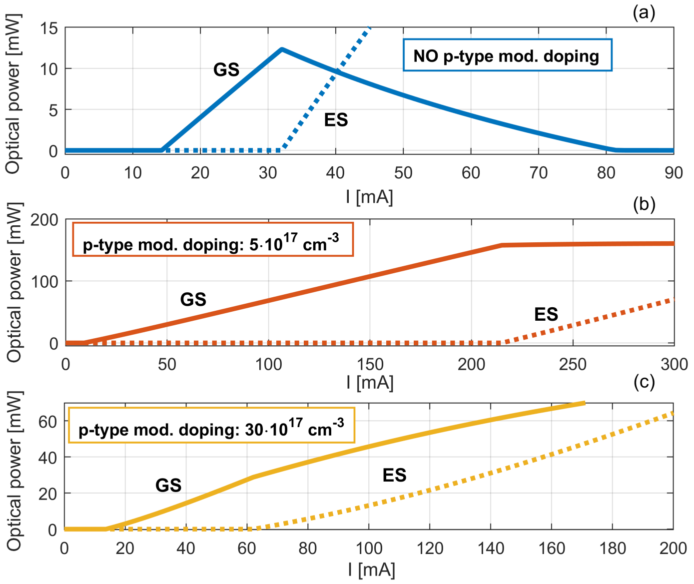

Figure 6.12: GS (solid) and ES (dotted) optical power with (a) no p-type modulation doping and a p-type modulation doping of (b) 5×10^{17} cm^{-3} and (c) 30×10^{17} cm^{-3}.

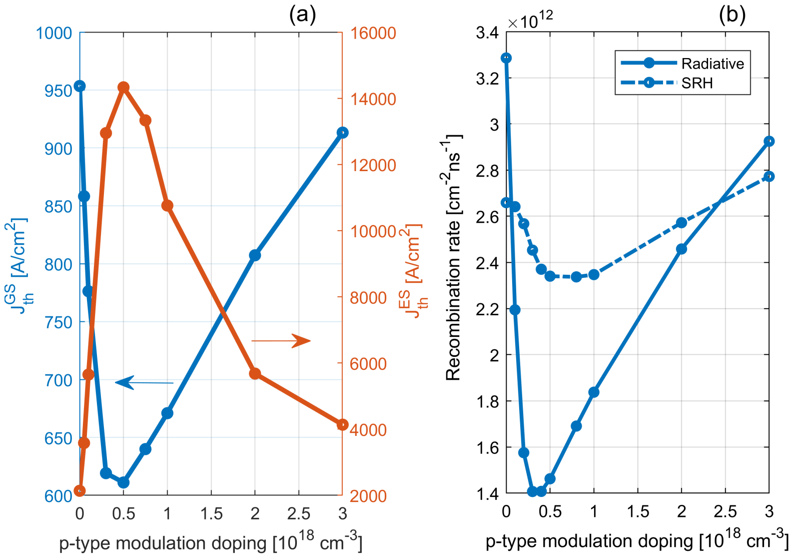

Figure 6.13: (a) GS (blue) and ES (red) threshold current density as functions of the p-type modulation doping density. (b) Total radiative and SRH recombination rates as functions of p-type modulation doping density calculated at the $J_{\mathrm{th}}^{\mathrm{GS}}$ values in (a).

Fig. 6.13(a) shows the GS (blue) and ES (red) threshold current density, $J_{\mathrm{th}}^{\mathrm{GS}}$ and $J_{\mathrm{th}}^{\mathrm{ES}}$

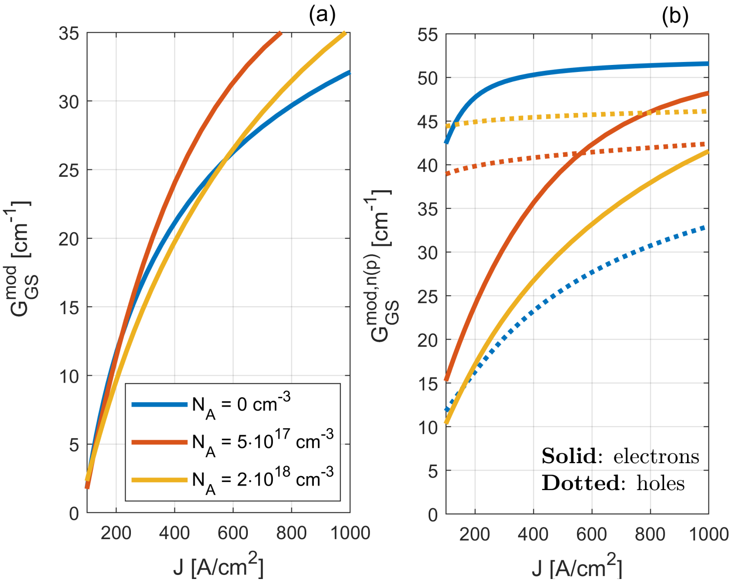

Figure 6.14: (a) GS modal gain versus current density. (b) Holes ($G_{\mathrm{GS}}^{\mathrm{mod},p}$, dashed) and electrons ($G_{\mathrm{GS}}^{\mathrm{mod},n}$, solid) contributions to the GS modal gain.

respectively, as functions of N_A. An optimum density of $5{\times}10^{17}$ cm^{-3} exists, as this concentration minimizes $J_{\mathrm{th}}^{\mathrm{GS}}$ and maximizes $J_{\mathrm{th}}^{\mathrm{ES}}$. These results, showing an optical doping density to minimize the GS threshold current, are consistent with the experiments in [186]. We have also verified that such an optimum is almost insensitive to the value of TDD. In [186], it was speculated that the optimum results from a trade-off between the increase of gain enabled by doping and the increase of non-radiative recombination caused by doping-induced defects. Regarding this, we have already noted that Eq. (6.5) is dominated by the effect of the TDs. In addition, the integrated radiative and non-radiative recombination rates reported in Fig. 6.13(b) versus N_A emphasize that the GS threshold minimum is strongly correlated to the doping dependence of the radiative recombination rate. On the other hand, the influence of doping on the SRH recombination rate turns out to be marginal. As we discuss in the following, the optimum appears instead as an intrinsic consequence of a non-monotonic dependence of the modal gain on doping density. In fact, the increase of the hole modal gain contribution with N_A, due to the larger density of holes, is counteracted at higher N_A values by a decrease of the electron modal gain contribution, due to electrostatic effects.

We report in Fig. 6.14(a) the modal gain versus current density for three different doping levels N_A and in Fig. 6.14(b) the separate contributions of electrons and holes to the modal gain. While the hole contribution to the gain increases (as expected for p-doping), we observe a decrease of the electron contribution to the GS gain. The balance between the increased hole contribution and reduced electron contribution makes the doped samples exhibit a higher or lower total gain — at fixed current injection —

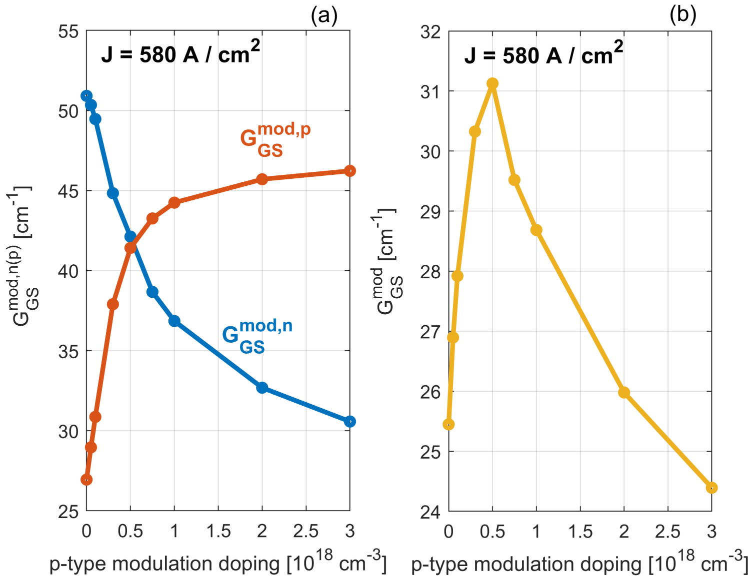

Figure 6.15: (a) Contribution of electrons (blue) and holes (red) to the GS modal gain at $J = 580$ A / cm^2 versus p-doping density and (b) corresponding GS modal gain.

with respect to the undoped sample. As a result, long devices with low threshold gain (e.g., lower than 15 cm^{-1} in this example) could not benefit too much from modulation doping, since their threshold current would be higher.

Fig. 6.15(a) shows the electron and hole contributions to the GS modal gain, $G_{GS}^{mod,n}$ (blue) and $G_{GS}^{mod,p}$ (red) respectively, versus N_A, at fixed current density $J = 580$ A/cm^2. Since this value is smaller than the minimum GS threshold current density (see Fig. 6.13(a)), the GS modal gain is not clamped for any of the considered doping levels. In addition, Fig. 6.15(b) shows the resulting GS modal gain. At low doping densities, the increase in $G_{GS}^{mod,p}$ outweighs the decrease in $G_{GS}^{mod,n}$, such that the GS modal gain grows. At $N_A = 5 \times 10^{17}$ cm^{-3}, the electron and hole contribution balance each other, maximizing the GS modal gain. At higher doping concentrations, the drop in $G_{GS}^{mod,n}$ is steeper as compared to the growth in $G_{GS}^{mod,p}$ and the GS modal gain is diminished. Therefore, the existence of an optimum value appears to stem from the impact of p-type modulation doping on the GS modal gain at a given injected current.

To shed further light on this mechanism, we report in Fig. 6.16(a) the conduction band energy (solid) and electron quasi-Fermi level (dashed) for the bulk states at $J = 580$ A/cm^2 and for the same N_A values in Fig. 6.12. The vertical lines delimit the SCH region. Notice that the multiple peaks observed in the SCH region arise because of the electric field modulation caused by the thin layers with p-type modulation doping. As the doping concentration increases, the energy barrier which electrons injected from the n-contact have to overcome to reach the QD active layer region steadily rises.

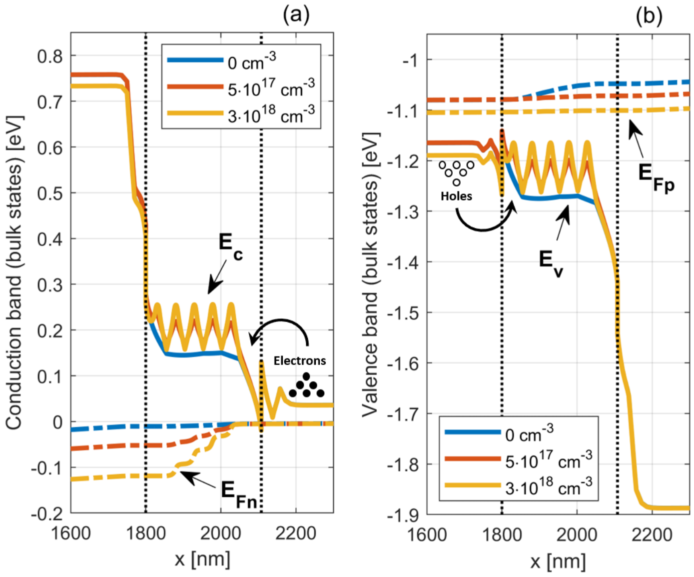

Figure 6.16: (a) Contribution of electrons (blue) and holes (red) to the GS modal gain at $J = 580$ A / cm^2 versus p-doping density and (b) corresponding GS modal gain. The vertical lines delimit the SCH region.

Concurrently, the electron quasi-Fermi level is pushed deeper in the energy gap. As a consequence, the bulk electrons in the active region diminish progressively, becoming unavailable to be captured by the QDs. Therefore, $G_{\text{GS}}^{\text{mod},n}$ in Fig. 6.15(a) steadily decreases as the doping increases. On the other hand, the valence band (solid) and hole quasi-Fermi level (dashed) for the bulk states of the SCH region at $J = 580$ A/cm^2 are shown in Fig. 6.16(b). The energy barrier experienced by the holes injected from the p-contact is not significantly affected by N_{A}. Therefore, the change of hole density in the active region is directly related to the sole variation in the concentration of p-type dopants, which act as a local source of extra holes. However, as the doping grows, holes almost entirely fill the GS, and $G_{\text{GS}}^{\text{mod},p}$ in Fig. 6.16(b) gradually saturates.

To corroborate this interpretation, we report in Fig. 6.17 for each QD layer the net capture rate of carriers from the bulk states to the WL (denoted by $R_{\text{NET}}^{\text{B}\to\text{WL}}$) at $J = 580$ A/cm^2. In the undoped case, the farther the QD layer is from the p-contact and the smaller $R_{\text{NET}}^{\text{B}\to\text{WL}}$ is. Indeed, while diffusing throughout the epitaxial structure upon injection from the p-contact, holes are progressively captured by the QD layers. As N_{A} grows, the electrostatic deformation of the band diagram reflects on $R_{\text{NET}}^{\text{B}\to\text{WL}}$. For doping levels higher than 10^{17} cm^{-3}, the closer the QD layer is to the n-contact and the larger $R_{\text{NET}}^{\text{B}\to\text{WL}}$ is. This signifies that most of electrons injected from the n-contact are blocked by the energy barrier induced by the doping.

The influence of doping on carrier injection also has a significant influence on the dependence of the SRH recombination rate on injection conditions. As depicted in

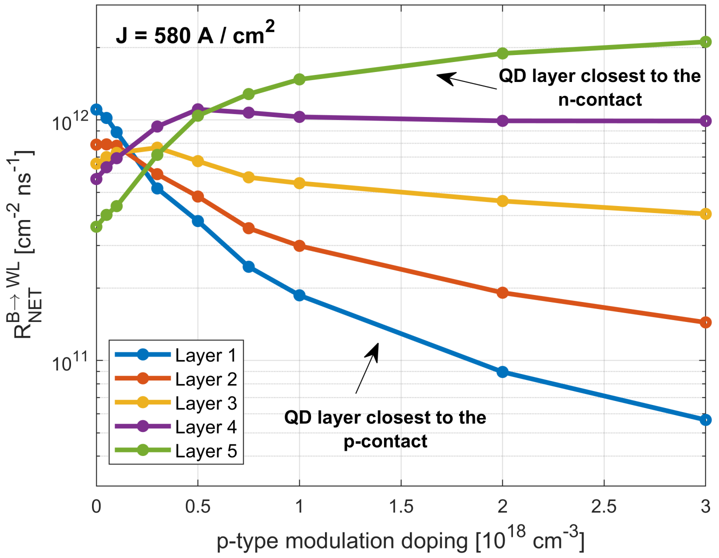

Figure 6.17: Net capture rate from the bulk states to the WL at $J = 580$ A/cm^2 for each layer of QDs.

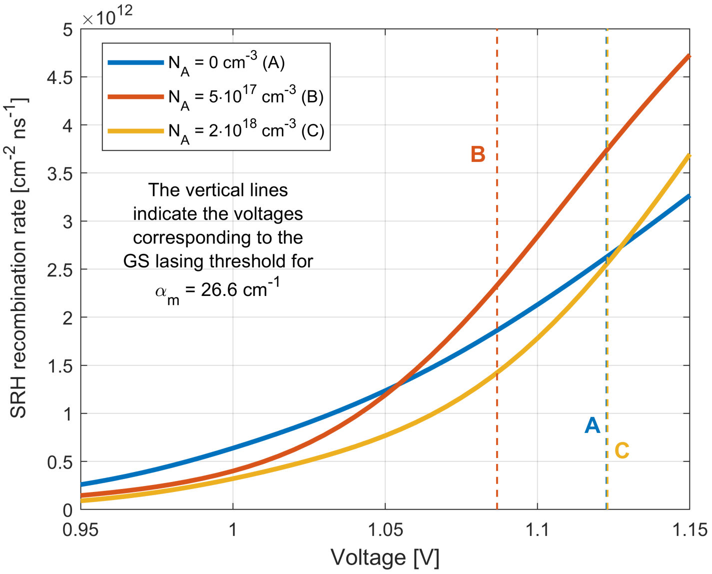

Figure 6.18: Total SRH recombination rate versus voltage at three different doping levels. The vertical dashed lines indicate the voltage value corresponding to the lasing threshold.

Fig. 6.18, at low voltages doping basically mitigates the (TD dominated) nonradiative recombination [16]. However, as carrier injection increases, non-radiative recombination in the doped samples starts to grow with a higher rate than it does in the undoped sample, owing to the higher hole density available in the DWELL layers. The increase is larger at the intermediate doping level than at the highest one, because in the latter case electron injection from the n-contact is hindered by the energy barrier induced by modulation doping. Despite the marked difference in the voltage dependence of the SRH recombination rate, all the three samples present a similar amount of SRH recombination at the lasing thresholds. This highlights that the most relevant factor for the GS threshold minimization is the change of the radiative recombination rate, and therefore of the GS modal gain, with doping density.

6.4 Conclusions

In summary, in this chapter we have presented an investigation of the mechanisms limiting the performance of QD lasers epitaxially grown on silicon, on the basis of a drift-diffusion transport model including QD carriers and photon rate equations. Overcoming the traditional lumped formulations based on rate equations, our approach can simulate the P-I-V characteristics of a dual-state lasing device by starting from the description of materials, doping, and geometry. In particular, we have illustrated how carrier transport and electrostatic effects are essential for catching and explaining the main static characteristics of these lasers.

In Sec. 6.3.1, we have analyzed the impact of threading dislocations (TDs) in the barrier and DWELL layers on the lasing performance. Our analysis pinpoints a dominant effect of the TDs in the DWELL layers (see Fig. 6.8). This result supports the hypothesis [14] that long-term reliability issues suffered by these lasers can be correlated to a thermally activated climbing of TDs towards the active region.

In Sec. 6.3.2, we have focused on the ground-state power quenching above the excited-state lasing threshold. When accounting for transport mechanisms, the reduction in the GS power naturally emerges as a consequence of the inherently asymmetric transport of electrons and holes (see Fig. 6.9). This explains the reason why conventional excitonic models cannot reproduce this effect. Furthermore, our analysis provides physical backgrounds for the usage in lumped rate equation models of phenomenological fitting parameters mimicking the asymmetric transport [38].

Finally, in Sec. 6.3.3 we have thoroughly investigated the physics behind the existence of an optimum p-type modulation doping minimizing the GS threshold current. This effect has recently received attention from the research community of QD lasers on silicon [186]. In contrast to previous studies [186], our analysis (see Fig. 6.14) reveals that the optimum doping level results from the trade-off between: 1) the doping-induced increase of the hole contribution to the modal gain, and 2) the associated decrease of the electron contribution (see Eq. (6.8) for the definition of these contributions). Therefore, the optimum also depends on the threshold gain of the specific sample under study. The reduction of the electron contribution is due to electrostatic effects, which hinder the electron injection (see Fig. 6.16).

Chapter 7

Conclusions and outlook

In this thesis, we have mainly investigated photonic crystal structures based on line-defect waveguides, with a primary focus on lasers and gain-induced slow-light effects. Photonic crystal lasers are promising candidates as semiconductor light sources for on-chip optical interconnects. Slow-light enhances the modal gain per unit length, with potential applications to shorter and more energy-efficient lasers. We have also covered QD lasers epitaxially grown on silicon, which represent an instrumental platform for exploring the properties of the active material. In fact, QDs are extremely attractive for epitaxial integration of lasers on silicon, thanks to their high tolerance to threading dislocations.

Our analysis of photonic crystal structures is directly based on the Bloch modes and dispersion relation of the underlying line-defect waveguide. In particular, we have shown how the modal properties of passive photonic crystal cavities naturally follow from the field expansion in the basis of the two counter-propagating Bloch modes. These properties include the resonance condition and field distribution, both in the real and reciprocal space. To describe active structures, we have employed a coupled-Bloch-mode approach. By this approach, the presence of material gain is viewed as a weak perturbation to a reference photonic crystal waveguide with purely real refractive index. Therefore, material gain leads to a gain-induced distributed feedback of the Bloch modes of the reference waveguide. This effect is inherently associated with slow-light and intrinsically limits the achievable slow-light gain enhancement. We have derived a scattering matrix formulation, which efficiently describes the optical propagation in active structures in the presence of slow-light, including distributed feedback. This formulation generally accounts for complex refractive index perturbations. The perturbation to the real part may be structural or induced by carrier density. We have shown that amplifiers based on active photonic crystal waveguides may offer better performance if having a smaller linewidth enhancement factor. In fact, the larger the linewidth enhancement factor is and the more the amplifier reflected power grows. Therefore, if one is interested in achieving a reasonable amplifier gain with minimum reflection, the linewidth enhancement factor should be small. Our scattering matrix formulation is a flexible and convenient tool to analyze the oscillation condition of photonic crystal lasers based on line-defect waveguides, with possibly multiple passive and active sections. We have shown how the gain-induced distributed feedback suppresses oscillation close to the band edge in lasers with photonic bandgap mirrors. Moreover, in the presence of significant mirror loss, the larger the linewidth enhancement factor is and the more the distributed feedback may reduce the threshold gain. This effect stems from the enhancement of the effective net modal gain, enabled by larger values of the linewidth enhancement factor at a given frequency and for a given material gain. We have also illustrated, for the first time, the impact of slow-light on the tuning characteristics of photonic crystal Fano lasers. Moderate slow-light may be beneficial to reduce the threshold gain, but operation too deep into the slow-light region should be probably avoided. Indeed, slow-light triggers a strong competition between the mode closest to the Fano mirror peak and the other longitudinal modes of the laser cavity. By expanding the oscillation condition around the lasing point, we have derived a rate equation model which self-consistently accounts for slow-light in photonic crystal lasers, including the gain-induced distributed feedback. We have applied the model to photonic crystal lasers with photonic bandgap mirrors and derived analytical expressions for the stationary and small-signal characteristics. Regarding the latter, a key parameter is the equivalent photon lifetime, which effectively reflects the impact of slow-light and associated distributed feedback on group velocity, optical confinement factor and differential gain. We have shown that the distributed feedback may improve, albeit slightly, threshold current, modulation bandwidth and energy cost.

Regarding QD lasers on silicon, we have analyzed their continuous wave operation by a drift-diffusion transport model, coupled with conventional rate equations for photons and carriers in the DWELL layers. We have shown that the ground state power quenching above the excited state lasing threshold under dual state emission is caused by the asymmetric transport of electrons and holes. In addition, we have discussed how the existence of an optimum p-type modulation doping, minimizing the ground state threshold current, stems from the reduction of the electron density. This reduction is due to electrostatic effects hindering electron injection and counteracts the benefits from the expected increase of the hole density.

Having summarized the main conclusions, we would like to briefly outline some future perspectives. These may include systematic numerical and experimental investigations on how tuning the mirror phases would affect the oscillation condition of photonic crystal lasers. In fact, in the slow-light regime, the oscillation condition is strongly influenced by the mirror phases, owing to the gain-induced distributed feedback. If a practical way were found to tune the mirror phases, one may pursue an experimental demonstration of this effect. However, this would also require the technology to be mature enough to reduce the fabrication disorder below a certain level. This would be necessary to allow for lasing oscillation close enough to the band edge. By using the rate equation model which we have derived, one may also explore the impact of this tuning on the stationary and small-signal characteristics. In this respect, a worthy extension could be the application of the model to Fano lasers, to explore the impact of slow-light effects on the small-signal characteristics. The rate equation model could be also useful to gain insight on the frequency chirp in the presence of slow-light in simple line-defect lasers. These few suggestions add up to others already outlined here and there throughout the thesis. These include, for instance, further investigations on the impact of disorder-induced radiation losses in photonic crystal cavities or disorder-induced multiple scattering in active waveguides.

Appendix A

Coupled-Bloch-mode equations: derivation

In this appendix, we derive the general form of the coupled-Bloch-mode equations presented in Chapter 3.

We start by considering a *reference* waveguide with *purely real* refractive index. For this waveguide, Maxwell's equations in the frequency domain read

$$\nabla \times \mathbf{E}_0(\mathbf{r}) = i\omega\mu_0\mathbf{H}_0(\mathbf{r}) \tag{A.1a}$$

$$\nabla \times \mathbf{H}_0(\mathbf{r}) = -i\omega\epsilon(\mathbf{r})\mathbf{E}_0(\mathbf{r}) \tag{A.1b}$$

where $\epsilon(\mathbf{r}) = \epsilon_0 n_b^2(\mathbf{r})$ is the dielectric permittivity and $n_b(\mathbf{r})$ the background refractive index. We then consider the actual waveguide which we are interested to study. This waveguide is seen as *perturbed* as compared to the reference waveguide. For the perturbed waveguide, Maxwell's equations read

$$\nabla \times \mathbf{E}(\mathbf{r}) = i\omega\mu_0\mathbf{H}(\mathbf{r}) \tag{A.2a}$$

$$\nabla \times \mathbf{H}(\mathbf{r}) = -i\omega\epsilon(\mathbf{r})\mathbf{E}(\mathbf{r}) - i\omega\mathbf{P}_{\mathbf{pert}}(\mathbf{r}) \tag{A.2b}$$

where $\mathbf{P}_{\mathbf{pert}}$ is a perturbing polarization accounting for the perturbation. We now introduce the Lorentz reciprocity theorem [79]

$$\nabla \cdot \left(\mathbf{E} \times \mathbf{H}_0^* + \mathbf{E}_0^* \times \mathbf{H}\right) = i\omega\mathbf{P}_{\mathbf{pert}} \cdot \mathbf{E}_0^* \tag{A.3}$$

holding for any two arbitrary sets of fields $(\mathbf{E}_0, \mathbf{H}_0)$ and $(\mathbf{E}, \mathbf{H})$. We define the vector $\mathbf{F} = \mathbf{E} \times \mathbf{H}_0^* + \mathbf{E}_0^* \times \mathbf{H}$ and insert it into the integral identify [120]

$$\int_A \nabla \cdot \mathbf{F}\, dA = \frac{\partial}{\partial z} \int_A \mathbf{F} \cdot \hat{\mathbf{z}}\, dA + \oint_{\partial A} \mathbf{F} \cdot \mathbf{n}\, dl \tag{A.4}$$

where A is a transverse section at posizion z. The second integral on the right-hand side (RHS) of Eq. (A.4) is a line integral along the contour of A. We assume the two sets

$(\mathbf{E}_0, \mathbf{H}_0)$ and $(\mathbf{E}, \mathbf{H})$ to be *guided* fields and we conveniently choose A such that the line integral vanishes. Therefore, Eq. (A.4) is reduced to

$$\frac{\partial}{\partial z}\int_A \left(\mathbf{E}\times\mathbf{H}_0^* + \mathbf{E}_0^*\times\mathbf{H}\right)\cdot\hat{\mathbf{z}}\,dA = i\omega\int_A \left(\mathbf{P}_{\mathbf{pert}}\cdot\mathbf{E}_0^*\right)\,dA \tag{A.5}$$

By neglecting nonlinear effects, we express the perturbing polarization as

$$\mathbf{P}_{\mathbf{pert}}(\mathbf{r}) = \epsilon_0\chi_{\text{pert}}(\mathbf{r})\mathbf{E}(\mathbf{r}) \tag{A.6}$$

with χ_{pert} being a complex susceptibility perturbation. We now assume the reference and perturbed waveguide to be *photonic crystal* waveguides. As a set of fields $(\mathbf{E}_0, \mathbf{H}_0)$, we take the guided *Bloch* modes of the reference waveguide

$$\begin{bmatrix}\mathbf{E}_{0,\pm}(\mathbf{r})\\ \mathbf{H}_{0,\pm}(\mathbf{r})\end{bmatrix} = \begin{bmatrix}\mathbf{e}_{0,\pm}(\mathbf{r})\\ \mathbf{h}_{0,\pm}(\mathbf{r})\end{bmatrix} e^{\pm ik_z z} \tag{A.7}$$

with $+$ $(-)$ denoting the forward-propagating (backward-propagating) mode and k_z the wavevector along the propagation direction z. The electric (magnetic) fields $\mathbf{e}_{0,\pm}$ $(\mathbf{h}_{0,\pm})$ are z periodic, with the period given by the lattice constant a. They are related by $\mathbf{e}_{0,-} = \mathbf{e}_{0,+}^*$ and similarly for the magnetic fields, with $*$ denoting the complex conjugate. Furthermore, they obey the orthogonality relation [94, 120, 141]

$$\frac{1}{4}\int_A (\mathbf{e}_{0,\sigma}\times\mathbf{h}_{0,\sigma'}^* + \mathbf{e}_{0,\sigma'}^*\times\mathbf{h}_{0,\sigma})\cdot\hat{\mathbf{z}}\,dA = \sigma P_0\delta_{\sigma,\sigma'} \tag{A.8}$$

with $\delta_{\sigma,\sigma'}$ being the Kronecker delta, $\sigma = \pm$ and $\sigma' = -\sigma$. Here, P_0 is real and positive and represents the time-averaged power carried by the forward-propagating mode [120]

$$P_0 = \frac{W_e + W_m}{a}v_g \tag{A.9}$$

with W_e and W_m given by

$$W_e = \frac{1}{4}\int_V \frac{\partial}{\partial\omega}\left[\omega\,\epsilon(\mathbf{r})\right]|\mathbf{e}_0(\mathbf{r})|^2\,dV \tag{A.10a}$$

$$W_m = \frac{1}{4}\int_V \mu_0|\mathbf{h}_0(\mathbf{r})|^2\,dV \tag{A.10b}$$

and v_g being the group velocity. Here, W_e and W_m are, respectively, the time-averaged electric and magnetic energy stored in a supercell, with V being the supercell volume. For Bloch modes, one finds $W_e = W_m$ [81]. Therefore, by neglecting *material* dispersion, we obtain

$$P_0 = \frac{v_g}{2a}\int_V \epsilon_0 n_b^2(\mathbf{r})|\mathbf{e}_0(\mathbf{r})|^2\,dV \tag{A.11}$$

Eqs. (A.8) and (A.11) together represent the orthonormality relation to which the Bloch modes of the reference waveguide are subject. In the limit of a *weak* perturbation, we expand the guided fields $(\mathbf{E}, \mathbf{H})$ in the perturbed waveguide as [19]

$$\begin{bmatrix} \mathbf{E}(\mathbf{r}) \\ \mathbf{H}(\mathbf{r}) \end{bmatrix} = \psi_+(z) \begin{bmatrix} \mathbf{E}_{0,+}(\mathbf{r}) \\ \mathbf{H}_{0,+}(\mathbf{r}) \end{bmatrix} + \psi_-(z) \begin{bmatrix} \mathbf{E}_{0,-}(\mathbf{r}) \\ \mathbf{H}_{0,-}(\mathbf{r}) \end{bmatrix} \tag{A.12}$$

with $\psi_\pm(z)$ being slowly-varying amplitudes. With these assumptions, Eq. (A.5) leads to a pair of coupled differential equations for the amplitudes $\psi_\pm$. In fact, by considering $(\mathbf{E}_0, \mathbf{H}_0) = (\mathbf{E}_{0,+}, \mathbf{H}_{0,+})$ and inserting it into Eq. (A.5), we obtain

$$\begin{aligned} \frac{\partial \psi_+(z)}{\partial z} = \frac{i\omega\epsilon_0}{4P_0} \Big\{ & \psi_+(z) \int_A \chi_{\text{pert}}(\mathbf{r}) |\mathbf{e}_0(\mathbf{r})|^2 dA + \\ & + \psi_-(z) e^{-2ik_z z} \int_A \chi_{\text{pert}}(\mathbf{r}) \left[\mathbf{e}_{0,-}(\mathbf{r}) \cdot \mathbf{e}^*_{0,+}(\mathbf{r}) \right] dA \Big\} \end{aligned} \tag{A.13}$$

Here, we have made use of Eqs. (A.6) and (A.12), as well as Eq. (A.8). By considering $(\mathbf{E}_0, \mathbf{H}_0) = (\mathbf{E}_{0,-}, \mathbf{H}_{0,-})$ and proceeding similarly, we obtain

$$\begin{aligned} -\frac{\partial \psi_-(z)}{\partial z} = \frac{i\omega\epsilon_0}{4P_0} \Big\{ & \psi_+(z) e^{+2ik_z z} \int_A \chi_{\text{pert}}(\mathbf{r}) \left[\mathbf{e}_{0,+}(\mathbf{r}) \cdot \mathbf{e}^*_{0,-}(\mathbf{r}) \right] dA + \\ & + \psi_-(z) \int_A \chi_{\text{pert}}(\mathbf{r}) |\mathbf{e}_0(\mathbf{r})|^2 dA \Big\} \end{aligned} \tag{A.14}$$

By using Eq. (A.11), we finally recast Eqs. (A.13) and (A.14) as

$$\frac{\partial \psi_+(z)}{\partial z} = i\kappa_{11}(z)\psi_+ + i\kappa_{12}(z) e^{-2ik_z z}\psi_- \tag{A.15a}$$

$$-\frac{\partial \psi_-(z)}{\partial z} = i\kappa_{21}(z) e^{+2ik_z z}\psi_+ + i\kappa_{11}(z)\psi_- \tag{A.15b}$$

which are the coupled-Bloch-mode equations as derived in [19]. Here, the self-coupling coefficient (κ_{11}) and cross-coupling coefficients (κ_{12} and κ_{21}) are given by

$$\kappa_{11} = \frac{1}{2}\left(\frac{\omega}{c}\right) n_g \frac{a \int_A \epsilon_0 \chi_{\text{pert}}(\mathbf{r}) |\mathbf{e}_0(\mathbf{r})|^2 dA}{\int_V \epsilon_0 n_b^2(\mathbf{r}) |\mathbf{e}_0(\mathbf{r})|^2 \, dV} \tag{A.16a}$$

$$\kappa_{12} = \frac{1}{2}\left(\frac{\omega}{c}\right) n_g \frac{a \int_A \epsilon_0 \chi_{\text{pert}}(\mathbf{r}) \left[\mathbf{e}_{0,-}(\mathbf{r}) \cdot \mathbf{e}^*_{0,+}(\mathbf{r}) \right] dA}{\int_V \epsilon_0 n_b^2(\mathbf{r}) |\mathbf{e}_0(\mathbf{r})|^2 \, dV} \tag{A.16b}$$

$$\kappa_{21} = \frac{1}{2}\left(\frac{\omega}{c}\right) n_g \frac{a \int_A \epsilon_0 \chi_{\text{pert}}(\mathbf{r}) \left[\mathbf{e}_{0,+}(\mathbf{r}) \cdot \mathbf{e}^*_{0,-}(\mathbf{r}) \right] dA}{\int_V \epsilon_0 n_b^2(\mathbf{r}) |\mathbf{e}_0(\mathbf{r})|^2 \, dV} \tag{A.16c}$$

with n_g being the group index.

A.1 Susceptibility perturbation

In this section, we express the susceptibility perturbation χ_{pert} in terms of a complex refractive index perturbation.

The perturbed waveguide may contain active material, with carrier density inducing material gain or absorption. Therefore, the Maxwell's equation including the curl of the magnetic field can be generally expressed as

$$\nabla \times \mathbf{H}(\mathbf{r}) = -i\omega\epsilon_0 \left[n_b(\mathbf{r}) + \Delta n_b(\mathbf{r}) + i n_i(\mathbf{r})\right]^2 \mathbf{E}(\mathbf{r}) \tag{A.17}$$

Here, n_i is the *imaginary* refractive index controlled by carrier density. Δn_b is a *real* refractive index perturbation, which we may split into two contributions, namely

$$\Delta n_b(\mathbf{r}) \quad = \quad \underbrace{\Delta n_b'(\mathbf{r})}_{\text{structural, thermal, etc.}} \quad + \quad \underbrace{\Delta n_b''(\mathbf{r})}_{\text{induced by carrier density}} \tag{A.18}$$

$\Delta n_b''$ is due to carrier density, while $\Delta n_b'$ generally accounts for any other source of refractive index perturbation (e.g. structural, thermal or electro-optic). By comparing Eq. (A.17) with Eq. (A.2b), we obtain

$$\chi_{\text{pert}}(\mathbf{r}) \approx 2n_b(\mathbf{r}) \left[\Delta n_b(\mathbf{r}) + 2i n_i(\mathbf{r})\right] \tag{A.19}$$

where second-order terms have been neglected. To compute the coupling coefficients in Eqs. (A.16a)-(A.16c), the spatial dependence of the susceptibility perturbation should be specified. On this regard, we assume the holes drilled in the reference photonic crystal waveguide to be completely filled with the cladding material. In this case, we may express the background refractive index as

$$n_b(\mathbf{r}) = (n_{\text{slab}} - n_{\text{clad}})F_{\text{PhC}}(\mathbf{r}) + n_{\text{clad}} \tag{A.20}$$

Here, n_{slab} (n_{clad}) is the slab (cladding) refractive index. $F_{\text{PhC}}(\mathbf{r})$ reflects the geometry of the reference waveguide, with $F_{\text{PhC}} = 1$ ($F_{\text{PhC}} = 0$) within the slab (within cladding and holes). The imaginary refractive index $n_i(\mathbf{r})$ and the associated real refractive index perturbation $\Delta n_b''(\mathbf{r})$ have the same spatial dependence. We may express it as

$$n_i(\mathbf{r}) = n_i F_{\text{carrier}}(\mathbf{r}) \tag{A.21}$$

and similarly for $\Delta n_b''(\mathbf{r})$. Here, $F_{\text{carrier}}(\mathbf{r})$ is the distribution function of the active layers of quantum wells or quantum dots, which are assumed to undergo spatially uniform pumping. One finds $F_{\text{carrier}} = 1$ ($F_{\text{carrier}} = 0$) within the active layers (elsewhere). Finally, the real refractive index perturbation $\Delta n_b'(\mathbf{r})$ generally has a different spatial dependence, which reflects the local refractive index tuning. We may write it as

$$\Delta n_b'(\mathbf{r}) = \Delta n_b' F_{\Delta n_b'}(\mathbf{r}) \tag{A.22}$$

with $F_{\Delta n_b'} = 1$ ($F_{\Delta n_b'} = 0$) where the refractive index has been tuned (elsewhere). For simplicity, we assume this tuning, if present, to be limited to the slab and to be spatially uniform along the waveguide propagation direction z. Under these assumptions, one finds

$$F_{\text{PhC}}(\mathbf{r})F_{\text{carrier}}(\mathbf{r}) = F_{\text{carrier}}(\mathbf{r}) \tag{A.23a}$$

$$F_{\text{PhC}}(\mathbf{r})F_{\Delta n_b'}(\mathbf{r}) = F_{\Delta n_b'}(\mathbf{r}) \tag{A.23b}$$

By inserting Eqs. (A.20)-(A.22) into Eq. (A.19) and leveraging Eqs. (A.23a) and (A.23b), we may conveniently recast the susceptibility perturbation as

$$\chi_{\text{pert}}(\mathbf{r}) = 2n_{\text{slab}} \left[\Delta n_b' F_{\Delta n_b'}(\mathbf{r}) + i \left(n_i - i\Delta n_b'' \right) F_{\text{carrier}}(\mathbf{r}) \right] \tag{A.24}$$

By inserting Eq. (A.24) into Eqs. (A.16a)-(A.16c), we finally obtain the coupling coefficients, as detailed in Sec. A.3.

A.2 Material gain

In this section, we relate to material gain the perturbation induced by carrier density. The imaginary refractive index n_i reflects the *material* gain g_{mat} by

$$n_i = -\frac{1}{2}\left(\frac{c}{\omega}\right) g_{\text{mat}} \tag{A.25}$$

In Eq. (A.25), the material gain is assumed for simplicity to be independent of frequency. However, incorporating a frequency-dependent material gain is straightforward, since the coupled-Bloch-mode equations are formulated in the frequency domain. This is shown explicitly in Sec. A.2.1 for a Lorentzian gain spectrum.

The refractive index perturbation induced by carrier density may be simply taken into account by introducing the linewidth enhancement factor (LEF), as illustrated in [139]. We denote by n_r the *real* part of the slab refractive index in the *perturbed* waveguide, which depends on the carrier density N. We expand n_r around the transparency carrier density N_{tr}

$$n_r(N) = n_r(N_{\text{tr}}) + \left.\frac{dn_r}{dN}\right|_{N_{\text{tr}}} (N - N_{\text{tr}}) \tag{A.26}$$

By introducing the LEF, $\alpha_H = -(dn_r/dN)/(dn_i/dN)$ [23], and assuming n_{slab} to coincide with n_r at the transparency carrier density, Eq. (A.26) can be written as

$$n_r(N) = n_{\text{slab}} - \alpha_H \left.\frac{dn_i}{dN}\right|_{N_{\text{tr}}} (N - N_{\text{tr}}) \tag{A.27}$$

We then assume the material gain to be linear with N, that is $g_{\text{mat}} = g_N(N - N_{\text{tr}})$, with g_N being the differential gain. Under these assumptions, from Eqs. (A.25) and (A.27) one easily finds $n_r(N) = n_{\text{slab}} + \alpha_H n_i(N)$, which gives

$$\Delta n_b'' = \alpha_H n_i \tag{A.28}$$

A.2.1 Lorentz model

As mentioned above, one may also include a frequency-dependent material gain. In the case of a Lorentzian gain spectrum, the permittivity of the *perturbed* waveguide within the active layers reads [149, 154]

$$\tilde{\epsilon}(\omega) = \epsilon_0 \left[n_{\text{slab}}^2 + \frac{\omega_{\text{a}}^2 \Delta\epsilon}{\omega_{\text{a}}^2 - \omega^2 + i\omega\Delta\omega_a} \right] \tag{A.29}$$

where ω_a is the resonance angular frequency, $\Delta\epsilon$ the oscillator strength and $\Delta\omega_a$ controls the gain bandwdith. By forcing $\tilde{\epsilon}$ to be equal to $\epsilon_0(n_{\text{slab}} + \Delta n_b'' + n_i)^2$ and neglecting second-order terms, one finds

$$\Delta n_b''(\omega) = \Delta\epsilon \frac{\omega_a^2 \left(\omega_{\text{a}}^2 - \omega^2\right)}{2n_{\text{slab}} \left[\left(\omega_{\text{a}}^2 - \omega^2\right)^2 + \omega^2 \Delta\omega_a^2 \right]} \tag{A.30a}$$

$$n_i(\omega) = \Delta\epsilon \frac{\omega_a^2 \, \omega \, \Delta\omega_a}{2n_{\text{slab}} \left[\left(\omega_{\text{a}}^2 - \omega^2\right)^2 + \omega^2 \Delta\omega_a^2 \right]} \tag{A.30b}$$

The oscillator strength depends on the peak material gain by

$$g_{\text{mat}}^{\text{peak}} = -2 \left(\frac{\omega}{c} \right) n_i(\omega) \Big|_{\omega_a} \tag{A.31}$$

By usage of Eq. (A.31), we may conveniently recast Eqs. (A.30a) and (A.30b) as

$$\Delta n_b''(\omega) = -\frac{1}{2} \left(\frac{c}{\omega} \right) g_{\text{mat}}^{\text{peak}} \frac{\Delta x}{1 + (\Delta x)^2} \tag{A.32a}$$

$$n_i(\omega) = -\frac{1}{2} \left(\frac{c}{\omega} \right) g_{\text{mat}}^{\text{peak}} \frac{1}{1 + (\Delta x)^2} \tag{A.32b}$$

where Δx is the normalized detuning

$$\Delta x = \frac{\omega_a^2 - \omega^2}{\omega \Delta\omega_a} \tag{A.33}$$

A.3 Coupling coefficients

As a result of Eq. (A.24), each coupling coefficient generally consists of two contributions, depending on $F_{\Delta n_b'}(\mathbf{r})$ and $F_{\text{carrier}}(\mathbf{r})$ respectively. Without lack of generality, in the following we assume $\Delta n_b' = 0$. In this case, one finds

$$\kappa_{11}(z) = i(\omega/c) S \left(n_i - i\Delta n_b'' \right) \Gamma_{11}(z) \tag{A.34a}$$

$$\kappa_{12}(z) = i(\omega/c) S \left(n_i - i\Delta n_b'' \right) \Gamma_{12}(z) \tag{A.34b}$$

$$\kappa_{21}(z) = i(\omega/c) S \left(n_i - i\Delta n_b'' \right) \Gamma_{12}^*(z) \tag{A.34c}$$

Here, $S = n_g/n_{\mathrm{slab}}$ is the *slow-down factor*, while the normalized coupling coefficients Γ_{11} and Γ_{12} are [137, 139]

$$\Gamma_{11}(z) = \frac{a \int_A \epsilon_0 n_{\mathrm{slab}}^2 |\mathbf{e}_0(\mathbf{r})|^2 F_{\mathrm{carrier}}(\mathbf{r}) dA}{\int_V \epsilon_0 n_b^2(\mathbf{r}) |\mathbf{e}_0(\mathbf{r})|^2 \, dV} \tag{A.35a}$$

$$\Gamma_{12}(z) = \frac{a \int_A \epsilon_0 n_{\mathrm{slab}}^2 \left[\mathbf{e}_{0,-}(\mathbf{r}) \cdot \mathbf{e}_{0,+}^*(\mathbf{r})\right] F_{\mathrm{carrier}}(\mathbf{r}) dA}{\int_V \epsilon_0 n_b^2(\mathbf{r}) |\mathbf{e}_0(\mathbf{r})|^2 \, dV} \tag{A.35b}$$

If $\Delta n_b'$ if different from zero, each coupling coefficient includes an additional contribution. This contribution can be readily obtained by replacing $i\left(n_i - i\Delta n_b''\right)$ with $\Delta n_b'$ in Eqs. (A.34a)-(A.34c) and $F_{\mathrm{carrier}}(\mathbf{r})$ with $F_{\Delta n_b'}(\mathbf{r})$ in Eqs. (A.35a) and (A.35b).

We note that Γ_{11} and Γ_{12} are 1) frequency-dependent and 2) z periodic, with the period given by the lattice constant a. This is due to the frequency dependence and spatial periodicty of the Bloch modes of the reference waveguide. Furthermore, it should be emphasized that Γ_{11} is real, while Γ_{12} is generally a complex coefficient.

A.3.1 Optical confinement factor Γ_y

In this section, we show how the normalized coupling coefficients can be conveniently recast by introducing an optical confinement factor which takes into account the field confinement within the active layers along the direction orthogonal to the slab.

For the sake of clarity, the reference waveguide with the reference system adopted throughout this thesis are shown in Fig. A.1(a). We denote the x-direction (y-direction) as *lateral* (*vertical*). The z-direction is instead the *longitudinal* direction. We start from Eq. (A.35a), which we divide and multiply by $a \int_A \epsilon_0 n_{\mathrm{slab}}^2 |\mathbf{e}_0(\mathbf{r})|^2 F_{\mathrm{carrier}}^{\mathrm{uniform}}(\mathbf{r}) dA$. Here, $F_{\mathrm{carrier}}^{\mathrm{uniform}}(\mathbf{r})$ coincides with $F_{\mathrm{carrier}}(\mathbf{r})$ along the x- and z-direction. On the other hand, $F_{\mathrm{carrier}}^{\mathrm{uniform}}(\mathbf{r})$ implies that the active layers homogeneously extend throughout the slab along the vertical direction. This gives

$$\Gamma_{11}(z) = \underbrace{\frac{\int_A |\mathbf{e}_0(\mathbf{r})|^2 F_{\mathrm{carrier}}(\mathbf{r}) dA}{\int_A |\mathbf{e}_0(\mathbf{r})|^2 F_{\mathrm{carrier}}^{\mathrm{uniform}}(\mathbf{r}) dA}}_{\Gamma_y} \underbrace{\frac{a \int_A \epsilon_0 n_{\mathrm{slab}}^2 |\mathbf{e}_0(\mathbf{r})|^2 F_{\mathrm{carrier}}^{\mathrm{uniform}}(\mathbf{r}) dA}{\int_V \epsilon_0 n_b^2(\mathbf{r}) |\mathbf{e}_0(\mathbf{r})|^2 \, dV}}_{\Gamma_{11}^{\mathrm{carrier}}} \tag{A.36}$$

The difference between $F_{\mathrm{carrier}}(\mathbf{r})$ and $F_{\mathrm{carrier}}^{\mathrm{uniform}}(\mathbf{r})$ is clarified by Fig. A.1(c) and (d). They show the cross-section view of (c) the actual active waveguide, with the active layers denoted by red, and (d) the active waveguide with the active region being *homogenized* along the y-direction. $F_{\mathrm{carrier}}(\mathbf{r})$ is unitary within the active layers in Fig. A.1(c) and zero elsewhere. Similarly, one finds $F_{\mathrm{carrier}}^{\mathrm{uniform}}(\mathbf{r}) = 1$ ($F_{\mathrm{carrier}}^{\mathrm{uniform}}(\mathbf{r}) = 0$) within the homogenized active region in Fig. A.1(d) (elsewhere). The structure in Fig. A.1(c) reflects

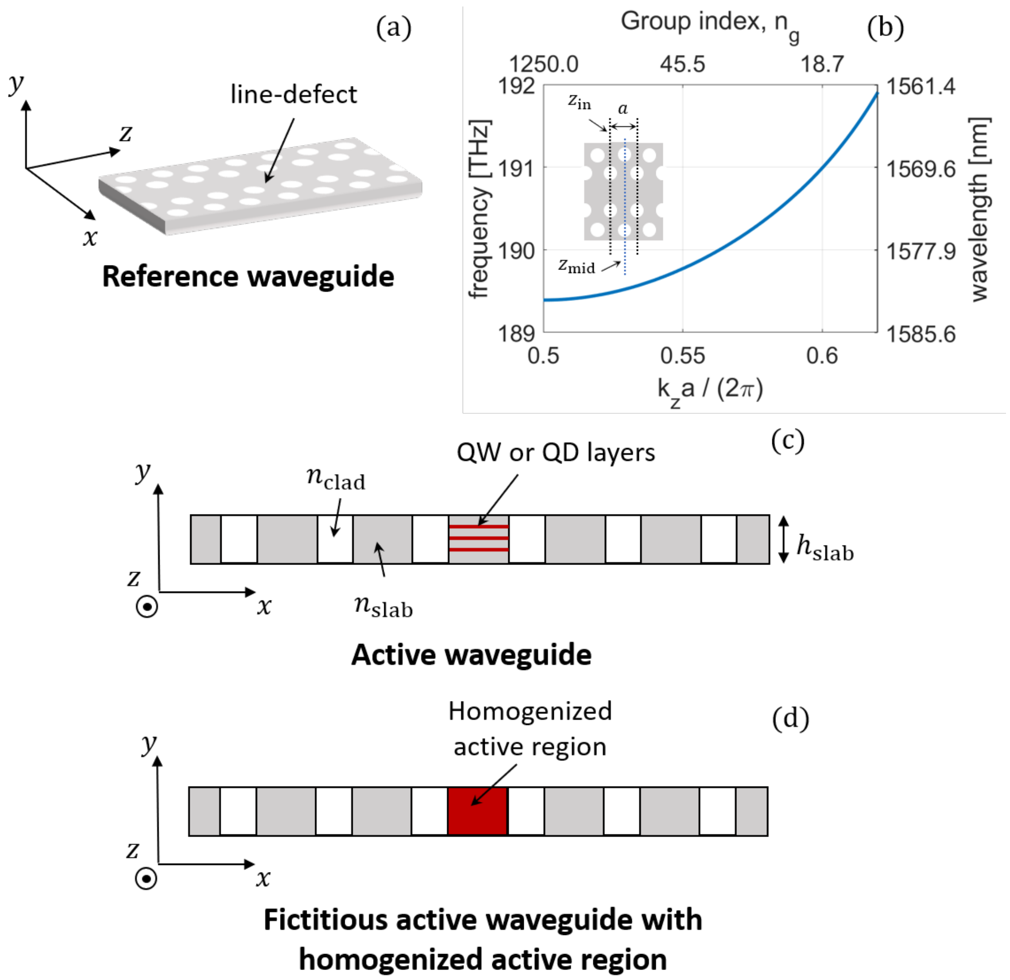

Figure A.1: (a) Reference photonic crystal waveguide and (b) corresponding dispersion relation. The inset in (b) shows a top view of the waveguide, with the unit cell reference planes. (c) Active photonic crystal waveguide (cross-section view). (d) Fictitious active waveguide with homogenized active region (cross-section view).

photonic crystal lasers based on line-defect waveguides with a buried heterostructure active region [88, 160]. From Eq. (A.36), we obtain the expression of Γ_y, which accounts for the electric field confinement within the active layers along the y-direction.

Strictly speaking, we should proceed similarly on the normalized coupling coefficient Γ_{12} in Eq. (A.35b), thus identifying a generally *complex* confinement factor Γ_y^{cross}. By doing so, we may express the normalized coupling coefficients as $\Gamma_{11}(z) = \Gamma_y \Gamma_{11}^{\text{carrier}}(z)$

and $\Gamma_{12}(z) = \Gamma_y^{\text{cross}}\,\Gamma_{12}^{\text{carrier}}(z)$, where

$$\Gamma_{11}^{\text{carrier}}(z) = \frac{a\int_A \epsilon_0 n_{\text{slab}}^2 |\mathbf{e}_0(\mathbf{r})|^2 F_{\text{carrier}}^{\text{uniform}}(\mathbf{r})dA}{\int_V \epsilon_0 n_b^2(\mathbf{r})|\mathbf{e}_0(\mathbf{r})|^2\,dV} \tag{A.37a}$$

$$\Gamma_{12}^{\text{carrier}}(z) = \frac{a\int_A \epsilon_0 n_{\text{slab}}^2 \left[\mathbf{e}_{0,-}(\mathbf{r})\cdot\mathbf{e}_{0,+}^*(\mathbf{r})\right] F_{\text{carrier}}^{\text{uniform}}(\mathbf{r})dA}{\int_V \epsilon_0 n_b^2(\mathbf{r})|\mathbf{e}_0(\mathbf{r})|^2\,dV} \tag{A.37b}$$

Here, $\Gamma_{11}^{\text{carrier}}$ ($\Gamma_{12}^{\text{carrier}}$) is the normalized self-coupling (cross-coupling) coefficient with the active region being homogenized along the y-direction. The confinement factors along the vertical direction are

$$\Gamma_y = \frac{\int_A |\mathbf{e}_0(\mathbf{r})|^2 F_{\text{carrier}}(\mathbf{r})dA}{\int_A |\mathbf{e}_0(\mathbf{r})|^2 F_{\text{carrier}}^{\text{uniform}}(\mathbf{r})dA} \tag{A.38a}$$

$$\Gamma_y^{\text{cross}} = \frac{\int_A \left[\mathbf{e}_{0,-}(\mathbf{r})\cdot\mathbf{e}_{0,+}^*(\mathbf{r})\right] F_{\text{carrier}}(\mathbf{r})dA}{\int_A \left[\mathbf{e}_{0,-}(\mathbf{r})\cdot\mathbf{e}_{0,+}^*(\mathbf{r})\right] F_{\text{carrier}}^{\text{uniform}}(\mathbf{r})dA} \tag{A.38b}$$

In principle, these confinement factors depend on frequency, as well as on z. To quantify these dependencies, we have computed the confinement factors Γ_y and Γ_y^{cross} by assuming a single active layer being 8 nm thick and placed in the middle of the waveguide slab. The parameters of the reference waveguide are summarized in Tab. 2.1 in Sec. 2.2.1. The dispersion relation of the fundamental guided mode is reported in Fig. A.1(b). Here, the inset shows a top view of the reference waveguide. The reference planes of the unit cell adopted throughout this thesis are also indicated. The input plane is denoted by z_{in}, while z_{mid} corresponds to the centre. Fig. A.2 shows (a) Γ_y and (b) the magnitude of Γ_y^{cross} versus the normalized wavenumber of the reference waveguide. Each colour corresponds to a different position z along the waveguide unit cell, with $z = z_{\text{in}}$ (blue), $z = (z_{\text{in}} + z_{\text{mid}})/2$ (red) and $z = z_{\text{mid}}$ (yellow). For the sake of comparison, Fig. A.2(c) and (d) show, respectively, the normalized self-coupling coefficient $\Gamma_{11}^{\text{carrier}}$ and the magnitude of the normalized cross-coupling coefficient $\Gamma_{12}^{\text{carrier}}$. The frequency and spatial dependence of these normalized coupling coefficients is thoroughly discussed in Chapter 3. Here, we emphasize that, as compared to $\Gamma_{11}^{\text{carrier}}$ and $\Gamma_{12}^{\text{carrier}}$:

- Γ_y and $|\Gamma_y^{\text{cross}}|$ are close to each other to a good approximation;
- they are weakly dependent on frequency and position z.

Furthermore, the phase of $\Gamma_{12}^{\text{carrier}}$ (not shown in Fig. A.2) is practically zero, independently of the frequency and position z. Therefore, we may assume Γ_y and Γ_y^{cross} to be constant and to coincide with each other. We have checked that this remains a valid approximation if more active layers are considered. Indeed, the field is confined along

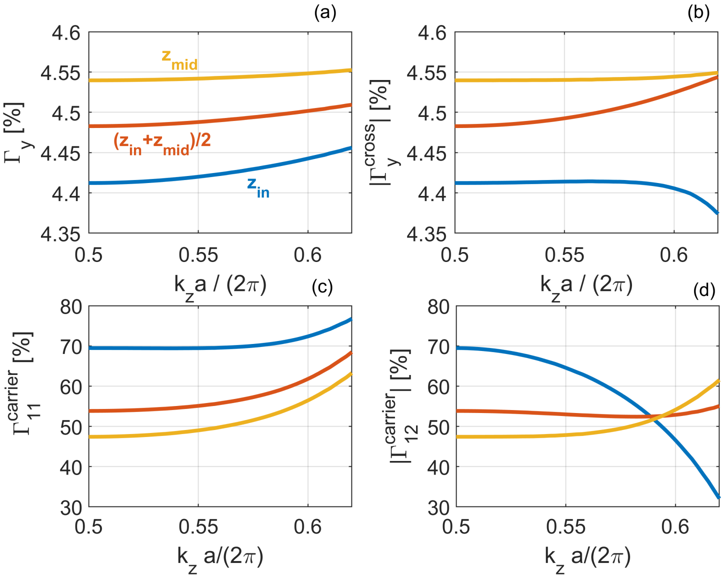

Figure A.2: (a) Confinement factor Γ_y and (b) magnitude of the complex confinement factor Γ_y^{cross} for a single active layer being 8 nm thick and placed in the middle of the waveguide slab. (c) Normalized self-coupling coefficient $\Gamma_{11}^{\text{carrier}}$ and (d) magnitude of the normalized cross-coupling coefficient $\Gamma_{12}^{\text{carrier}}$. In each plot, the x-axis reports the normalized wavenumber. Each colour corresponds to a different z-coordinate along the waveguide unit cell (see the inset of Fig. A.1(b)), with $z = z_{\text{in}}$ (blue), $z = (z_{\text{in}} + z_{\text{mid}})/2$ (red) and $z = z_{\text{mid}}$ (yellow).

the vertical direction by total internal reflection. Owing to the high refractive index contrast between the cladding and slab material, this confinement is weakly dependent on frequency and position z as compared to confinement along the lateral direction, which is due to the photonic band gap.

As a result, throughout this thesis we adopt the following approach [137, 139] when computing the coupling coefficients by Eqs. (A.34a)-(A.34c):

- we evaluate Γ_{11} and Γ_{12} by assuming the material gain to be *homogeneous* within the slab along the vertical direction, *as if* the active layers entirely filled the slab along this direction. That is, we compute Γ_{11} as $\Gamma_{11}^{\text{carrier}}$ and Γ_{12} as $\Gamma_{12}^{\text{carrier}}$;
- we assume $\Gamma_y = \Gamma_y^{\text{cross}}$ and embed this confinement factor into the imaginary refractive index n_i. Under these conditions, n_i reflects the *modal* gain coefficient $g_0 = \Gamma_y g_{\text{mat}}$, with

$$n_i = -\frac{1}{2}\left(\frac{c}{\omega}\right)\Gamma_y g_{\text{mat}} \tag{A.39}$$

This approach is convenient because, for a given reference waveguide, the normalized coupling coefficients are only computed once. One can then account for any number of active layers by appropriately scaling Γ_y.

Appendix B

Reduced coupled-Bloch-mode equations: analytical solution

In this appendix, we focus on the *reduced* coupled-Bloch-mode (CBM) equations presented in Sec. 3.3. Firstly, we solve them as an initial value problem. This approach provides the Bloch modes of the *perturbed* photonic crystal waveguide, possibly including active material, and the associated dispersion relation. Then, we derive the power flow in the perturbed waveguide. Here, we highlight the impact of the dispersion relation. Finally, we solve the reduced CBM equations as a boundary value problem. This approach provides the spatial evolution of the forward- and backward-propagating field in a typical scattering experiment.

The reduced coupled-Bloch-mode (CBM) equations are

$$\frac{\partial \psi_+(z)}{\partial z} = i\kappa_{\mathrm{FF}}\psi_+ + i\kappa_{\mathrm{FB}}e^{+i2\delta z}\psi_- \tag{B.1a}$$

$$-\frac{\partial \psi_-(z)}{\partial z} = i\kappa_{\mathrm{BF}}e^{-i2\delta z}\psi_+ + i\kappa_{\mathrm{FF}}\psi_- \tag{B.1b}$$

Here, the self- (κ_{FF}) and cross-coupling coefficients (κ_{FB} and κ_{BF}) depend on frequency, as well as on the perturbation (that is, refractive index tuning and/or material gain). However, they do *not* depend on position z. The detuning δ is equal to $\pi/a - k_z$, with a being the lattice constant and k_z the wavenumber of the Bloch modes of the reference waveguide. Finally, ψ_+ (ψ_-) is the slowly-varying amplitude which the forward-propagating (backward-propagating) Bloch mode of the reference waveguide acquires within the perturbed waveguide as a result of the perturbation. These amplitudes are generally *complex*.

B.1 Initial value problem

We perform the change of variable

$$\begin{bmatrix} \psi_+(z) \\ \psi_-(z) \end{bmatrix} = \begin{bmatrix} e^{+i\delta z} & 0 \\ 0 & e^{-i\delta z} \end{bmatrix} \begin{bmatrix} \tilde{c}_+(z) \\ \tilde{c}_-(z) \end{bmatrix} \tag{B.2}$$

and subsequently turn Eqs. (B.1a) and (B.1b) into

$$\frac{\partial}{\partial z} \begin{bmatrix} \tilde{c}_+(z) \\ \tilde{c}_-(z) \end{bmatrix} = i\underline{\underline{H}} \begin{bmatrix} \tilde{c}_+(z) \\ \tilde{c}_-(z) \end{bmatrix} \tag{B.3}$$

where the matrix $\underline{\underline{H}}$ is

$$\underline{\underline{H}} = \begin{bmatrix} \kappa_{\text{FF}} - \delta & \kappa_{\text{FB}} \\ -\kappa_{\text{BF}} & -\left(\kappa_{\text{FF}} - \delta\right) \end{bmatrix} \tag{B.4}$$

By adding an initial condition, we obtain the initial value problem

$$\frac{\partial}{\partial z} \begin{bmatrix} \tilde{c}_+(z) \\ \tilde{c}_-(z) \end{bmatrix} = i\underline{\underline{H}} \begin{bmatrix} \tilde{c}_+(z) \\ \tilde{c}_-(z) \end{bmatrix} \tag{B.5a}$$

$$\begin{bmatrix} \tilde{c}_+(0) \\ \tilde{c}_-(0) \end{bmatrix} = \begin{bmatrix} \tilde{c}_{0_+} \\ \tilde{c}_{0_-} \end{bmatrix} \tag{B.5b}$$

which can be solved analytically. The solution is

$$\begin{bmatrix} \tilde{c}_+(z) \\ \tilde{c}_-(z) \end{bmatrix} = \underline{\underline{M}} \begin{bmatrix} e^{+i\lambda_+ z} & 0 \\ 0 & e^{-i\lambda_+ z} \end{bmatrix} \underline{\underline{M}}^{-1} \begin{bmatrix} \tilde{c}_{0_+} \\ \tilde{c}_{0_-} \end{bmatrix} \tag{B.6}$$

Here, λ_+ is one of the two eigenvalues of the matrix $\underline{\underline{H}}$ (the other eigenvalue being $-\lambda_+$). It is given by

$$\lambda_+ = \pm\sqrt{(\kappa_{\text{FF}} - \delta)^2 - \kappa_{\text{FB}}\kappa_{\text{BF}}} \tag{B.7}$$

In the presence of optical gain, the sign of the square root is selected such that $\text{Im}\left\{\lambda_+\right\}$ and $\text{Im}\left\{\kappa_{\text{FF}}\right\}$ have the same sign. The matrix $\underline{\underline{M}}$ is

$$\underline{\underline{M}} = \begin{bmatrix} u_{11} & u_{12} \\ u_{21} & u_{22} \end{bmatrix} \tag{B.8}$$

with $\underline{u}_1 = [u_{11} \quad u_{21}]^T$ and $\underline{u}_2 = [u_{12} \quad u_{22}]^T$ being the eigenvectors of $\underline{\underline{H}}$, where T denotes the transpose operator. Each eigenvector is determined up to a multiplicative constant, but the ratio between its two elements is *uniquely* defined. We denote by r_+ (r_-) the ratio u_{21}/u_{11} (u_{12}/u_{22})

$$r_+ = \frac{u_{21}}{u_{11}} = -\frac{(\kappa_{\mathrm{FF}} - \delta) - \lambda_+}{\kappa_{\mathrm{FB}}} = -\frac{\kappa_{\mathrm{BF}}}{(\kappa_{\mathrm{FF}} - \delta) + \lambda_+} \tag{B.9a}$$

$$r_- = \frac{u_{12}}{u_{22}} = -\frac{(\kappa_{\mathrm{FF}} - \delta) - \lambda_+}{\kappa_{\mathrm{BF}}} = -\frac{\kappa_{\mathrm{FB}}}{(\kappa_{\mathrm{FF}} - \delta) + \lambda_+} \tag{B.9b}$$

and reformulate the matrix $\underline{\underline{M}}$ as

$$\underline{\underline{M}} = \begin{bmatrix} u_{11} & u_{22}r_- \\ u_{11}r_+ & u_{22} \end{bmatrix} \tag{B.10}$$

The elements u_{11} and u_{22} can be chosen freely, e.g. $u_{11} = u_{22} = 1$. By inserting Eqs. (B.7) and (B.10) into Eq. (B.6), we solve the initial value problem in the unknows $\tilde{c}_\pm$. Then, by usage of Eq. (B.2), we retrieve the amplitudes $\psi_\pm$.

B.2 Bloch modes and disperson relation of the *perturbed* waveguide

As seen in Appendix A, the electromagnetic state of the perturbed waveguide can be represented as

$$\begin{bmatrix} \mathbf{E}(\mathbf{r}) \\ \mathbf{H}(\mathbf{r}) \end{bmatrix} = c_+(z) \begin{bmatrix} \mathbf{e}_+(\mathbf{r}) \\ \mathbf{h}_+(\mathbf{r}) \end{bmatrix} + c_-(z) \begin{bmatrix} \mathbf{e}_-(\mathbf{r}) \\ \mathbf{h}_-(\mathbf{r}) \end{bmatrix} \tag{B.11}$$

Here, the electric (magnetic) fields $\mathbf{e}_\pm$ ($\mathbf{h}_\pm$) are z periodic, with the period given by the lattice constant a. The amplitudes $c_\pm$ are directly related to $\psi_\pm$ by

$$c_\pm(z) = \psi_\pm(z) e^{\pm i k_z z} \tag{B.12}$$

Therefore, by usage of Eq. (B.2), one finds

$$\begin{bmatrix} c_+(z) \\ c_-(z) \end{bmatrix} = \begin{bmatrix} e^{+i\frac{\pi}{a}z} & 0 \\ 0 & e^{-i\frac{\pi}{a}z} \end{bmatrix} \begin{bmatrix} \tilde{c}_+(z) \\ \tilde{c}_-(z) \end{bmatrix} \tag{B.13}$$

By inserting Eq. (B.13) into Eq. (B.11), we can reformulate the electromagnetic state as

$$\begin{bmatrix} \mathbf{E}(\mathbf{r}) \\ \mathbf{H}(\mathbf{r}) \end{bmatrix} = \begin{bmatrix} \mathbf{e}_+(\mathbf{r}) & \mathbf{e}_-(\mathbf{r}) \\ \mathbf{h}_+(\mathbf{r}) & \mathbf{h}_-(\mathbf{r}) \end{bmatrix} \begin{bmatrix} e^{+i\frac{\pi}{a}z} & 0 \\ 0 & e^{-i\frac{\pi}{a}z} \end{bmatrix} \begin{bmatrix} \tilde{c}_+(z) \\ \tilde{c}_-(z) \end{bmatrix} \tag{B.14}$$

We can now exploit the solution of the initial value problem obtained in Sec. B.1. By inserting Eq. (B.6) into Eq. (B.14) and making use of Eq. (B.10), we finally obtain

$$\begin{bmatrix} \mathbf{E}(\mathbf{r}) \\ \mathbf{H}(\mathbf{r}) \end{bmatrix} = \tilde{F} \begin{bmatrix} \tilde{\mathbf{e}}_+(\mathbf{r}) \\ \tilde{\mathbf{h}}_+(\mathbf{r}) \end{bmatrix} e^{+i\tilde{k}_z z} + \tilde{B} \begin{bmatrix} \tilde{\mathbf{e}}_-(\mathbf{r}) \\ \tilde{\mathbf{h}}_-(\mathbf{r}) \end{bmatrix} e^{-i\tilde{k}_z z} \tag{B.15}$$

Here, the electric (magnetic) fields $\tilde{\mathbf{e}}_\pm$ and ($\tilde{\mathbf{h}}_\pm$) are the Bloch modes of the *perturbed* waveguide

$$\tilde{\mathbf{e}}_\pm(\mathbf{r}) = \mathbf{e}_\pm(\mathbf{r}) + r_\pm e^{\mp i\frac{2\pi}{a}z}\mathbf{e}_\mp(\mathbf{r}) \tag{B.16a}$$

$$\tilde{\mathbf{h}}_\pm(\mathbf{r}) = \mathbf{h}_\pm(\mathbf{r}) + r_\pm e^{\mp i\frac{2\pi}{a}z}\mathbf{h}_\mp(\mathbf{r}) \tag{B.16b}$$

Each of them results from the interference of the forward- and backward-propagating Bloch modes of the reference waveguide, with r_+ and r_- determining the strength of the backward component as compared to the forward one and viceversa. The amplitudes $\tilde{F}$ and $\tilde{B}$ are related to the initial condition by

$$\begin{bmatrix}\tilde{F}\\ \tilde{B}\end{bmatrix} = \begin{bmatrix}u_{11}\\ u_{22}\end{bmatrix}^T \underline{\underline{M}}^{-1}\begin{bmatrix}\tilde{c}_{0_+}\\ \tilde{c}_{0_-}\end{bmatrix} \tag{B.17}$$

Finally, the wavenumber $\tilde{k}_z$ is generally *complex* and given by

$$\tilde{k}_z = \beta_{\text{eff}} - \frac{i}{2}g_{\text{eff}} \tag{B.18}$$

where the effective propagation constant β_{eff} and *net* modal gain g_{eff} are

$$\beta_{\text{eff}} = \text{Re}\left\{\lambda_+\right\} + \frac{\pi}{a} \tag{B.19a}$$

$$g_{\text{eff}} = -2\text{Im}\left\{\lambda_+\right\} \tag{B.19b}$$

Eqs.(B.19a) and (B.19b) define the dispersion relation of the perturbed waveguide, which is thoroughly discussed in Sec. 3.4.

B.3 Power flow

The time-averaged power flowing in the waveguide is defined as [53]

$$P(z) = \frac{1}{2}\text{Re}\left\{\int_A \left[\mathbf{E}(\mathbf{r}) \times \mathbf{H}^*(\mathbf{r})\right] \cdot \hat{z}\, dA\right\} \tag{B.20}$$

with A being the transverse section at position z. Here, we are assuming that the electric field in the time-domain is

$$\mathbf{E}(\mathbf{r}, t) = \text{Re}\left\{\mathbf{E}(\mathbf{r})e^{-i\omega t}\right\} = \frac{1}{2}\mathbf{E}(\mathbf{r})e^{-i\omega t} + c.c. \tag{B.21}$$

and similarly for the magnetic field, with $c.c.$ denoting the complex conjugate. Therefore, by *time-averaged* we mean over a time interval equal to $2\pi/\omega$.

We may express the power by two equivalent formulations. In either case, we need the orthonormality relation of the Bloch modes of the reference waveguide. From Appendix A, we may recall

$$\frac{1}{4}\int_A (\mathbf{e}_\sigma \times \mathbf{h}^*_{\sigma'} + \mathbf{e}^*_{\sigma'} \times \mathbf{h}_\sigma) \cdot \hat{\mathbf{z}}\, dA = \sigma P_0 \delta_{\sigma,\sigma'} \tag{B.22a}$$

$$P_0 = \frac{v_g}{2a}\int_V \epsilon_0 n_b^2(\mathbf{r})|\mathbf{e}_+(\mathbf{r})|^2\, dV \tag{B.22b}$$

Here, $\delta_{\sigma,\sigma'}$ is the Kronecker delta, with $\sigma = \pm$ and $\sigma' = -\sigma$. v_g is the group velocity in the reference waveguide, $n_b(\mathbf{r})$ the background refractive index and V the volume of a supercell.

B.3.1 Formulation I

By inserting (B.11) into Eq. (B.20) and using the orthonormality relation, we obtain

$$P(z) = \underbrace{|c_+(z)|^2 P_0}_{P_+(z)} - \underbrace{|c_-(z)|^2 P_0}_{P_-(z)} \tag{B.23}$$

Here, the forward- (P_+) and backward-propagating power (P_-) are coupled and generally *not* monotonic with position z.

The important message behind Eq. (B.23) is that the forward-propagating (backward-propagating) power is proportional to the squared magnitude of c_+ (c_-). We compute these powers explicitly in Sec. B.4.

B.3.2 Formulation II

Equivalently, we may insert Eq. (B.14) into Eq. (B.20). In this case, we firstly derive the useful relations

$$\frac{1}{4}\int_A \left(\tilde{\mathbf{e}}_+ \times \tilde{\mathbf{h}}^*_+ + \tilde{\mathbf{e}}^*_+ \times \tilde{\mathbf{h}}_+\right) \cdot \hat{z}\, dA = \left(1 - |r_+|^2\right) P_0 \tag{B.24a}$$

$$\frac{1}{4}\int_A \left(\tilde{\mathbf{e}}_- \times \tilde{\mathbf{h}}^*_- + \tilde{\mathbf{e}}^*_- \times \tilde{\mathbf{h}}_-\right) \cdot \hat{z}\, dA = -\left(1 - |r_-|^2\right) P_0 \tag{B.24b}$$

$$\frac{1}{4}\int_A \left(\tilde{\mathbf{e}}_+ \times \tilde{\mathbf{h}}^*_- + \tilde{\mathbf{e}}^*_- \times \tilde{\mathbf{h}}_+\right) \cdot \hat{z}\, dA = e^{-i\frac{2\pi}{a}z}\left(r^*_- - r_+\right) P_0 \tag{B.24c}$$

Here, we have employed the expressions of the Bloch modes of the perturbed waveguide from Eqs. (B.16a) and (B.16b), as well as the orthonormality relation from Eqs. (B.22a) and (B.22b). It is important to note that the integral in Eq. (B.24c) is generally different from zero. This means that the Bloch modes of the perturbed waveguide are generally *not* power orthogonal. We will return to the consequences in a few lines. By exploiting

Eqs. (B.24a)-(B.24c), we may now insert Eq. (B.14) into Eq. (B.20) and express the power as the sum of three *uncoupled* contributions

$$P(z) = \tilde{P}_+(z) - \tilde{P}_-(z) + \tilde{P}_{\mathrm{cross}}(z) \tag{B.25}$$

The first two contribution are the forward- (+) and backward-propagating power (−) of the Bloch modes of the *perturbed* waveguide

$$\tilde{P}_+(z) = |\tilde{F}|^2 e^{g_{\mathrm{eff}} z} \left(1 - |r_+|^2\right) P_0 \tag{B.26a}$$

$$\tilde{P}_-(z) = |\tilde{B}|^2 e^{-g_{\mathrm{eff}} z} \left(1 - |r_-|^2\right) P_0 \tag{B.26b}$$

These contributions are obviously monotonic with position z and they exponentially increase with the net effective modal gain g_{eff}. However, they are also scaled down by the factor $(1 - |r_\pm|^2)$. Depending on $r_\pm$, this factor might be much smaller than unity. The third contribution is the cross power

$$\tilde{P}_{\mathrm{cross}}(z) = 2\mathrm{Re}\left\{ \tilde{F}\tilde{B}^* e^{2i\beta_{\mathrm{eff}} z} e^{-i\frac{2\pi}{a}z}(r_-^* - r_+) \right\} P_0 \tag{B.27}$$

This contribution is *periodic* with position z, with the periodicity determined by the effective propagation constant β_{eff}. It arises because, as mentioned above, the Bloch modes of the perturbed waveguide are generally *not* power orthogonal. In addition, it should be emphasized that, in dependence of $r_\pm$, the cross power is not necessarily negligible as compared to the other two contributions.

In light of these considerations, the important message behind Eq. (B.25) is that a larger net effective modal gain g_{eff} does *not* necessarily translate into more power. In fact, the impact of $r_\pm$, as well as the cross power, should be also taken into account.

B.4 Boundary value problem

In Sec. B.1, we have solved the reduced CBM equations as an initial value problem. Here instead we wish to solve them as a boundary value problem.

For this purpose, we take advantage of results of Sec. B.2. Eqs. (B.11) and (B.15) are two equivalent formulations of the electromagnetic state. By comparing them, one finds

$$c_+(z) = e^{+i\frac{\pi}{a}z}\left(\tilde{F}e^{+i\lambda_+ z} + r_-\tilde{B}e^{-i\lambda_+ z}\right) \tag{B.28a}$$

$$c_-(z) = e^{-i\frac{\pi}{a}z}\left(r_+\tilde{F}e^{+i\lambda_+ z} + \tilde{B}e^{-i\lambda_+ z}\right) \tag{B.28b}$$

The amplitudes $\tilde{F}$ and $\tilde{B}$ depend on the boundary conditions. We assume that the waveguide extends from $z = 0$ (input) to $z = L$ (output). As boundary conditions, we impose

$$c_+(z=0) = \tilde{F} + r_-\tilde{B} = c_{0_+} \tag{B.29a}$$

$$c_-(z=L) = e^{-i\frac{\pi}{a}L}\left(r_+\tilde{F}e^{+i\lambda_+ L} + \tilde{B}e^{-i\lambda_+ L}\right) = 0 \tag{B.29b}$$

As seen in Sec. B.3.1, the forward-propagating (backward-propagating) power is proportional to $|c_+|^2$ ($|c_-|^2$). Therefore, the boundary conditions which we have imposed reflect a typical scattering experiment, with power being solely injected from the input. By solving Eqs. (B.29a) and (B.29b), we obtain

$$\tilde{F} = \frac{c_{0_+}}{1 - r_+ r_- e^{+2i\lambda_+ L}} \tag{B.30a}$$

$$\tilde{B} = \frac{-r_+ c_{0_+} e^{+2i\lambda_+ L}}{1 - r_+ r_- e^{+2i\lambda_+ L}} \tag{B.30b}$$

By inserting these values into Eqs. (B.28a) and (B.28b), we obtain the spatial evolution of the forward- and backward-propagating field in the perturbed waveguide. From these, one may easily compute the forward- and backward-propagating power in compliance with Eq. (B.23).

As mentioned above, in practice one injects a given power from the waveguide input. Therefore, we may directly relate c_{0_+} to the input power $P_{\mathrm{in}} = P_+(z = 0)$. In this case, from Eq. (B.23) we obtain

$$|c_{0_+}| = \sqrt{\frac{P_{\mathrm{in}}}{P_0}} \tag{B.31}$$

with P_0 being the normalization term given by Eq. (B.22b). Here, it should be emphasized that, owing to the frequency dependence of P_0, a given input power results in *different* values of $|c_{0_+}|$ in dependence of the frequency. In addition, we note that the constraint on the input power does not fix the phase of c_{0_+} (that is, the phase of the forward-propagating field at the waveguide input).

Appendix C

Active Photonic Crystal Waveguides: transmission matrix, scattering matrix and block diagram

In this appendix, we derive the transmission and scattering matrices of photonic crystal waveguides including active material. For this purpose, we exploit the analytical solution of the *reduced* coupled-Bloch-mode (CBM) equations which is fully derived in Appendix B. Finally, we derive a block diagram of the active waveguide, which further elucidates the physics behind the mathematical expressions.

As seen in Appendix A, the electromagnetic state of a photonic crystal waveguide with a generally *complex* refractive index can be represented as

$$\begin{bmatrix}\mathbf{E}(\mathbf{r})\\ \mathbf{H}(\mathbf{r})\end{bmatrix} = c_+(z)\begin{bmatrix}\mathbf{e}_+(\mathbf{r})\\ \mathbf{h}_+(\mathbf{r})\end{bmatrix} + c_-(z)\begin{bmatrix}\mathbf{e}_-(\mathbf{r})\\ \mathbf{h}_-(\mathbf{r})\end{bmatrix} \tag{C.1}$$

Here, $\mathbf{e}_\pm$ are the forward- (+) and backward-propagating (−) electric field of the guided Bloch mode of a *reference* waveguide with purely real refractive index. Similarly, $\mathbf{h}_\pm$ are the magnetic fields. The amplitudes $c_\pm$ are given by

$$c_\pm(z) = \psi_\pm(z)e^{\pm ik_z z} \tag{C.2}$$

where k_z is the wavenumber of the reference waveguide along the propagation direction z and $\psi_\pm$ are slowly-varying amplitudes. The spatial evolution of these amplitudes is governed by the reduced CBM equations derived in Sec. 3.3.

In the following, we simply denote the waveguide of interest (with a generally complex refractive index) as *active* waveguide. We derive the transmission and scattering matrix for the amplitudes $c_\pm(z)$.

C.1 Transmission matrix

We assume that the waveguide extends from $z = 0$ (input) to $z = L$ (output). We set $z = L$ in Eq. (B.6), which gives

$$\begin{bmatrix} \tilde{c}_+(L) \\ \tilde{c}_-(L) \end{bmatrix} = \underline{\underline{M}}\,\underline{\underline{\Lambda}}\,\underline{\underline{M}}^{-1} \begin{bmatrix} \tilde{c}_+(0) \\ \tilde{c}_-(0) \end{bmatrix} \tag{C.3}$$

The matrix $\underline{\underline{\Lambda}}$ is

$$\underline{\underline{\Lambda}} = \begin{bmatrix} e^{+i\lambda_+ L} & 0 \\ 0 & e^{-i\lambda_+ L} \end{bmatrix} \tag{C.4}$$

while the matrix $\underline{\underline{M}}$ and its inverse read

$$\underline{\underline{M}} = \begin{bmatrix} u_{11} & u_{22} r_- \\ u_{11} r_+ & u_{22} \end{bmatrix} \tag{C.5a}$$

$$\underline{\underline{M}}^{-1} = \frac{1}{u_{11} u_{22}(1 - r_+ r_-)} \begin{bmatrix} u_{22} & -u_{22} r_- \\ -\,u_{11} r_+ & u_{11} \end{bmatrix} \tag{C.5b}$$

We refer to Appendix B for details on the various quantities. In addition, we exploit Eq. (B.13). This equation provides the relationship between the amplitudes $c_\pm(z)$, which we are interested in, and $\tilde{c}_\pm(z)$, appearing in Eq. (C.3). At the input ($z = 0$), one finds $c_\pm(0) = \tilde{c}_\pm(0)$. At the output ($z = L$), it turns out

$$\begin{bmatrix} c_+(L) \\ c_-(L) \end{bmatrix} = \underline{\underline{\Phi}} \begin{bmatrix} \tilde{c}_+(L) \\ \tilde{c}_-(L) \end{bmatrix} \tag{C.6}$$

where the matrix $\underline{\underline{\Phi}}$ reads

$$\underline{\underline{\Phi}} = \begin{bmatrix} e^{+i\frac{\pi}{a}L} & 0 \\ 0 & e^{-i\frac{\pi}{a}L} \end{bmatrix} \tag{C.7}$$

By combining Eq. (C.6) with Eq. (C.3), we obtain

$$\begin{bmatrix} c_+(L) \\ c_-(L) \end{bmatrix} = \underline{\underline{T}} \begin{bmatrix} c_+(0) \\ c_-(0) \end{bmatrix} \tag{C.8}$$

where the *transmission* matrix $\underline{\underline{T}}$ is

$$\underline{\underline{T}} = \underline{\underline{\Phi}}\,\underline{\underline{M}}\,\underline{\underline{\Lambda}}\,\underline{\underline{M}}^{-1} \tag{C.9}$$

This is the transmission matrix of the active waveguide in the basis of the Bloch modes of the reference waveguide. The laser cavity block diagram which we thoroughly discuss in Sec. 4.3.1 is directly based on Eq. (C.9). By carrying out the multiplications, one finds the elements

$$T_{11} = \frac{1}{1 - r_- r_+} \left(e^{+i\lambda_+ L} - r_+ r_- e^{-i\lambda_+ L} \right) e^{+i\frac{\pi}{a} L} \tag{C.10a}$$

$$T_{12} = \frac{-r_-}{1 - r_- r_+} \left(e^{+i\lambda_+ L} - e^{-i\lambda_+ L} \right) e^{+i\frac{\pi}{a} L} \tag{C.10b}$$

$$T_{21} = \frac{r_+}{1 - r_- r_+} \left(e^{+i\lambda_+ L} - e^{-i\lambda_+ L} \right) e^{-i\frac{\pi}{a} L} \tag{C.10c}$$

$$T_{22} = \frac{1}{1 - r_- r_+} \left(-r_+ r_- e^{+i\lambda_+ L} + e^{-i\lambda_+ L} \right) e^{-i\frac{\pi}{a} L} \tag{C.10d}$$

C.2 Scattering matrix

The *scattering* matrix $\underline{\underline{S}}$ relates the amplitudes $c_\pm$ of the Bloch modes entering and exiting the active waveguide, that is

$$\begin{bmatrix} c_-(0) \\ c_+(L) \end{bmatrix} = \underline{\underline{S}} \begin{bmatrix} c_+(0) \\ c_-(L) \end{bmatrix} \tag{C.11}$$

By applying the usual relations between the elements of a scattering and transmission matrix [23], from Eqs. (C.10a)-(C.10d) one finds

$$S_{11} = \frac{-T_{21}}{T_{22}} = \frac{-\left(e^{+2i\lambda_+ L} - 1 \right) r_+}{1 - r_+ r_- e^{+2i\lambda_+ L}} e^{-i\frac{2\pi}{a} L} \tag{C.12a}$$

$$S_{12} = \frac{1}{T_{22}} = \frac{(1 - r_+ r_-) e^{+i\lambda_+ L}}{1 - r_+ r_- e^{+2i\lambda_+ L}} e^{+i\frac{\pi}{a} L} \tag{C.12b}$$

$$S_{21} = \frac{\det \left\{ \underline{\underline{T}} \right\}}{T_{22}} = S_{12} \tag{C.12c}$$

$$S_{22} = \frac{T_{12}}{T_{22}} = \frac{-\left(e^{+2i\lambda_+ L} - 1 \right) r_-}{1 - r_+ r_- e^{+2i\lambda_+ L}} e^{+i\frac{2\pi}{a} L} \tag{C.12d}$$

As seen in Sec. B.3.1, the forward- and backward-propagating power at position z are proportional to $|c_+(z)|^2$ and $|c_-(z)|^2$ respectively. Therefore, the squared magnitude of S_{12} (or S_{21}) represents the power transmitted through the waveguide at one end normalized to the power injected from the other side. Similarly, the squared magnitude of S_{11} (S_{22}) is the power reflected at the input (output) normalized to the power injected from the input (output).

C.3 Block diagram

Based on Eq. (C.9), we can derive a block diagram of the active waveguide. For this purpose, we recast the equation as

$$\underline{\underline{T}} = \left[\underline{\underline{\Phi}}\,\underline{\underline{M}}\right]\,\underline{\underline{\Lambda}}\,\left[\underline{\underline{M}}^{-1}\right] \tag{C.13}$$

Such recasting leads to the following interpretation, summarized by Fig. C.1. $\underline{\underline{\Lambda}}$ is the transmission matrix in the basis of the Bloch modes of the *active* waveguide. While propagating, they remain uncoupled, because $\underline{\underline{\Lambda}}$ is diagonal. The matrix $\underline{\underline{\Phi}}\,\underline{\underline{M}}$ accounts for the *mismatch* (i.e. change of basis) between the Bloch modes of the active waveguide and those of the reference waveguide (used as original basis) at the right end. Similarly, $\underline{\underline{M}}^{-1}$ takes into account the mismatch at the left end. These matrices play the role of equivalent dielectric interfaces between the active waveguide and the reference waveguide, which is supposed to extend on either side.

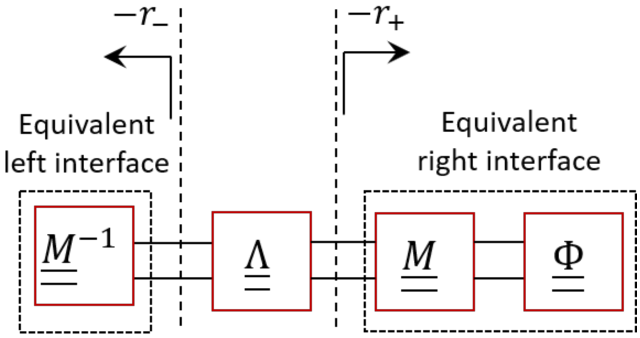

Figure C.1: Block diagram of an active photonic crystal waveguide.

C.3.1 Right interface

The transmission matrix describing the equivalent right interface is

$$\underline{\underline{T_r}} = \underline{\underline{\Phi}}\,\underline{\underline{M}} = \begin{bmatrix} u_{11}e^{+i\frac{\pi}{a}L} & u_{22}r_-e^{+i\frac{\pi}{a}L} \\ u_{11}r_+e^{-i\frac{\pi}{a}L} & u_{22}e^{-i\frac{\pi}{a}L} \end{bmatrix} \tag{C.14}$$

The elements of the corresponding scattering matrix $\underline{\underline{S}}_r$ are obtained as

$$S_{r_{11}} = \frac{-T_{r_{21}}}{T_{r_{22}}} = -\frac{u_{11}}{u_{22}} r_+ \tag{C.15a}$$

$$S_{r_{12}} = \frac{1}{T_{r_{22}}} = \frac{1}{u_{22}} e^{+i\frac{\pi}{a}L} \tag{C.15b}$$

$$S_{r_{21}} = \frac{\det\left\{\underline{\underline{T}}_r\right\}}{T_{r_{22}}} = u_{11}(1 - r_+ r_-) e^{+i\frac{\pi}{a}L} \tag{C.15c}$$

$$S_{r_{22}} = \frac{T_{r_{12}}}{T_{r_{22}}} = r_- e^{+i\frac{2\pi}{a}L} \tag{C.15d}$$

As already noted in Appendix B, u_{11} and u_{22} can be chosen freely, e.g. $u_{11} = u_{22}$. Therefore, Eq. (C.15a) reveals that r_+ can be interpreted (within a phase shift of π) as the reflection coefficient of the equivalent right interface indicated in Fig. C.1. This explains why the power contribution $\tilde{P}_+(z)$ associated with the forward-propagating Bloch mode of the active waveguide is scaled down by the factor $1 - |r_+|^2$ (see Eq. (B.26a)).

C.3.2 Left interface

The transmission matrix describing the equivalent left interface is

$$\underline{\underline{T}}_l = \underline{\underline{M}}^{-1} = \frac{1}{u_{11}u_{22}(1 - r_+ r_-)} \begin{bmatrix} u_{22} & -u_{22} r_- \\ -u_{11} r_+ & u_{11} \end{bmatrix} \tag{C.16}$$

from which we compute the elements of the corresponding scattering matrix $\underline{\underline{S}}_l$

$$S_{l_{11}} = \frac{-T_{l_{21}}}{T_{l_{22}}} = r_+ \tag{C.17a}$$

$$S_{l_{12}} = \frac{1}{T_{l_{22}}} = u_{22}(1 - r_+ r_-) \tag{C.17b}$$

$$S_{l_{21}} = \frac{\det\left\{\underline{\underline{T}}_l\right\}}{T_{r_{22}}} = \frac{1}{u_{11}} \tag{C.17c}$$

$$S_{l_{22}} = \frac{T_{l_{12}}}{T_{l_{22}}} = -\frac{u_{22}}{u_{11}} r_- \tag{C.17d}$$

By choosing $u_{11} = u_{22}$ in Eq. (C.17d), we can interpret r_- (within a phase shift of π) as the reflection coefficient of the equivalent left interface. This explains why the power contribution $\tilde{P}_-(z)$ associated with the backward-propagating Bloch mode of the active waveguide is scaled down by the factor $1 - |r_-|^2$ (see Eq. (B.26b)).

Appendix D

Stimulated emission rate in slow-light photonic crystal lasers: derivation

In this appendix, we derive in detail the stimulated emission rate to be used in the rate equation model of photonic crystal lasers presented in Chapter 5.

We assume that the electric field in the time-domain is

$$\mathbf{E}(\mathbf{r},t) = \mathrm{Re}\left\{\mathbf{E}(\mathbf{r})e^{-i\omega_s t}\right\} = \frac{1}{2}\mathbf{E}(\mathbf{r})e^{-i\omega_s t} + c.c. \tag{D.1}$$

and similarly for the magnetic field, with $c.c.$ denoting the complex conjugate. From Poynting's theorem, the time-averaged energy transferred per unit time and unit volume from the electromagnetic field to the active medium is [149]

$$\left\langle \frac{dU}{dt} \right\rangle = \frac{1}{2}\epsilon_0\omega_s|\mathbf{E}(\mathbf{r})|^2\,\mathrm{Im}\left\{\chi_{\mathrm{pert}}(\mathbf{r})\right\} \tag{D.2}$$

Here, ϵ_0 is the vacuum dielectric permittivity and χ_{pert} the susceptibility perturbation due to the active medium, while $\langle\rangle$ denotes the time average. This average is performed over a wave cycle, that is a time interval equal to $2\pi/\omega_s$. The *local* stimulated emission rate is defined as

$$R_{\mathrm{st}}(\mathbf{r}) = -\frac{1}{\hbar\omega_s}\left\langle \frac{dU}{dt} \right\rangle \tag{D.3}$$

corresponding to the average generation rate of photons of energy $\hbar\omega_s$ in a generic point $\mathbf{r}$ of the active medium.

Travelling wave description

We consider a laser cavity based on a line-defect photonic crystal waveguide, as those discussed in Chapter 4. The active region may either uniformly extend throughout the slab or be limited to the line-defect (see Fig. 3.7 in Sec. 3.2.1). From Eq. (A.24) in Sec. A.1, we obtain

$$\mathrm{Im}\left\{\chi_{\text{pert}}(\mathbf{r})\right\} = 2n_{\text{slab}}n_i F_{\text{carrier}}(\mathbf{r}) \tag{D.4}$$

Here, n_{slab} is the slab refractive index. $F_{\text{carrier}}(\mathbf{r})$ is the distribution function of the active layers of quantum wells or quantum dots, which are assumed to undergo spatially uniform pumping. One finds $F_{\text{carrier}} = 1$ ($F_{\text{carrier}} = 0$) within the active layers (elsewhere). The imaginary refractive index n_i reflects the *material* gain g_{mat}. We are interested in the *global* stimulated emission rate

$$\begin{aligned} R_{\text{st}} &= \int_{V_{\text{act}}} R_{\text{st}}(\mathbf{r})\, dV_{\text{act}} \\ &= -\frac{\epsilon_0 n_{\text{slab}} n_i}{\hbar} \int_{V_{\text{act}}} |\mathbf{E}(\mathbf{r})|^2 F_{\text{carrier}}(\mathbf{r})\, dV_{\text{act}} \\ &= -\frac{\epsilon_0 n_{\text{slab}} n_i}{\hbar} \int_0^L \int_A |\mathbf{E}(\mathbf{r})|^2 F_{\text{carrier}}(\mathbf{r})\, dA\, dz \end{aligned} \tag{D.5}$$

with V_{act} being the active region volume, L the length of the active region and A the transverse section at position z. This rate corresponds to the average number of photons generated per unit time in the whole active region.

From Eq. (3.2) in Sec. 3.2, we may express the electric field as

$$\mathbf{E}(\mathbf{r}) = c_+(z)\mathbf{e}_+(\mathbf{r}) + c_-(z)\mathbf{e}_-(\mathbf{r}) \tag{D.6}$$

Here, $\mathbf{e}_\pm$ are the forward- (+) and backward-propagating (−) electric field of the guided Bloch mode of a *reference* waveguide. As explained in Sec. 3.2, the active waveguide on which the laser cavity is based is viewed as perturbed as compared to this reference waveguide, having purely real refractive index. The perturbation is represented by the material gain induced by carrier density. The Bloch fields $\mathbf{e}_\pm$ are z periodic, with the period given by the lattice constant a. The complex amplitudes $c_\pm(z)$ reflect the spatial dependence which the Bloch fields acquire within the laser cavity at the lasing threshold. The electric field squared magnitude is

$$\begin{aligned} |\mathbf{E}(\mathbf{r})|^2 = |c_+(z)|^2|\mathbf{e}_+(\mathbf{r})|^2 + |c_-(z)|^2|\mathbf{e}_-(\mathbf{r})| \\ + c_+(z)c_-^*(z)\left[\mathbf{e}_-^*(\mathbf{r})\cdot\mathbf{e}_+(\mathbf{r})\right] + c_-(z)c_+^*(z)\left[\mathbf{e}_-(\mathbf{r})\cdot\mathbf{e}_+^*(\mathbf{r})\right] \end{aligned} \tag{D.7}$$

From Eq. (A.10a) in Appendix A, we recall the time-averaged electric field energy stored in a supercell

$$W_e = \frac{1}{4}\int_V \epsilon_0 n_b^2(\mathbf{r})|\mathbf{e}_\pm(\mathbf{r})|^2\, dV \tag{D.8}$$

with V being the supercell volume and n_b the background refractive index. We consider the third line of Eq. (D.5). We multiple and divide the right-hand side by the quantity

$\left(\epsilon_0 a\, n_{\rm slab}^2\right) / \left(4W_e\right)$. Then, by inserting the expression of $|\mathbf{E}(\mathbf{r})|^2$ from Eq.(D.7), we obtain

$$\begin{aligned} R_{\rm st} = -\frac{4W_e}{\hbar}\frac{n_i}{a\,n_{\rm slab}}\Bigg[\int_0^L |c_+(z)|^2\Gamma_{11}(z)\,dz + \int_0^L |c_-(z)|^2\Gamma_{11}(z)\,dz \\ + \int_0^L c_+(z)c_-^*(z)\Gamma_{21}(z)\,dz + \int_0^L c_-(z)c_+^*(z)\Gamma_{12}(z)\,dz\Bigg] \end{aligned} \tag{D.9}$$

Here, Γ_{11} and Γ_{12} are the normalized coupling coefficients from Eqs. (A.35a) and (A.35b) in Sec. A.3, while Γ_{21} is the complex conjugate of Γ_{12}. By recalling our discussion in Sec. A.3.1, we may conveniently evaluate Γ_{11} and Γ_{12} by assuming the material gain to be *homogeneous* within the slab along the vertical direction, *as if* the active layers entirely filled the slab along this direction. In this case, n_i reflects the *modal* gain $\Gamma_y g_{\rm mat}$, with

$$n_i = -\frac{1}{2}\left(\frac{c}{\omega_s}\right)\Gamma_y g_{\rm mat} \tag{D.10}$$

Here, Γ_y is the optical confinement factor within the active layers along the vertical direction (see Eq. (A.38a) in Sec. A.3.1). Thus, we may recast Eq. (D.9) as

$$\begin{aligned} R_{\rm st} = \frac{2W_e}{\hbar\omega_s}\left(\frac{c}{n_{\rm slab}}\right)\frac{\Gamma_y g_{\rm mat}}{a}\Bigg[\int_0^L |c_+(z)|^2\Gamma_{11}^{\rm carrier}(z)\,dz + \int_0^L |c_-(z)|^2\Gamma_{11}^{\rm carrier}(z)\,dz \\ + \int_0^L c_+(z)c_-^*(z)\Gamma_{21}^{\rm carrier}(z)\,dz + \int_0^L c_-(z)c_+^*(z)\Gamma_{12}^{\rm carrier}(z)\,dz\Bigg] \end{aligned} \tag{D.11}$$

Here, $\Gamma_{11}^{\rm carrier}$ and $\Gamma_{12}^{\rm carrier}$ are given by Eqs. (A.37a) and (A.37b) in Sec. A.3.1, which we recall for the sake of convenience

$$\Gamma_{11}^{\rm carrier}(z) = \frac{a\int_A \epsilon_0 n_{\rm slab}^2 |\mathbf{e}_0(\mathbf{r})|^2 F_{\rm carrier}^{\rm uniform}(\mathbf{r})dA}{\int_V \epsilon_0 n_b^2(\mathbf{r})|\mathbf{e}_0(\mathbf{r})|^2\,dV} \tag{D.12a}$$

$$\Gamma_{12}^{\rm carrier}(z) = \frac{a\int_A \epsilon_0 n_{\rm slab}^2 \left[\mathbf{e}_{0,-}(\mathbf{r})\cdot\mathbf{e}_{0,+}^*(\mathbf{r})\right] F_{\rm carrier}^{\rm uniform}(\mathbf{r})dA}{\int_V \epsilon_0 n_b^2(\mathbf{r})|\mathbf{e}_0(\mathbf{r})|^2\,dV} \tag{D.12b}$$

while $\Gamma_{21}^{\rm carrier}$ is the complex conjugate of $\Gamma_{12}^{\rm carrier}$. $F_{\rm carrier}^{\rm uniform}(\mathbf{r})$ coincides with $F_{\rm carrier}(\mathbf{r})$ along the lateral and longitudinal direction. On the other hand, $F_{\rm carrier}^{\rm uniform}(\mathbf{r})$ implies that the active layers homogeneously extend throughout the slab along the vertical direction.

The normalized coupling coefficients $\Gamma_{11}^{\rm carrier}$ and $\Gamma_{12}^{\rm carrier}$ are z periodic. Therefore, they can be expanded in a Fourier series. As thoroughly discussed in Sec. 3.2.1 and

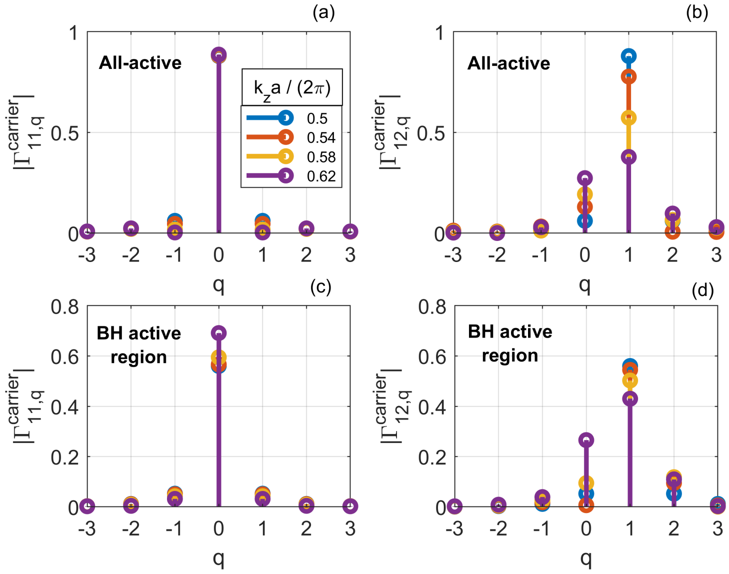

Figure D.1: Magnitude of the spatial harmonics of the normalized coupling coefficients of (a) and (b) an all-active waveguide and (c) and (d) a waveguide with a BH active region. The spatial harmonics of the self-coupling coefficient $\Gamma_{11}^{\text{carrier}}$ are in (a) and (c), those of the cross-coupling coefficient $\Gamma_{12}^{\text{carrier}}$ in (b) and (d). Each color corresponds to a different value of the wavenumber, as indicated by the legend in (a).

Sec. 3.3, one finds

$$\Gamma_{11}^{\text{carrier}}(z) = \sum_q \Gamma_{11,q}^{\text{carrier}} e^{+iq\frac{2\pi}{a}z} \approx \underbrace{\Gamma_{11,q=0}^{\text{carrier}}}_{\Gamma_{\text{FF}}} \tag{D.13a}$$

$$\Gamma_{12}^{\text{carrier}}(z) = \sum_q \Gamma_{12,q}^{\text{carrier}} e^{+iq\frac{2\pi}{a}z} \approx \underbrace{\Gamma_{12,q=1}^{\text{carrier}}}_{\Gamma_{\text{FB}}} e^{+i\frac{2\pi}{a}z} \tag{D.13b}$$

$$\Gamma_{21}^{\text{carrier}}(z) = \sum_q \Gamma_{21,q}^{\text{carrier}} e^{+iq\frac{2\pi}{a}z} \approx \underbrace{\Gamma_{21,q=-1}^{\text{carrier}}}_{\Gamma_{\text{BF}}} e^{-i\frac{2\pi}{a}z} \tag{D.13c}$$

with $\Gamma_{\text{BF}} = \Gamma_{\text{FB}}^*$. For the sake of convenience, we include Fig. D.1, already discussed in Sec. 3.2.1. As shown in the figure, the approximation in Eqs. (D.13b) becomes increasingly better as the frequency approaches the band edge at $k_z = \pi/a$, with k_z being the wavenumber of the reference waveguide. Away from the band edge, the approximation may become inaccurate and one should also retain the spatial average (corresponding to $q = 0$) in the Fourier series expansion of the cross-coupling coefficient $\Gamma_{12}^{\text{carrier}}$. However, this additional term would be smaller as compared to the spatial average of the self-coupling coefficient $\Gamma_{11}^{\text{carrier}}$. Therefore, the impact of this additional term on the stimulated emission rate in Eq. (D.11) is expected be limited. In order to proceed analytically, in the following we employ the approximate Fourier series expansions from Eqs. (D.13a)-(D.13c). Under this assumption, we may recast Eq. (D.11) as

$$R_{\mathrm{st}} = \frac{2W_e}{\hbar\omega_s}\left(\frac{c}{n_{\mathrm{slab}}}\right)\Gamma_y g_{\mathrm{mat}}\frac{\left(\mathrm{I}' + \mathrm{I}''\right)}{a} \tag{D.14}$$

where I' and I'' are the integrals

$$\mathrm{I}' = \Gamma_{\mathrm{FF}}\int_0^L \left[|c_+(z)|^2 + |c_-(z)|^2\right] dz \tag{D.15a}$$

$$\mathrm{I}'' = 2\mathrm{Re}\left\{\Gamma_{\mathrm{FB}}\int_0^L c_+^*(z)c_-(z)\,e^{+i\frac{2\pi}{a}z}\,dz\right\} \tag{D.15b}$$

Γ_{FF} is real and positive, while Γ_{FB} is complex. However, we should recall from Sec. 3.2.1 our discussion on the phase of the cross-coupling coefficient $\Gamma_{12}^{\mathrm{carrier}}$. For the choice of a unit cell adopted throughout this thesis (see the inset of Fig. 3.8 in Sec. 3.2.1), one may approximate the phase of $\Gamma_{12}^{\mathrm{carrier}}$ with $\frac{2\pi}{a}z-\pi$ (see Fig. 3.12 in Sec. 3.2.1). Thus, one finds

$$\Gamma_{\mathrm{FB}} = \frac{1}{a}\int_a \Gamma_{12}^{\mathrm{carrier}}(z)e^{-i\frac{2\pi}{a}z} \approx e^{-i\pi}\langle|\Gamma_{12}^{\mathrm{carrier}}(z)|\rangle \tag{D.16}$$

with $\langle\rangle$ denoting here the spatial average. Therefore, Γ_{FB} is real and *negative* to a good approximation. The magnitude of Γ_{FF} and Γ_{FB} is shown in Fig. 3.15 in Sec. 3.3.

Amplitudes $c_\pm$

In the following, we wish to compute the integrals in Eqs. (D.15a) and (D.15b). For this purpose, first of all we recall the expressions of $c_\pm(z)$ from Eqs. (3.30a) and (3.30b) in Sec. 3.5

$$c_+(z) = e^{+i\frac{\pi}{a}z}\left(\tilde{F}e^{+i\lambda_+ z} + r_-\tilde{B}e^{-i\lambda_+ z}\right) \tag{D.17a}$$

$$c_-(z) = e^{-i\frac{\pi}{a}z}\left(r_+\tilde{F}e^{+i\lambda_+ z} + \tilde{B}e^{-i\lambda_+ z}\right) \tag{D.17b}$$

Here, $\tilde{F}$ and $\tilde{B}$ are the amplitudes of the forward- and backward-propagating Bloch mode of the *active* waveguide on which the laser cavity is based (see Sec. 3.4). From Eqs. (3.24a) and (3.24b) in Sec. 3.4, the complex propagation constant λ_+ may be expressed as

$$\lambda_+ = \left(\beta_{\mathrm{eff}} - \frac{\pi}{a}\right) - \frac{i}{2}g_{\mathrm{eff}} \tag{D.18}$$

where β_{eff} is the effective propagation constant and g_{eff} the effective net modal gain, both evaluated at the lasing threshold.

Coefficients $r_\pm$

The coefficients $r_\pm$ are given by Eqs. (3.26a) and (3.26b) in Sec. 3.4, which we recall for the sake of convenience

$$r_+ = -\frac{\kappa_{\mathrm{BF}}}{(\kappa_{\mathrm{FF}} - \delta) + \lambda_+} \tag{D.19a}$$

$$r_- = -\frac{\kappa_{\mathrm{FB}}}{(\kappa_{\mathrm{FF}} - \delta) + \lambda_+} \tag{D.19b}$$

Here, the self- (κ_{FF}) and cross-coupling coefficients (κ_{FB} and κ_{BF}) are generally given by Eq. (3.19) in Sec. 3.3. Therefore, r_+ and r_- are complex and generally different one from the other.

However, to simplify the calculations of the integrals in Eqs. (D.15a) and (D.15b), we assume that any real refractive index perturbation, if present, is spatially uniform and limited to the active region. Under this assumption, from Eq. (3.19) in Sec. 3.3 one finds

$$\kappa_{\mathrm{FF}} = \left(\frac{\omega_s}{c}\right) S\left[i\left(n_i - i\Delta n_b\right)\right]\Gamma_{\mathrm{FF}} \tag{D.20a}$$

$$\kappa_{\mathrm{FB}} = \left(\frac{\omega_s}{c}\right) S\left[i\left(n_i - i\Delta n_b\right)\right]\Gamma_{\mathrm{FB}} \tag{D.20b}$$

$$\kappa_{\mathrm{BF}} = \left(\frac{\omega_s}{c}\right) S\left[i\left(n_i - i\Delta n_b\right)\right]\Gamma_{\mathrm{BF}} \tag{D.20c}$$

Here, S is the slow-down factor and Δn_b is the real refractive index perturbation. This term accounts for refractive index variations induced by carrier density (via the linewidth enhancement factor) and/or due to different reasons, such as structural or thermal tuning. Since Γ_{FB} is the complex conjugate of Γ_{BF}, one finds

$$|r_+| = |r_-| \tag{D.21}$$

In addition, since Γ_{FB} is approximately real (see Eq. (D.16)), one also finds

$$\phi_+ \approx \phi_- \tag{D.22}$$

with ϕ_+ (ϕ_-) denoting the phase of r_+ (r_-).

Boundary and oscillation conditions

To link $\tilde{F}$ and $\tilde{B}$ in Eqs. (D.17a) and (D.17b), we make us of the right mirror boundary condition. To illustrate this condition, we recall by Fig. D.2 the block diagram of the active cavity discussed in Sec. 4.3.1. $\underline{\underline{T_L}}$ ($\underline{\underline{T_R}}$) is the left (right) mirror transmission matrix in the basis of the Bloch modes of the *reference* waveguide. The left and right mirror reflection coefficient are r_L and r_R respectively. For a detailed discussion on the

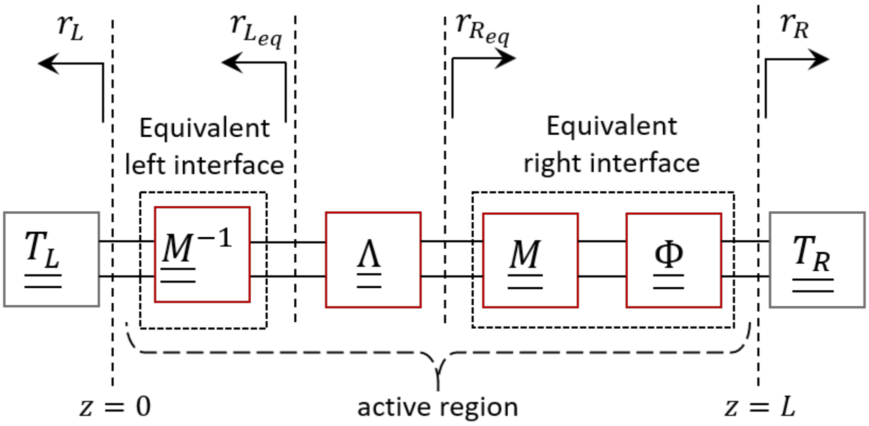

Figure D.2: Block diagram of a photonic crystal laser with slow-light and gain-induced distributed coupling.

group of blocks denoted by ”active region”, we refer to Sec. C.3. Here, it is sufficient to know that $\underline{\underline{\Lambda}}$ is the transmission matrix in the basis of the Bloch modes of the *active* waveguide. Owing to the gain-induced distributed feeback associated with slow-light, equivalent dielectric interfaces originate at the left- and right-hand side of the active region. These interfaces account for the mismatch between the Bloch modes of the active waveguide and those of the reference waveguide. As a result, the Bloch modes of the active waveguide experience an *equivalent* right (left) mirror reflection coefficient $r_{R_{eq}}$ ($r_{L_{eq}}$). Thus, the boundary condition at the equivalent right mirror is

$$\tilde{B}\left[e^{-i\left(\beta_{\text{eff}}-\frac{\pi}{a}\right)L}\,e^{-\frac{1}{2}g_{\text{eff}}L}\right]=\tilde{F}\left[e^{+i\left(\beta_{\text{eff}}-\frac{\pi}{a}\right)L}\,e^{+\frac{1}{2}g_{\text{eff}}L}\right]r_{R_{eq}} \tag{D.23}$$

We conveniently recast this condition as

$$\tilde{B}=\tilde{F}\left[e^{+2i\left(\beta_{\text{eff}}-\frac{\pi}{a}\right)L}\,e^{+g_{\text{eff}}L}\right]r_{R_{eq}} \tag{D.24}$$

which is equivalent to Eq. (4.3a) in Sec. 4.2 under the assumption of L/a being an integer. As explained therein, we make indeed this assumption and embed any possible deviation into the phase of r_L and r_R. The integrals in Eqs. (D.15a) and (D.15b) must be evaluated at the lasing threshold. Therefore, in addition to Eq. (D.24), we need the laser oscillation condition. As derived in Sec. 4.2, this is given by

$$g_{\text{eff}}=\frac{1}{L}\ln\left(\frac{1}{|r_{L_{eq}}||r_{R_{eq}}|}\right) \tag{D.25a}$$

$$2\left(\beta_{\text{eff}}-\frac{\pi}{a}\right)L+\phi_{L_{eq}}+\phi_{R_{eq}}=2\pi m \tag{D.25b}$$

where $\phi_{L_{eq}}$ ($\phi_{R_{eq}}$) is the phase of $r_{L_{eq}}$ ($r_{R_{eq}}$) and m is an integer. We conveniently recast Eq. (D.25a) as

$$e^{g_{\text{eff}}L} = \frac{1}{|r_{L_{eq}}||r_{R_{eq}}|} \tag{D.26}$$

which will turn out to be useful in the computations below.

Computation of the integral I'

Having introduced the necessary ingredients, we can now proceed to compute the integral I' in Eq. (D.15a). To simplify the notation, we recal from Eq. (3.36) in Sec. 3.5 the effective detuning

$$\delta_{\text{eff}} = -\left(\beta_{\text{eff}} - \frac{\pi}{a}\right) \tag{D.27}$$

From Eq. (D.17a), the squared magnitude of $c_+(z)$ reads

$$|c_+(z)|^2 = |\tilde{F}|^2\, e^{g_{\text{eff}}z} + |r_-|^2|\tilde{B}|^2\, e^{-g_{\text{eff}}z} + 2\mathrm{Re}\left\{\tilde{F}\tilde{B}^*\, r_-^*\, e^{-2i\delta_{\text{eff}}z}\right\} \tag{D.28}$$

By inserting the boundary condition from Eq. (D.24), one finds

$$\begin{aligned} |c_+(z)|^2 = |\tilde{F}|^2 \Big\{ & e^{+g_{\text{eff}}z} + |r_-|^2|r_{R_{eq}}|^2\, e^{-g_{\text{eff}}(z-2L)} \\ & +2|r_-||r_{R_{eq}}|e^{+g_{\text{eff}}L}\, \cos\left[-2\delta_{\text{eff}}\,(z-L) - \phi_{R_{eq}} - \phi_-\right]\Big\} \end{aligned} \tag{D.29}$$

Similarly, from Eq. (D.17b) the squared magnitude of $c_-(z)$ reads

$$|c_-(z)|^2 = |r_+|^2|\tilde{F}|^2\, e^{g_{\text{eff}}z} + |\tilde{B}|^2\, e^{-g_{\text{eff}}z} + 2\mathrm{Re}\left\{\tilde{F}\tilde{B}^*\, r_+\, e^{-2i\delta_{\text{eff}}z}\right\} \tag{D.30}$$

which, by using Eq. (D.24), becomes

$$\begin{aligned} |c_-(z)|^2 = |\tilde{F}|^2 \Big\{ & |r_+|^2\, e^{+g_{\text{eff}}z} + |r_{R_{eq}}|^2\, e^{-g_{\text{eff}}(z-2L)} \\ & +2|r_+||r_{R_{eq}}|e^{+g_{\text{eff}}L}\, \cos\left[-2\delta_{\text{eff}}\,(z-L) - \phi_{R_{eq}} + \phi_+\right]\Big\} \end{aligned} \tag{D.31}$$

In the following, computations are carried out step by step. If not interested in these detailed steps, the reader may directly move on to the result.

Exponential terms

In the following, we compute the contribution to the integral I' due to those terms in Eqs. (D.29) and (D.31) which depend exponentially on z

$$\begin{aligned} \mathrm{I}'_{\text{exp}} &= |\tilde{F}|^2\Gamma_{\text{FF}} \int_0^L \left[\left(1+|r_+|^2\right) e^{+g_{\text{eff}}z} + \left(1+|r_-|^2\right)|r_{R_{eq}}|^2\, e^{-g_{\text{eff}}(z-2L)}\right] dz \\ &= |\tilde{F}|^2\Gamma_{\text{FF}}\left(1+|r_\pm|^2\right) \int_0^L \left[e^{+g_{\text{eff}}z} + |r_{R_{eq}}|^2\, e^{-g_{\text{eff}}(z-2L)}\right] dz \end{aligned} \tag{D.32}$$

with Eq. (D.21) being used in the second line. By employing the integrals

$$\int_0^L e^{+g_{\text{eff}} z}\, dz = \left(e^{+g_{\text{eff}} L} - 1\right)/g_{\text{eff}} \tag{D.33a}$$

$$\int_0^L e^{-g_{\text{eff}}(z-2L)}\, dz = e^{+g_{\text{eff}} L}\left(e^{+g_{\text{eff}} L} - 1\right)/g_{\text{eff}} \tag{D.33b}$$

we further develop Eq. (D.32) into

$$\begin{aligned} \mathrm{I}'_{\text{exp}} &= |\tilde{F}|^2 \Gamma_{\text{FF}} \left(1 + |r_\pm|^2\right) \left[\left(e^{+g_{\text{eff}} L} - 1\right) + |r_{R_{eq}}|^2 e^{+g_{\text{eff}} L}\left(e^{+g_{\text{eff}} L} - 1\right)\right]/g_{\text{eff}} \\ &= |\tilde{F}|^2 \Gamma_{\text{FF}} \left(1 + |r_\pm|^2\right)\left(e^{+g_{\text{eff}} L} - 1\right)\left[1 + |r_{R_{eq}}|^2 e^{+g_{\text{eff}} L}\right]/g_{\text{eff}} \end{aligned} \tag{D.34}$$

Finally, by exploiting Eq. (D.26), we obtain

$$\mathrm{I}'_{\text{exp}} = |\tilde{F}|^2 \Gamma_{\text{FF}} \frac{\left(1 + |r_\pm|^2\right)\left(1 - |r_{L_{eq}}||r_{R_{eq}}|\right)\left(|r_{L_{eq}}| + |r_{R_{eq}}|\right)}{g_{\text{eff}} |r_{R_{eq}}||r_{L_{eq}}|^2} \tag{D.35}$$

Cosinusoidal terms

In the following, we compute the contribution to the integral I′ due to those terms in Eqs. (D.29) and (D.31) which depend cosinusoidally on z

$$\begin{aligned} \mathrm{I}'_{\cos} &= 2|\tilde{F}|^2 \Gamma_{\text{FF}} |r_\pm||r_{R_{eq}}|\, e^{+g_{\text{eff}} L} \left\{\int_0^L \cos\left[-2\delta_{\text{eff}}(z - L) - \phi_{R_{eq}} - \phi_-\right] dz \right. \\ &\left. + \int_0^L \cos\left[-2\delta_{\text{eff}}(z - L) - \phi_{R_{eq}} + \phi_+\right] dz \right\} \end{aligned} \tag{D.36}$$

Firstly, we compute the integral

$$\int_0^L \cos\left[-2\delta_{\text{eff}}(z - L) - \phi_{R_{eq}} + \phi\right] dz = \frac{\sin\left(-\phi_{R_{eq}} + \phi\right) - \sin\left(\phi_{L_{eq}} + \phi\right)}{-2\delta_{\text{eff}}} \tag{D.37}$$

where we have exploited Eq. (D.25b). Then, by using this integral, as well as Eq. (D.26), we further develop Eq. (D.36) into

$$\begin{aligned} \mathrm{I}'_{\cos} &= |\tilde{F}|^2 \Gamma_{\text{FF}} \frac{|r_\pm|}{-|r_{L_{eq}}|\delta_{\text{eff}}} \left[\sin\left(-\phi_{R_{eq}} - \phi_-\right) - \sin\left(\phi_{L_{eq}} - \phi_-\right) \right. \\ &\left. + \sin\left(-\phi_{R_{eq}} + \phi_+\right) - \sin\left(\phi_{L_{eq}} + \phi_+\right)\right] \end{aligned} \tag{D.38}$$

This result may be further simplified by recalling that $\phi_+ \approx \phi_-$ (see Eq.(D.22)). Thus, by denoting ϕ_+ and ϕ_- by $\phi_\pm$, one finds

$$\mathrm{I}'_{\cos} \approx 2|\tilde{F}|^2 \Gamma_{\text{FF}} \frac{|r_\pm| \cos\left(\phi_\pm\right)\left[\sin\left(\phi_{L_{eq}}\right) + \sin\left(\phi_{R_{eq}}\right)\right]}{|r_{L_{eq}}|\delta_{\text{eff}}} \tag{D.39}$$

Result

The integral I′ to be used in Eq. (D.14) is

$$\mathrm{I}' = \Gamma_{\mathrm{FF}} \int_0^L \left[|c_+(z)|^2 + |c_-(z)|^2 \right] dz = \mathrm{I}'_{\exp} + \mathrm{I}'_{\cos} \tag{D.40}$$

Here, $\mathrm{I}'_{\exp}$ ($\mathrm{I}'_{\cos}$) reflects those terms in the expressions of $|c_+(z)|^2$ and $|c_-(z)|^2$ which depend exponentially (cosinusoidally) on z. $\mathrm{I}'_{\exp}$ and $\mathrm{I}'_{\cos}$ are given by Eqs. (D.35) and (D.39) respectively.

Computation of the integral I''

In the following, we are interested in computing the integral I′′ in Eq. (D.15b). From Eqs. (D.17a) and (D.17b), one finds

$$\begin{aligned} c_+^*(z)c_-(z) = e^{-i\frac{2\pi}{a}z} \Big(& r_+ |\tilde{F}|\, e^{+g_{\mathrm{eff}}z} + r_-^* |\tilde{B}|^2\, e^{-g_{\mathrm{eff}}z} \\ & + \tilde{F}^* \tilde{B}\, e^{+2i\delta_{\mathrm{eff}}z} + r_-^* \tilde{B}^* r_+ \tilde{F}\, e^{-2i\delta_{\mathrm{eff}}z} \Big) \end{aligned} \tag{D.41}$$

By inserting the boundary condition from Eq. (D.24), we obtain

$$\begin{aligned} c_+^*(z)c_-(z) = e^{-i\frac{2\pi}{a}z} |\tilde{F}|^2 \Big[& r_+\, e^{+g_{\mathrm{eff}}z} + r_-^* |r_{R_{eq}}|^2\, e^{-g_{\mathrm{eff}}(z-2L)} \\ & + r_{R_{eq}}\, e^{+2i\delta_{\mathrm{eff}}(z-L)} e^{+g_{\mathrm{eff}}L} + r_-^* r_+ r_{R_{eq}}^*\, e^{-2i\delta_{\mathrm{eff}}(z-L)} e^{+g_{\mathrm{eff}}L} \Big] \end{aligned} \tag{D.42}$$

In the following, computations are carried out step by step. If not interested in these detailed steps, the reader may directly move on to the result.

Exponential terms

In the following, we compute the contribution to the integral I′′ due to those terms in Eq. (D.42) whose dependence on z is governed by exponentials with real argument

$$\mathrm{I}''_{\exp} = 2|\tilde{F}|^2 \mathrm{Re} \left\{ \Gamma_{\mathrm{FB}} \left[r_+ \int_0^L e^{+g_{\mathrm{eff}}z}\, dz + r_-^* |r_{R_{eq}}|^2 \int_0^L e^{-g_{\mathrm{eff}}(z-2L)}\, dz \right] \right\} \tag{D.43}$$

By exploiting the integrals from Eqs. (D.33a) and (D.33b), we obtain

$$\begin{aligned} \mathrm{I}''_{\exp} &= 2|\tilde{F}|^2 \mathrm{Re} \left\{ \Gamma_{\mathrm{FB}} \left[r_+ \left(e^{+g_{\mathrm{eff}}L} - 1 \right) + r_-^* |r_{R_{eq}}|^2 e^{+g_{\mathrm{eff}}L} \left(e^{+g_{\mathrm{eff}}L} - 1 \right) \right] / g_{\mathrm{eff}} \right\} \\ &= 2|\tilde{F}|^2 \frac{\left(e^{+g_{\mathrm{eff}}L} - 1 \right)}{g_{\mathrm{eff}}} \mathrm{Re} \left\{ \Gamma_{\mathrm{FB}} \left(r_+ + r_-^* |r_{R_{eq}}|^2 e^{+g_{\mathrm{eff}}L} \right) \right\} \end{aligned} \tag{D.44}$$

By using Eq. (D.26), we further develop Eq. (D.44) into

$$\begin{aligned}
\mathrm{I}''_{\mathrm{exp}} &= 2|\tilde{F}|^2 \frac{1-|r_{L_{eq}}||r_{R_{eq}}|}{|r_{R_{eq}}||r_{L_{eq}}|g_{\mathrm{eff}}} \mathrm{Re}\left\{ \Gamma_{\mathrm{FB}} \left(r_+ + r_-^* \frac{|r_{R_{eq}}|}{|r_{L_{eq}}|} \right) \right\} \\
&= 2|\tilde{F}|^2 \frac{1-|r_{L_{eq}}||r_{R_{eq}}|}{|r_{R_{eq}}||r_{L_{eq}}|g_{\mathrm{eff}}} |\Gamma_{\mathrm{FB}}||r_\pm| \mathrm{Re}\left\{ e^{+i\phi_{\mathrm{FB}}} \left(e^{+i\phi_+} + e^{-i\phi_-} \frac{|r_{R_{eq}}|}{|r_{L_{eq}}|} \right) \right\}
\end{aligned} \tag{D.45}$$

where ϕ_{FB} denotes the phase of Γ_{FB}. Finally, by further step, one finds

$$\mathrm{I}''_{\mathrm{exp}} = 2|\tilde{F}|^2 |\Gamma_{\mathrm{FB}}| \frac{|r_\pm| \left(1-|r_{L_{eq}}||r_{R_{eq}}|\right) \left[|r_{L_{eq}}| \cos\left(\phi_{\mathrm{FB}} + \phi_+\right) + |r_{R_{eq}}| \cos\left(\phi_{\mathrm{FB}} - \phi_-\right) \right]}{g_{\mathrm{eff}} |r_{R_{eq}}||r_{L_{eq}}|^2} \tag{D.46}$$

This result may be further simplified by recalling that the phase of Γ_{FB} is approximately equal to $-\pi$ (see Eq. (D.16)) and that ϕ_+ is approximately equal to ϕ_- (see Eq. (D.22)). Thus, one finds

$$\mathrm{I}''_{\mathrm{exp}} \approx -2|\tilde{F}|^2 |\Gamma_{\mathrm{FB}}| \frac{|r_\pm| \cos\left(\phi_\pm\right) \left(1-|r_{L_{eq}}||r_{R_{eq}}|\right) \left(|r_{L_{eq}}| + |r_{R_{eq}}|\right)}{g_{\mathrm{eff}} |r_{R_{eq}}||r_{L_{eq}}|^2} \tag{D.47}$$

Cosinusoidal terms

In the following, we compute the contribution to the integral I'' due to those terms in Eq. (D.42) whose dependence on z is governed by exponentials with imaginary argument

$$\begin{aligned}
\mathrm{I}''_{\cos} = 2|\tilde{F}|^2\, e^{+g_{\mathrm{eff}}L} \mathrm{Re}\left\{ \Gamma_{\mathrm{FB}} \left[r_{R_{eq}} \int_0^L e^{+2i\delta_{\mathrm{eff}}(z-L)}\, dz \right.\right. \\
\left.\left. + r_-^* r_+ r_{R_{eq}}^* \int_0^L e^{-2i\delta_{\mathrm{eff}}(z-L)}\, dz \right] \right\}
\end{aligned} \tag{D.48}$$

The equation can be recast as

$$\begin{aligned}
\mathrm{I}''_{\cos} = 2|\tilde{F}|^2 |\Gamma_{\mathrm{FB}}||r_{R_{eq}}|\, e^{+g_{\mathrm{eff}}L} \left\{ \int_0^L \cos\left[+2\delta_{\mathrm{eff}}(z-L) + \phi_{\mathrm{FB}} + \phi_{R_{eq}} \right] dz \right. \\
\left. + |r_\pm|^2 \int_0^L \cos\left[-2\delta_{\mathrm{eff}}(z-L) + \phi_{\mathrm{FB}} - \phi_{R_{eq}} + \phi_+ - \phi_- \right] dz \right\}
\end{aligned} \tag{D.49}$$

where ϕ_{FB} denotes the phase of Γ_{FB}. To simplify the final result, we recall that $\phi_{\mathrm{FB}} \approx -\pi$ (see Eq. (D.16)) and that $\phi_+ \approx \phi_-$ (see Eq. (D.22)). Therefore, we may write

$$\begin{aligned}\mathrm{I}''_{\cos} &\approx -2|\tilde{F}|^2|\Gamma_{\mathrm{FB}}||r_{R_{eq}}|\, e^{+g_{\mathrm{eff}}L} \left\{ \int_0^L \cos\left[+2\delta_{\mathrm{eff}}(z-L)+\phi_{R_{eq}}\right] dz \right. \\ &\quad \left. + |r_\pm|^2 \int_0^L \cos\left[-2\delta_{\mathrm{eff}}(z-L)-\phi_{R_{eq}}\right] dz \right\} \\ &= -2|\tilde{F}|^2|\Gamma_{\mathrm{FB}}||r_{R_{eq}}| \left(1+|r_\pm|^2\right) \, e^{+g_{\mathrm{eff}}L} \int_0^L \cos\left[-2\delta_{\mathrm{eff}}(z-L)-\phi_{R_{eq}}\right] dz\end{aligned} \tag{D.50}$$

By using the integral from Eq. (D.37), as well as Eq. (D.26), one finally finds

$$\mathrm{I}''_{\cos} \approx -|\tilde{F}|^2|\Gamma_{\mathrm{FB}}| \frac{\left(1+|r_\pm|^2\right)\left[\sin\left(\phi_{L_{eq}}\right)+\sin\left(\phi_{R_{eq}}\right)\right]}{|r_{L_{eq}}|\delta_{\mathrm{eff}}} \tag{D.51}$$

Result

The integral I'' to be used in Eq. (D.14) is

$$\mathrm{I}'' = 2\mathrm{Re}\left\{ \Gamma_{\mathrm{FB}} \int_0^L c_+^*(z)c_-(z)\, e^{+i\frac{2\pi}{a}z}\, dz \right\} = \mathrm{I}''_{\exp} + \mathrm{I}''_{\cos} \tag{D.52}$$

Here, $\mathrm{I}''_{\exp}$ ($\mathrm{I}''_{\cos}$) reflects those terms in the expression of $c_+^*(z)c_-(z)$ whose dependence on z is governed by exponentials with real (imaginary) argument. $\mathrm{I}''_{\exp}$ and $\mathrm{I}''_{\cos}$ are given by Eqs. (D.47) and (D.51) respectively.

Forward field at the right mirror

As seen above, I' and I'' in Eq. (D.14) are proportional to $|\tilde{F}|^2$. The amplitude of the forward-propagating electric field on the left-hand side of the right mirror ($z = L$ in Fig. D.2) is

$$\mathscr{E}^+_{\omega_s}(L,t) = \mathrm{Re}\left\{c_+(L)e^{-i\omega_s t}\right\} = \frac{1}{2}c_+(L)e^{-i\omega_s t} + c.c. \tag{D.53}$$

In the following, we define the complex field

$$\mathscr{A}^+_{\omega_s} = \frac{1}{2}c_+(L) \tag{D.54}$$

We are interested in relating $|\mathscr{A}^+_{\omega_s}|^2$ to $|\tilde{F}|^2$. For this purpose, from Eq.(D.29) we obtain

$$\begin{aligned}|c_+(L)|^2 &= |\tilde{F}|^2\, e^{+g_{\mathrm{eff}}L}\left[1+|r_-|^2|r_{R_{eq}}|^2+2|r_-||r_{R_{eq}}|\cos\left(\phi_{R_{eq}}+\phi_-\right)\right] \\ &= |\tilde{F}|^2\, e^{+g_{\mathrm{eff}}L}\left|1+r_{R_{eq}}r_-\right|^2 = |\tilde{F}|^2\frac{\left|1+r_{R_{eq}}r_-\right|^2}{|r_{L_{eq}}||r_{R_{eq}}|}\end{aligned} \tag{D.55}$$

with Eq. (D.26) being used in the last step. Finally, by combining Eqs. (D.55) and (D.54), one finds

$$|\tilde{F}|^2 = \frac{4|r_{L_{eq}}||r_{R_{eq}}|}{\left|1 + r_{R_{eq}} r_-\right|^2} \left|\mathscr{A}^+_{\omega_s}\right|^2 \tag{D.56}$$

Global stimulated emission rate

We are ready to derive the global stimulated emission rate to be used in the rate equation model presented in Chapter 5. By inserting Eqs. (D.40) and (D.52) into Eq. (D.14) and employing the expression of $|\tilde{F}|^2$ from Eq. (D.56), we obtain

$$R_{\mathrm{st}} = \frac{8W_e}{\hbar\omega_s} \left(\frac{c}{n_{\mathrm{slab}}}\right) \Gamma_y g_{\mathrm{mat}} \frac{\left(\xi_{\mathrm{exp}} + \xi_{\mathrm{cos}}\right)}{a} \left|\mathscr{A}^+_{\omega_s}\right|^2 \tag{D.57}$$

Here, ξ_{exp} is given by

$$\begin{aligned}\xi_{\mathrm{exp}} &= \frac{|r_{L_{eq}}||r_{R_{eq}}|}{\left|1 + r_{R_{eq}} r_-\right|^2} \left(\mathrm{I}'_{\mathrm{exp}} + \mathrm{I}''_{\mathrm{exp}}\right) \\ &= \Gamma_{\mathrm{FF}} \left[1 + |r_\pm|^2 - 2\frac{|\Gamma_{\mathrm{FB}}|}{\Gamma_{\mathrm{FF}}} |r_\pm| \cos\left(\phi_\pm\right)\right] \frac{\left(1 - |r_{L_{eq}}||r_{R_{eq}}|\right)\left(|r_{L_{eq}}| + |r_{R_{eq}}|\right)}{g_{\mathrm{eff}} |r_{L_{eq}}| \left|1 + r_{R_{eq}} r_-\right|^2}\end{aligned} \tag{D.58}$$

while ξ_{cos} reads

$$\begin{aligned}\xi_{\mathrm{cos}} &= \frac{|r_{L_{eq}}||r_{R_{eq}}|}{\left|1 + r_{R_{eq}} r_-\right|^2} \left(\mathrm{I}'_{\mathrm{cos}} + \mathrm{I}''_{\mathrm{cos}}\right) \\ &= \Gamma_{\mathrm{FF}} \left[2|r_\pm| \cos\left(\phi_\pm\right) - \frac{|\Gamma_{\mathrm{FB}}|}{\Gamma_{\mathrm{FF}}} \left(1 + |r_\pm|^2\right)\right] \frac{|r_{R_{eq}}| \left[\sin\left(\phi_{L_{eq}}\right) + \sin\left(\phi_{R_{eq}}\right)\right]}{\delta_{\mathrm{eff}} \left|1 + r_{R_{eq}} r_-\right|^2}\end{aligned} \tag{D.59}$$

Strictly speaking, Eq. (D.57) only applies in the continuous wave limit, i.e. for time-harmonic fields oscillating at the lasing angular frequency ω_s (see Eqs.(D.1) and (D.53)). However, it is common practice [167] to extend its application to the case of fields with a slowly-varying time-domain envelope

$$\mathscr{E}^+(L, t) = \mathscr{A}^+(t)\, e^{-i\omega_s t} + c.c. \tag{D.60}$$

Therefore, we may replace $\mathscr{A}^{+}_{\omega_s}$ with the slowly-varying envelope $\mathscr{A}^{+}(t)$ and let the material gain vary with time. By assuming the material gain to be linear with the time-dependent carrier density $N(t)$, the global stimulated emission rate becomes

$$R_{\mathrm{st}}(t) = \frac{8W_e}{\hbar\omega_s}\left(\frac{c}{n_{\mathrm{slab}}}\right)\Gamma_y g_N\left[N(t) - N_{\mathrm{tr}}\right]\frac{\left(\xi_{\mathrm{exp}} + \xi_{\mathrm{cos}}\right)}{a}\left|\mathscr{A}^{+}(t)\right|^2 \tag{D.61}$$

where g_N is the differential gain and N_{tr} the transparency carrier density. As already mentioned, this rate corresponds to the average number of photons generated per unit time inside the laser.

Without gain-induced distributed feedback

It is instructive to derive Eq. (D.61) in the absence of gain-induced distributed feedback associated with slow-light.

In this limiting case, one finds $\Gamma_{\mathrm{FB}} = 0$, implying $r_{\pm} = 0$ (see Eqs. (D.19a) and (D.19b)). Therefore, ξ_{cos} is identically equal to zero. On the other hand, $r_{\pm} = 0$ implies that $r_{L_{eq}}$ and $r_{R_{eq}}$ are reduced, respectively, to r_L and r_R (see Eqs. (4.9) and (4.10) in Sec. 4.3.1). In fact, in the absence of distributed feedback the equivalent dielectric interfaces in Fig. D.2 simply disappear. Thus, ξ_{exp} is reduced to

$$\xi_{\mathrm{exp}} = \Gamma_{\mathrm{FF}}\frac{\left(1 - |r_L||r_R|\right)\left(|r_L| + |r_R|\right)}{g_{\mathrm{eff}}|r_L|} \tag{D.62}$$

Without distributed feedback, the effective net modal gain reads

$$g_{\mathrm{eff}} = S\left(\Gamma_{\mathrm{FF}}\Gamma_y g_{\mathrm{mat}_s} - \alpha_1\right) \tag{D.63}$$

with the disorder-induced backscattering loss being neglected. Here, $S = n_g/n_{\mathrm{slab}}$ is the slow-down factor, with n_g being the group index. g_{mat_s} is the material gain at the lasing threshold, while α_1 accounts for the disorder-induced loss due to coupling with radiation modes [117]. It is convenient to introduce the quantity

$$\begin{aligned}\Phi(t) &= \frac{8W_e}{\hbar\omega_s}\frac{S}{\Gamma_{\mathrm{FF}}}\frac{\xi}{a}\left|\mathscr{A}^{+}(t)\right|^2 \\ &= \frac{1}{2}\frac{1}{\hbar\omega_s}\frac{\left(1 - |r_L||r_R|\right)\left(|r_L| + |r_R|\right)}{a\,|r_L|\left(\Gamma_{\mathrm{FF}}\Gamma_y g_{\mathrm{mat}_s} - \alpha_1\right)}\left|\mathscr{A}^{+}(t)\right|^2\int_V \epsilon_0 n_b^2(\mathbf{r})|\mathbf{e}_{\pm}(\mathbf{r})|^2\,dV\end{aligned} \tag{D.64}$$

With this definition, the global stimulated emission rate from Eq. (D.61) is reduced to

$$R_{\mathrm{st}}(t) = \left(\frac{c}{n_g}\right)\Gamma_{\mathrm{FF}}\Gamma_y g_N\left[N(t) - N_{\mathrm{tr}}\right]\Phi(t) \tag{D.65}$$

Formally, this is the familiar expression of the stimulated emission rate employed in conventional rate equation models [23], with $\Phi(t)$ clearly playing the role of the photon number. Furthermore, the total optical confinement factor is $\Gamma_{\mathrm{FF}}\Gamma_y$. In order to exactly mimic the formulation of [23], we may define the mode volume

$$V_\Phi = \frac{V_{\mathrm{act}}}{\Gamma_{\mathrm{FF}}\Gamma_y} \tag{D.66}$$

and introduce the normalized stimulated emission rate

$$\bar{R}_{\mathrm{st}}(t) = \frac{R_{\mathrm{st}}(t)}{V_{\mathrm{act}}} = \left(\frac{c}{n_g}\right) g_N \left[N(t) - N_{\mathrm{tr}}\right] \frac{\Phi(t)}{V_\Phi} \tag{D.67}$$

with $\Phi(t)/V_\Phi$ being the photon density. $\bar{R}_{\mathrm{st}}(t)$ is the average number of carriers per unit time undergoing stimulated recombination, normalized to the active region volume V_{act}.

Bibliography

[1] A. Sugitatsu and S. Noda. "Room temperature operation of 2D photonic crystal slab defect-waveguide laser with optical pump." English. In: *Electronics Letters* 39 (2 Jan. 2003), 213–215(2). ISSN: 0013-5194. DOI: 10.1049/el:20030097.

[2] Yoshihiro Akahane et al. "Fine-tuned high-Q photonic-crystal nanocavity." In: *Opt. Express* 13.4 (Feb. 2005), pp. 1202–1214. DOI: 10.1364/OPEX.13.001202.

[3] Yoshihiro Akahane et al. "High-Q photonic nanocavity in a two-dimensional photonic crystal." In: *Nature* 425.6961 (2003), pp. 944–947. DOI: 10.1038/nature02063.

[4] Yariv Amnon and Pocji Yeh. *Photonics : Optical Electronics In Modern Communications*. 6th ed. New York: Oxford University Press, 2007.

[5] Anders Andrae and Tomas Edler. "On Global Electricity Usage of Communication Technology: Trends to 2030." In: *Challenges* 6.1 (Apr. 2015), pp. 117–157. DOI: 10.3390/challe6010117.

[6] CL Andre et al. "Impact of dislocations on minority carrier electron and hole lifetimes in GaAs grown on metamorphic SiGe substrates." In: *Applied physics letters* 84.18 (2004), pp. 3447–3449. DOI: 10.1063/1.1736318.

[7] T. Asano et al. "Ultrahigh-Q Nanocavities in Two-Dimensional Photonic Crystal Slabs." In: *IEEE Journal of Selected Topics in Quantum Electronics* 12.6 (2006), pp. 1123–1134. DOI: 10.1109/JSTQE.2006.881639.

[8] N. W. Ashcroft and N. D. Mermin. *Solid State Physics*. Brooks/Cole, 1976.

[9] Toshihiko Baba. "Slow light in photonic crystals." In: *Nature Photonics* 2.8 (2008). DOI: 10.1038/nphoton.2008.146.

[10] Dagmawi Bekele et al. "In-Plane Photonic Crystal Devices using Fano Resonances." In: *Laser & Photonics Reviews* 13.12 (2019), p. 1900054. DOI: 10.1002/lpor.201900054.

[11] B. Ben Bakir et al. "Surface-emitting microlaser combining two-dimensional photonic crystal membrane and vertical Bragg mirror." In: *Applied Physics Letters* 88.8 (2006), p. 081113. DOI: 10.1063/1.2172730.

[12] H. Benisty et al. “From modal control to spontaneous emission and gain in photonic crystal waveguides.” In: *Photonics and Nanostructures - Fundamentals and Applications* 4.1 (2006), pp. 1–11. ISSN: 1569-4410. DOI: `10.1016/j.photonics.2005.10.002`.

[13] Robert W. Boyd and Daniel J. Gauthier. “Controlling the Velocity of Light Pulses.” In: *Science* 326.5956 (2009), pp. 1074–1077. ISSN: 0036-8075. DOI: `10.1126/science.1170885`.

[14] M. Buffolo et al. “Investigation of Current-Driven Degradation of 1.3 μm Quantum-Dot Lasers Epitaxially Grown on Silicon.” In: *IEEE Journal of Selected Topics in Quantum Electronics* 26.2 (Mar. 2020), pp. 1–8. ISSN: 1558-4542. DOI: `10.1109/JSTQE.2019.2939519`.

[15] William Cartar, Jesper Mørk, and Stephen Hughes. “Self-consistent Maxwell-Bloch model of quantum-dot photonic-crystal-cavity lasers.” In: *Phys. Rev. A* 96 (2 Aug. 2017), p. 023859. DOI: `10.1103/PhysRevA.96.023859`.

[16] A. P. Cédola et al. “Physics-Based Modeling and Experimental Study of Si-Doped InAs/GaAs Quantum Dot Solar Cells.” In: *International Journal of Photoenergy* 2018 (2018). DOI: `10.1155/2018/721584`.

[17] Siming Chen et al. “Electrically pumped continuous-wave III–V quantum dot lasers on silicon.” In: *Nature Photonics* 10.5 (2016), pp. 307–311. ISSN: 1749-4893. DOI: `10.1038/nphoton.2016.21`.

[18] Yaohui Chen and Jesper Mørk. “Theory of carrier depletion and light amplification in active slow light photonic crystal waveguides.” In: *Opt. Express* 21.24 (Dec. 2013), pp. 29392–29400. DOI: `10.1364/OE.21.029392`.

[19] Yaohui Chen et al. “Impact of slow-light enhancement on optical propagation in active semiconductor photonic-crystal waveguides.” In: *Phys. Rev. A* 92 (5 2015), p. 053839. DOI: `10.1103/PhysRevA.92.053839`.

[20] E. Chow et al. “Ultracompact biochemical sensor built with two-dimensional photonic crystal microcavity.” In: *Opt. Lett.* 29.10 (May 2004), pp. 1093–1095. DOI: `10.1364/OL.29.001093`.

[21] Weng W. Chow and Frank Jahnke. “On the physics of semiconductor quantum dots for applications in lasers and quantum optics.” In: *Progress in Quantum Electronics* 37.3 (2013), pp. 109–184. ISSN: 0079-6727. DOI: `10.1016/j.pquantelec.2013.04.001`.

[22] *Cisco Visual Networking Index: Forecast and Trends, 2017–2022.* Cisco, 2019.

[23] Larry A. Coldren, Scott W. Corzine, and Milan Mašanović. *Diode Lasers and Photonic Integrated Circuits.* 2nd ed. John Wiley & Sons, Inc., 2012.

[24] Guillaume Crosnier et al. "Hybrid indium phosphide-on-silicon nanolaser diode." In: *Nature Photonics* 11.5 (2017), pp. 297–300. DOI: 10.1038/nphoton.2017.56.

[25] Jonathan P. Dowling et al. "The photonic band edge laser: A new approach to gain enhancement." In: *Journal of Applied Physics* 75.4 (1994), pp. 1896–1899. DOI: 10.1063/1.356336.

[26] Jianan Duan et al. "Dynamic and nonlinear properties of epitaxial quantum dot lasers on silicon for isolator-free integration." In: *Photon. Res.* 7.11 (Nov. 2019), pp. 1222–1228. DOI: 10.1364/PRJ.7.001222.

[27] Hemant Sankar Dutta et al. "Coupling light in photonic crystal waveguides: A review." In: *Photonics and Nanostructures - Fundamentals and Applications* 20 (2016), pp. 41–58. ISSN: 1569-4410. DOI: 10.1016/j.photonics.2016.04.001.

[28] Harris Stephen E. "Electromagnetically induced transparenc." In: *Physics Today* 50.7 (1997), pp. 36–42. DOI: 10.1063/1.881806.

[29] Sara Ek et al. "Slow-light-enhanced gain in active photonic crystal waveguides." In: *Nature Communications* 5.1 (2014), p. 5039. DOI: 10.1038/ncomms6039.

[30] Bryan Ellis et al. "Ultralow-threshold electrically pumped quantum-dot photonic-crystal nanocavity laser." In: *Nature Photonics* 5.5 (2011), pp. 297–300. DOI: 10.1038/nphoton.2011.51.

[31] Shanhui Fan, Wonjoo Suh, and J. D. Joannopoulos. "Temporal coupled-mode theory for the Fano resonance in optical resonators." In: *J. Opt. Soc. Am. A* 20.3 (Mar. 2003), pp. 569–572. DOI: 10.1364/JOSAA.20.000569.

[32] U. Fano. "Effects of Configuration Interaction on Intensities and Phase Shifts." In: *Phys. Rev.* 124 (6 Dec. 1961), pp. 1866–1878. DOI: 10.1103/PhysRev.124.1866.

[33] Dimitris Fitsios and Fabrice Raineri. "Chapter Five - Photonic Crystal Lasers and Nanolasers on Silicon." In: *Silicon Photonics*. Ed. by Sebastian Lourdudoss, Ray T. Chen, and Chennupati Jagadish. Vol. 99. Semiconductors and Semimetals. Elsevier, 2018, pp. 97–137. DOI: 10.1016/bs.semsem.2018.08.003.

[34] Lars H. Frandsen et al. "Photonic crystal waveguides with semi-slow light and tailored dispersion properties." In: *Opt. Express* 14.20 (Oct. 2006), pp. 9444–9450. DOI: 10.1364/OE.14.009444.

[35] Ilya Fushman et al. "Ultrafast nonlinear optical tuning of photonic crystal cavities." In: *Applied Physics Letters* 90.9 (2007), p. 091118. DOI: 10.1063/1.2710080.

[36] G. Vecchi et al. "Photonic-crystal surface-emitting laser near 1.55 µm on gold-coated silicon wafer." English. In: *Electronics Letters* 43 (6 Mar. 2007), 343–345(2). ISSN: 0013-5194. DOI: `10.1049/el:20073816`.

[37] J. M. Gérard, O. Cabrol, and B. Sermage. "InAs quantum boxes: Highly efficient radiative traps for light emitting devices on Si." In: *Applied Physics Letters* 68.22 (1996), pp. 3123–3125. DOI: `10.1063/1.115798`.

[38] M. Gioannini. "Ground-state power quenching in two-state lasing quantum dot lasers." In: *Jornal of Applied Physics* 111 (2012), p. 043108. DOI: `10.1063/1.3682574`.

[39] M. Gioannini et al. "Simulation of Quantum Dot Solar Cells Including Carrier Intersubband Dynamics and Transport." In: *IEEE Journal of Photovoltaics* 3.4 (Oct. 2013), pp. 1271–1278. ISSN: 2156-3403. DOI: `10.1109/JPHOTOV.2013.2270345`.

[40] D. Gready and G. Eisenstein. "Carrier Dynamics and Modulation Capabilities of 1.55-μm Quantum-Dot Lasers." In: *IEEE Journal of Selected Topics in Quantum Electronics* 19.4 (July 2013), pp. 1900307–1900307. ISSN: 1558-4542. DOI: `10.1109/JSTQE.2013.2238610`.

[41] Jure Grgic et al. "Fundamental Limitations to Gain Enhancement in Periodic Media and Waveguides." In: *Phys. Rev. Lett.* 108 (18 May 2012), p. 183903. DOI: `10.1103/PhysRevLett.108.183903`.

[42] E. Haglund et al. "High-Speed VCSELs With Strong Confinement of Optical Fields and Carriers." In: *Journal of Lightwave Technology* 34.2 (2016), pp. 269–277. DOI: `10.1109/JLT.2015.2458935`.

[43] Y. Halioua et al. "Hybrid InP-based photonic crystal lasers on silicon on insulator wires." In: *Applied Physics Letters* 95.20 (2009), p. 201119. DOI: `10.1063/1.3265743`.

[44] Laurent-Daniel Haret et al. "Schottky MSM junctions for carrier depletion in silicon photonic crystal microcavities." In: *Opt. Express* 21.8 (Apr. 2013), pp. 10324–10334. DOI: `10.1364/OE.21.010324`.

[45] Lene Vestergaard Hau et al. "Light speed reduction to 17 metres per second in an ultracold atomic gas." In: *Nature* 397.6720 (1999), pp. 594–598. DOI: `10.1038/17561`.

[46] H. A. Haus and W. Huang. "Coupled-mode theory." In: *Proceedings of the IEEE* 79.10 (1991), pp. 1505–1518. DOI: `10.1109/5.104225`.

[47] K. M. Ho, C. T. Chan, and C. M. Soukoulis. "Existence of a photonic gap in periodic dielectric structures." In: *Phys. Rev. Lett.* 65 (25 Dec. 1990), pp. 3152–3155. DOI: `10.1103/PhysRevLett.65.3152`.

[48] Shuren Hu and Sharon M. Weiss. "Design of Photonic Crystal Cavities for Extreme Light Concentration." In: *ACS Photonics* 3.9 (2016), pp. 1647–1653. DOI: 10.1021/acsphotonics.6b00219.

[49] Heming Huang et al. "Analysis of the optical feedback dynamics in InAs/GaAs quantum dot lasers directly grown on silicon." In: *J. Opt. Soc. Am. B* 35.11 (Nov. 2018), pp. 2780–2787. DOI: 10.1364/JOSAB.35.002780.

[50] S. Hughes et al. "Extrinsic Optical Scattering Loss in Photonic Crystal Waveguides: Role of Fabrication Disorder and Photon Group Velocity." In: *Phys. Rev. Lett.* 94 (3 Jan. 2005), p. 033903. DOI: 10.1103/PhysRevLett.94.033903.

[51] J. P. Hugonin et al. "Coupling into slow-mode photonic crystal waveguides." In: *Opt. Lett.* 32.18 (Sept. 2007), pp. 2638–2640. DOI: 10.1364/OL.32.002638.

[52] Daisuke Inoue et al. "Directly modulated 1.3 μm quantum dot lasers epitaxially grown on silicon." In: *Opt. Express* 26.6 (Mar. 2018), pp. 7022–7033. DOI: 10.1364/OE.26.007022.

[53] John David Jackson. *Classical Electrodynamics*. 3rd ed. John Wiley & Sons, Inc., 1999.

[54] Kwang-Yong Jeong et al. "Electrically driven nanobeam laser." In: *Nature Communications* 4.1 (2013), p. 2822. DOI: 10.1038/ncomms3822.

[55] John D. Joannopoulos et al. *Photonic Crystals: Molding the Flow of Light (Second Edition)*. 2nd ed. Princeton University Press, 2008.

[56] Steven G. Johnson and J. D. Joannopoulos. "Block-iterative frequency-domain methods for Maxwell's equations in a planewave basis." In: *Opt. Express* 8.3 (Jan. 2001), pp. 173–190. DOI: 10.1364/OE.8.000173.

[57] D. Jung et al. "Highly Reliable Low-Threshold InAs Quantum Dot Lasers on On-Axis (001) Si with 87% Injection Efficiency." In: *ACS photonics* 5 (2018), p. 1094. DOI: 10.1021/acsphotonics.7b01387.

[58] Daehwan Jung et al. "High efficiency low threshold current 1.3 μm InAs quantum dot lasers on on-axis (001) GaP/Si." In: *Applied Physics Letters* 111.12 (2017), p. 122107. DOI: 10.1063/1.4993226.

[59] Daehwan Jung et al. "Impact of threading dislocation density on the lifetime of InAs quantum dot lasers on Si." In: *Applied Physics Letters* 112.15 (2018), p. 153507. DOI: 10.1063/1.5026147.

[60] Kazuaki Kiyota et al. "Various low group velocity effects in photonic crystal line defect waveguides and their demonstration by laser oscillation." In: *Applied Physics Letters* 88.20 (2006), p. 201904. DOI: 10.1063/1.2204647.

[61] W. Kobayashi et al. “50-Gb/s Direct Modulation of a 1.3-μm InGaAlAs-Based DFB Laser With a Ridge Waveguide Structure.” In: *IEEE Journal of Selected Topics in Quantum Electronics* 19.4 (2013), pp. 1500908–1500908. DOI: 10.1109/JSTQE.2013.2238509.

[62] T. Komljenovic et al. “Photonic Integrated Circuits Using Heterogeneous Integration on Silicon.” In: *Proceedings of the IEEE* 106.12 (Dec. 2018), pp. 2246–2257. ISSN: 1558-2256. DOI: 10.1109/JPROC.2018.2864668.

[63] V. V. Korenev et al. “Analytical approach to the multi-state lasing phenomenon in quantum dot lasers.” In: *Applied Physics Letters* 102 (2013), p. 112101. DOI: 10.1063/1.4795628.

[64] V. V. Korenev et al. “Effect of modulation p-doping level on multi-state lasing in InAs/InGaAs quantum dot lasers having different external loss.” In: *Applied Physics Letters* 111 (2017), p. 132103. DOI: 10.1063/1.5004268.

[65] T F Krauss. “Slow light in photonic crystal waveguides.” In: *Journal of Physics D: Applied Physics* 40.9 (Apr. 2007), pp. 2666–2670. DOI: 10.1088/0022-3727/40/9/s07.

[66] Thomas F. Krauss. “Why do we need slow light?” In: *Nature Photonics* 2.8 (2008), pp. 448–450. DOI: 10.1038/nphoton.2008.139.

[67] A. V. Krishnamoorthy et al. “Progress in Low-Power Switched Optical Interconnects.” In: *IEEE Journal of Selected Topics in Quantum Electronics* 17.2 (2011), pp. 357–376. DOI: 10.1109/JSTQE.2010.2081350.

[68] Shousaku Kubo, Daisuke Mori, and Toshihiko Baba. “Low-group-velocity and low-dispersion slow light in photonic crystal waveguides.” In: *Opt. Lett.* 32.20 (Oct. 2007), pp. 2981–2983. DOI: 10.1364/OL.32.002981.

[69] Soon-Hong Kwon et al. “Photonic bandedge lasers in two-dimensional square-lattice photonic crystal slabs.” In: *Applied Physics Letters* 83.19 (2003), pp. 3870–3872. DOI: 10.1063/1.1626004.

[70] P. Lalanne, C. Sauvan, and J.P. Hugonin. “Photon confinement in photonic crystal nanocavities.” In: *Laser & Photonics Reviews* 2.6 (2008), pp. 514–526. DOI: 10.1002/lpor.200810018.

[71] Jakob Rosenkrantz de Lasson et al. “Benchmarking five numerical simulation techniques for computing resonance wavelengths and quality factors in photonic crystal membrane line defect cavities.” In: *Opt. Express* 26.9 (Apr. 2018), pp. 11366–11392. DOI: 10.1364/OE.26.011366.

[72] N. Le Thomas et al. “Light transport regimes in slow light photonic crystal waveguides.” In: *Phys. Rev. B* 80 (12 Sept. 2009), p. 125332. DOI: 10.1103/PhysRevB.80.125332.

[73] Q. Li et al. "Development of Modulation p-Doped 1310 nm InAs/GaAs Quantum Dot Laser Materials and Ultrashort Cavity Fabry-Perot and Distributed-Feedback Laser Diodes." In: *ACS Photonics* 5 (2018), p. 1084. DOI: 10.1021/acsphotonics.7b01355.

[74] Mengya Liao et al. "III-V quantum-dot lasers monolithically grown on silicon." In: *Semiconductor Science and Technology* 33.12 (Oct. 2018), p. 123002. DOI: 10.1088/1361-6641/aae6a5.

[75] Mikhail F. Limonov et al. "Fano resonances in photonics." In: *Nature Photonics* 11.9 (2017), pp. 543–554. DOI: 10.1038/nphoton.2017.142.

[76] A. Y. Liu and J. Bowers. "Photonic Integration With Epitaxial III–V on Silicon." In: *IEEE Journal of Selected Topics in Quantum Electronics* 24.6 (Nov. 2018), pp. 1–12. ISSN: 1558-4542. DOI: 10.1109/JSTQE.2018.2854542.

[77] Alan Y. Liu et al. "Electrically pumped continuous-wave 1.3 μm quantum-dot lasers epitaxially grown on on-axis (001) GaP/Si." In: *Opt. Lett.* 42.2 (Jan. 2017), pp. 338–341. DOI: 10.1364/OL.42.000338.

[78] Alan Y. Liu et al. "Quantum dot lasers for silicon photonics." In: *Photon. Res.* 3.5 (Oct. 2015), B1–B9. DOI: 10.1364/PRJ.3.0000B1.

[79] Jia-ming Liu. *Photonic Devices.* Cambridge University Press, 2005. DOI: 10.1017/CBO9780511614255.

[80] Z. Liu et al. "Origin of defect tolerance in InAs/GaAs quantum dot lasers grown on silicon." In: *Journal of Lightwave Technology* 38.2 (2019), pp. 240–248. ISSN: 1558-2213. DOI: 10.1109/JLT.2019.2925598.

[81] B. Lombardet et al. "Bloch wave propagation in two-dimensional photonic crystals: Influence of the polarization." In: *Optical and Quantum Electronics* 37.1 (2005), pp. 293–307. DOI: 10.1007/s11082-005-1186-4.

[82] Matthew P Lumb et al. "Incorporating photon recycling into the analytical drift-diffusion model of high efficiency solar cells." In: *Journal of Applied Physics* 116.19 (2014), p. 194504. DOI: 10.1063/1.4902320.

[83] A. Markus et al. "Impact of intraband relaxation on the performance of a quantum-dot laser." In: *IEEE Journal of Selected Topics in Quantum Electronics* 9.5 (Sept. 2003), pp. 1308–1314. ISSN: 1558-4542. DOI: 10.1109/JSTQE.2003.819494.

[84] A. Markus et al. "Simultaneous two-state lasing in quantum-dot lasers." In: *Applied Physics Letters* 82.12 (2003), pp. 1818–1820. DOI: 10.1063/1.1563742.

[85] S. Matsuo et al. "Ultralow Operating Energy Electrically Driven Photonic Crystal Lasers." In: *IEEE Journal of Selected Topics in Quantum Electronics* 19.4 (2013), pp. 4900311–4900311. DOI: 10.1109/JSTQE.2013.2249048.

[86] Shinji Matsuo. "Chapter Two - Heterogeneously integrated III–V photonic devices on Si." In: *Future Directions in Silicon Photonics*. Ed. by Sebastian Lourdudoss, John E. Bowers, and Chennupati Jagadish. Vol. 101. Semiconductors and Semimetals. Elsevier, 2019, pp. 43–89. DOI: 10.1016/bs.semsem.2019.07.001.

[87] Shinji Matsuo and Takaaki Kakitsuka. "Low-operating-energy directly modulated lasers for short-distance optical interconnects." In: *Adv. Opt. Photon.* 10.3 (Sept. 2018), pp. 567–643. DOI: 10.1364/AOP.10.000567.

[88] Shinji Matsuo et al. "High-speed ultracompact buried heterostructure photonic-crystal laser with 13 fJ of energy consumed per bit transmitted." In: *Nature Photonics* 6.4 (2010), pp. 648–654. DOI: 10.1038/nphoton.2010.177.

[89] Shinji Matsuo et al. "Photonic crystal lasers using wavelength-scale embedded active region." In: *Journal of Physics D Applied Physics* 47.2 (Dec. 2013), p. 023001. DOI: 10.1088/0022-3727/47/2/023001.

[90] S. Mazoyer, J. P. Hugonin, and P. Lalanne. "Disorder-Induced Multiple Scattering in Photonic-Crystal Waveguides." In: *Phys. Rev. Lett.* 103 (6 Aug. 2009), p. 063903. DOI: 10.1103/PhysRevLett.103.063903.

[91] S. Mazoyer et al. "Statistical fluctuations of transmission in slow light photonic-crystal waveguides." In: *Opt. Express* 18.14 (July 2010), pp. 14654–14663. DOI: 10.1364/OE.18.014654.

[92] M. Meier et al. "Laser action from two-dimensional distributed feedback in photonic crystals." In: *Applied Physics Letters* 74.1 (1999), pp. 7–9. DOI: 10.1063/1.123116.

[93] Daniele Melati, Andrea Melloni, and Francesco Morichetti. "Real photonic waveguides: guiding light through imperfections." In: *Adv. Opt. Photon.* 6.2 (June 2014), pp. 156–224. DOI: 10.1364/AOP.6.000156.

[94] D. Michaelis et al. "Reciprocity theorem and perturbation theory for photonic crystal waveguides." In: *Phys. Rev. E* 68 (6 Dec. 2003), p. 065601. DOI: 10.1103/PhysRevE.68.065601.

[95] D. A. B. Miller. "Device Requirements for Optical Interconnects to Silicon Chips." In: *Proceedings of the IEEE* 97.7 (July 2009), pp. 1166–1185. ISSN: 1558-2256. DOI: 10.1109/JPROC.2009.2014298.

[96] Andrey E. Miroshnichenko, Sergej Flach, and Yuri S. Kivshar. "Fano resonances in nanoscale structures." In: *Rev. Mod. Phys.* 82 (3 Aug. 2010), pp. 2257–2298. DOI: 10.1103/RevModPhys.82.2257.

[97] Eiichi Mizuta, Hideki Watanabe, and Toshihiko Baba. "All Semiconductor Low-Δ Photonic Crystal Waveguide for Semiconductor Optical Amplifier." In: *Japanese Journal of Applied Physics* 45.8A (Aug. 2006), pp. 6116–6120. DOI: 10.1143/jjap.45.6116.

[98] Daisuke Mori and Toshihiko Baba. "Dispersion-controlled optical group delay device by chirped photonic crystal waveguides." In: *Applied Physics Letters* 85.7 (2004), pp. 1101–1103. DOI: `10.1063/1.1783014`.

[99] F. Morichetti et al. "The first decade of coupled resonator optical waveguides: bringing slow light to applications." In: *Laser & Photonics Reviews* 6.1 (2012), pp. 74–96. DOI: `10.1002/lpor.201100018`.

[100] J. Mørk, Y. Chen, and M. Heuck. "Photonic Crystal Fano Laser: Terahertz Modulation and Ultrashort Pulse Generation." In: *Phys. Rev. Lett.* 113 (16 Oct. 2014), p. 163901. DOI: `10.1103/PhysRevLett.113.163901`.

[101] J. Mørk and G. L. Lippi. "Rate equation description of quantum noise in nanolasers with few emitters." In: *Applied Physics Letters* 112.14 (2018), p. 141103. DOI: `10.1063/1.5022958`.

[102] J. Mørk et al. "Semiconductor Fano Lasers." In: *IEEE Journal of Selected Topics in Quantum Electronics* 25.6 (2019), pp. 1–14. DOI: `10.1109/JSTQE.2019.2922067`.

[103] Jesper Mørk and Torben R. Nielsen. "On the use of slow light for enhancing waveguide properties." In: *Opt. Lett.* 35.17 (Sept. 2010), pp. 2834–2836. DOI: `10.1364/OL.35.002834`.

[104] K. Nakahara et al. "Direct Modulation at 56 and 50 Gb/s of 1.3- μ m InGaAlAs Ridge-Shaped-BH DFB Lasers." In: *IEEE Photonics Technology Letters* 27.5 (2015), pp. 534–536. DOI: `10.1109/LPT.2014.2384520`.

[105] C. Z. Ning. "Semiconductor nanolasers." In: *physica status solidi (b)* 247.4 (2010), pp. 774–788. DOI: `10.1002/pssb.200945436`.

[106] Cun-Zheng Ning. "Semiconductor nanolasers and the size-energy-efficiency challenge: a review." In: *Advanced Photonics* 1.1 (2019), pp. 1–10. DOI: `10.1117/1.AP.1.1.014002`.

[107] K. Nishi et al. "Development of Quantum Dot Lasers for Data-Com and Silicon Photonics Applications." In: *IEEE Journal of Selected Topics in Quantum Electronics* 23.6 (Nov. 2017), pp. 1–7. ISSN: 1558-4542. DOI: `10.1109/JSTQE.2017.2699787`.

[108] Susumu Noda. "Seeking the Ultimate Nanolaser." In: *Science* 314.5797 (2006), pp. 260–261. DOI: `10.1126/science.1131322`.

[109] Masahiro Nomura et al. "Room temperature continuous-wave lasing in photonic crystal nanocavity." In: *Opt. Express* 14.13 (June 2006), pp. 6308–6315. DOI: `10.1364/OE.14.006308`.

[110] Justin Norman et al. "Electrically pumped continuous wave quantum dot lasers epitaxially grown on patterned, on-axis (001) Si." In: *Opt. Express* 25.4 (Feb. 2017), pp. 3927–3934. DOI: `10.1364/OE.25.003927`.

[111] Justin C. Norman et al. "Perspective: The future of quantum dot photonic integrated circuits." In: *APL Photonics* 3.3 (2018), p. 030901. DOI: 10.1063/1.5021345.

[112] M. Notomi et al. "Extremely Large Group-Velocity Dispersion of Line-Defect Waveguides in Photonic Crystal Slabs." In: *Phys. Rev. Lett.* 87 (25 Nov. 2001), p. 253902. DOI: 10.1103/PhysRevLett.87.253902.

[113] Masaya Notomi. "Manipulating light with strongly modulated photonic crystals." In: *Reports on Progress in Physics* 73.9 (Aug. 2010), p. 096501. DOI: 10.1088/0034-4885/73/9/096501.

[114] Masaya Notomi and Takasumi Kuramochi Eiichi Tanabe. "Large-scale arrays of ultrahigh-Q coupled nanocavities." In: *Nature Photonics* 2.12 (Nov. 2008), pp. 741–747. DOI: 10.1038/nphoton.2008.226.

[115] Masaya Notomi and Hideaki Taniyama. "On-demand ultrahigh-Q cavity formation and photon pinning via dynamic waveguide tuning." In: *Opt. Express* 16.23 (Nov. 2008), pp. 18657–18666. DOI: 10.1364/OE.16.018657.

[116] Ian O'Driscoll et al. "Electron and hole dynamics of InAs/GaAs quantum dot semiconductor optical amplifiers." In: *Applied Physics Letters* 91 (Sept. 2007), p. 071111. DOI: 10.1063/1.2771374.

[117] L. O'Faolain et al. "Loss engineered slow light waveguides." In: *Opt. Express* 18.26 (Dec. 2010), pp. 27627–27638. DOI: 10.1364/OE.18.027627.

[118] M Okano et al. "Analysis of two-dimensional photonic crystal L-type cavities with low-refractive-index material cladding." In: *Journal of Optics* 12.7 (June 2010), p. 075101. DOI: 10.1088/2040-8978/12/7/075101.

[119] O. Painter et al. "Two-Dimensional Photonic Band-Gap Defect Mode Laser." In: *Science* 284.5421 (1999), pp. 1819–1821. ISSN: 0036-8075. DOI: 10.1126/science.284.5421.1819.

[120] N. C. Panoiu, J. F. McMillan, and C. W. Wong. "Theoretical Analysis of Pulse Dynamics in Silicon Photonic Crystal Wire Waveguides." In: *IEEE Journal of Selected Topics in Quantum Electronics* 16.1 (2010), pp. 257–266. ISSN: 1558-4542. DOI: 10.1109/JSTQE.2009.2025392.

[121] Hong-Gyu Park et al. "Electrically Driven Single-Cell Photonic Crystal Laser." In: *Science* 305.5689 (2004), pp. 1444–1447. ISSN: 0036-8075. DOI: 10.1126/science.1100968.

[122] M Patterson and S Hughes. "Theory of disorder-induced coherent scattering and light localization in slow-light photonic crystal waveguides." In: *Journal of Optics* 12.10 (Sept. 2010), p. 104013. DOI: 10.1088/2040-8978/12/10/104013.

[123] M. Patterson et al. "Disorder-Induced Coherent Scattering in Slow-Light Photonic Crystal Waveguides." In: *Phys. Rev. Lett.* 102 (25 June 2009), p. 253903. DOI: 10.1103/PhysRevLett.102.253903.

[124] M. Patterson et al. "Disorder-induced incoherent scattering losses in photonic crystal waveguides: Bloch mode reshaping, multiple scattering, and breakdown of the Beer-Lambert law." In: *Phys. Rev. B* 80 (19 Nov. 2009), p. 195305. DOI: 10.1103/PhysRevB.80.195305.

[125] M. L. Povinelli, Steven G. Johnson, and J. D. Joannopoulos. "Slow-light, band-edge waveguides for tunable time delays." In: *Opt. Express* 13.18 (Sept. 2005), pp. 7145–7159. DOI: 10.1364/OPEX.13.007145.

[126] Fabrice Raineri, Alexandre Bazin, and Rama Raj. "Optically Pumped Semiconductor Photonic Crystal Lasers." In: *Compact Semiconductor Lasers.* John Wiley & Sons, Ltd, 2014. Chap. 2, pp. 33–90. ISBN: 9783527655342. DOI: 10.1002/9783527655342.ch2.

[127] Thorsten S. Rasmussen. "Light-matter interaction and laser dynamics in nanophotonic structures." PhD thesis. 2020.

[128] Thorsten S. Rasmussen, Yi Yu, and Jesper Mørk. "All-optical non-linear activation function for neuromorphic photonic computing using semiconductor Fano lasers." In: *Opt. Lett.* 45.14 (July 2020), pp. 3844–3847. DOI: 10.1364/OL.395235.

[129] Thorsten S. Rasmussen, Yi Yu, and Jesper Mørk. "Modes, stability, and small-signal response of photonic crystal Fano lasers." In: *Opt. Express* 26.13 (June 2018), pp. 16365–16376. DOI: 10.1364/OE.26.016365.

[130] Thorsten S. Rasmussen, Yi Yu, and Jesper Mørk. "Photonic crystal laser based on Fano interference allows for ultrafast frequency modulation in the THz range." In: *Novel In-Plane Semiconductor Lasers XVIII.* Ed. by Alexey A. Belyanin and Peter M. Smowton. Vol. 10939. International Society for Optics and Photonics. SPIE, 2019, pp. 20–28. DOI: 10.1117/12.2506236.

[131] Thorsten S. Rasmussen, Yi Yu, and Jesper Mørk. "Suppression of Coherence Collapse in Semiconductor Fano Lasers." In: *Phys. Rev. Lett.* 123 (23 Dec. 2019), p. 233904. DOI: 10.1103/PhysRevLett.123.233904.

[132] Thorsten S. Rasmussen, Yi Yu, and Jesper Mørk. "Theory of Self-pulsing in Photonic Crystal Fano Lasers." In: *Laser & Photonics Reviews* 11.5 (2017), p. 1700089. DOI: 10.1002/lpor.201700089.

[133] B. Rigal et al. "Propagation losses in photonic crystal waveguides: effects of band tail absorption and waveguide dispersion." In: *Opt. Express* 25.23 (Nov. 2017), pp. 28908–28913. DOI: 10.1364/OE.25.028908.

[134] Atsushi Sakai, Go Hara, and Toshihiko Baba. In: 40 (2001), pp. L383–L385. DOI: 10.1143/jjap.40.l383.

[135] K. Sakai, E. Miyai, and S. Noda. "Coupled-Wave Theory for Square-Lattice Photonic Crystal Lasers With TE Polarization." In: *IEEE Journal of Quantum Electronics* 46.5 (2010), pp. 788–795. DOI: `10.1109/JQE.2009.2037597`.

[136] M. Saldutti, J. Mørk, and M. Gioannini. "Resonance condition and field distribution in line-defect photonic crystal cavities." In: *Proceedings Volume 11301, Novel In-Plane Semiconductor Lasers XIX* (2020), p. 30. DOI: `10.1117/12.2545149`.

[137] M. Saldutti et al. "A Simple Coupled-Bloch-Mode Approach to Study Active Photonic Crystal Waveguides and Lasers." In: *IEEE Journal of Selected Topics in Quantum Electronics* 25.6 (Nov. 2019), pp. 1–11. DOI: `10.1109/JSTQE.2019.2922377`.

[138] Marco Saldutti et al. "Impact of carrier transport on the performance of QD lasers on silicon: a drift-diffusion approach." In: *Photon. Res.* 8.8 (Aug. 2020), pp. 1388–1397. DOI: `10.1364/PRJ.394076`.

[139] Marco Saldutti et al. "Theory of slow-light semiconductor optical amplifiers." In: *Opt. Lett.* 45.21 (Nov. 2020), pp. 6022–6025. DOI: `10.1364/OL.403446`.

[140] Bahaa E. A. Saleh and Malvin Carl Teich. *Fundamentals of photonics*. 3rd ed. John Wiley & Sons, Inc., 2019.

[141] M. Santagiustina et al. "Theory of slow light enhanced four-wave mixing in photonic crystal waveguides." In: *Opt. Express* 18.20 (Sept. 2010), pp. 21024–21029. DOI: `10.1364/OE.18.021024`.

[142] T. Sato et al. "Photonic Crystal Lasers for Chip-to-Chip and On-Chip Optical Interconnects." In: *IEEE Journal of Selected Topics in Quantum Electronics* 21.6 (2015), pp. 728–737. DOI: `10.1109/JSTQE.2015.2420991`.

[143] C. Sauvan, J. P. Hugonin, and P. Lalanne. "Difference between penetration and damping lengths in photonic crystal mirrors." In: *Applied Physics Letters* 95.21 (2009), p. 211101. DOI: `10.1063/1.3266840`.

[144] C. Sauvan et al. "Modal-reflectivity enhancement by geometry tuning in Photonic Crystal microcavities." In: *Opt. Express* 13.1 (Jan. 2005), pp. 245–255. DOI: `10.1364/OPEX.13.000245`.

[145] Vincenzo Savona. "Electromagnetic modes of a disordered photonic crystal." In: *Phys. Rev. B* 83 (8 Feb. 2011), p. 085301. DOI: `10.1103/PhysRevB.83.085301`.

[146] E. S. Semenova et al. "Epitaxial growth of quantum dots on InP for device applications operating in the 1.55 μm wavelength range." In: *Quantum Dots and Nanostructures: Synthesis, Characterization, and Modeling XI*. Ed. by Diana L. Huffaker, Frank Szmulowicz, and Holger Eisele. Vol. 8996. International Society for Optics and Photonics. SPIE, 2014, pp. 9–17. DOI: `10.1117/12.2039567`.

[147] Yuting Shi et al. "Optical pumped InGaAs/GaAs nano-ridge laser epitaxially grown on a standard 300-mm Si wafer." In: *Optica* 4.12 (Dec. 2017), pp. 1468–1473. DOI: 10.1364/OPTICA.4.001468.

[148] A. Shinya et al. "Single-mode lasing of Lambda-scale Embedded Active-region Photonic-crystal (LEAP) laser with in-line coupled waveguide." In: *2013 IEEE Photonics Conference*. 2013, pp. 448–449. DOI: 10.1109/IPCon.2013.6656630.

[149] Anthony E. Siegman. *Lasers*. University Science Books, 1986.

[150] Maksim Skorobogatiy and Jianke Yang. *Fundamentals of Photonic Crystal Guiding*. Cambridge University Press, 2008. DOI: 10.1017/CBO9780511575228.

[151] P. M. Smowton and I. C. Sandall. "Gain in p-doped quantum dot lasers." In: *Journal of Applied Physics* 101 (2007), p. 013107. DOI: 10.1063/1.2405738.

[152] A. Sobiesierski and P.M. Smowton. "6.09 - Quantum-Dot Lasers: Physics and Applications." In: *Comprehensive Semiconductor Science and Technology*. Ed. by Pallab Bhattacharya, Roberto Fornari, and Hiroshi Kamimura. Elsevier, 2011, pp. 353–384. DOI: 10.1016/B978-0-44-453153-7.00034-1.

[153] Marin Soljačić and J. D. Joannopoulos. "Enhancement of nonlinear effects using photonic crystals." In: *Nature Materials* 3.4 (2005), pp. 211–219. DOI: 10.1038/nmat1097.

[154] Bong-Shik Song et al. "Transmission and reflection characteristics of in-plane hetero-photonic crystals." In: *Applied Physics Letters* 85.20 (2004), pp. 4591–4593. DOI: 10.1063/1.1823035.

[155] Bong-Shik Song et al. "Ultra-high-Q photonic double-heterostructure nanocavity." In: *Nature Materials* 4.3 (2005), pp. 207–210. DOI: 10.1038/nmat1320.

[156] S. Spiga et al. "Single-Mode High-Speed 1.5-µm VCSELs." In: *Journal of Lightwave Technology* 35.4 (2017), pp. 727–733. DOI: 10.1109/JLT.2016.2597870.

[157] Toshiaki Suhara. *Semiconductor laser fundamentals*. Optical engineering. Marcel Dekker, 2004.

[158] S. M. Sze and Kwok K. Ng. *Physics of Semiconductor Devices*. John Wiley & Sons, Ltd, 2006.

[159] K. Takeda et al. "Si nanowire waveguide coupled current-driven photonic-crystal lasers." In: *2017 Conference on Lasers and Electro-Optics Europe European Quantum Electronics Conference (CLEO/Europe-EQEC)*. 2017, pp. 1–1. DOI: 10.1109/CLEOE-EQEC.2017.8087147.

[160] Koji Takeda et al. "Few-fJ/bit data transmissions using directly modulated lambda-scale embedded active region photonic-crystal lasers." In: *Nature Photonics* 7.7 (2013), pp. 569–575. DOI: 10.1038/nphoton.2013.110.

[161] Masato Takiguchi et al. "Systematic study of thresholdless oscillation in high-β buried multiple-quantum-well photonic crystal nanocavity lasers." In: *Opt. Express* 24.4 (Feb. 2016), pp. 3441–3450. DOI: `10.1364/OE.24.003441`.

[162] Takasumi Tanabe et al. "Dynamic Release of Trapped Light from an Ultrahigh-Q Nanocavity via Adiabatic Frequency Tuning." In: *Phys. Rev. Lett.* 102 (4 Jan. 2009), p. 043907. DOI: `10.1103/PhysRevLett.102.043907`.

[163] Yoshinori Tanaka, Takashi Asano, and Susumu Noda. "Design of Photonic Crystal Nanocavity With Q-Factor of $\sim 10^9$." In: *J. Lightwave Technol.* 26.11 (June 2008), pp. 1532–1539. DOI: `10.1109/JLT.2008.92`.

[164] M. Tang et al. "Optimizations of Defect Filter Layers for 1.3-μm InAs/GaAs Quantum-Dot Lasers Monolithically Grown on Si Substrates." In: *IEEE Journal of Selected Topics in Quantum Electronics* 22.6 (Nov. 2016), pp. 50–56. ISSN: 1558-4542. DOI: `10.1109/JSTQE.2016.2551941`.

[165] A. Tibaldi et al. "VENUS: A Vertical-Cavity Surface-Emitting Laser Electro-Opto-Thermal NUmerical Simulator." In: *IEEE Journal of Selected Topics in Quantum Electronics* 25.6 (Nov. 2019), pp. 1–12. ISSN: 1558-4542. DOI: `10.1109/JSTQE.2019.2893755`.

[166] Quynh Vy Tran et al. "Photonic crystal membrane waveguides with low insertion losses." In: *Applied Physics Letters* 95.6 (2009), p. 061105. DOI: `10.1063/1.3205452`.

[167] B. Tromborg et al. "Transmission line description of optical feedback and injection locking for Fabry-Perot and DFB lasers." In: *IEEE Journal of Quantum Electronics* 23.11 (1987), pp. 1875–1889. ISSN: 1558-1713. DOI: `10.1109/JQE.1987.1073251`.

[168] R. S. Tucker et al. "Propagation delays and transition times in pulse-modulated semiconductor lasers." In: *Applied Physics Letters* 48.25 (1986), pp. 1707–1709. DOI: `10.1063/1.96810`.

[169] Kerry J. Vahala. "Optical microcavities." In: *Nature* 424.6950 (2003), pp. 839–846. DOI: `10.1038/nature01939`.

[170] Yurii A. Vlasov et al. "Active control of slow light on a chip with photonic crystal waveguides." In: *Nature* 438.7064 (2005), pp. 65–69. DOI: `10.1038/nature04210`.

[171] J. Vučković et al. "Optimization of the Q factor in photonic crystal microcavities." In: *IEEE Journal of Quantum Electronics* 38.7 (2002), pp. 850–856. DOI: `10.1109/JQE.2002.1017597`.

[172] Yating Wan et al. "1.3 μm submilliamp threshold quantum dot micro-lasers on Si." In: *Optica* 4.8 (Aug. 2017), pp. 940–944. DOI: `10.1364/OPTICA.4.000940`.

[173] Fengwen Wang et al. "Maximizing the quality factor to mode volume ratio for ultra-small photonic crystal cavities." In: *Applied Physics Letters* 113.24 (2018), p. 241101. DOI: 10.1063/1.5064468.

[174] Shyh Wang. "Energy velocity and effective gain in distributed–feedback lasers." In: *Applied Physics Letters* 26.3 (1975), pp. 89–91. DOI: 10.1063/1.88091.

[175] Zhechao Wang et al. "Novel Light Source Integration Approaches for Silicon Photonics." In: *Laser & Photonics Reviews* 11.4 (2017), p. 1700063. DOI: 10.1002/lpor.201700063.

[176] Fengnian Xia, Lidija Sekaric, and Yurii Vlasov. "Ultracompact optical buffers on a silicon chip." In: *Nature Photonics* 1.1 (2007), pp. 65–71. DOI: 10.1038/nphoton.2006.42.

[177] Weiqi Xue et al. "Thermal analysis of line-defect photonic crystal lasers." In: *Opt. Express* 23.14 (July 2015), pp. 18277–18287. DOI: 10.1364/OE.23.018277.

[178] Weiqi Xue et al. "Threshold Characteristics of Slow-Light Photonic Crystal Lasers." In: *Phys. Rev. Lett.* 116 (6 Feb. 2016), p. 063901. DOI: 10.1103/PhysRevLett.116.063901.

[179] E. Yablonovitch et al. "Donor and acceptor modes in photonic band structure." In: *Phys. Rev. Lett.* 67 (24 Dec. 1991), pp. 3380–3383. DOI: 10.1103/PhysRevLett.67.3380.

[180] Masafumi Yamaguchi, Akio Yamamoto, and Yoshio Itoh. "Effect of dislocations on the efficiency of thin-film GaAs solar cells on Si substrates." In: *Journal of applied physics* 59.5 (1986), pp. 1751–1753.

[181] A. Yariv. "Coupled-mode theory for guided-wave optics." In: *IEEE Journal of Quantum Electronics* 9.9 (1973), pp. 919–933. DOI: 10.1109/JQE.1973.1077767.

[182] Amnon Yariv et al. "Coupled-resonator optical waveguide: a proposal and analysis." In: *Opt. Lett.* 24.11 (June 1999), pp. 711–713. DOI: 10.1364/OL.24.000711.

[183] Tingting Yu, Lei Wang, and Jian-Jun He. "Bloch wave formalism of photon lifetime in distributed feedback lasers." In: *J. Opt. Soc. Am. B* 26.9 (Sept. 2009), pp. 1780–1788. DOI: 10.1364/JOSAB.26.001780.

[184] Yi Yu et al. "Demonstration of a self-pulsing photonic crystal Fano laser." In: *Nature Photonics* 11.2 (2017), pp. 1749–4893. DOI: 10.1038/nphoton.2016.248.

[185] Yi Yu et al. "Nonreciprocal transmission in a nonlinear photonic-crystal Fano structure with broken symmetry." In: *Laser & Photonics Reviews* 9.2 (2015), pp. 241–247. DOI: 10.1002/lpor.201400207.

[186] Z. Z. Zhang et al. “Effects of modulation p doping in InAs quantum dot lasers on silicon.” In: *Applied Physics Letters* 113 (2018), p. 061105. DOI: 10.1063/1.5040792.

[187] Taojie Zhou et al. “Continuous-wave quantum dot photonic crystal lasers grown on on-axis Si (001).” In: *Nature Communications* 11.1 (2020), p. 977. DOI: 10.1038/s41467-020-14736-9.

This Ph.D. thesis has been typeset by means of the TEX-system facilities. The typesetting engine was LuaLATEX. The document class was `toptesi`, by Claudio Beccari, with option `tipotesi =scudo`. This class is available in every up-to-date and complete TEX-system installation.